

University of Nottingham
UK | CHINA | MALAYSIA

A Two Degrees of Freedom Permanent Magnet Conical Motor

Sara Roggia

A dissertation submitted

in partial fulfilment of the requirements for the degree of

Doctor of Philosophy

at the University of Nottingham

School of Electrical and Electronic Engineering

August, 2017

ABSTRACT

This thesis focuses on the development of an innovative, electrical machine topology, which is based around a permanent magnet, synchronous machine that comprises a conical shape in order to achieve a two degrees of freedom machine. Such a machine is able to produce the rotational torque while also allowing for controlled movement in the axial direction. The proposed topology combines the high-performance capabilities of a permanent magnet machine with the desired axial movement that can be capitalised upon in order to remove traditional clutching-declutching technologies.

The main aim of this work is to prove the validity of the proposed technology. This is achieved by meeting the work's objectives of 1) describing the fundamental concepts of the proposed technology, 2) proposing and providing validated tools that can be used for the design of such a motor and 3) implementing the proposed machine for a real-world application. In order to clearly highlight the achieved objectives, the thesis focuses on the theory behind the proposed motor and the development of its model. The presented methodology has been successively used to compare the design results with those of an equivalent, conventional machine. The last part of the thesis is focused on the implementation of the proposed machine towards a specific traction application, where the application's particular, system-level challenges are identified, highlighting the significant benefits that can be achieved if the proposed machine is used as an alternative to the traditional solutions. A small-scale prototype of the proposed new machine technology has been completed and integrated into a mock-up system that replicates the final traction application. A "custom-built" control strategy has been implemented using specialised algorithms.

ACKNOWLEDGEMENTS

I would like to take this opportunity to thank Prof. Christopher Gerada, for his directions and constructive advice. I am deeply grateful to Dr Michael Galea for his constant help, motivating support and professional guidance. I must also express my gratitude to Prof. Cupertino for his precious interventions and his valuable contribution.

I would like to extend my thanks to Prof. Herve Morvan, the IAT team, PEMC research group and the technicians that make the realisation of this work possible.

Special thanks to my colleagues and friends for their help and support during the course of this work and for all the memories collected over the last years.

My deepest gratitude goes to my parents, my brother and my 'sisters', for their enduring encouragement, and, most of all, to my younger brother who shared with me this intense journey since the very beginning toward the completion of the final objective.

Sara

30.08.2017

TABLE OF CONTENTS

ABSTRACT ..... **i**

ACKNOWLEDGEMENTS ..... **ii**

LIST OF FIGURES ..... **viii**

LIST OF TABLES ..... **xii**

ACRONYMS ..... **xiii**

GLOSSARY OF SYMBOLS ..... **xv**

Chapter 1 Introduction, Background and Evolution **1**

1.1 Motivations 2

1.2 High Torque Density Machines 4

1.2.1 PM Machines 5

1.3 Conical Machines 6

1.3.1 Single-Sided PMCM 8

1.4 Contribution to knowledge 9

1.5 List of Publications 9

1.6 Thesis Outline 10

1.7 Conclusion 11

Chapter 2 Proposed Application **12**

2.1 Background 13

2.1.1 MEA 13

2.1.2 Electric Taxiing System 13

2.1 Existing E-Taxiing Schemes 15

2.1 The DD Actuator 16

2.1.1 Problem Definition 17

2.1.2 Electro-Magnetic Clutch System 18

2.2 Proposed Solution 20

2.3 Conclusion 23

Chapter 3 Basic Theory and Design Guidelines 24

3.1 Introduction 25

3.2 Geometry Description 25

3.2.1 Medium Radius and Equivalent Axial Length 25

3.2.2 Rotor and Magnets 27

3.2.3 Stator and Slots 28

3.3 Two-Dimensional Analysis of Conical Machines 29

3.4 Preliminary Design 33

3.4.1 Initial Requirements 33

3.4.2 Magnetic Circuit Design 36

3.4.3 Other Considerations 40

3.5 Forces in Conical Machines 42

3.6 Chapter Highlights and Contribution to Research 46

3.7 Conclusion 46

Chapter 4 Development of a High-Performing PMCM 47

4.1 High Performing Cylindrical Motor 48

4.1.1 Cylindrical Motor Analyses 49

4.1.2 Cylindrical Machine Forces and Torque 53

4.2 Conical Motor 57

4.2.1 The Proposed Two-Dimensional Analysis Methodology 58

4.2.2 Application of the Proposed Methodology 58

4.2.3 Conical Motor Performances 60

4.3 Cylindrical versus Conical Motor Performances 65

4.4 Torque Design Formula and 2D Model Guidelines 67

4.4.1 Correct 2D Model Approximation 68

4.4.2 Analytical Torque Rationale 71

4.4.3 Final Torque Design formula 73
4.5 Axial Force Estimation 74
4.6 Chapter Highlights and Contribution to Research 76
4.7 Conclusion 77
Chapter 5 Applied Design 79
5.1 Design Parameters 80
5.1.1 The Machine Stator 80
5.2 Rotor Design Choices 83
5.2.1 Magnets Material Choice 83
5.3 Two-Dimensional PMCM Model 86
5.4 Magnet Configuration Choice 89
5.4.1 Possible Configurations 89
5.4.2 Rotor Configuration 91
5.5 Sensitivity Analyses of the Main Geometric Parameters 95
5.5.1 Different Air-gap Length 96
5.5.2 Combined Skewing and Offset Analysis and Final Selection 97
5.6 Final Design Performances 98
5.7 Axial Force Calculation 101
5.8 Chapter Highlights and Contribution to Research 102
5.9 Conclusion 103
Chapter 6 Manufacturing, Testing and Control 104
6.1 Conical PM Rotor Manufacturing 105
6.2 Experimental Set-up 106
6.3 Tests without Motor Control 110
6.3.1 Measurements of Motor Parameters 110
6.3.2 No-Load Tests 111
6.3.3 Load-Tests with Disengaged Rotor 112

6.4 Motor Control and Testing 115
6.4.1 Current Control Loop and Speed Loop 116
6.4.2 Load-Tests Engaged Rotor 117
6.4.3 Axial Position Control 119
6.5 Axial Force Measurements 122
6.6 Chapter Highlights and Contribution to Research 123
6.7 Conclusion 123
Chapter 7 Implementation of the PMCM for a Particular Aerospace Traction Application 125
7.1 Conical E-Taxiing System 126
7.2 Small-size Demonstrator 128
7.2.1 System Implementation with ICM (as proof of concept) 129
7.2.2 System Implementation with PMCM 132
7.3 Chapter Highlights and Contribution to Research 133
7.4 Conclusion 133
Chapter 8 Sensorless Monitoring of Rotor Axial Position 135
8.1 The Available ICM 136
8.2 Axial Position Monitoring Procedure 137
8.2.1 Monitoring System Rational 138
8.2.2 The Basic Theory 139
8.2.3 Monitoring System Implementation 142
8.3 Experimental Results 144
8.3.1 Preliminary Experiments 145
8.3.2 Monitoring Results 150
8.4 Axial Force Measurements 154
8.5 Chapter Highlights and Contribution to Research 156
8.6 Conclusion 156

Chapter 9 Conclusion **157**

9.1 Overview of the Work 158

9.1.1 2D Approach for Analyses and Design of CMs 158

9.1.2 Single-Sided PMCM Advantages 159

9.1.3 Cylindrical versus Conical Machines 161

9.1.4 Applicability of PMCM 163

9.2 Main Contributions to Research 164

9.3 Future Work 166

REFERENCES **167**

Appendixes **175**

Appendix A PM Conical Rotor Design Parameters: Additional Tables . **176**

Appendix B Test-Rig Equipment Specifics **181**

LIST OF FIGURES

Figure 1.1 – Cross Section of a Cylindrical Machine 3
Figure 1.2 – Cross Section of a Conical Machine 3
Figure 1.3 – Conical Induction Motor Cross Section [27] 8
Figure 2.1 – Calculated Short Circuit Current and Torque of Cylindrical DDWA 19
Figure 2.2 – Possible System Configurations 22
Figure 3.1 – Cross-Sectional View of the Conical Machine 26
Figure 3.2 – Conical Shaped Magnet 27
Figure 3.3 – Conical Shaped Magnet Sectors 27
Figure 3.4 – Slot and Tooth Dimensions 28
Figure 3.5 – 2D Conical Machine Model 29
Figure 3.6 – "Twins" Cylindrical and Conical Machines 31
Figure 3.7 – 3D FEA Result Comparison of Cylindrical vs Conical No-Load Axial Flux Density (Half-Way Airgap z=25mm) 31
Figure 3.8 – Comparison of 3D FE vs Analytical No-Load Axial Flux Density in the Conical Machine (Half-Way Airgap z=25mm) 32
Figure 3.9 – Integration Area Elements on the Conical Lateral Surface 33
Figure 3.10 – Comparison of No-Load Axial Flux Density at Half-Way Airgap and Different z-axis Coordinates 33
Figure 3.11 – Air-gap Variation 34
Figure 3.12 – Main and Leakage Flux Paths in Magnetic Circuit 38
Figure 3.13 – Forces Acting on the Conical Machine 42
Figure 3.14 – Forces Acting on the Cylindrical Machine 45
Figure 4.1 – Torque and Speed Duty Cycles 48
Figure 4.2 – Main Cylindrical Motor Features 49
Figure 4.3 – Main Dimensions of the Cylindrical Motor 50
Figure 4.4 – Star of Slots of the Cylindrical Motor Winding 52
Figure 4.5 – No-Load Performances of the Cylindrical Motor 53
Figure 4.6 – Analytical vs FEM Forces of the Cylindrical Motor 54
Figure 4.7 – Flux Density Distribution in the Cylindrical Motor Air-Gap 55
Figure 4.8 – Stress Distribution on the Cylindrical Motor Rotor Surface 56

Figure 4.9 – Analytical vs FEM Torque of the Cylindrical Motor 56
Figure 4.10 – Equivalent Conical Motor 59
Figure 4.11 – Normal and Tangential Stress Distribution Sub-Motor 1 61
Figure 4.12 – Normal and Tangential Stress Distribution Sub-Motor 2 62
Figure 4.13 – Normal and Tangential Stress Distribution Sub-Motor 3 63
Figure 4.14 – Analytical vs FEM Total Force of the Conical Motor 64
Figure 4.15 – Total Torque of the Conical Motor 64
Figure 4.16 – Cylindrical vs Conical Motor Torque 66
Figure 4.17 – Cylindrical vs Conical Motor Voltage 66
Figure 4.18 – Cylindrical vs Conical Motor Flux 66
Figure 4.19 – Correct Cone Enclosing Volume 69
Figure 4.20 – Analytical vs FEM Torque of the Conical Motor 70
Figure 4.21 – Equivalent Cylindrical Model of the Conical Motor 71
Figure 4.22 – Flux Density at Peak Load Conditions Calculated at Half-Way Airgap 72
Figure 4.23 – Flux Density at No-Load Conditions Calculated at Half-Way Airgap 72
Figure 4.24 – Conical Motor Axial Force 76
Figure 5.1 – PMCM Prototype Stator Section View 80
Figure 5.2 – Slot and Tooth Dimensions of the PMCM Prototype 81
Figure 5.3 – Winding Layout of the PMCM Prototype 82
Figure 5.4 – Winding Configuration of the PMCM Prototype 82
Figure 5.5 – Magnet PMCM Prototype Shape 85
Figure 5.6 – Equivalent Model of the PMCM Prototype 87
Figure 5.7 – Global View of the 2D Equivalent Model of the PMCM Prototype 87
Figure 5.8 – Total Configurations Comparison 94
Figure 5.9 – Final Rotor Design of the PMCM Prototype 99
Figure 5.10 – No-Load Performances of the PMCM Prototype 99
Figure 5.11 – Load Performances of the PMCM Prototype 100
Figure 5.12 – Demagnetization Prediction for Sub-Motor M1 100
Figure 5.13 – Axial Force of the PMCM Prototype 101
Figure 5.14 – Axial Force and Axial Displacement with Original Spring 101
Figure 6.1 – 3D Printed PM Conical Rotor 105

Figure 6.2 – “Off-the-shelf” Magnets 105
Figure 6.3 – Rotor Recesses Manufacturing 105
Figure 6.4 – PM Rotor with Magnets 105
Figure 6.5 – Test Rig Configuration 107
Figure 6.6 – Test-Rig Connection Scheme 108
Figure 6.7 – PM Conical Motor with Encoder 109
Figure 6.8 – Engaging Mechanism Detail 109
Figure 6.9 – Connection Scheme for Motor Parameters Evaluation 111
Figure 6.10 – FEM vs Experimental No-Load Voltage 111
Figure 6.11 – FEM vs Experimental No-Load Voltage Harmonics 112
Figure 6.12 – Load Test Configuration 112
Figure 6.13 – T-I Curves at Different Speeds with Disengaged Rotor 114
Figure 6.14 – T-ω and I-ω Curves at Different Load with Disengaged Rotor 115
Figure 6.15 – Complete Control Scheme 116
Figure 6.16 – d-axis Current PI Controller 116
Figure 6.17 – q-axis Current PI Controller 116
Figure 6.18 – Speed PI Controller 117
Figure 6.19 – T-$\mathbf{i_q}$ Curves at Different Speeds with Engaged Rotor 118
Figure 6.20 – T-ω Curves at Different Load Levels with Engaged Rotor 118
Figure 6.21 – $\mathbf{i_q}$-ω Curves at Different Load Levels with Engaged Rotor 118
Figure 6.22 – Linear Encoder Mounting 119
Figure 6.23 – Axial Position Measurements 120
Figure 6.24 – Axial Position Control 121
Figure 6.25 – Axial Force Measurements 122
Figure 6.26 – End-Stop Plate and Load Cell 122
Figure 7.1 – Taxi Route [95] 127
Figure 7.2 – Taxiing Procedure Before Take-Off 127
Figure 7.3 – E-Taxiing System Design 129
Figure 7.4 – Conical E-Taxiing Demonstrator 130
Figure 7.5 – Reference Angle for I-*f* Control System 131
Figure 7.6 – Control Scheme of the Induction Conical E-taxiing Motor 131
Figure 7.7 – Measured Phase Currents for I-*f* Control 132
Figure 8.1 – ICM Stator and Rotor 137
Figure 8.2 – Axial Estimation and Control Scheme 143

Figure 8.3 – Magnetizing Current Sequence 145
Figure 8.4 – I_n Trends with 500Hz and 1000Hz Injected Signal (Original Spring) 146
Figure 8.5 – Impedance Calculation at Positive Frequency of the Injected Signal 147
Figure 8.6 – Impedance Calculation at Negative Frequency of the Injected Signal 147
Figure 8.7 – LPF Magnitude Response 148
Figure 8.8 – Notch Filter Magnitude Response 148
Figure 8.9 – End-Stop Plate Test-Rig Configuration 149
Figure 8.10 – 3D LUT with 30% Weaker Spring 149
Figure 8.11 – I_n vs Axial Position Curves for 2D LUT Extracted from Figure 8.10 150
Figure 8.12 – Spectrum Comparison between Disengaged and Engaged Position 150
Figure 8.13 – Transient in d-axis Current 151
Figure 8.14 – LPF Output Current (Original Spring) 152
Figure 8.15 – Axial Position Estimation 152
Figure 8.16 – Spectrum Comparison with I-*f* Ctrl 153
Figure 8.17 – I_n Comparison at Standstill and Rotation (30% Weaker Spring) 153
Figure 8.18 – I_n Comparison at Standstill and Rotation (Original Spring) 154
Figure 8.19 – End Stop Plate with Load Cell 155
Figure 8.20 – Analytical vs Experimental Axial Force 155
Figure 9.1 – Analytical vs FEM Torque Computation 159
Figure A.1 – Sm_2Co_{17} Magnet Demagnetization Curve 179
Figure B. 1 – Technosoft Inverter 182
Figure B. 2 – DSpace Controller Board 182
Figure B. 3 – Induction Load Machine 182
Figure B. 4 – Torque Sensor 183
Figure B. 5 – Industrial Drive 183
Figure B. 6 – Incremental encoder 183
Figure B. 7 – Linear Encoder and Magnetic Band 184

LIST OF TABLES

Table 2.1 – E-Taxiing Configuration Comparison 21
Table 4.1 – Cylindrical Motor Specifications 48
Table 4.2 – Cylindrical Motor Details 50
Table 4.3 – Cylindrical Motor Performances 53
Table 5.1 – PMCM Prototype Stator Dimensions 81
Table 5.2 – Winding Properties of the PMCM Prototype 83
Table 5.3 – Magnet Features of the PMCM Prototype (Max Values) 86
Table 5.4 – PMCM Prototype Sub-Motors M_1, M_2, M_3 Main Features (in mm) 88
Table 5.5 – PMCM Prototype Sub-Motor M_4, M_5, M_6 Main Features (in mm) 88
Table 5.6 – Rotor Magnet Combinations 90
Table 5.7 – Magnets per Pole to Full Pole Pitch Ratio 91
Table 5.8 – Configuration Classification 92
Table 5.9 – Selected Configuration Comparison 95
Table 5.10 – Configuration Comparison with Different Air-gap Length 96
Table 5.11 – Combined Skewing and Offset Results 98
Table 6.1 – FEM vs Experimental Structural Analyses of PMCM Prototype 106
Table 6.2 – MUT Main Features 106
Table 8.1 – ICM Features 136
Table 8.2 – Measured Negative-Sequence of Carrier Current Signal at Different Level of Magnetizing Current and Axial Rotor Position with 30% Weaker Spring 147
Table 9.1 – ICM vs PMCM Qualitative Comparison 161
Table 9.2 – Cylindrical vs Conical Motor Performances 162
Table A.1 – Slot and Winding Properties Calculation 177
Table A.2 – Star of Slots and k_w Calculation 178
Table A. 3 – Sub-Motor Cross-Sections 180
Table B. 1 – Test-rig Components 182

ACRONYMS

CM	Conical Machine
CS	Current Sensor
CU	Control Unit
DD	Direct Drive
DSP	Digital Signal Processing
EGTS	Electric Green Taxiing System
ETS	Electric Taxiing System
FE	Finite Element
G.C.D.	Greatest Common Divisor
GT	Green Taxiing
GUI	Graphical User Interface
HF	High Frequency
ICM	Induction Conical Machine
IM	Induction Motor
IPM	Interior Permanent Magnet
LM	Load Motor
LG	Landing Gear
LPF	Low-pass Filter
LUT	Look-up Table
MEA	More Electric Aircraft
MMF	Magneto-Motive Force
MST	Maxwell Stress Tensor
MUT	Motor Under Test
PC	Permeance Coefficient
PM	Permanent Magnet
PMCM	Permanent Magnet Conical Machine
PS	Position Sensor
SMPM	Surface Mounted Permanent Magnet
TRV	Torque per Rotor Volume
UoN	University of Nottingham
VS	Voltage Sensor

WA	Wheel Actuator
WT	Wheel Tug

GLOSSARY OF SYMBOLS

a	Load ratio
A	Electric loading (A)
A_w	Conductor area (mm^2)
A_g	Equivalent air-gap pole area (mm^2)
A_M	Equivalent magnet pole area (mm^2)
A_p	Equivalent pole area (mm^2)
A_s	Bare slot area (mm^2)
b	Stator tooth width (mm)
$(BH)_{max}$	Magnet normal maximum energy product (kJ/m^3)
B	Magnetic loading (T)
$\bar{B}_g$	Air-gap flux density at the medium radius (T)
$\bar{B}_m$	Equivalent magnet working point (T)
b_{max}	Stator tooth width at the maximum cone radius (mm)
b_{min}	Stator tooth width at the minimum cone radius (mm)
B_n	Normal component of the flux density (T)
B_r	Magnet residual induction (T)
B_r	Radial component of normal flux density (T)
B_t	Tangential flux density (T)
B_z	Axial component of normal density (T)
$\bar{D}$	Medium diameter of the conical machine (mm)
D_e	Outer stator diameter of the PMCM prototype (mm)
D_{ew}	End winding outer diameter (mm)
$D_{i,1}$	Maximum internal stator diameter of the PMCM prototype (mm)
$D_{i,2}$	Minimum internal stator diameter of the PMCM prototype (mm)
D_m	Magnet diameter of the PMCM prototype sub-motors (mm)
D_{max}	Maximum diameter of the conical machine (mm)
D_{min}	Minimum diameter of the conical machine (mm)
dq	Time-independent rotary reference frame
D_{re}	Outer rotor diameter of the PMCM prototype sub-motors (mm)
D_{ri}	Inner rotor diameter of the PMCM prototype sub-motors (mm)

D_{si}	Inner stator diameter of the PMCM prototype sub-motors (*mm*)
D_w	Bare wire diameter (*mm*)
$(\vec{e_r}, \vec{e_\vartheta}, \vec{e_z})$	Cylindrical coordinate system
$(\vec{e_1}, \vec{e_2}, \vec{e_3})$	Generic orthogonal coordinate system
f	Frequency (*Hz*)
$\vec{f}$	Force density in the air-gap (N/mm^2)
f^*	Reference frequency (*Hz*)
F_1, F_2, F_3	Total force of sub-motor 1, 2 and 3 of the conical motor model (*N*)
F_a	Magneto-Motive Force (*Ampere-turn*)
f_{LKG}	Leakage factor
$F_{n,1}, F_{n,2}, F_{n,3}$	Normal force of sub-motor 1, 2 and 3 of the conical motor model (*N*)
$F_{n,tot}$	Total normal force of conical motor model (*N*)
f_r	Radial component of force density (N/mm^2)
F_r	Radial component of the total force (*N*)
F_t	Tangential component of the total force (*N*)
$F_{t,1}, F_{t,2}, F_{t,3}$	Tangential force of sub-motor 1, 2 and 3 of the conical motor model (*N*)
$F_{t,tot}$	Total tangential force of conical motor model (*N*)
F_{tot}	Total force of conical motor model (*N*)
f_z	Axial component of force density (N/mm^2)
F_z	Axial component of the total force (*N*)
g'	Effective air-gap length (*mm*)
h_{br}	Rotor back-iron height (*mm*)
h_{bs}	Stator back-iron height (*mm*)
H_{cb}	Magnet coercitive force (*kA/m*)
H_{ci}	Magnet intrinsic coercitive force (*kA/m*)
h_{ew}	End winding height (*mm*)
h_g	End winding gap height (*mm*)
$\vec{H}$	Vector field strength (*A/m*)
H_n	Normal component of the magnetic field (*A/m*)
h_s	Slot height (*mm*)

h_{sb}	Stator back-iron (*mm*)
H_t	Tangential component of the magnetic field (*A/m*)
i	Index of motors in the conical PM model
I	RMS phase current (*A*)
I^*	Reference amplitude current (*A*)
$\mathbf{i}_s^d$	Conical induction motor magnetising current (*A*)
$\mathbf{i}_{shf}^{\alpha\beta}$	High-frequency carrier current signal (*A*)
I-f	Current-frequency control method
I_n	Amplitude of negative sequence of carrier current sugnal (*A*)
I_p	Amplitude of positive sequence of carrier current signal (*A*)
I_{pk}	Peak current (*A*)
I_{sc}	Short-circuit current (*A*)
J_{pk}	Peak current density (A/mm^2)
k_d	Distribution factor
k_p	Pitch factor
k_{fill}	Bare slot fill factor
l_{ax}	Cylindrical motor axial length (*mm*)
$l_{ax,\gamma}$	Equivalent axial length of the conical motor model (*mm*)
$l_{ax,\gamma 13}$	Equivalent axial length of the conical motor model with 13° cone angle (*mm*)
$l_{ax,\gamma 20}$	Equivalent axial length of the conical motor model with 20° cone angle (*mm*)
L_d	d-axis inductance (*mH*)
l_{Fe}	Effective axial length of the ICM (*mm*)
L_{Fe}	Effective axial length of the conical machine (*mm*)
$L_{Fe,\gamma}$	Equivalent axial length of the conical machine (*mm*)
L_m	Conical induction motor magnetizing inductance (*mH*)
L_M	Magnet length (*mm*)
L_q	q-axis inductance (*mH*)
l_{stk}	Effective axial length of each sub-motor of the PMCM prototype (*mm*)
L_{stk}	Total effective axial length of the PMCM prototype (*mm*)

$l_{stk,\gamma}$	Equivalent axial length of each sub-motor of the PMCM prototype (*mm*)
$L_{stk,\gamma}$	Total equivalent axial length of the PMCM prototype (*mm*)
m	Number of phases
M_1, M_2, M_3,	Sub-Motors 1, 2, 3 of the PMCM prototype model
M_4, M_5, M_6	Sub-Motors 4, 5, 6 of the PMCM prototype model
MLT	Mean length turn (*mm*)
n	Normal vector to the lateral rotor surface
n	Number of motors of conical 2D model
N	Number of turns
N_c	Number of coils per phase
N_{ph}	Number of turns in series per phase
n_r	Radial component of the normal vector
N_s	Number of stator slot
N_t	Number of coils per turn
n_z	Axial component of the normal vector
p	Number of pole pairs
P_L	Rotor internal permeance (*H*)
P_{m0}	Internal magnet permeance (*H*)
Q	Number of slots for the star of slots
q_{ph}	Spokes per phasor
$\bar{r}$	Medium radius of the conical machine (*mm*)
$\bar{r}_g$	Medium air-gap radius (*mm*)
$\bar{r}_i$	Medium rotor bore radius of the conical motor model (*mm*)
$\bar{r}_{i,13}$	Medium rotor bore radius of the conical motor model with 13° cone angle (*mm*)
$\bar{r}_{i,20}$	Medium rotor bore radius of the conical motor model with 20° cone angle (*mm*)
$\bar{r}_M$	Medium magnet radius (*mm*)
$\bar{r}_{si}$	Medium stator bore radius of the PMCM and ICM prototype (*mm*)
$r_{si,max}$	Maximum radius at stator bore (*mm*)
$r_{si,min}$	Minimum radius at stator bore (*mm*)

$R_{ph,tot}$	Total phase resistance (Ω)
R_c	Coil resistance (Ω)
R_e	External rotor radius of the cylindrical motor (mm)
r_g	Effective air-gap radius (mm)
R_g	Air-gap reluctance (H^{-1})
R_i	Cylindrical motor internal rotor radius (mm)
R_{i1}, R_{i2}, R_{i3}	Internal rotor radii of sub-motors 1, 2 and 3 of conical motor model (mm)
R_{LL}	Line-to-line resistance (Ω)
r_M	Effective magnet radius (mm)
r_{max}	Maximum radius of the conical machine (mm)
r_{min}	Minimum radius of the conical machine (mm)
$r_{min,13}$	Minimum cone radius of the conical motor model with 13° cone angle (mm)
$r_{min,20}$	Minimum cone radius of the conical motor model with 20° cone angle (mm)
R_{ph}	Phase resistance (Ω)
R_s	Stator resistance (Ω)
R_{si}	Stator internal radius of the cylindrical motor (mm)
$r_{si,max}$	Maximum stator bore radius of the PMSM and ICM prototype (mm)
$r_{si,min}$	Minimum stator bore radius of the PMSM and ICM prototype (mm)
S_2	Rotor lateral surface (mm^2)
t	Motor periodicity
$\overleftrightarrow{T}$	Maxwell stress tensor (N/mm^2)
T_1, T_2, T_3	Torque of sub-motor 1, 2 and 3 of conical motor model (N)
T_{amb}	Ambient temperature ($^{\circ}C$)
T_M	Torque sensor
T_{sc}	Braking torque (N)
T_{tot}	Total torque of conical motor model (N)
$T_{\gamma=13°}$	Total torque of the conical motor model with 13° cone angle (N)

$T_{\gamma=20°}$	Total torque of the conical motor model with 20° cone angle (N)
$\mathbf{u}_{\mathrm{shf}}^{\alpha\beta}$	High frequency voltage vector (V)
U_{Inj}	Amplitude of HF injection voltage (V)
V/Hz	Volts/Hertz control method
$V_{Con,Fe}$	Iron volume of the truncated cone (mm^3)
$V_{Cyl,Fe}$	Iron volume of the cylindrical machine (mm^3)
V_{dc}	DC-link voltage (V)
V_r	Rotor truncated cone volume (mm^3)
V_{slot}	Slot volume (mm^3)
w	Slot width (mm)
w_{so}	Slot opening (mm)
w_t	Tooth width (mm)
$w_{t,tot}$	Total tooth witdh (mm)
x	Axial rotor displacement in the conical machine (mm)
y_q	Coil pitch
α_{PM}	Magnet lineat span
$\alpha^e{}_s$	Electrical angle between adjacent slots ($^\circ$)
α_{ph}	Angle between two consecutive spokes ($^\circ$)
α_s	Angle between two adjacent slots ($^\circ$)
$\alpha\beta$	Time-dependent stationary frame
β_{PM}	Full pole linear span
β_s	Slot pitch
γ	Cone angle ($^\circ$)
δ	Material density (kg/m^3)
Δg	Air-gap length variation in the conical machine (mm)
Δl	Sub-motor axial length (mm)
Δr	Radius reduction rate (mm)
Δr_i	Radius increment in each sub-motor of the PMCM prototype (mm)
$\Delta r_{tot,13}$	Difference between maximum and minimum radii of the conical motor model with 13° cone angle (mm)
$\Delta r_{tot,20}$	Difference between maximum and minimum radii of the conical motor model with 20° cone angle (mm)

$\Delta\sigma\mathbf{L}_s$	Differential stator inductance (*mH*)
$\sum\sigma\mathbf{L}_s$	Average stator inductance (*mH*)
η	Percentage of torque reduction (*%*)
ϑ	Angle on rotor circumference (°)
ϑ_{ctrl}	Reference angle (°)
ϑ_e	Angle of rotating saliency (°)
λ_R	Rotor flux space vector (*Wb, Vs*)
μ	Material permeability (*H/m*)
μ_0	Vacuum permeability (*H/m*)
μ_r	Relative permeability
μ_{rec}	Recoil permeability
σ	Leakage factor
σ	Normal component of Maxwell stress tensor (N/mm^2)
$\sigma_1, \sigma_2, \sigma_3$	Normal stresses on rotor surface of sub-motor 1, 2 and 3 of the conical motor model (N/mm^2)
$\sigma\mathbf{L}_S$	Stator transient inductance (*mH*)
τ	Tangential component of Maxwell stress tensor (N/mm^2)
τ_1, τ_2, τ_3	Tangential stresses on rotor surface of sub-motor 1, 2 and 3 of the conical motor model (N/mm^2)
Φ_g	Air-gap flux (*Wb, Vs*)
Φ_L	Leakage Flux (*Wb, Vs*)
Φ_m	Magnet flux (*Wb, Vs*)
ω	Angular speed (*rpm*)
ω*	Reference angular speed (*rpm*)
ω_{Inj}	Injection frequency of the HF signal (*rad/s*)
ω_φ	Angular speed of rotor flux space vector (*rad/s*)

Chapter 1
Introduction, Background and Evolution

This Chapter introduces the overall project and the main motivations that led to the choice of a new topology of machine. A brief overview of the state-of-the-art of high torque dense machine technologies and existing conical machines is also offered.

The intent is to illustrate the scientific path that led to the choice of a new conical machine solution that combines the advantages of torque dense motors with the benefits obtained from a conical actuator.

At the end of the Chapter, a system solution for the new PM machine concept is suggested based on an existing conical machine arrangement.

1.1 Motivations

This research work is aimed at industrial applications that involve the use of torque-producing, rotating electrical machines that require an in-line (with the main power train) active engagement/disengagement mechanism. Various systems exist today to achieve the required linear movement that results in the desired 'linear displacement' and thus disengagement. These include electrical solutions (solenoids and linear motors), hydraulic actuators, mechanical clutches and/or complex hybrid systems such as electro-mechanical active clutches.

An area of interest that is very dependent on having an active and controllable engagement is that of traction for mobile applications, such as for aircraft and automotive vehicles where the presence of an active clutch usually cannot be prevented. These types of applications are usually required to cater for high levels of performance in terms of rotational power/torque density (especially if a direct drive solution with no gear-boxes is chosen) but also in terms of reliability and safety.

In general, automotive and aerospace traction systems achieve the required engagement, through the use of complex mechanical systems such as clutches and gear-boxes. These systems imply an extra component count, extra manufacturing costs and extra design effort. Thus, a 'one-body solution' that could produce the linear engagement/disengagement required while at the same time providing also the required rotational torque/power would be an ideal achievement.

Such a solution does exist and is generally known as a conical electrical machine. The basic principle of a Conical Machine (CM) relies on its conical geometry [1-3]. While conventional machines have the rotor and the stator lying in a concentric fashion as shown in Figure 1.1, a conical machine is configured in such a way as to have a coned shape, as shown in Figure 1.2.

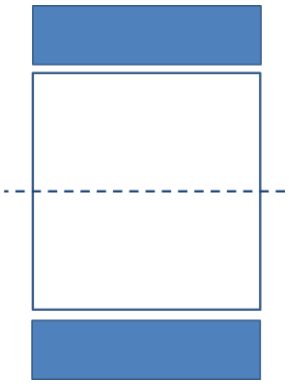


FIGURE 1.1 – CROSS SECTION OF A CYLINDRICAL MACHINE

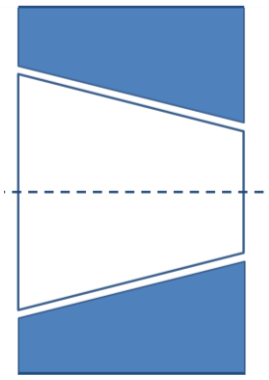


FIGURE 1.2 – CROSS SECTION OF A CONICAL MACHINE

The main advantage offered by a conical machine is that, thanks to its conical geometry, an extra degree of freedom is achieved. In fact, apart from the rotational movement, with an appropriate mechanical fixture/bearing design, the motor can be configured to achieve an axial movement of the rotor. Due to the conical shape and the appropriate bearing system, the inherent attraction between the machine's rotor and stator can be exploited such that rotational and axial movements occur simultaneously. The resulting horizontal force can in turn be exploited to 'emulate' linear actuation. For the right application, this can provide the required engagement/disengagement without having to resort to a secondary clutching system.

However, the main point to note is that all commercially-available CMs today are from the Induction Machine (IM) family. The main reason for this is the passive nature of IMs. An IM has no excitation source on its rotor and therefore the rotor is "attracted" to the stator only when the machine is being fed by the stator currents. As explained later in Section 1.3, this makes the IM an ideal solution for active engagement/disengagement through the stator/rotor attraction phenomenon, as the only extra effort required (when compared to a conventional machine) is a basic mechanical spring that returns the rotor to its original axial position when the machine is 'switched off'. While the above indicates the benefits and strengths of Induction Conical Machines (ICM), however in practice, the low values of power and torque densities synonymous with IMs, prevent a more wide-spread implementation of IMs as one-body solutions for traction in mobile applications, especially in aerospace where the torque to mass ratio plays such an important role.

In fact, it is well known that today the technology of choice for mobile applications is usually Permanent Magnet (PM) machines [4]. This is due to the capability of PM machines to achieve much higher torque and power densities and much better efficiencies when compared to all other machine technologies.

However, when considering PM technology for a conical motor configuration, significant challenges come into play. The inherent permanent excitation nature of the machine (due to the PMs) means that there is a permanent attraction between the rotor and stator which needs careful management in order to achieve appropriate, reliable and robust axial movement control in addition to the rotational torque. The highly challenging nature of the methodologies required to achieve this means that, today, there is no commercially available PM Conical Machine (PMCM). Thus, a one-body solution that combines the advantages of PM machines (high power density and high efficiency) with a conical geometry (axial movement) does not exist.

Therefore, this thesis is focused on the development and proof of concept of a PMCM and acts as the first step towards the achievement of PM electrical machines that can achieve the required linear movement, while at the same time providing excellent rotational power density levels. The work is done within the remit of a high performance, aerospace traction application. Appropriate design methodologies for such machines are developed and proposed and used to produce a machine prototype that fulfils and proves the concept of a PMCM. The scheme of the proposed motor is shown Section 1.3.1. The concept of PMCM is validated through the experimental testing of a manufactured prototype.

1.2 High Torque Density Machines

Traction applications, especially when no mechanical advantages (gear-boxes) are present, usually require machines that can deliver a high level of torque and power density (*Nm/kg* and Nm/m^3). In general, main objective functions for traction actuators (especially in aerospace and automotive) are a high torque/weight ratio, a high torque/ampere ratio and a high efficiency throughout the full speed range.

For the larger part of traction or actuation applications, the most preferred candidates among traditional machine families are IMs and PM motors.

IMs are still very much present all over the industrial world, however for mobile applications the last two decades have seen an ever-increasing presence of PM motors. While their robustness, elegance and low-cost features are still very attractive, the IM's inherent disadvantages related to higher losses, lower efficiency, lower power factor and above all their lower torque density performance, when compared to PM brushless machines [5]. This indicates why the general trend in transport research activities is mainly towards PM machines.

1.2.1 PM Machines

PM machines are characterised by high power density and efficiency, high torque/inertia and torque/volume ratios [6, 7]. The main disadvantage of these motors is the presence of a constant excitation due to the PMs. The other disadvantage is the possibility of demagnetizing the PMs, a risk which is very dependent on the machine temperature.

PM motors can be in general classified into different families according to the excitation voltage waveform, the direction of the flux and the position of the magnets on the rotor. The various topologies and categorisations of PM machines, based on the excitation voltage waveform, can be found in [5] and [8], where a general comparison is provided, whereas [9-13] offer classification and investigation studies on PM motors based on the flux behaviour.

For the scope of this work, the main important consideration to keep in mind is the configuration of the PMs. Based on the location of the magnets on the rotor, two main categories can be distinguished [14], namely Surface Mounted PM (SMPM) motors and PM motors with Interior PMs (IPM) (i.e. buried in the rotor laminations). The main advantages of IPM motors, such as their larger flux weakening capability, fault tolerance capability and better handling of short circuit current with respect to SMPM machines, are highlighted in [14-17], whereas, as it emerges from [18, 19], figures of merit of SMPM machines are the higher efficiency, fewer rotor losses, better utilisation of PM materials, the use of larger air-gap and reduction in machine volume and mass. These features help to improve torque density capabilities. Considering the early stage of the

technology that has been developed in this work of thesis, a SMPM motor configuration has been considered as the most sensible choice to prove the concept of the PMCMs.

1.3 Conical Machines

A conical machine is an electrical machine with a tapered air-gap. Conical machines behave magnetically and electrically in the same way as traditional electrical cylindrical machines. Whether the motor is an asynchronous or synchronous machine, in conical machines, the principles for magnetic field generation, armature reaction, the interaction between stator and rotor fields, torque production remains the same as in classical cylindrical machines.

In all electrical machines, the attraction between the rotor and stator can be represented by a set of forces acting on the rotor surface. In fact, the actual attraction force is one component of a 3D set of forces that acts in the axial, tangential and radial directions. In a cylindrical motor, due to the concentric nature of the rotor and stator, the axial force is theoretically null (and the other forces are constrained by the bearing assemblies). In a conically-shaped machine, the axial component does actually have a finite value and by an appropriate bearing configuration can be exploited to produce an axial movement. In fact, conical motors are sometimes also called sliding-rotor machines.

In 1992, an Induction Conical Machine (ICM) was engineered and patented by Bitsch et al. [20]. This ICM is accessorised with a braking system. The whole assembly was realised to use the axial force produced by the conical machine to overcome the force of the braking system that prevents the rotor from rotating during intermittent operations. Apart from this application, no consequent industrial use has been associated with the afore-mentioned ICM. In 2015, some studies [21, 22] revealed a sudden new interest in the technology. In [21, 22], thermal analyses are conducted on the same machine of [20]. The study conducted in [21] has the aim to assess the motor's reliability, even though the contextualization of the problem is not provided. The authors of [22] use the motor configuration of [20] to realise the model of a new thermal network

architecture; as in [21], also in [22], the implications of the study are not clarified.

Recently, the concept of conical motors has been introduced in a completely new context. In [23, 24], a new scheme is presented as a novel bearingless motor system. This invention is the evolution of the idea of conical magnetic bearings exposed in [25, 26]. The structure reported in [23, 24] envisages the presence of two identical PMCMs connected on the same shaft. The field produced by the PMs, mounted on the conical surface of the rotor, contains an axial component constantly acting on the rotor surface. In order to obtain a balanced system, the effects of the axial magnetic force in the two conical PM machines are compensated mounting the two motors on the same shaft with an opposite orientation. In this way, the pulling effects of the axial thrust produced in one motor are nullified by the pushing effects generated by the mirroring conical machine.

The aforementioned examples of conical motors [20, 23, 24] have in common the exploitation of the effects of the axial component of the force for diversified applications and objectives achieved by employing different solutions in terms of motor topology and system arrangement. However, it can be said that none of the previous conical machine systems are utilised to take advantage of the benefits that a conical motor can offer if utilised as a proper linear actuator in combination to its rotational movement.

At this stage, it is worth pointing out that no single-ended conical PM motor, such as that being proposed in this thesis has been found in literature. The challenge related to the need to compensate for the no-load axial force produced by the magnets has prevented this ideal PMCM configuration from being fully developed. The elegant solution presented in [23, 24] with two opposite ‘half’ conical PM motors to compensate each other is a very clever way of how to address the resultant attractive force challenges. This arrangement, of course, results in a cancelling-out of any possible axial movement and comes at the cost of a doubling of component count, resulting in a significant deterioration of reliability and power/torque densities.

1.3.1 Single-Sided PMCM

As mentioned above, conical motors exist in the form IMs and double-sided PM motors, whereas the main aim of this research is the study of a single-sided PM machine. Considering the lack of literature or previous examples of such a concept with PMs, a brief introduction to the closest and most relevant example is given in this section.

In this work, the motor configuration has been conceived similarly to the system of the ICM of [20] and [27]. A cross-sectional view of the existing ICM system is shown in Figure 1.3, whose source is [27]. This prototype is a braking system that envisages the presence of a spring in the front part of the rotor shaft and a disk in the final part of the machine. The spring pushes the rotor against the disk in order to prevent it from rotation when the machine is not operated. When current is applied, the axial force moves the rotor horizontally away from the disk: the spring is compressed and the rotor is free to rotate.

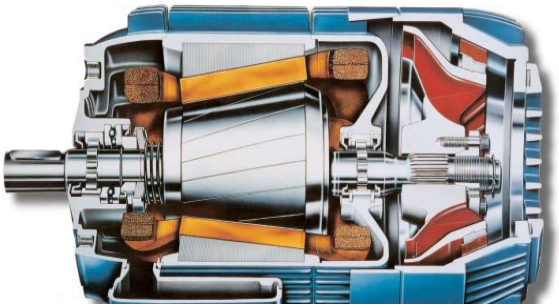


FIGURE 1.3 – CONICAL INDUCTION MOTOR CROSS SECTION [27]

While the above is all fine for a ICM, however for a PMCM, the constant presence of the axial force due to the field generated by the magnets needs to be considered carefully. A mechanical arrangement similar to [27] could be applied to achieve the required single-sided PM conical actuator. This will be investigated in Chapter 5.

1.4 Contribution to knowledge

The work in this thesis can claim to have provided new insight or product in the following aspects.

- Design of a new topology of PM machine that can operate with two degrees of freedom.
- Characterisation of 3D motor attributes into a two-dimensional domain.
- Definition of conical machines' design procedure using standard formulae, typically employed for cylindrical machines.
- Validation of the proposed models through experimental results.
- Realisation of the motor control using direct and quadrature axis current for the axial and rotational motor movements, respectively.
- Demonstration of a possible implementation of the proposed new motor technology and control strategy for a real-world application through a small-size prototype.
- Design of the mechanical system for clutching and declutching purposes.
- Formulation and implementation of a sensorless algorithm for monitoring the rotor axial position inside the stator.

1.5 List of Publications

Part of this work has been disseminated through different conferences and journal papers. One patent has been filed with the University of Nottingham.

- One patent filed with the University of Nottingham.
  Title: "A two degrees of freedom PM conical motor".
  Author: S. **Roggia**, M. Galea, F. Cupertino, C. Gerada.
- S. **Roggia**, F. Cupertino, C. Gerada, and M. Galea, "Axial position estimation of conical shaped motors for aerospace traction applications," *IEEE Transactions on Industry Applications*, vol. 53, pp. 5405 - 5414, 2017.
- S. **Roggia**, F. Cupertino, C. Gerada, and M. Galea, "A Two degrees of freedom system for wheel traction applications," *IEEE Transactions on Industrial Electronics*, vol. 65, pp. 4483-4491, 2017.

- S. **Roggia**, F. Cupertino, M. Galea, and C. Gerada, "Axial position estimation of conical shaped motor for electric taxiing application," presented at the IEEE Energy Conversion Congress and Expo (ECCE), Milwaukee, WI, 2016.
- S. **Roggia**, H. Morvan, M. Galea, “An overview of two UAV projects developed within the INNOVATE program”, in MEA Conference 2015, Toulouse, France.
- M. Galea, S. **Roggia**, L. Papini, Z. Xu, C. Tighe, M. Hamiti, et al., "Design aspects of a high torque density machine for an aerospace traction application," in Electrical Machines and Systems (ICEMS), 2014 17th International Conference on, 2014, pp. 2773-2778.

1.6 Thesis Outline

This first part of the thesis, specifically the first part of **Chapter 1**, focuses on the motivations that led to this motor concept. The existing state-of-the-art and similar technologies are summarised and surveyed in the following sections of **Chapter 1**. In the same chapter, the concept of the final machine structure is suggested based on a pre-existing assembly and a possible application for the CMs implementation is proposed.

In **Chapter 2** a traction application is suggested as a system example where the implementation of CMs can have significant contribution. The limits of the existing systems are described and the new configuration with an integrated conical machine is proposed.

In **Chapter 3** essential concepts employed in the rest of the thesis are explained. The theory behind conical motors is developed and a detailed approach for modelling the motor in a simplified manner is proposed and justified through Finite Element Analyses (FEA).

In **Chapter 4** the concepts and formulae developed in Chapter 3 are applied for the development of a PMCM equivalent to an existing cylindrical PM motor. Thus, a direct comparison between the performances of the two motor topologies is accomplished. The chapter also proposes a method to obtain an accurate 2D

equivalent model of the CM and a design formula for limiting the torque reduction in CMs.

Chapter 5 describes the design and development procedures of a small-scale prototype realised to prove the functioning motor concept. The exercise involves the real application of the concepts exposed in Chapter 3 and Chapter 4.

In **Chapter 6** the experimental results obtained from the testing procedure of the prototype are displayed. A conventional control technique has been implemented for the rotational movement of the motor, while an innovative control scheme is proposed and employed for the axial motion. Challenges are set to improve the control strategy and ameliorate motor performances.

In **Chapter 7** the aerospace traction application proposed for the CMs in Chapter 2 is analysed and developed. A small-size model of the suggested traction system has been realised with the ICM and the PMCM to prove the advantages of employing such a motor as a one-body solution to the existing system issues.

An additional feature to the system developed in Chapter 7 is proposed in **Chapter 8**. This consists in a control algorithm realised with the purpose of monitoring the rotor axial position inside the stator without the use of any sensor.

Conclusions are drawn in **Chapter 9** and further investigations on the research topic are suggested.

1.7 Conclusion

In this Chapter, an introduction to the work presented in this thesis is given. The need for a one-body solution to a high torque density machine with active engagement/disengagement capability was discussed and shown to be the rationale behind the idea of a PMCM that can achieve the required functionalities.

A real-word application has been suggested for the implementation of the PMCM proving how CMs can offer real advantges to the clutching and decluthing functionalities in traction systems.

The next Chapter tackles the basic theory of conical machines and derives a model, that is able to describe analytically the whole operation of a PMCM.

Chapter 2
Proposed Application

This work has been part of an European research project together with the Institute of Aerospace Technology of the University of Nottingham (UoN). The project is named INNOVATE. The acronym stands for Integration of Novel Aerospace Technology.

As a part of an aerospace research program, a traction application for an aircraft system, called electric-taxiing (ET), has been suggested as an example of the integration of the proposed motor technology in a real-world system. An explanatory description and contextualization of the electric-taxiing concept is given in this Chapter. The conical machine system has been offered as a substitute to the current system architectures where electro-mechanical challenges exist.

The proposed application is just an example of the possible implementation of CMs in real-world technologies. In fact, the new motor topology described in Chapter 1 results particularly advantageous in numerous traction applications where different problems exist due to the short-circuiting practice commonly used in PM machines.

2.1 Background

2.1.1 MEA

The present aerospace engineering research and development is investing resources in the area of more electric systems. Due to the ever-increasing constraints in terms of carbon emissions and economic restraints, over the last few decades, there has been a general move towards more electric systems. This is nowhere more evident in the field of mobile applications and transport systems, with the aerospace industry at the forefront.

Aircraft system designers are working toward the goal of having an all-electric aircraft [28], especially since NASA and ACARE called on aviation to meet stringent environmental requirements [29, 30]. Meanwhile, stepwise goals have been addressed and they are currently named the “More Electric Aircraft” (MEA) [31, 32]. The main objectives of the MEA concept are the use of electricity for powering the aircraft systems, new power distribution and management systems, and the replacement of the hydraulic and pneumatic actuators with electrical equivalences for the secondary power [31, 33, 34].

Electrical machines play an important role in the MEA context. They can be adopted for electrical power generation [35-39], for the main propulsion [40, 41], cabin pressurization systems [42, 43], for the realization of electro-mechanical actuators [44, 45] and/or electro–hydraulic actuators [46-50] . Main advantages of the switch away from pneumatic, hydraulic and mechanical systems toward the electrification are the reduction in fire risk, oil leaks or jamming, quicker and less costly installation, and lower maintenance requirements. Coherently, a high level of reliability should be guaranteed in aircraft systems with electrical actuators; thus, demanding fault tolerance capabilities are required in designing machines for MEA applications [51, 52].

2.1.2 Electric Taxiing System

A MEA activity, which is currently capturing a lot of attention, is to make all on-ground operations more feasible and responsible. Currently, all the aircraft movements between the airport terminals and runaway holding areas (i.e. taxiing and push-back) are realised through the use of the main engines and airport tow-trucks. A relatively-new concept aimed at more responsible and aircraft

autonomous taxiing and push-back is currently being investigated by a number of efforts. One particular scheme [53] is focused on the integration of an electrical motor (actuator) into the main Landing Gear (LG) to accomplish aircraft traction on the ground. This system has been labelled as Electric Taxiing System (ETS).

The main reason that is forcing technology toward this direction is the necessity to reduce the fuel costs and greenhouse emissions due to the aircraft traffic. A number of studies have estimated the actual benefits of having an ETS [54-56]. Main advantages can be summarised as: fuel saving [57], reduced amount of emissions [58], less noise and on-time performances in the airports [59-63], lower tyre maintenance [61]. These benefits have been confirmed through the electric taxiing system implementation and testing on real aircraft [58, 64].

In order to optimise the taxiing and push-back operations, a number of projects have been undertaken. In 2008, a major multi-national company involved in the Clean Sky European research program has launched the Green Taxiing™ (GT) project [53] and delivered an innovative new electric Green Taxiing system for new and existing aircraft in 2011 [65]. Nonetheless, parallel projects showed equivalently valuable solutions for this application. All of them have in common the effort of achieving taxiing requirements, listed below:

- Maximise the torque per volume ratio of the actuator, trying to maximise the dimensions of the actuator within the available space (i.e. rotor external diameter and length of the motor).
- Optimise the space available in the wheel by reducing the presence of any other device, particularly mechanical devices such as gearbox or clutch.
- Maximise motor fault-tolerance capabilities (due to the high level of temperature, shock, and vibrations in the wheel, the ET actuator should be designed with high resistance to any type of stress, i.e. thermal and mechanical).
- Minimise the risk of failure in the mechanical parts such as jamming or leaks.

Generally speaking, the first two requisites are related to the electrical taxiing actuator torque performances whereas the last two are associated with the whole

system reliability capability. Different factors can influence these two main objectives. Existing electric taxiing solutions try to achieve the best compromise in terms of torque and reliability performances approaching to different expedients. The next section gives an overview about some of the present electric-taxiing system arrangements.

2.1 Existing E-Taxiing Schemes

Looking at current e-taxiing solutions, one should differentiate not simply with regard to the electrical design of the actuator but also to the assembly inside the LG as a whole. The overall aim of this Section is to examine existing solutions and compare different taxiing in-wheel apparatus, to understand what are the main challenges and how to contribute to enhancing the state-of-the-art. No scheme that involves devices external to the aircraft is admitted [66]. As part of the evaluation process, the topology of connection between the actuator and wheel represents a discriminating feature.

The location of the actuator, for instance, is an important parameter that sets multiple constraints in the design procedure. An example is offered by two e-Taxiing schemes that are already in certification processes [67], namely the EGTS and WheelTug (WT). EGTS (Electric Green Taxiing System) is the acronym for the e-taxi solution designed for the Airbus A320 family [68, 69] from Honeywell and Safran. WheelTug is a system realised by a German start-up; it has been successfully tested on Boeing 737-800 aircraft [69, 70]. The WheelTug apparatus is driven by twin gear-mounted induction machines from Chorus Motor integrated within the strut of the nose wheel [71]. The EGTS is a dual system that uses an electric motor mounted on a wheel on each main LG unit. The difference in pulling using the nose wheel versus pushing using the main gear results in differences in speed, efficiency, turning radius, and other factors such as required torque and environmental conditions [72]. From some aircraft analysts, one criticism emerged about nose-wheel location, mainly based around the system’s inability to provide enough traction to push-back or taxi a plane when the weather is snowy or icy. On the other hand, challenges for EGTS are harsher than those set for WheelTug. Due to its proximity to the plane’s carbon brakes, the EGTS is exposed to extremely high temperatures, potential

hydraulic leaks, brake dust and considerable landing stress. This imposes more severe limits on EGTS joule losses with respect to WT since no brake is in the nose landing gear.

Obviously, the design procedure of the whole system is a trade-off between the torque requirements and all the implementing questions. The major point remains to reach the maximum deliverable traction force minimizing the impact of the e-taxiing system on the aircraft. The performances of the system in terms of traction depends on the size of the actuator that in turn is limited by the allocated space in the wheel.

Both EGTS and WT are geared-mounted on the aircraft wheel and employ a mechanical clutch to selectively engage and disengage the wheel. The gear system trades speed for torque and provides a lower speed, higher torque. The wheel, however, is expected to operate at much higher velocity than normal motoring speeds, especially during take-off and landing phases. This presents a significant problem, because, in these cases, the load may accelerate the motor via the gearing system. Therefore, there is a need for a selectively engageable electric taxiing system acting via a clutch. The advantage of having a clutch is that the wheel needs only to be engaged after landing and disengaged from the motor during take-off. A wealth of literature [73-76] exists about patented embodiments that try to make the clutch system more compact and lighter, i.e. a self-disengaging bi-directional clutch, magnetorheological fluid clutch, etc. This and other solutions could possibly ameliorate the compactness of the mechanical system in favour of the motor performances. However, issues related to potential jamming in the mechanical parts constitute a constant risk that does not depend on the dimension on the clutch.

2.1 The DD Actuator

As already stated, the Green Taxiing^{TM} initiative is a scheme launched in 2008 by Safran–Messier Bugatti Dowty within the SGO-CleanSky Project. In the same program, other companies have been involved, such as DLR for the control, Adeneo for the power electronics and Airbus. The University of Nottingham was one of the co-partners, in charge for the design of the electrical actuator. The GT system integrates into the main LG the actuator built and tested

in UoN laboratories; the actuator is connected to the wheel through a Direct Drive (DD) configuration. The term direct refers to the fact that the actuator drives the wheel without any interposed mechanism (i.e. gearbox) so that all the torque produced is directly transferred to the aircraft. The clutch is also excluded in this kind of configuration; hence, the actuator is never disconnected from the wheel.

The motor exploits permanent magnet technology with a Halbach Array arrangement [6, 77, 78]. It has been designed to deliver 7*kNm* of torque, with a 54*Nm/kg* torque to volume ratio. Namely, the actuator designed for this application responds to the configuration of the cylindrical motor described in Chapter 4. The great advantage of the DD configuration is that it removes the presence of mechanical gear-boxes. The exclusion of any other mechanism enables to augment the length of the motor; appreciable torque increment is consequently obtained. The problem of jamming is entirely avoided since no mechanical device is included. On the other hand, the main disadvantages include thermal and shock stresses. The Wheel Actuator (WA), in fact, has been conceived to withstand a high level of vibrations (8-10*cm* of deflection at the moment of landing). It survives a wide range of temperature without experiencing any demagnetization. The ambient temperature in the wheel goes from -10°C to 70°C and reaches 500°C when there is brake generation.

The DD-ET configuration offers a solution to the challenges faced in geared variants of the ETS analysed in Section 2.1 and it is an explanatory example of how the system arrangement can be modified and adapted in order to meet torque and reliability requirements. However, some hidden challenges should be addressed.

2.1.1 Problem Definition

The benefits of the DD configuration represent a good remedy to space-related questions where compactness is the highest figure of merit of this system. With regards to the reliability, even though the possibility of mechanical jamming no longer subsists, there are some risks associated with the fact that the motor is always connected to the wheel.

Since the actuator is a PM machine, hazardous voltages can be induced in the motor when the wheel over-exceeds the rated speed of the motor. Considering that taxiing speeds never exceed 170*rpm* at the wheel, then the original WA was designed as a low speed machine. However, with an always connected machine, then during landing and take-off phases, dangerous voltages on the terminals can be reached. The landing speed, in fact, is in the range of 2000*rpm*. Since no physical disconnection between the motor and the wheel can be operated, an electro-magnetic clutch system is adopted. The risk of excessive voltage levels on the motor terminals is eliminated by short-circuiting all the phases. In order to perform this operation, it is essential for the actuator to have excellent fault-tolerance properties. The machine requires the ability to electromagnetically and thermally withstand the considerable braking currents. Even though the motor is able to tolerate the short-circuiting conditions, this expedient introduces significant drawbacks. The short circuit current results in an increase in winding temperature, whilst an unwanted braking torque is generated to the aircraft LG.

When a DD solution is adopted, shocks and vibrations have also limiting effects on torque. With this configuration, in fact, there is an additional constraint on the air-gap length due to the possible deflection during landing. In consideration of the former evaluations, measures to actively engage/disengage the WA from the wheel are highly desirable.

2.1.2 Electro-Magnetic Clutch System

As already stated in the previous section, the main issue in DD electric-taxiing solution with PM motor is the risk to induce unacceptable voltages in the motor windings. During landing and take-off, in fact, the wheel of the aircraft experiences high rotating speed of approximately 1800*rpm* over a period time of 40*s*, roughly. Since the motor and the wheel are directly connected, the drive will turn at speed level way higher than the rated speed.

If the motor is left free to rotate with the wheel and all the phases are completely open-circuited, the voltage established at motor terminals will over-exceed the motor capabilities and insulation limits. In [8] FE analyses have been conducted to test this condition, with the result of 4.2*kV* voltage across each phase.

The solution found to overcome the probability of causing serious damages to the motor is an electro-magnetic clutch system. This does not consist in a physical clutch but in a method adopted during landing and take-off in which all the phases of the motor are short-circuited. In this case the motor can be kept directly connected to the wheel even at high speed; however, it will be exposed to high demanding conditions related to the short-circuiting current that it must be able to withstand.

For the present GT system, the short-circuiting current was estimated to be 160 *A*. This value does not compromise the functioning of the system but it produces an unwanted temperature raising in the in windings and undesirable braking torque to the aircraft wheel. The calculated short-circuiting current I_{sc} and torque T_{sc} are represented in Figure 2.1 of which the source is [8].

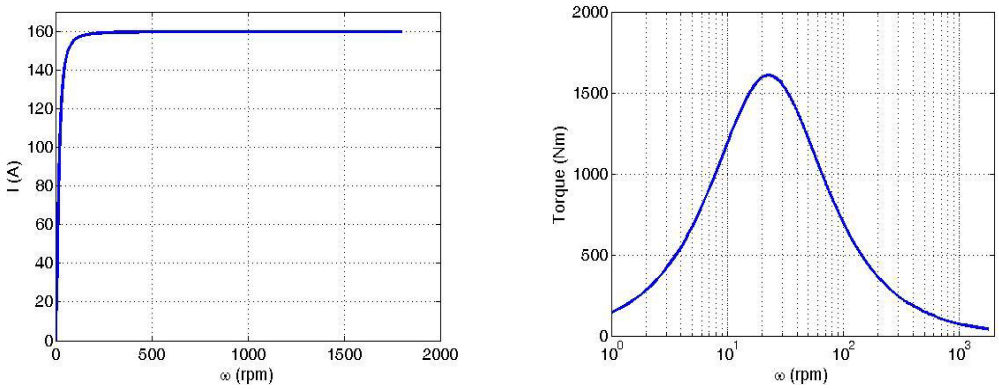


FIGURE 2.1 – CALCULATED SHORT CIRCUIT CURRENT AND TORQUE OF CYLINDRICAL DDWA

Even though all the requirements to perform this operation are within the admitted limits of the motor, this solution does not represent the safest way to tackle the problem. If one of the phases is not properly closed, the whole system fails. A compact solution for having a complete disconnection of the motor from the wheel and enhance the level of system reliability would be preferable.

2.2 Proposed Solution

The current DD configuration is the result of a trade-off study. Before approaching to the final design, additional studies have been conducted. A version of the system with an external clutch has been also considered (Figure 2.2-a). Even though the clutch would avoid damaging the motor during landing and take-off, its presence nullifies all the benefits achieved with the DD set-up, in particular with respect to its compactness and lightness. The estimated weight of the total system doubles when the clutch is added; the volume allocated to the actuator reduces and the exposure to jamming events presents.

In this research work, some other system schemes have been proposed in other to overcome the reliability issues faced with DD configuration. An electromagnetic clutch [79-81] with a solenoid attached to the motor's hub was also taken into account as a possible solving (Figure 2.2-b). In addition to the problem of extra weight (half of the motor weight), this topology of clutch needs an extra control technique and its functioning might be affected in the harsh LG environment. High level of acceleration and temperature might result unbearable.

A successful suggestion was the use of the conical machine without any added clutch (Figure 2.2-c). The conjoined axial and rotational movement avoids the presence of the clutch. In this way, the motor can be actively engaged and disengaged from the wheel whenever is needed. During landing and take-off, the motor can be maintained at the retracted position with the actuator completely uncoupled from the wheel. The engagement happens when taxiing starts; the inherent current control of the machine is exploited to couple the motor to the wheel. During the disengagement, the air gap length increases excluding the risks due by the shaft deflection caused by the high level of vibrations; on the contrary, when the motor is aligned, the air gap reduces and contributes to enhance the torque performances. As demonstrated in the rest of the thesis, particularly in Chapter 4, the taper of the CM is only a few degrees order; thus, the delivered torque is comparable to the cylindrical actuator since the outmost diameter and the length of the motor remain the same.

With the conical solution, the risk of damaging the motor during acceleration phases is excluded. The choice of the conical actuator might require some more efforts in its outline and conceptualization. As already seen in the previous chapters, the manufacturing of a conical machine might require additional time or resources, particularly for the lamination cut. Moreover, due to the novelty and singularity of the application, there is a lack of literature and no terms of comparison for conical in-wheel actuator have been found.

An enlarged picture about all three-proposed electric-taxiing schemes has been summarised and reported in Table 2.1, including the advantages and disadvantages provided by each solution.

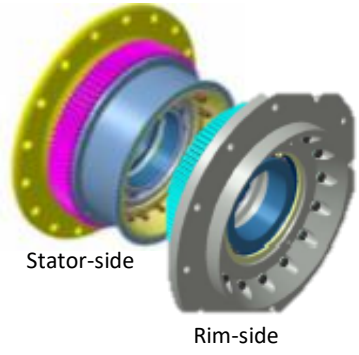
TABLE 2.1 – E-TAXIING CONFIGURATION COMPARISON

CYLINDRICAL SYSTEM WITH AN EXTERNAL ACTIVE CLUTCH (Figure 2.2a)		
Concept	*Feasibility/Comments*	*Benefits*
External mechanical clutch system.	Interposed between the wheel and the motor.	a) No need to realize an extra control technique for engagement/disengagement.
Efforts		
a) The weight of the overall system doubles (the clutch has roughly the same weight of the motor). b) Space in the LG needs to be allocated to the clutch system at the expenses of the actuator. *c)* The clutch system amplifies the risk of jamming.		
Total expected weight:130kg + 100kg[1]		
CYLINDRICAL SYSTEM WITH AN ELECTROMAGNETIC INTEGRATED CLUTCH (Figure 2.2b)		
Concept	*Feasibility/Comments*	*Benefits*
Solenoid clutch embedded in the motor case.	"Extra" coil generating a magnetic field able to move the motor and detach it from the wheel.	a) No additional space required.

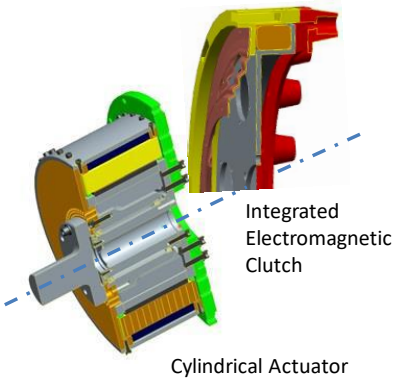
[1] For each solution, the first value is weight of the GT Actuator. The added value indicates the weight of the clutch.

Efforts
a) More copper losses, therefore temperature rise. b) System complexity, especially for manufacturing. c) Extra weight due to large additional coil (almost 50% of the actuator weight). d) May not survive the harsh environment. e) Extra control technique.
Total expected weight: 130kg + 50kg

CYLINDRICAL SYSTEM WITH CONICAL ACTUATOR (Figure 2.2c)		
Concept	*Feasibility/Comments*	*Benefits*
Innovative topology of motor that can move the actuator toward the wheel and push it back.	Motor with a conical shape directly connected to the wheel in case of taxiing acting on motor current.	a) No additional system (clutch or gearbox). b) No added weight. c) The mass of the overall system is approximately the same. d) Traditional control loop to move the motor axially.
Efforts		
a) Complex manufacturing: laminations have different dimensions. b) Lack of knowledge about this topology of motor.		
Total expected weight:130kg		



(a) External clutch



(b) Integrated clutch



(c) Conical motor

FIGURE 2.2 – POSSIBLE SYSTEM CONFIGURATIONS

2.3 Conclusion

In this Chapter, an explicative example of the employment of the conical machine in a real system has been reported. The implementation of the motor for the proposed traction application is a supportive illustration of the benefits that the use of a conical machine could provide to existing technologies where big challenges related to clutch and declutching actions are present.

The electric-taxiing has been suggested as a possible application where the integration of the proposed motor technology could offer several advantages. The PMCM could be a suitable solution to the risk of high induced voltages faced in the present DD-ET arrangement. In fact, the motor can be declutched from the rest of the system without the use of any mechanical artifact, thus simply relying on the axial force developed by the machine. No need to short-circuit the motor phases during take-off or landing therefore exists.

A small-size demonstrator that replicates the CM behavior inside the ET system has been realized and described in Chapter 7. A conical version of the ET has been conceived together with an appropriate control technique that enables the engagement of the motor during taxiing and the disengagement during take-off and landing phases.

However, it is worth clarifying that the application considered and proposed in this work of thesis it is just an example of how the PMCM can be an advantageous expedient for the short-circuiting problems faced when PMs are employed. This is a common issue, particularly recurring in automotive, or, in traction systems in general.

Chapter 3
Basic Theory and Design Guidelines

In this Chapter, the fundamental concepts for the design of conical machines are addressed. Basic guidelines for the preliminary design of the conical machines are provided.

Considering that the analysis of a conical machine is basically a 3D problem, then this Chapter introduces an equivalent 2D model of the conical motor, aimed at providing a sustainable and computationally-efficient design methodology for the design and analysis of such systems. The basics of the model are appropriately explained and validated through the use of three-dimensional analyses.

The theory of the forces present in conical machines is developed and a formulation of the force, relative to the generated axial force, is described at the end of the Chapter.

3.1 Introduction

In this work, two different approaches have been adopted respectively for the design and the analyses of the conical machine.

A preliminary design procedure for conical machines, similar to standard motor design procedures is first introduced in Section 3.4, where the concepts of equivalent radius and equivalent length are utilized, as described in Section 3.2.1. These concepts enable standard design formulae, commonly utilized for cylindrical machines, to be also implemented for the design of conical machines.

However, when it comes to FEA, conical machines, due to the inherent three-dimensional shape, need to be simulated in a 3D environment. Since 3D simulations can be time-consuming and require a considerable computational power, a two-dimensional model has been adopted during the entire research study. The rationale for the 2D model is presented in Section 3.3.

The two approaches have been combined for the numerical computation of the forces and the torque. The evaluation of the forces and torque, formulated in Section 3.5 and directly employed in Chapter 4, proposes the integral of the magnetic field values obtained from 2D model FEA on an equivalent rotor surface calculated using the aforementioned equivalent motor dimensions.

3.2 Geometry Description

Before going into the main design and analysis procedures of a PMCM, it is important to introduce the general conical motor's basic theory and develop/describe the fundamental concepts that govern its operation. These are then employed for the preliminary calculation of the conical motor performances and the numerical analyses of the conical machines, described in Section 3.4.

3.2.1 Medium Radius and Equivalent Axial Length

A conical motor is an electrical machine in which both the stator and the rotor have a tapered shape. In Figure 3.1, a cross-sectional view of the machine is shown. The rotor is a truncated cone. The stator has tapered internal surface and a cylindrical outer shape. This has a practical implication, namely that the cylindrical exterior of the stator avoids complications with standard cylindrical

casings. The taper of the rotor and stator internal are determined by the cone angle γ, calculated at the vertex of the cone, as highlighted in Figure 3.1.

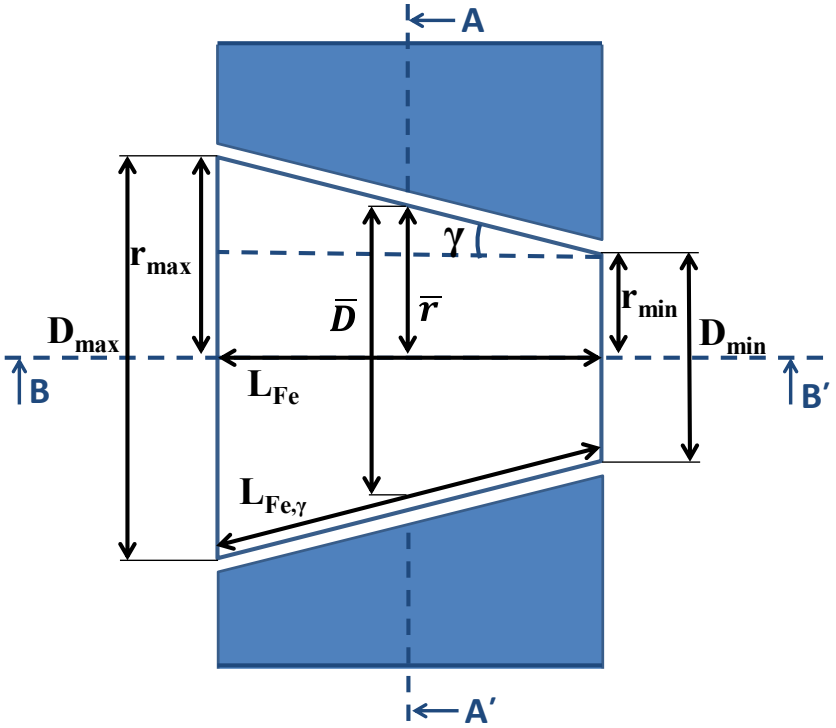


FIGURE 3.1 – CROSS-SECTIONAL VIEW OF THE CONICAL MACHINE

As it can be seen in Figure 3.1, the motor radius is not constant along the whole length of the machine. The motor, in fact, has a minimum and maximum cone radius, r_{min} and r_{max}. The radius at the central vertical cross section axis AA′ is assumed to be the main reference dimension. This assumed reference dimension will help to simplify all the ensuing calculations. Having this reference dimension is also very important in that it will also act as the main "common feature" on which the design of a cylindrical counterpart motor is based. The cylindrical counterpart is extremely relevant as it will allow direct comparisons between itself and the proposed PMCM. The central radius corresponds to the medium radius $\bar{r}$, calculated as in (3.1). The same concept applies to the maximum, minimum and medium diameters, respectively D_{max}, D_{min} *and* $\bar{D}$ indicated in Figure 2.1.

$$\bar{r} = \frac{r_{max} + r_{min}}{2} \tag{3.1}$$

$$L_{Fe,\gamma} = \frac{L_{Fe}}{\cos\gamma} \tag{3.2}$$

The length of the motor calculated on the tapered surface, called equivalent axial length of the conical machine $L_{Fe,\gamma}$ is longer than the effective axial length of the machine L_{Fe} calculated on the axis BB′. The actual length of the motor, in fact, is as given by (3.2). The equivalent dimensions of the conical machine mainly depend on γ. The dimensions $L_{Fe,\gamma}$ and $\bar{r}$ are influential for the electrical design procedure, particularly for the torque computation as well as for the determination of electrical parameters such as the resistance and inductances of the motor windings.

3.2.2 Rotor and Magnets

In a PM conical machine, magnets do not have a rectangular shape as in cylindrical machines. Due to their roof-tile shape, as shown in Figure 3.2, the linear measure of pole pitch is not constant with the axial length. The pole pitch, in fact, depends on the diameter and this measure is not constant along the motor axial length.

The magnet shape can be recreated using different magnet slices, as represented in Figure 3.3. For each slice the full pole span β_{PM} can be calculated using equation (3.3), where r_M is the effective radius of the magnet at one-third of the way through the magnet measured from the inner radius. The effective magnet radius of each slice changes with axial length and it is proportional to the chosen cone angle.

$$\beta_{PM} = \frac{2\pi r_M}{2p}; \tag{3.3}$$

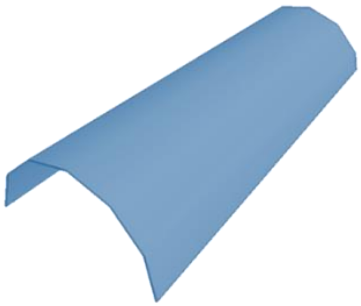


FIGURE 3.2 – CONICAL SHAPED MAGNET



FIGURE 3.3 – CONICAL SHAPED MAGNET SECTORS

3.2.3 Stator and Slots

As it can be seen in the cross-section of a conical machine reported in Figure 1.2, in the conical machines the stator shape varies with the axial length. As for the magnet radius, also the inner stator radius decreases toward the smaller side of the motor (see Figure 3.1). On the contrary, the stator back-iron thickness increases where the rotor is smaller. This is due to due outer stator cylindrical shape.

While all the stator dimensions vary with the axial length, the area of the slots is constant along the length of the whole motor. In fact, the slot width *w*, as indicated in Figure 3.4, is maintained constant for the whole length of the conical motor, whereas the stator tooth width *b* reduces accordingly to the radius reduction of the cone. Consequently, the total slot pitch β_s, calculated as in (3.4), varies with the reduction of stator tooth. The slot pitch depends on the considered stator diameter *D* evaluated at a specific axial length.

$$\beta_s = \frac{\pi D}{N_s} \tag{3.4}$$

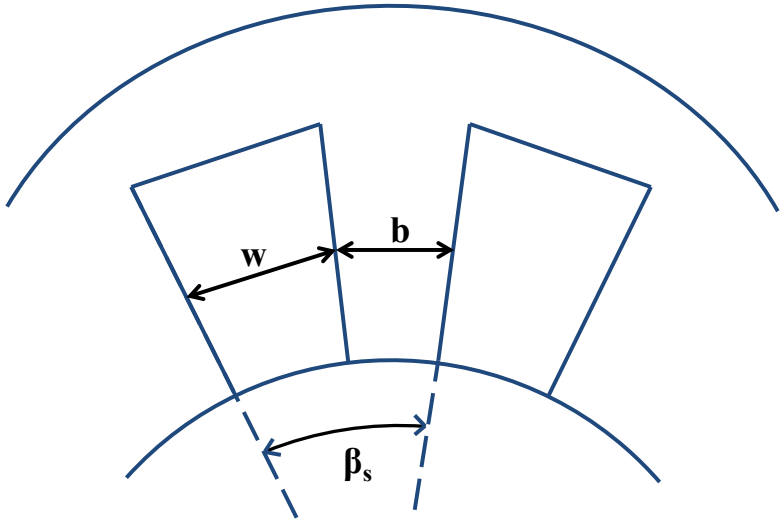


FIGURE 3.4 – SLOT AND TOOTH DIMENSIONS

3.3 Two-Dimensional Analysis of Conical Machines

In this work, the performances of the conical motor will be assessed using a 2D version of the conical machine. A very important feature of this thesis is the proposal to assume a conical motor as a series of 'thin' cylindrical motor sections that can be analyzed and simulated as multiple 2D cylindrical motors, as shown in Figure 3.5. Specifically, the conical machine has been divided into a number of cylindrical motors with the same axial length, as a stack of disks assembled together to reconstruct the cone volume. The performances of each motor can be evaluated singularly and then coherently manipulated in order to obtain the overall performances of the conical motor. The total torque and the total axial force have been calculated as the algebraic sum of the performances of each motor, applying the superimposition principle. However, some aspects need to be clarified in order to prove that no conceptual mistakes are committed when this simplification is introduced.

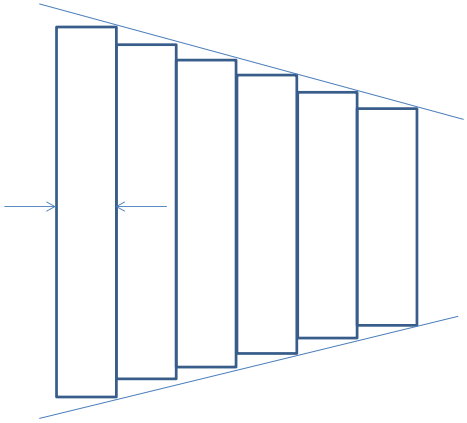


FIGURE 3.5 – 2D CONICAL MACHINE MODEL

a) First Hypothesis

In the case of the numerical approach, the results of two-dimensional Finite Element (FE) analyses of each cylindrical motor are extracted and then post-processed to complete the analytical calculations. In each cylindrical motor, the computation of forces and torque is based on the 2D Maxwell Stress Tensor (MST) $\vec{\vec{T}}$. This means that third column and the third row that represent the third dimension of the 3D MST, reported in (3.5) are excluded from the calculation.

In (3.5), B_1, B_2 and B_3 are the flux density components in a generic orthogonal system calculated in the airgap.

$$\overleftrightarrow{T} = \frac{1}{\mu_0}\begin{pmatrix} B_1^2 - B^2/2 & B_1B_2 & B_1B_3 \\ B_2B_1 & B_2^2 - B^2/2 & B_2B_3 \\ B_3B_1 & B_3B_2 & B_3^2 - B^2/2 \end{pmatrix} \tag{3.5}$$

Since, in the present work, the first two dimensions of the MST are associated with the normal and tangential vectors to the lateral rotor surface and the third dimension corresponds to the axial direction (as specified in (3.32)), then not considering the third column and third row of (3.5) implies the exclusion of the axial flux density, B_z, during the computation of the forces. Therefore, the axial force is simplistically calculated as the projection of the normal force obtained using the 2D MST. The assumption behind this concept is that there is direct linearity between B_z and the sine of the cone angle and this linearity can be directly transferred on the force computation. In order to prove that this assumption will not compromise the computation of the conical motor's performances, 3D FE analyses have been performed on two twin motors (one cylindrical and one conical). The B_z results of 3D FE analyses on the conical machine have been compared to the one obtained analytically as in (3.6). The axial flux density B_z in (3.6) is calculated as the projection of the flux-density normal component B_r of the cylindrical machine on the z-axis in consideration of the adopted cone angle γ. It should be noted that in cylindrical machines, the normal component and the radial component of the flux density represent the same quantity (B_n=B_r), as explained in Section 3.5 relative to the force computation.

$$B_z = B_r \sin\gamma \tag{3.6}$$

For simplicity, a basic model of a PM conical motor with three slots and two poles, as shown in Figure 3.6, has been utilised for three-dimensional simulations. The conical motor is derived as an equivalent of a cylindrical machine by implementing an own-built "vertex distortion" code from Matlab® into Magnet® Infolytica environment. The tapering has been obtained using a cone angle of 10° as an example. The angle has been chosen using the conical

motor of [27] as a reference. As described in Chapter 5, the motor of [27] is built using a cone angle in the same range of value.



a) Cylindrical b) Conical

FIGURE 3.6 – "TWINS" CYLINDRICAL AND CONICAL MACHINES

The axial flux density computed in FEA has been extracted for both motors. As expected the axial component of the flux density for the cylindrical motor is null. This emerges from Figure 3.7 where the no-load flux density calculated for the cylindrical and conical machine at half-way of the air-gap length and half-way of the axial length (z=25*mm*) is reported. In Figure 3.8, the no-load half-way airgap axial flux density extracted at z=25*mm* from the 3D Finite Element Model (FEM) of the conical machine has been compared with one obtained analytically by implementing the no-load radial flux density of the cylindrical motor at z=25*mm* and half air-gap length in (3.6). The results showed very good similarities proving that the concept behind (3.6) is correct. The 3D MST, in fact, can be determined using the 2D MST and introducing the axial component of the flux density calculated as in (3.6). The integration of the 3D MST on the cone volume will lead to the same results of the proposed 2D equivalent solution with only a marginal computational error.

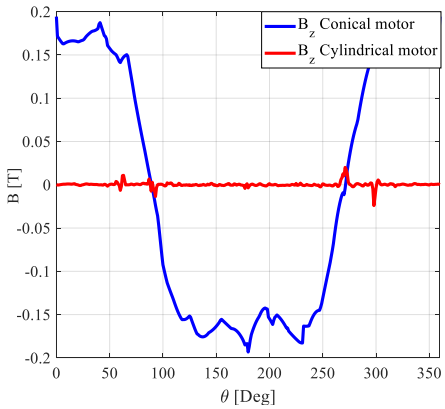


FIGURE 3.7 – 3D FEA RESULT COMPARISON OF CYLINDRICAL VS CONICAL NO-LOAD AXIAL FLUX DENSITY (HALF-WAY AIRGAP Z=25MM)

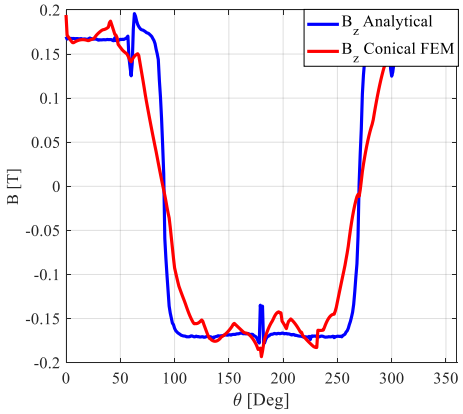


FIGURE 3.8 – COMPARISON OF 3D FE VS ANALYTICAL NO-LOAD AXIAL FLUX DENSITY IN THE CONICAL MACHINE (HALF-WAY AIRGAP Z=25MM)

b) Second Hypothesis

Within the force calculation procedure, the normal σ and tangential τ stresses are integrated on each surface area element of the cone as shown in Figure 3.9. In the 2D simplified model, the variation of the stress along the z-axis is neglected and the forces acting on the conical rotor are obtained using the normal and tangential flux densities obtained from one of the cylindrical motors used to approximate the cone shape supposing that the air-gap flux density remains constant in each of the cylindrical machines. This concept has been demonstrated and proven in Chapter 4. The argument that could be raised regarding this approximation is the possible variation of the flux density with the horizontal coordinate in case of the 3D conical motor. To prove that the flux density does not vary with the axial length, the field in the air-gap of the 3D conical motor at no-load conditions has been extracted at two different axial coordinate levels (25*mm* and 50*mm*) and compared. As shown in Figure 3.10, there is an appropriate overlap between the two trends, showing also that the flux density is not influenced by the end effects at z=50*mm*. Therefore, the described approximation does not represent a computational issue when the two-dimensional simplification is adopted.

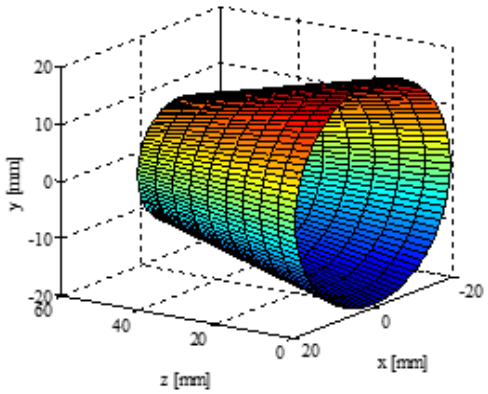


FIGURE 3.9 – INTEGRATION AREA ELEMENTS ON THE CONICAL LATERAL SURFACE

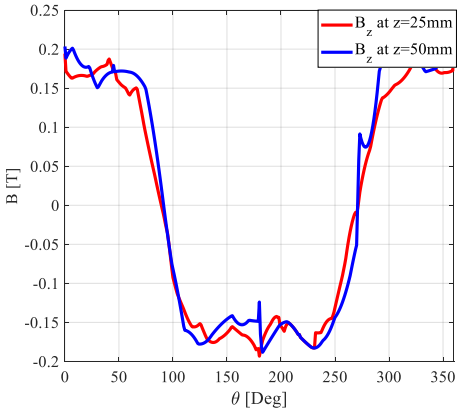


FIGURE 3.10 – COMPARISON OF NO-LOAD AXIAL FLUX DENSITY AT HALF-WAY AIRGAP AND DIFFERENT Z-AXIS COORDINATES

3.4 Preliminary Design

In this section, a design procedure is outlined to define the preliminary motor dimensions (equivalent motor length and cone angle) in accordance with the motor initial requirements. The procedure uses standard cylindrical machine design approach adapted to the conical machine geometry through the concepts of "equivalent" dimensions of the conical PM motor described in Section 3.2.1 and the two-dimensional model rationalized and confirmed in Section 3.3.

3.4.1 Initial Requirements

A. Nominal performances

In this work, the nominal performances of the conical machine are evaluated when the rotor is completely aligned to the stator, as depicted by Position 1 in Figure 3.11. The engaged position of the rotor represents the operating configuration in which the motor is able to deliver the maximum torque. Therefore, the extended rotor position (Position 1) is considered as the

configuration in which the motor needs to meet the set torque requirements. The design procedure is thus carried out considering the air-gap and the active length of the machine corresponding to Position 1. In fact, all the motor analyses shown in this thesis consider the rotor at this position.

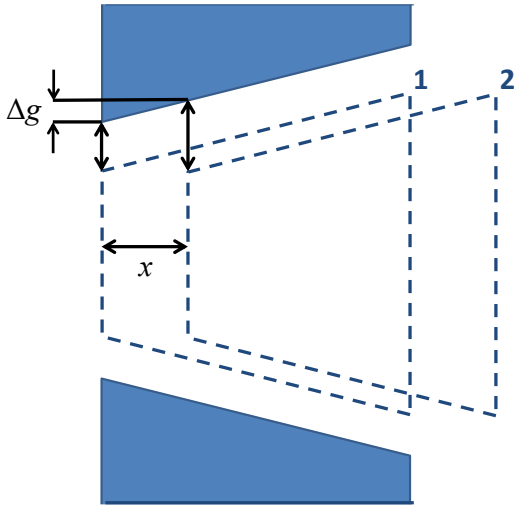


FIGURE 3.11 – AIR-GAP VARIATION

However, this approach should not be considered as a fixed rule to be followed for the design of conical machines. Depending on the specified application, the machine might be designed for different requirements with respect to the extended and retracted position of the rotor (respectively Position 1 and Position 2 in Figure 3.11). In both cases, it is obvious that the maximum torque is achieved having the rotor aligned with the stator, due to the smaller air-gap and to the actual effective length of 'matching' rotor and stator. However, for the scope of this work, it is assumed that any reference to rated values of the machine (i.e. rated torque, rated current, etc.) is related to Position 1.

B. Axial Displacement

The air-gap variation Δg, as indicated in Figure 3.11, depends on the axial displacement of the rotor x and it is calculated by (3.7). The axial displacement is a parameter that should be set in accordance with the mechanical requirements (e.g. necessary movement of the rotor to perform declutching). The maximum rotor retraction, from Position 1 to Position 2 can be limited through the mechanical system arrangement (i.e. limiting the clearance in the motor casing) unless a position control exists on the axial movement.

The variation Δg represents the air-gap increment that should be added to the air-gap length chosen for the aligned position performances in order to obtain the corresponding air-gap length when the rotor is retracted.

$$\Delta g = x \tan \gamma \tag{3.7}$$

C. Geometry Definition

The concepts of the mean radius or mean diameter of the machine, and the equivalent axial length can be adopted for the initial sizing process of the motor. These "equivalent" dimensions, in fact, can be used to choose the preliminary maximum external diameter and the axial length of the machine based on the constraints fixed by the maximum size of the motor.

As suggested in [82], the design procedure can start from the specifications in terms of torque or Torque per Rotor Volume (TRV). This is particularly applicable in the case of traction applications where volume constraints and torque and speed prerequisites are usually set. The output equation of (3.9) relates the electric loading A and the magnetic loading B to the output torque of the motor calculated per rotor volume unit. Considering that A corresponds to the linear current density around the airgap circumference, then it can be calculated by (3.8), where I is the RMS phase current, m is the number of phases, N_{ph} is the number of turns in series per phase and D is the diameter of the air-gap. In this case, D corresponds to the medium diameter $\overline{D}$ between the maximum and minimum air-gap diameter of the conical machine. The value of B is the average flux density on the rotor surface computed as illustrated in Section 3.4.2.

$$A = \frac{2mN_{ph}I}{\pi \overline{D}} \tag{3.8}$$

$$TRV = \frac{T}{\pi \overline{D^2} L_{Fe,\gamma} / 4} = \frac{T}{V_r} = \frac{\pi}{\sqrt{2}} k_{w1} AB \tag{3.9}$$

The ratio of TRV can be obtained also by (3.10), as function of the air-gap shear stress σ. In this case, the volume of the rotor, V_r, can be computed using the typical values of σ, as given in [14, 82, 83]. It should be noted that V_r in (3.10)

corresponds to the volume of a truncated cone as reported in Figure 3.1 to be used in order to obtain $\bar{D}$ and the $L_{Fe,\gamma}$ of the machine.

$$TRV = \frac{T}{V_r} = 2\sigma \tag{3.10}$$

As can be seen in (3.1) and (3.2), the use of the $\bar{r}$ and the $L_{Fe,\gamma}$ of the motor takes into account the influence that the cone angle has on motor performances, particularly with respect to torque. A conical shaped motor has inherently lower performances than a cylindrical machine (if the same electrical configuration and geometry are maintained); this is mainly due to the smaller volume of the rotor and thus a lower rotor surface area resulting in a smaller σ. In order to limit performance degradation of the conical machine, an appropriate cone angle should be chosen. This will be discussed and investigated in Chapter 4.

The use of the medium radius and the equivalent axial length are employed for both electric and magnetic design of the motor that can be achieved following traditional rules. No particular measures are taken for the electrical design since this follows regular procedures suggested and acknowledged in literature [14, 82, 83] (when $L_{Fe,\gamma}$ and $\bar{r}$ are adopted). However, some points, regarding the magnetic design, should be addressed, as discussed in the next section.

3.4.2 Magnetic Circuit Design

Particular attention should be paid to the magnetic circuit design. The main points to consider for a good magnetic design of the PMCM are:

1) the no-load axial force, extremely influential for the design of the mechanical system;
2) the potential of partial demagnetization of the PMs, since flux-weakening techniques are used in order to retract the rotor and move it axially;
3) the shape of the PMs, as a constant pole span should be guaranteed;
4) the air-gap flux density, as this will determine the motor performances.

Common magnetic design formulae can be adopted to determine the working point of the magnets and opportunely choose the length of the magnet and the air-gap, even if the PMs do not have a conventional shape.

If the rotor is sliced and divided into several sub-motors, as proposed in Section 3.2, for each machine the magnetic circuit can be drawn and the air-gap flux-density can be determined.

As demonstrated in Section 3.2-b) and confirmed in Chapter 4, FEA show that the flux-density can be assumed constant at the motor air-gap for different points of the axial length; therefore, the effect of the cone angle on the flux density can be neglected. For this reason, an equivalent model of the magnetic circuit is drawn in correspondence of the medium point of the rotor, in order to obtain a medium value of the air-gap flux-density $\bar{B}_g$. The value of the "medium" flux-density is computed using the medium rotor diameter concept and the equivalent stack length as defined in (3.1) and (3.2).

If the full pole span β_{PM}, defined in (3.3), is determined using the medium effective magnet radius $\bar{r}_M$, then the effective magnet-span α_{PM} can be represented as a fraction k of β_{PM}, as in (3.11). The dimension $\bar{r}_{\mathrm{M}}$ is marked with an accent since it represents the medium quantity of r_M calculated at the half of the axial length of the motor as indicated in Figure 3.1 and obtained as in (3.1). If the value of k is maintained constant for each sub-motor, then a good approximation of the magnet operating point can be obtained from the equivalent circuit using average radii and average magnet and air-gap area calculated as in (3.15) and (3.16).

$$\beta_{PM} = \frac{2\pi \bar{r}_M}{2p}; \qquad \alpha_{PM} = k\beta_{PM} \qquad k < 0 \tag{3.11}$$

The analysis procedure is based on the determination of the flux produced by the PMs, which indicates the "operating point" of the PMs. The magnet flux can be calculated approximately with the magnetic equivalent circuit method. Under open-circuit conditions (corresponding to the no-load axial force produced by the magnets), it is usually sufficient to consider only one pole and make use of symmetry. The simplified magnetic circuit, shown in Figure 3.12 can be employed for this calculation. In Figure 3.12, the armature Magneto-Motive Force (MMF) F_a due to the phase current is considered zero in open-circuit conditions, P_{m0} is the internal magnet permeance, P_L is the rotor internal permeance, calculated in per-unit leakage permeance of the internal rotor permeance ($p_{rl}= P_L/P_{m0}$), R_g is the air-gap reluctance.

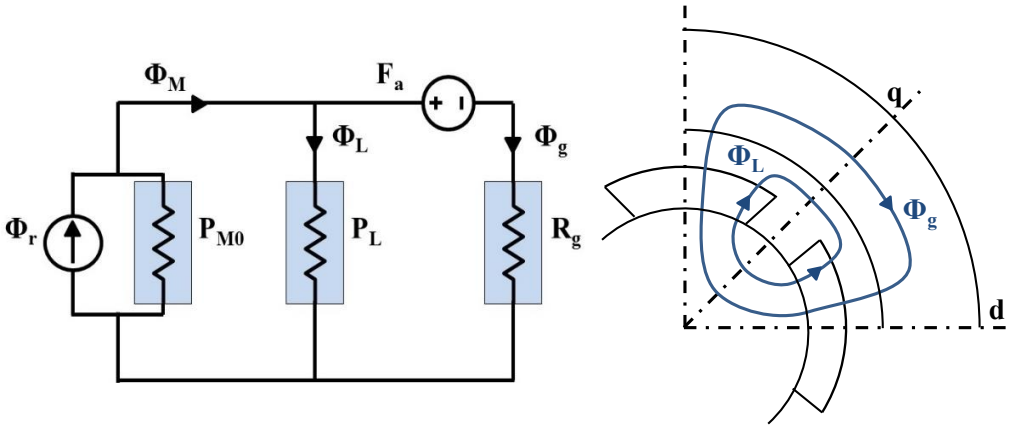


FIGURE 3.12 – MAIN AND LEAKAGE FLUX PATHS IN MAGNETIC CIRCUIT

The parameters P_{m0} and R_g can be obtained by (3.12) and (3.13) respectively, where μ_0 is the vacuum permeability, μ_{rec} is the recoil permeability (usually quoted as relative permeability, calculated as $\mu_r\mu_0$ [H/m]) that represents the slope of the recoil line (the minor loop of the B-H loop, in fact, can be approximated as a line called, recoil line), g' is the effective value of the air-gap length determined by the use of Carter's factor to allow for the slotting, L_M is the magnets length in the direction of magnetization, A_M is the magnet pole area, obtained as the ratio (k) of the full pole area A_p, computed as in (3.14) and (3.15), A_g is the pole area of the air-gap obtained as in (3.16) , r_g effective radius of the air-gap (midway through the physical air-gap) and $\bar{r}_g$ is the medium radii calculated at the half of the axial length.

$$P_{m0} = \mu_{rec}\mu_0 \frac{A_M}{L_M} = \mu_{rec}\mu_0 \frac{\alpha_{PM}\bar{r}_M L_{Fe,\gamma}}{L_M} \tag{3.12}$$

$$R_g = \frac{g'}{\mu_0 A_g} = \frac{1}{\mu_0 L_{Fe,\gamma}} \frac{g'}{\alpha_M \bar{r}_g} \tag{3.13}$$

$$A_p = \frac{2\pi \bar{r}_M L_{Fe,\gamma}}{2p} = \beta_{PM} L_{Fe,\gamma} \tag{3.14}$$

$$A_M = kA_p = k\frac{2\pi \bar{r}_M L_{Fe,\gamma}}{2p} = \alpha_{PM} L_{Fe,\gamma} \tag{3.15}$$

$$A_g = k\frac{2\pi \bar{r}_g L_{Fe,\gamma}}{2p} \tag{3.16}$$

The fluxes shown in Figure 3.12 are all defined on a per-pole basis and computed by (3.17) and (3.18), where f_{LKG} is the leakage factor with typical value 0.8-0.9 [84]. Namely, Φ_m is the magnet flux, actually passing through the magnets, Φ_L is the leakage flux, part of the magnet flux which falls to link the phase winding. Only the fraction $P_g = (P_{m0} + P_L + P_g)$ of the total flux that crosses the air-gap, with $P_g = 1/R_g$, i.e. the main air-gap flux that links the coils of the phase winding is indicated as Φ_g in Figure 3.12. Given $\Phi_g = B_g A_g$ and $\Phi_m = B_m A_M$, the air-gap flux density $\bar{B}_g$ can be computed as in (3.20).

$$\Phi_m = \frac{1}{1+ f_{LKG} P_{m0} R_g} \Phi_r \tag{3.17}$$

$$\Phi_g = \frac{f_{LKG}}{1+ f_{LKG} P_{m0} R_g} \Phi_r \tag{3.18}$$

$$f_{LKG} = \frac{\Phi_g}{\Phi_M} = \frac{\Phi_g}{\Phi_M + \Phi_L} < 1 \tag{3.19}$$

$$\bar{B}_g = \frac{f_{LKG}}{1+ f_{LKG} P_{m0} R_g} \frac{A_M}{A_g} B_r \tag{3.20}$$

As stated above, the Permeance Coefficient (PC) characterises the operating point of the magnet within the magnet circuit. As suggested in [84], in surface-magnet motors $A_M \approx A_g$ and it is acceptable to use $g=g'$ since air-gap modification for slotting is small so that the PC can be obtained as in (3.21),

$$PC = \frac{1}{f_{LKG}} \frac{L_M}{g'} \frac{A_M}{A_g} \approx \frac{L_M}{g} \tag{3.21}$$

The arc-tangent of PC determines also the angle of the load-line of the magnets from the x-axis of the demagnetization curve, where the slope of the load line is the product of PC and μ_0. Since $B_m = B_r + \mu_{rec}\mu_0 H_m$ and $PC = B_m/(\mu_0 |H_m|)$, the magnet working point $\bar{B}_m$ can be determined as in (3.22).

$$\bar{B}_m = \frac{PC}{\mu_{rec} + PC} B_r \quad B_m > B_k \tag{3.22}$$

The magnet working point, as calculated by (3.22), represents a good approximation of the exact working point of the magnets and it is effective especially for checking if the operating point of the magnet is above the knee point of the demagnetizing characteristic. Based on (3.21), if L_M and g are opportunely chosen and the considered value of PC is verified, any risk of demagnetization can be avoided, as demonstrated in Chapter 5.

3.4.3 Other Considerations

A. Losses

Some considerations about the machine losses should be taken into account in order approximately compare the level of losses in the conical machine with a cylindrical machine. In the conical machine, due to (3.2), the length of the winding will be inevitably longer than a cylindrical motor with the same axial length. However, as can be expected, if a small conical angle is required to develop the necessary axial force, then the copper losses are comparable to a cylindrical counterpart.

The effects on the iron losses need to be carefully evaluated since they do not depend uniquely on the length of the motor but on the volume. Assuming that a cylindrical and conical machine with the same axial length have the same amount of losses per mass unit [W/kg], then, if the same material with δ [kg/m^3] density is adopted for stator and rotor cores, the losses between the two motors will differ because of the different amount of iron volume. The iron volume in the cylindrical machine ($V_{Cyl,Fe}$) is obtained as in (3.23), where Δr_{max} is the difference between the outer and inner radii of the cylindrical motor corresponding to the maximum radii of an equivalent conical machine and V_{slot} represents the volume of the slots that remains the same quantity in both cases (conical and cylindrical). Since in conical machines, the area of the slots is constant along the length of the whole motor, the amount of stator and rotor iron volume is computed respectively adding and subtracting the quantity $V_{Con,Fe}$ of (3.24) to $V_{Cyl,Fe}$. The volume $V_{Con,Fe}$ represents the volume of a cone whose radius is the difference between the maximum and minimum radius of the conical motor rotor. If the volume of the stator and rotor are calculated as a cylindrical ring volume using the maximum radii, then the quantity $V_{Con,Fe}$ should be added

to the stator iron volume since the stator radius increases where the rotor radius decreases, on the contrary, should be subtracted to the volume of the rotor. This quantity is almost one-third of the cylinder volume. This means that the iron losses in the rotor decrease by roughly one-third with respect to the cylindrical machines, however, the opposite situation is verified in the stator. These effects should be carefully considered during the design process.

$$V_{Cyl,Fe} = \pi \Delta r_{\max}^2 L_{Fe} - V_{slot} \tag{3.23}$$

$$V_{Con,Fe} = \frac{\pi}{3}\left(r_{\max} - r_{\min}\right)^2 L_{Fe} \tag{3.24}$$

B. Saturation

Even though, during the preliminary design procedure, the slot pitch is determined at the medium stator diameter $\overline{D}$ as in (3.25), particular attention should be paid to the saturation effects, due to the variable width of the stator teeth along the axial length.

The stator teeth, indicated as *b* in Figure 3.4, decreases toward the shorter side of the motor. Equations (3.26) and (3.27) subsist between the maximum and minimum diameters of the motor, D_{max} *and* D_{min}, and the tooth widths b_{max} and b_{min}, calculated respectively at the larger and smaller radius of the stator. As the teeth width is smaller at the smallest side of the motor, a major tendency to saturation exists on this side of the machine. Even though these effects are compensated by the reduction of the pole pitch with motor radius, saturation effects in the smallest teeth should be investigated during the design process of the conical machine. The choice of the conical angle, in fact, can be influenced by the level of saturation experienced in the teeth of the smaller side of the stator.

$$\beta_s = \frac{\pi \overline{D}}{N_s} \tag{3.25}$$

$$b_{\max} = \frac{\pi D_{\max}}{N_s} - w \tag{3.26}$$

$$b_{\min} = \frac{\pi D_{\min}}{N_s} - w \tag{3.27}$$

3.5 Forces in Conical Machines

The forces developed on the rotor surface are estimated using the MST. By definition, the MST is a force per unit area. In fact, $\overleftrightarrow{T}$ represents a force density with a magnetic origin that depends on the vector field strength $\vec{H}$. If calculated on an element area with permeability μ_0 and expressed in a generic orthogonal coordinate system $(\vec{e_1}, \vec{e_2}, \vec{e_3})$, the MST is determined through the diagonal symmetric matrix of (3.28) [24].

$$\overleftrightarrow{T} = \begin{pmatrix} \mu_0 H_1^2 - \mu_0 H^2/2 & \mu_0 H_1 H_2 & \mu_0 H_1 H_3 \\ \mu_0 H_2 H_1 & \mu_0 H_2^2 - \mu_0 H^2/2 & \mu_0 H_2 H_3 \\ \mu_0 H_3 H_1 & \mu_0 H_3 H_2 & \mu_0 H_3^2 - \mu_0 H^2/2 \end{pmatrix}. \quad (3.28)$$

As for any traditional, cylindrical electrical machine, the magnetic field strength has a tangential and normal component, H_t and H_n. The tangential component is directly related to the torque-producing shear stress. The normal component is oriented perpendicularly to the lateral surface of the rotor (surface S_2 in Figure 3.13) in the direction of the normal vector **n** of Figure 3.13. When a cylindrical coordinates system $(\vec{e_r}, \vec{e_\vartheta}, \vec{e_z})$ is adopted, the projections of the vector **n** on each axis have the same direction of those reported in (3.29). The radial and axial projections of **n** are function of the cone angle γ. The radial component n_r follows the cone radius direction whereas the axial component n_z is parallel to the longitudinal direction of the motor. Previous considerations about the unit vector **n**, can be extended to the normal component of $\vec{H}$; in the same way, the normal component H_n can be separated into radial and axial contributions calculated as in (3.30).

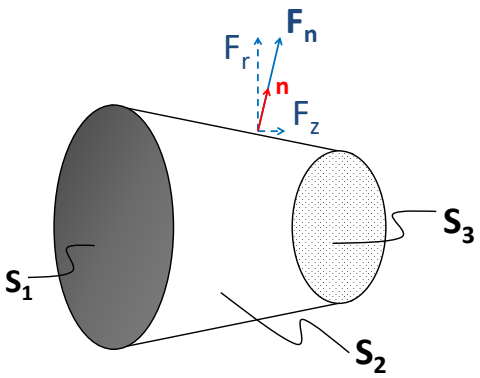


FIGURE 3.13 – FORCES ACTING ON THE CONICAL MACHINE

$$\mathbf{n} = \begin{bmatrix} n_r \\ n_t \\ n_z \end{bmatrix} = \begin{bmatrix} \cos\gamma \\ 0 \\ \sin\gamma \end{bmatrix} \tag{3.29}$$

$$\vec{H} = \begin{bmatrix} H_r \\ H_t \\ H_z \end{bmatrix} = \begin{bmatrix} H_n \cos\gamma \\ H_t \\ H_n \sin\gamma \end{bmatrix} \tag{3.30}$$

When applied on the conical air gap area element, the MST can be expressed as a function of the normal and tangential air gap flux densities, B_n and B_t. Thus, an equivalent expression of (3.28) is obtained as in (3.32) using the relation of (3.31) where the value μ_0 is the vacuum permeability. The symbols B_r and B_z indicate respectively the radial and the axial projections of the normal flux density B_n in the cylindrical frame system.

$$B = H / \mu_0 \tag{3.31}$$

$$\overleftrightarrow{T} = \frac{1}{\mu_0}\begin{pmatrix} B_n^2 - B^2/2 & B_n B_t & B_n B_z \\ B_t B_r & B_t^2 - B^2/2 & B_t B_z \\ B_z B_n & B_z B_t & B_z^2 - B^2/2 \end{pmatrix} \tag{3.32}$$

Combining (3.29) and (3.32), the expression of the force density $\vec{f}$ in the conical air-gap is obtained as in (3.33). The radial and axial components, f_r and f_z, are function of the normal stress σ whereas the tangential component of the force density is derived from the expression of the tangential stress τ; normal and tangential stresses are defined in (3.34) [85].

$$\vec{f} = \begin{bmatrix} f_r \\ f_t \\ f_z \end{bmatrix} = \frac{1}{2\mu_0}\begin{bmatrix} (B_n^2 - B_t^2)\cos\gamma \\ 2B_n B_t \\ (B_n^2 - B_t^2)\sin\gamma \end{bmatrix} \tag{3.33}$$

$$\sigma = \frac{B_n^2 - B_t^2}{2\mu_0}; \quad \tau = \frac{B_n B_t}{\mu_0} \tag{3.34}$$

The total force is calculated as the integral of the force density $\vec{f}$ on the truncated cone volume of the rotor V_r. The force density, in turn, is determined as the divergence of MST, as clarified in (3.35).

$$\mathbf{F} = \int_{V_r} \vec{f} dv = \int_{V_r} \nabla \vec{\vec{T}} dv \tag{3.35}$$

Considering the divergence theorem, in vector calculus, the problem can be simplified as the integral on the surface enclosing the conical body (area S_2 in Figure 3.13) as described in (3.36), where **n** is the normal vector to the conical surface S_2 formulated in (3.29).

$$\mathbf{F} = \int_{S_2} \vec{f} \mathbf{n} ds \tag{3.36}$$

Due to the variation of the flux density with the angle on the rotor circumference ϑ, the computation of each component of the force on the conical air-gap is reduced to the expressions (3.37)-(3.39).

$$F_r = \frac{L_{Fe,\gamma} \overline{r_{si}}}{2\mu_0} \int_0^{2\pi} (B_n^2 - B_t^2) \cos\gamma d\vartheta \tag{3.37}$$

$$F_t = \frac{L_{Fe,\gamma} \overline{r_{si}}}{\mu_0} \int_0^{2\pi} (B_n B_t) d\vartheta \tag{3.38}$$

$$F_z = \frac{L_{Fe,\gamma} \overline{r_{si}}}{2\mu_0} \int_0^{2\pi} (B_n^2 - B_t^2) \sin\gamma d\vartheta \tag{3.39}$$

In (3.37)-(3.39), $L_{Fe,\gamma}$ is the equivalent stator length, calculated as in (3.2), and $\bar{r}_{si}$ is the medium stator bore radius of the conical machine quantified in (3.40), where $r_{si,max}$ and $r_{si,min}$ are respectively the maximum and minimum stator bore radii.

$$\overline{r_{si}} = \frac{r_{si,\max} + r_{si,\min}}{2} \tag{3.40}$$

The above force expressions lead to the conclusion that the presence of the axial force in conical motors is due to the axial component of the normal vector of the magnetic field to the lateral surface. In cylindrical machines, in fact, the axial component does not appear, since the normal vector is perpendicular to the cylindrical lateral surface (see Figure 3.14) and it is oriented in the radial direction. This can be easily appreciated by implementing a cone angle γ=0 in (3.29). In this case, the radial component n_r will be equal to one whereas the

axial component n_z will be null; thus, no axial force will be developed. In cylindrical machines, in fact, the normal and the radial components of the magnetic field strength overlap as highlighted in Figure 3.14.

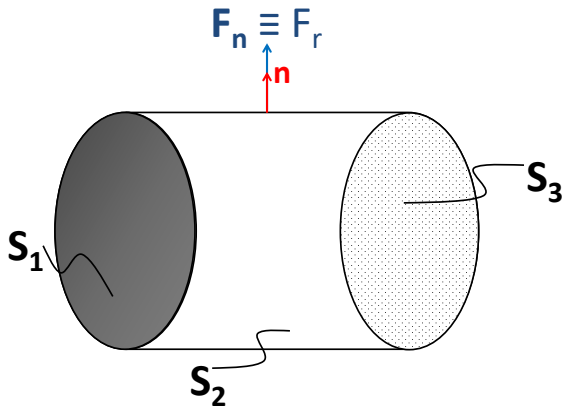


FIGURE 3.14 – FORCES ACTING ON THE CYLINDRICAL MACHINE

The computation of F_z in (3.39) can be adopted as a design formula for the axial force. In the same way, the tangential force F_t is used for the calculation of the torque as in (3.41). It is important to have an idea of this value in order to verify if the conical motor is able to meet the torque requirements and if the axial force is enough to move the motor horizontally.

$$T = F_t \overline{r_{si}} \tag{3.41}$$

For the sake of clarity, the presence of the radial component of the total force, F_r, also needs to be considered. These radial forces are partly dependent on the inherent attraction between the stator and the rotor. For a magnetically balanced machine, the total effect of these forces is usually negligible as the resulting vector sum of radial stresses over the rotor circumference approaches zero. Any remaining unbalanced pull is usually absorbed and held rigid by the machine bearings.

3.6 Chapter Highlights and Contribution to Research

The major milestones and highlights of this Chapter can be listed as follows:

1) A solution in terms of simplifying an intrinsic 3D problem (conical machine) into a simplified 2D problem has been proposed. This uses an analytical calculation for the third dimension of the MST.
2) An innovative equivalent analytical model and 2D equivalent FE model using several cylindrical machines is proposed that simplifies greatly the analysis and design of conical machines. This was validated through a 3D FEM.
3) Through the use of the proposed concept of equivalent dimensions, an analytical design methodology for CMs based on the traditional design formulae for cylindrical machines has been developed. This will accelerate understanding in terms of CMs.
4) A detailed explanation of the forces in conical motors in relation to the motor field compiled in a complete and comprehensive manner. To the author's knowledge, no such analytical explanation is available in literature.
5) Design guidelines for the design of conical machines, taking in account possible motor limitations (such as the effects of saturation or losses).

3.7 Conclusion

The concepts of the equivalent axial length and mean radius expressed in this Chapter are extremely important for the rest of this dissertation, where in the next chapters a prototype PMCM is developed and manufactured.

This concept has shown how the basic 2D equivalent model can be used in order to facilitate the design of PMCMs. Most importantly, this Chapter has validated and shown that this methodology of approximation is valid even when compared against a full, 3D simulation using a FEA commercial package.

Chapter 4
Development of a High-Performing PMCM

In this Chapter the basic processes for development of PMCM are proposed and investigated. As a benchmark machine, a high performing cylindrical motor is considered. Starting from this conventional machine, the Chapter takes the reader through a series of steps aimed at converting the conventional machine into a conical counterpart. The performances of the conical motor are then compared against those of the initial cylindrical machine.

The Chapter begins by describing the design of the cylindrical motor and its main features. The motor that has been selected is a cylindrical machine already optimised [8] to meet specific requirements of torque and speed. The FE model of the cylindrical motor has been reproduced and verified by comparing against the original results that were achieved in a previous work. The theory of forces, proposed in Section 3.5 and employed for the calculation of the forces acting on the conical motor, has been confirmed on the cylindrical machine.

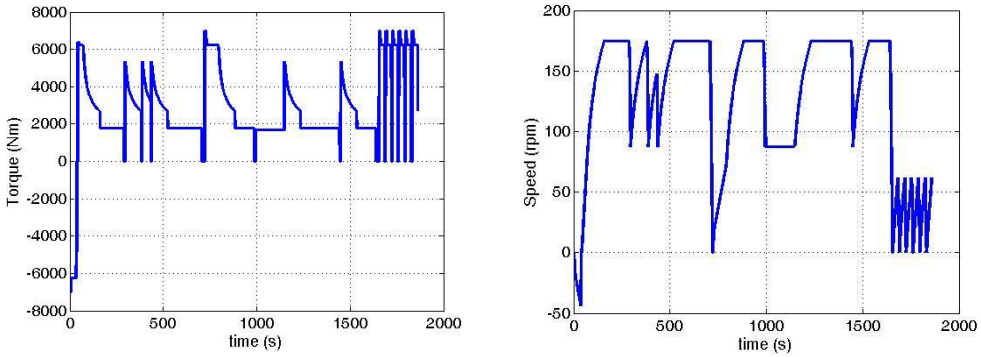
In the second part of the Chapter, steps for building the FE equivalent model of the conical machine are presented with the aim of obtaining a model that returns a valid level of accuracy. Finally, the forces and torque of the conical motor are computed and compared with the cylindrical counterpart in order to achieve the formulation of the torque in relation to the conical angle.

4.1 High Performing Cylindrical Motor

The cylindrical motor chosen for the following study is used for traction applications in aircraft and has been previously realised in the University of Nottingham (UoN) [8]. The motor has been optimised in order to achieve a high level of torque density. The fundamental requirements for such a system are reported in Table 4.1. The torque and speed duty cycles that were indicated as the main specifications for the project are shown in Figure 4.1.

TABLE 4.1 – CYLINDRICAL MOTOR SPECIFICATIONS

Converter VA_{max} Ratings	$I_{pk} = 225A$, $V_{dc} = 525V$
Torque	$7kNm$
Maximum Mass	$130kg$
Volume	$0.0337m^3$
Torque Density	$53.84Nm/kg$
Torque Density	$207.72kNm/\ m^3$
Max Speed	$171rpm$
Ambient Temperature	-10◦ ÷ 70◦



a) Torque Duty Cycle b) Speed Duty Cycle

FIGURE 4.1 – TORQUE AND SPEED DUTY CYCLES

The main aim during the design process of the system in hand was to attain the highest rate of torque per volume possible with a motor robust enough to survive the harsh temperature conditions defined in Table 4.1. The optimisation procedure described in [77] led to the construction of an electrical motor, whose features are shown in Figure 4.2 and summarised as follows:

- Single air-gap, radial configuration.
- Outer rotor solution.
- CoFe stator laminations.
- Fractional-slot concentrated windings.
- Double layer, double star winding with open slot configuration.
- Five-stage, Full-Halbach array magnet arrangement.

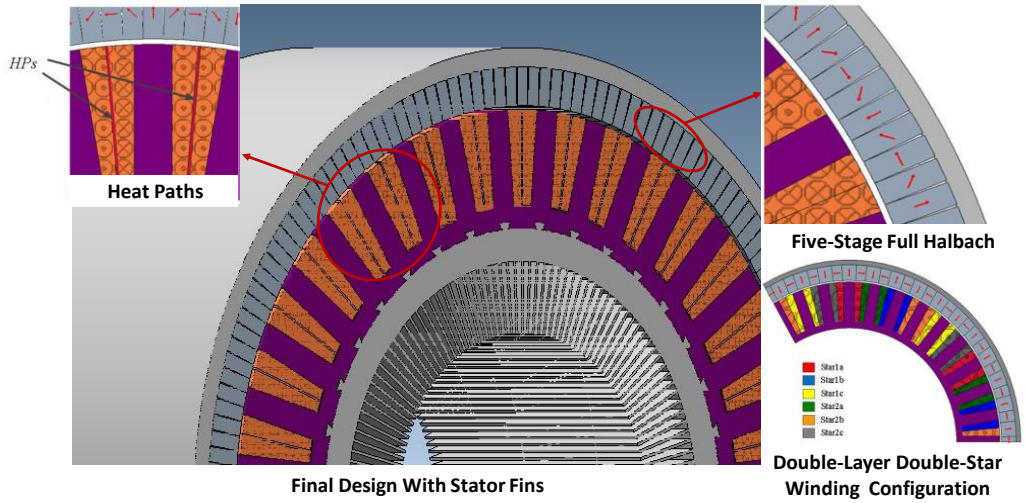


FIGURE 4.2 – MAIN CYLINDRICAL MOTOR FEATURES

4.1.1 Cylindrical Motor Analyses

In order to compare the motor performances with a conical version of the benchmark machine, a detailed study has been undertaken about the machine configuration of [77]. In the following sections, the motor dimensions, as well as winding arrangement and performances, are described.

A. Motor Dimensions

In this work, the motor model of [77] has been built through the use of Matlab® code implemented in Infolytica® Magnet environment for FE analyses. Results were successively verified analytically. The motor representation as appears in Figure 4.3 is a simplified model of the full design shown in Figure 4.2. The structural dimensions utilised for the motor simulations are reported in Table 4.2 and indicated in Figure 4.3.

TABLE 4.2 – CYLINDRICAL MOTOR DETAILS

Quantity	Symbol	Value
Slots/Poles		36/42
Axial Length	l_{ax}	151mm
External Rotor Radius	R_e	235.5mm
Internal Stator Radius	R_{si}	142mm
Air-gap Length	g	2mm
Magnet Length	L_M	20mm
Rotor Back Iron	h_{br}	10.5mm
Stator Back Iron	h_{bs}	11.5mm
Slot Area	A_s	11.84mm^2
Slot Height	h_s	50mm
Active Mass		108kg
Active Volume		0.0254m^3
Number of Turns	N	33
Peak Current Density	J_{pk}	38A/mm^2
Ambient Temperature	T_{amb}	50°C

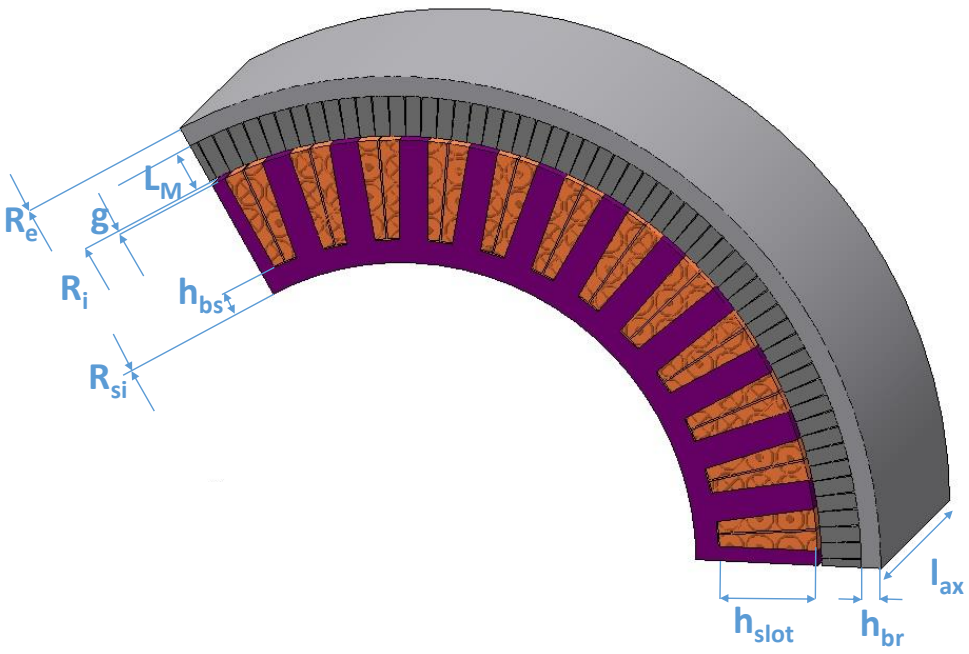


FIGURE 4.3 – MAIN DIMENSIONS OF THE CYLINDRICAL MOTOR

B. Winding Arrangement

The criteria for the allocation of the windings within the motor slots is here explained with the star-of-slots theory [86]. The machine has a 36-slot/42-pole combination. Since the slots over poles ratio is not an integer value, the theory of fractional slot-pole combination has been adopted for this study [86]. The motor is fed with two different tri-phase windings (double-star). Each slot is divided into two halves (double layer) assigned to each star. In one slot both stars coexist as can be observed in Figure 4.2. The star-of-slots helps to understand how each side of the slot (Slot Side A and Slot Side B) has been assigned to each phase of a selected star.

In Figure 4.4-a and Figure 4.4-b, the two stars represent the left and right side of each slot (side A and side B). It should be noted that during the design procedure the optimal phase shift between the two sets of windings was found to be 30 electrical degrees. The same angle physically separates two spokes that co-exist within the same sector of Figure 4.4-d. The number assigned to each phasor of the star spokes corresponds to the slot number and the colour of each sector is associated with the phases of each winding Figure 4.4-c.

The periodicity of the motor model is one-third of the whole machine (same as reported in Figure 4.3). This value has been obtained as in (4.1), where the *t* represents the periodicity of the star and is calculated as the Greatest Common Divisor (G.C.D.) between the number of slots *Q* and the number of pole pairs *p*. The quantity *t* corresponds also to the number of phasors on each spoke. Each star has *Q/t* number of spokes.

$$t = G.C.D\{Q, p\} \tag{4.1}$$

The physical angle between two adjacent slots is α_s, turned into its electrical corresponding α^e_s as in (4.2). The angle used between two consecutive spokes α_{ph} is calculated as in (4.3) and reported in Figure 4.4-a.

$$\alpha^e_s = p\alpha_s; \quad \alpha_s = 2\pi / Q \tag{4.2}$$

$$\alpha_{ph} = \frac{2\pi}{Qt} = \frac{t}{p}\alpha^e_s \tag{4.3}$$

Each slot (phasor of the spoke) is assigned to a specific sector (Figure 4.4-c). The sector associates the numbered slots to a specific phase (Figure 4.4-d). The angle between one sector and the other is calculated as π/m, where m is the number of phases.

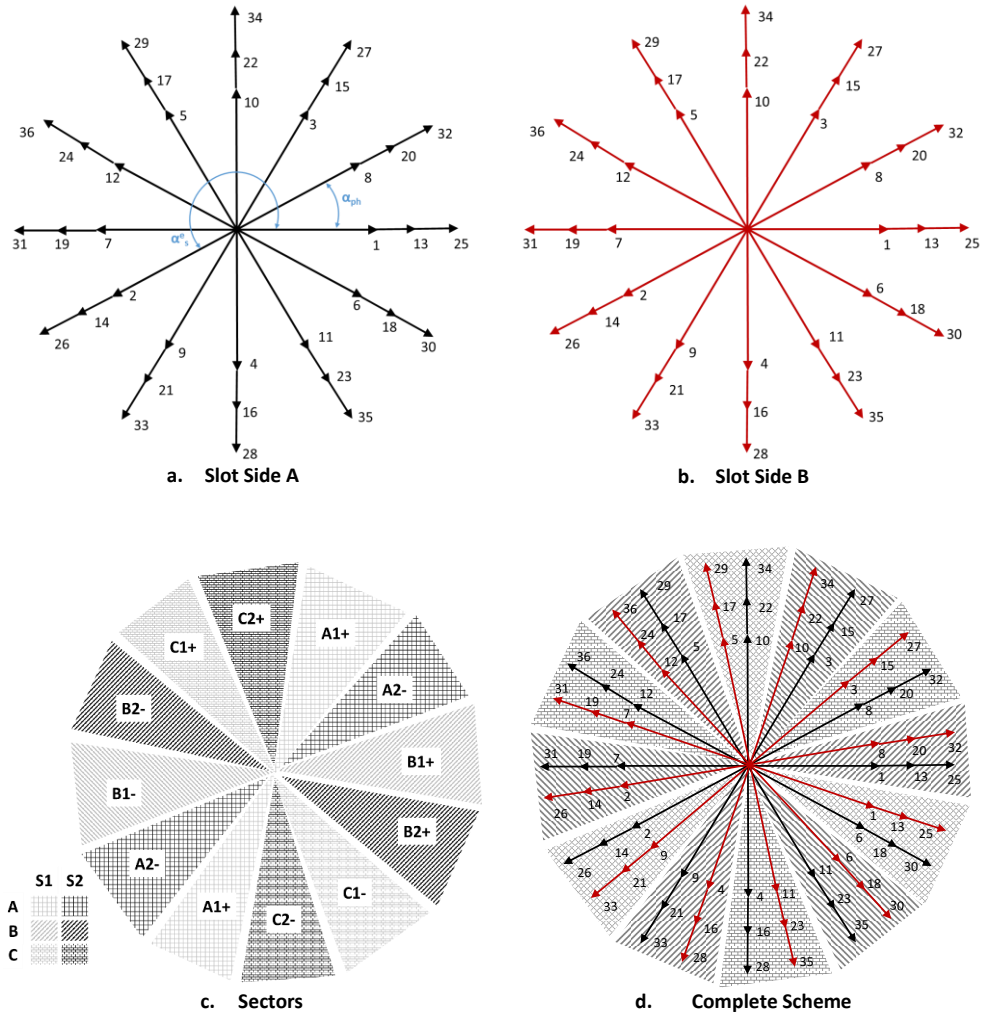


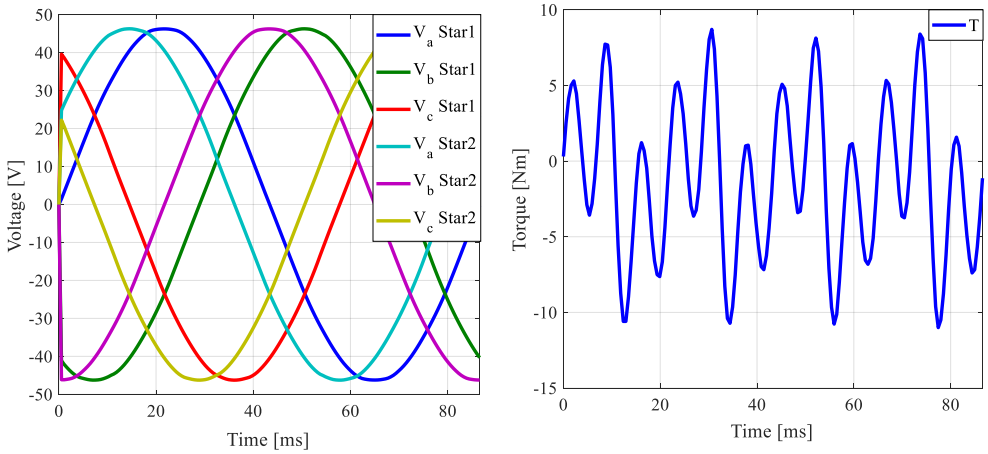
FIGURE 4.4 – STAR OF SLOTS OF THE CYLINDRICAL MOTOR WINDING

C. *Performances*

Key performances of the cylindrical motor after the optimisation procedure given in [8] are reported in Table 4.3. These values have been confirmed through experimental tests on the assembled machine, as reported in [8]. Together with the high level of delivered peak torque, a distinctive aspect of the final design is also the quality of back-EMFs and torque. The model adopted in the present work has also been validated against the experimental and simulation results given in [87]. The on-load conditions are compared in next section in Figure 4.9, while the no-load conditions are validated in Figure 4.5.

TABLE 4.3 – CYLINDRICAL MOTOR PERFORMANCES

Total active mass	108.8kg
Total volume	0.0254m^3
Mean torque at peak load condition	7049.6Nm
Shear stress at peak load condition	175.9kN/m^2
Torque ripple at peak load condition	0.7%
Copper loss at peak load condition	26.26kW
Torque density at peak load condition	64.79Nm/kg
Torque density at peak load condition	277.54kN/m^3



a) No-Load voltage b) Cogging Torque

FIGURE 4.5 – NO-LOAD PERFORMANCES OF THE CYLINDRICAL MOTOR

4.1.2 Cylindrical Machine Forces and Torque

In this context, supplementary investigations on the cylindrical motor at hand have been accomplished with the aim of validating the analytical method for the calculation of the forces in the air-gap, as explained in Section 3.5.

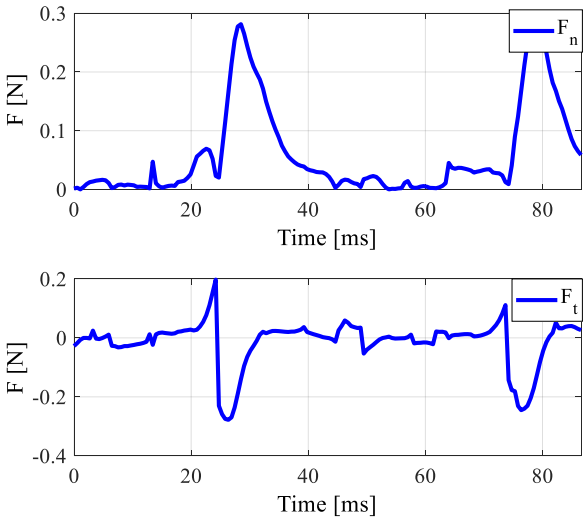
In Figure 4.6-a), the normal and tangential forces (F_n and F_t) acting on the entire rotor surface are reported. For each instant of the electric cycle showed in Figure 4.6-a), the static forces have been calculated using (4.4) and (4.5). The sum of the static forces approach to zero proving that the total effect of the stresses acting on the rotor is effectively balanced. However, if only one third of the machine is considered, due to the periodicity t, then the calculation of the forces through the use (3.37)-(3.39) can be proven. In Figure 4.6-b), the total amplitude of the force ($|F|$) calculated on one-third of the machine using (4.6) is reported and compared with the numerical simulation results. Each component that

contributes to the total magnitude of the force has been obtained as in (3.37)-(3.39) where the equivalent radius and length of the conical motor have been replaced with rotor internal radius (R_i) of the cylindrical motor and the real axial length (l_{ax}) of the machine. In this case, the cone angle is equal to zero, thus the axial force of (3.39) is null. The radial force of (3.37) is simplified as in (4.4) whereas the tangential force remains unvaried from (3.38) to (4.5).

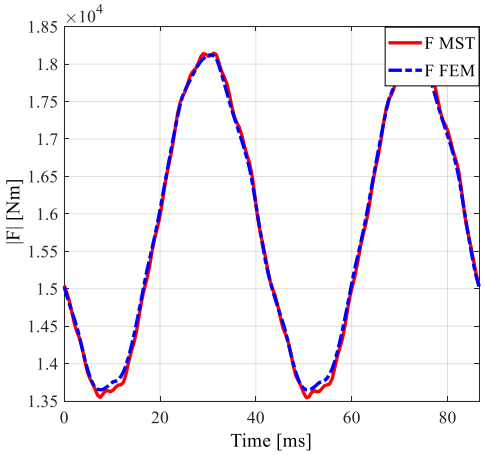
$$F_r = l_{ax} R_i \int_0^{2\pi} \sigma d\vartheta = \frac{l_{ax} R_i}{2\mu_0} \int_0^{2\pi} (B_n^2 - B_t^2) d\vartheta \tag{4.4}$$

$$F_t = l_{ax} R_i \int_0^{2\pi} \tau d\vartheta = \frac{l_{ax} R_i}{\mu_0} \int_0^{2\pi} (B_n B_t) d\vartheta \tag{4.5}$$

$$|F| = \sqrt{F_r^2 + F_t^2} \tag{4.6}$$



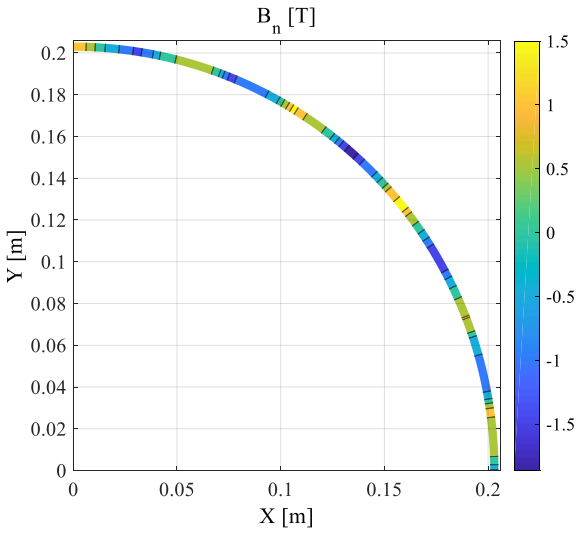
a) Force on the entire motor



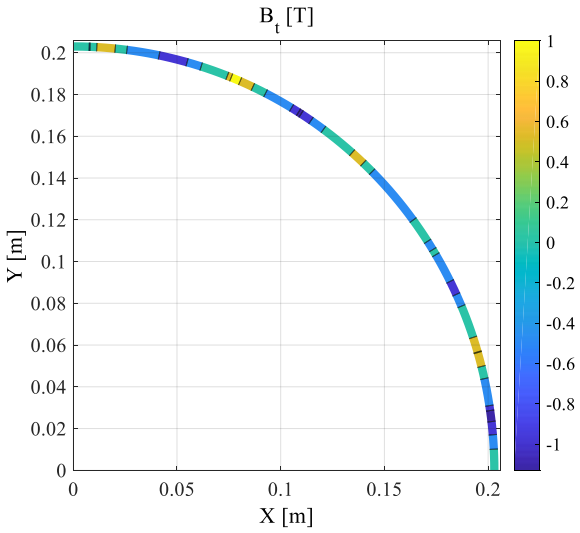
b) Force on one motor symmetry

FIGURE 4.6 – ANALYTICAL VS FEM FORCES OF THE CYLINDRICAL MOTOR

As stated in Section 3.5 and clarified in (4.4) and (4.5), the determination of the forces derives from the integral of the radial and tangential stress (σ and τ) over the rotor lateral surface which in turn depends on the distribution of the flux density. For sake of clarity, both distributions of the flux density and stresses are reported in Figure 4.7 and Figure 4.8, respectively.

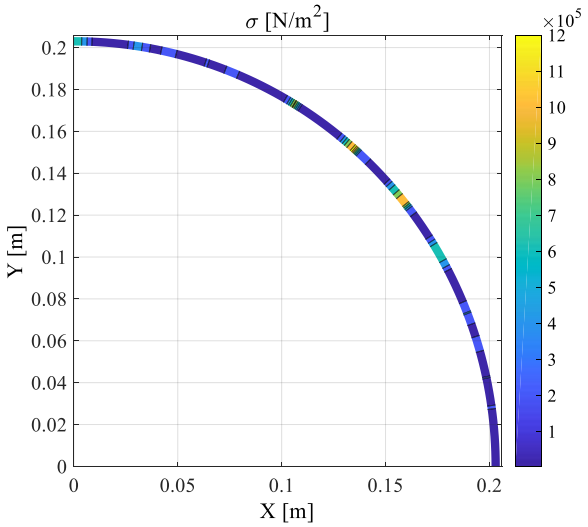


a) Normal Flux Density

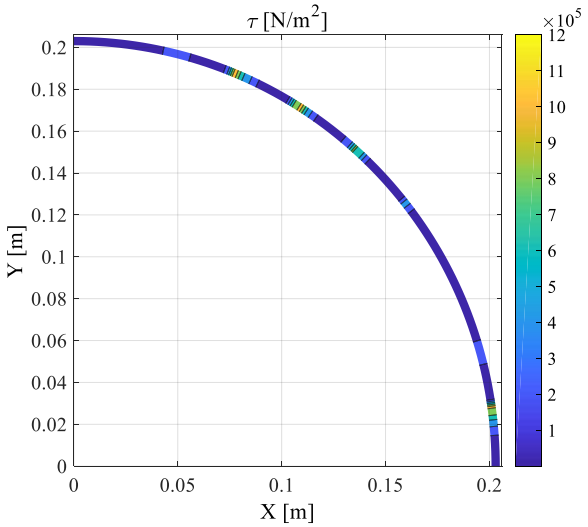


b) Tangential Flux Density

FIGURE 4.7 – FLUX DENSITY DISTRIBUTION IN THE CYLINDRICAL MOTOR AIR-GAP



a) Normal Stress



b) Tangential Stress

FIGURE 4.8 – STRESS DISTRIBUTION ON THE CYLINDRICAL MOTOR ROTOR SURFACE

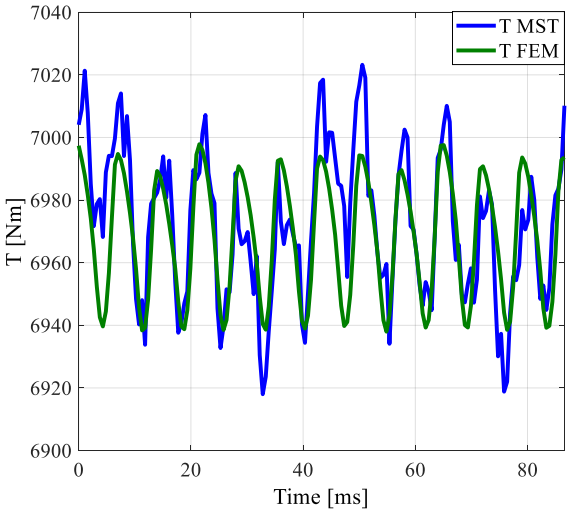


FIGURE 4.9 – ANALYTICAL VS FEM TORQUE OF THE CYLINDRICAL MOTOR

The analytical torque has been obtained utilising the tangential force calculated as in equation (4.5). The tangential force has been determined on one-third of the motor so that the torque on one symmetry is calculated multiplying the tangential force of equation (4.5) by the internal rotor radius as follow.

$$T = R_i F_t = l_{ax} R_i^2 \int_0^{2\pi} \tau d\vartheta = \frac{l_{ax} R_i^2}{\mu_0} \int_0^{2\pi} (B_n B_t) d\vartheta \tag{4.7}$$

The total torque is obtained as the torque on one periodicity times the number of periodic units (t) obtained as in (4.1).

As in can be seen in Figure 3.9, small differences exist between the calculated torque and the torque using FEA, mainly due to the exploitation of symmetries and the integration operation. Only a percentage of 0.055 difference exists between the FEM average torque and the MST torque, considering a peak torque of 7kNm.

As shown in Figure 4.9, this method produces accurate results, proving that even when forces are analysed on a cylindrical machine in which the effects are perfectly balanced, the use of the symmetries can be exploited to assess the forces acting on the rotor surface. This principle will be employed in the next section for the study of the forces acting on the conical counterpart's rotor lateral surface.

4.2 Conical Motor

As in the case of the cylindrical motor, a high level of torque is one of the main requirements of the conical motor since this is to be employed for a traction application. However, while the delivered torque is necessary to perform traction, the axial force is fundamental to attach and detach the motor to rest of the system. It is, in fact, this axial movement which will replace the presence of the clutch.

4.2.1 The Proposed Two-Dimensional Analysis Methodology

The basic concept for the FE analysis of PMCMs that is being proposed in this thesis is based on a simple but elegant methodology where the PMCM is considered to be a number of conventional, cylindrical machines. As already, explained in Section 3.2, the simplification of the conical machine studies using several two-dimensional cylindrical motors removes the need for 3D models. The validity of this 2D model philosophy has been confirmed in Section 3.2.

This section walks the reader through the procedure utilized for building the 2D equivalent model, via the use of a stack of cylindrical machines, named "sub-motors". A two-dimensional equivalent model of a PMCM is hereafter built based on the cylindrical motor configuration presented in Section 4.1. The sub-motors' dimensions are derived with respect to the selected conical angle. FE results obtained for each sub-motor are numerically manipulated to obtain the performances of the whole PMCM. Force and torque are computed for each sub-motor and, successively, their effects are summed to obtain the total PMCM torque, based on the superimposition principle. The same superimposition principle is adopted for the motor voltages, flux-linkage, as shown in the next Section 4.3.

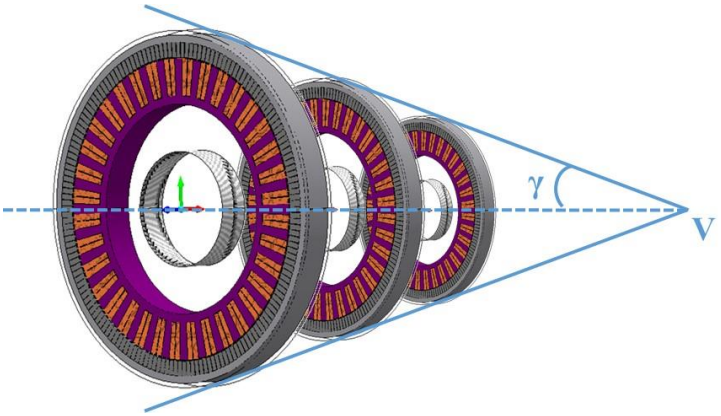
To explain the concept in a simple and clear manner, three sub-motors have been chosen for the approximation of the cone volume. The higher the number of sub-motors the more accurate are the total conical motor results. However, the two-dimensional model set with three sub-motors provided a good level of estimation of the PMCM performances when compared against its cylindrical counterpart, as demonstrated in Section 4.3.

4.2.2 Application of the Proposed Methodology

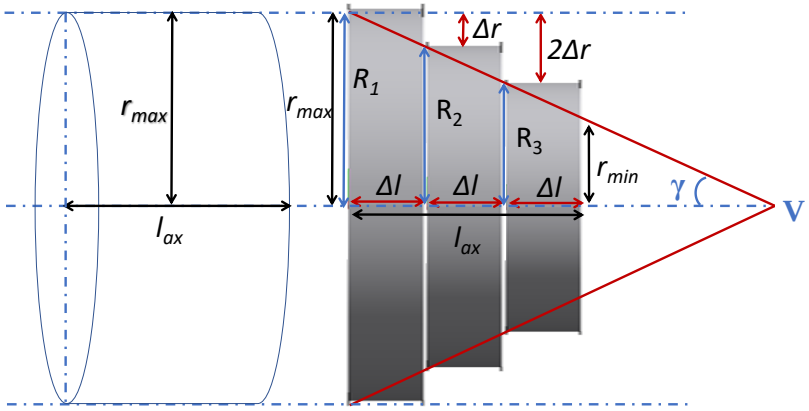
For this analysis and hereafter, it is worth to underline that two motors (one cylindrical and its corresponding conical version) are considered "twin" or equivalent if the maximum radius r_{max} and the overall axial length l_{ax}, as indicated in Figure 4.10, remain the same in the case of both shapes.

The conical version of the cylindrical machine of Figure 4.3, has been modelled using three two-dimensional cylindrical machines with the same configuration

of the original cylindrical motor shown in Section 4.1.1 (same slot/poles combination, number of turns, slot outline, winding and magnets arrangement, material etc.). The dimensions of the three motors have been obtained through a homothetic transformation of the cylindrical model with respect to the homothetic centre V of Figure 4.10-a). The centre of the transformation corresponds to the apex of a cone with a vertex angle γ.



a) Homothetic Transformation



b) Isometric View

FIGURE 4.10 – EQUIVALENT CONICAL MOTOR

In the isometric view of Figure 4.10-b), the main dimensions of the motors are highlighted and the existing correlation between the radii of each machine is visually represented. This type of relation is applicable to any radii of the three motors and it is mainly dependent on the selected conical angle. The cone angle adopted for the following evaluations is 20°. This was an indicative choice; no significant reasons were behind this decision.

Since the force and torque are evaluated at the rotor bore, the relation between the radii of each motor is demonstrated on the internal rotor radius, designated as R_i in Figure 4.3. The rotor radius of the first motor (R_{i1}) corresponds to the

radius of the original cylindrical machine (R_i) and it is set as the maximum internal rotor radius of the conical machine (r_{max}). The following two radii, R_{i2} and R_{i3}, are derived as the difference between the maximum radius and a factor Δr that represents the reduction rate of the radii along the conical shape. All this is described by (4.8)-(4.10).

$$R_{i1} = R_i = r_{\max} \tag{4.8}$$

$$R_{i2} = r_{\max} - \Delta r \tag{4.9}$$

$$R_{i3} = r_{\max} - 2\Delta r \tag{4.10}$$

The quantity Δr is directly related to the cone angle γ, as observable in (4.11). This value is important for the definition of the minimum radius of the conical motor. The smallest radius of the conical machine (r_{min} in Figure 4.10) is a determining factor in the torque analytical calculation, as illustrated later on. The sub-motors of Figure 4.10 all have the same axial length. The total length of the original cylindrical motor l_{ax} has been divided equally by the number of motors used for approximating the cone volume. In this case, three motors have been adopted so that each motor length Δl is calculated as in (4.12).

$$\Delta r = \Delta l \tan \gamma \tag{4.11}$$

$$\Delta l = \frac{l_{ax}}{3} \tag{4.12}$$

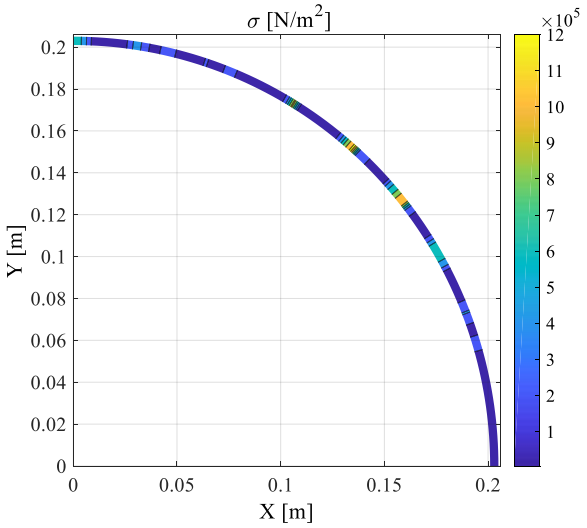
The measurements reported in (4.8)-(4.12) are critical for the calculation of whole conical motor performances addressed in the next section.

4.2.3 Conical Motor Performances

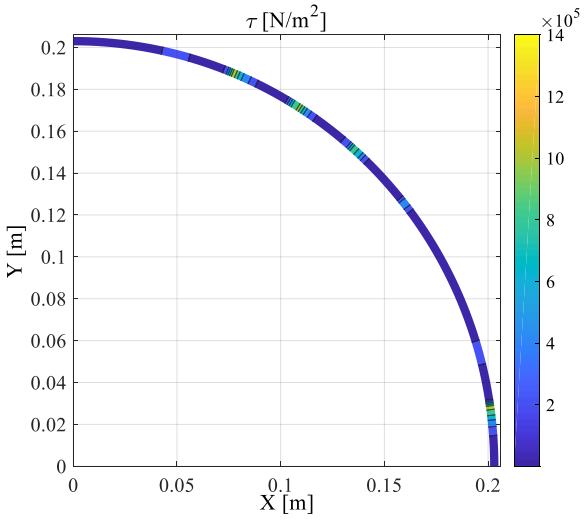
As mentioned above, the essential aspects of the conical motor assessment are the performances in terms of axial force and torque. The axial force, as described in Section 3.5, is the projection of the total normal force on the horizontal axis with respect to the chosen cone angle whereas the torque is obtained from the tangential force times the rotor radius.

In Figure 4.11-Figure 4.13, not much difference can be observed between the stress distributions of the three sub-motors. The flux density, at load and no-load

conditions, in fact, can be assumed constant in the whole conical machine generating a similar stress distribution between the three motors. On the contrary, forces and torque vary consistently between one motor and the other since they are directly related to the dimensions of three machines. The forces, in fact, are obtained as the integration of the stresses on the rotor surface of each motor; the motors have the same axial length whereas their diameters are different in a proportion that depends on the conical angle.

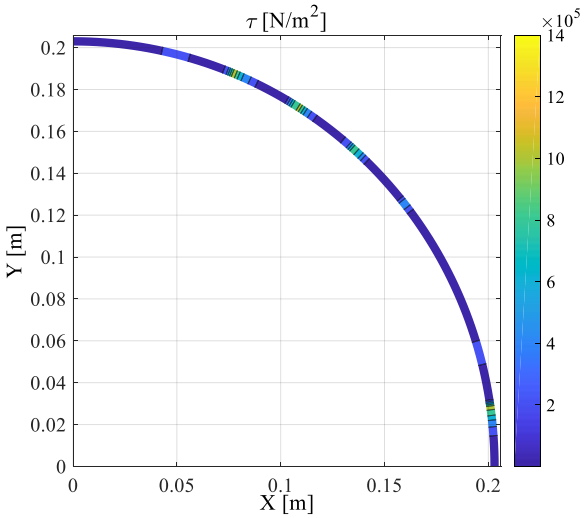


a) Normal

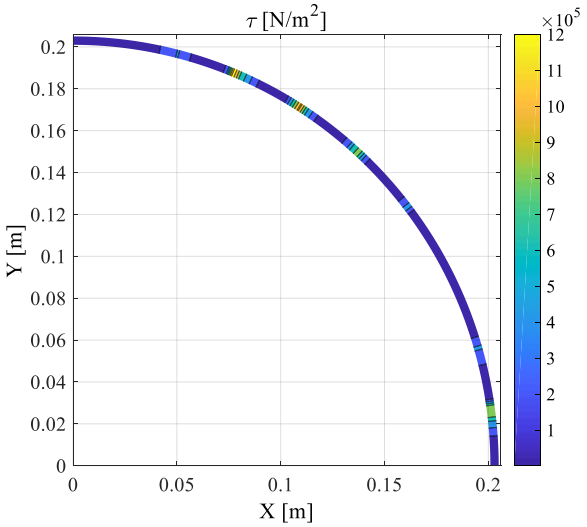


b) Tangential

FIGURE 4.11 – NORMAL AND TANGENTIAL STRESS DISTRIBUTION SUB-MOTOR 1

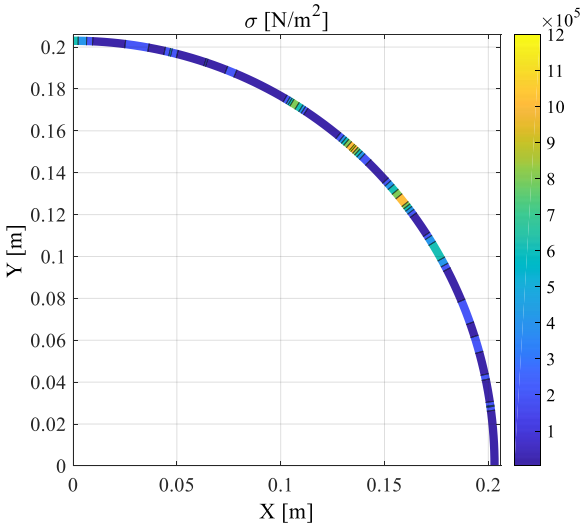


a) Normal

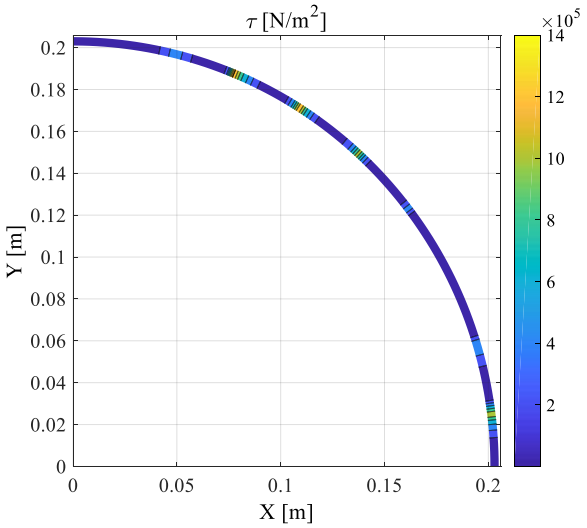


b) Tangential

FIGURE 4.12 – NORMAL AND TANGENTIAL STRESS DISTRIBUTION SUB-MOTOR 2



a) Normal



b) Tangential

FIGURE 4.13 – NORMAL AND TANGENTIAL STRESS DISTRIBUTION SUB-MOTOR 3

In the following analyses, the individual performances of the motors are not emphasised. The attention is focused on the contribution of each machine to the total torque and force. The force and torque of the whole conical motor are determined as the algebraic sum of the forces developed on the rotor surface of each motor.

The forces are calculated separately ($F_{n,1}$, $F_{n,2}$, $F_{n,3}$ and $F_{t,1}$, $F_{t,2}$, $F_{t,3}$) and successively added into the conical forces $F_{n,tot}$ and $F_{t,tot}$, as reported in equations (4.13) and (4.14). For sake of brevity, normal and tangential forces developed by each motor are not shown individually. In Figure 4.14, the total force of each sub-motor (F_1, F_2, F_3) and the total conical force (F_{tot}) are displayed and can be calculated by (4.15).

$$F_{n,tot} = F_{n,1} + F_{n,2} + F_{n,3} = \Delta l R_{i1} \int_0^{2\pi} \sigma_1 d\vartheta + \Delta l R_{i2} \int_0^{2\pi} \sigma_2 d\vartheta + \Delta l R_{i3} \int_0^{2\pi} \sigma_3 d\vartheta \tag{4.13}$$

$$F_{t,tot} = F_{t,1} + F_{t,2} + F_{t,3} = \Delta l R_{i1} \int_0^{2\pi} \tau_1 d\vartheta + \Delta l R_{i2} \int_0^{2\pi} \tau_2 d\vartheta + \Delta l R_{i3} \int_0^{2\pi} \tau_3 d\vartheta \tag{4.14}$$

$$\begin{aligned} &|F_{tot}| = |F_1| + |F_2| + |F_3|; \\ &|F_1| = \sqrt{F_{1n}^2 + F_{1t}^2};\ |F_2| = \sqrt{F_{2n}^2 + F_{3t}^2};\ |F_3| = \sqrt{F_{3n}^2 + F_{3t}^2}; \end{aligned} \tag{4.15}$$

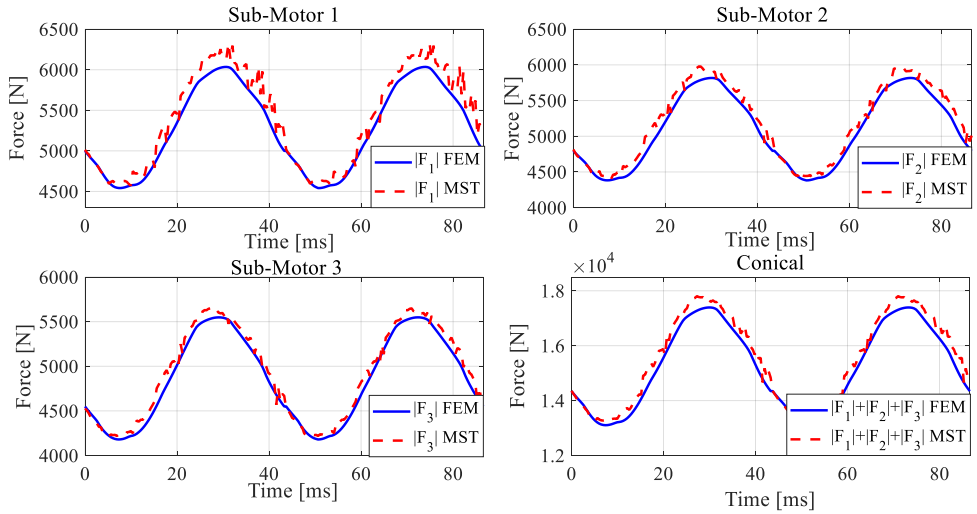


FIGURE 4.14 – ANALYTICAL VS FEM TOTAL FORCE OF THE CONICAL MOTOR

The same superimposition principle, embraced for the calculation of the overall force, applies to the total torque. The conical torque T_{tot} is consequent to the torque developed by each machine (T_1, T_2, T_3). Each torque input is obtained from the tangential forces $F_{t,1}$,$F_{t,2}$,$F_{t,3}$; so that, the same procedure of (4.14) is followed in (4.16) for the estimation of the whole torque. Both individual and total torque trends are presented in Figure 4.15. The greatest contribution to the final torque is thus from the first motor, since it has the maximum radius R_{i1}, whereas the smallest torque is associated with the third machine.

$$T_{tot} = T_1 + T_2 + T_3 = R_{i1}F_{t,1} + R_{i2}F_{t,2} + R_{i3}F_{t,3} = \\ = \Delta l R_{i1}^2 \int_0^{2\pi} \tau_1 d\vartheta + \Delta l R_{i2}^2 \int_0^{2\pi} \tau_2 d\vartheta + \Delta l R_{i3}^2 \int_0^{2\pi} \tau_3 d\vartheta \tag{4.16}$$

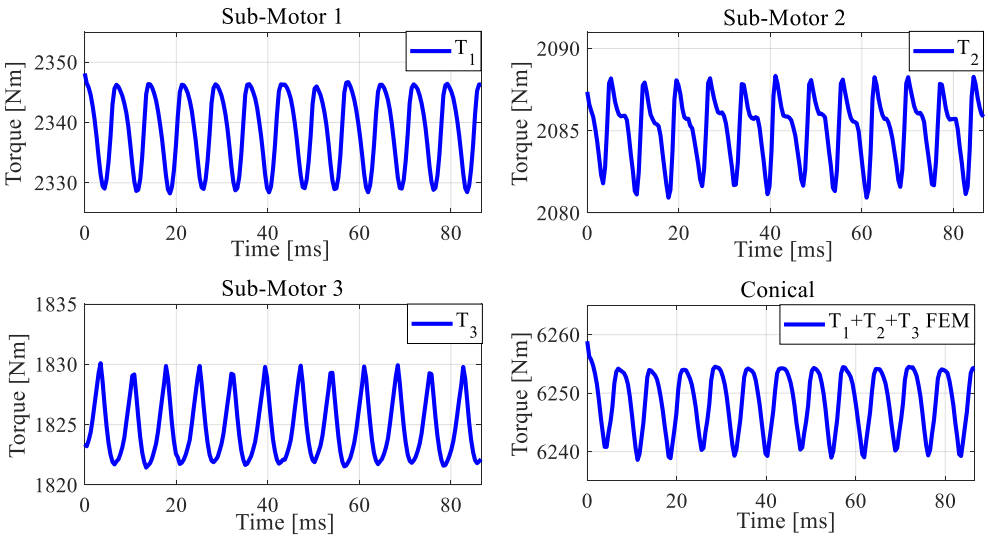


FIGURE 4.15 – TOTAL TORQUE OF THE CONICAL MOTOR

In Figure 4.11-Figure 4.13, the total normal and tangential stresses do not appear. The superimposition principle, in fact, cannot be applied to the stress computation. Stresses are utilised for the calculation of the forces as in equations (4.13) and (4.14). If their sum is computed before the integral operation, a conceptual mistake is made. This concept is mathematically expressed in (4.17) and (4.18), where (σ_1, σ_2, σ_3) and (τ_1, τ_2, τ_3) are respectively the normal and tangential quantities of the stresses calculated for each motor of the conical model.

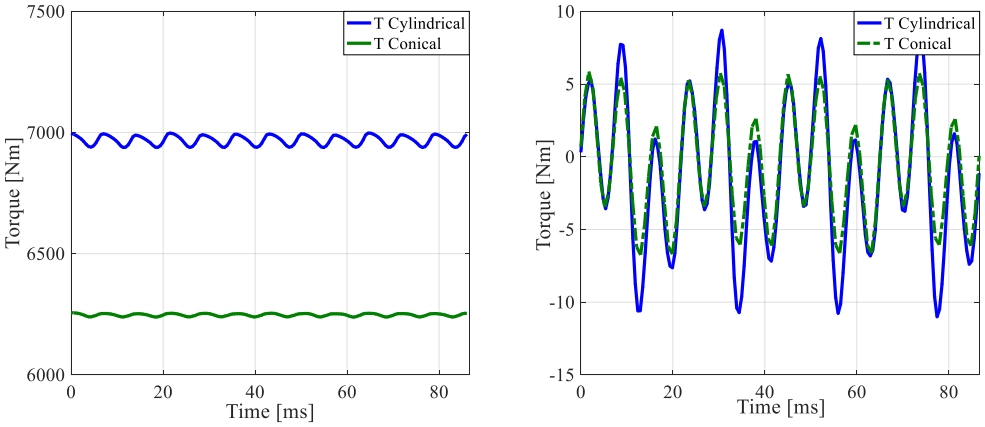
$$\Delta lR_{i1}\int_0^{2\pi}\sigma_1 d\vartheta+\Delta lR_{i2}\int_0^{2\pi}\sigma_2 d\vartheta+\Delta lR_{i3}\int_0^{2\pi}\sigma_3 d\vartheta\neq l_{ax}(R_{i1}+R_{i2}+R_{i3})\int_0^{2\pi}(\sigma_1+\sigma_2+\sigma_3)d\vartheta \tag{4.17}$$

$$\Delta lR_{i1}\int_0^{2\pi}\tau_1 d\vartheta+\Delta lR_{i2}\int_0^{2\pi}\tau_2 d\vartheta+\Delta lR_{i3}\int_0^{2\pi}\tau_3 d\vartheta\neq l_{ax}(R_{i1}+R_{i2}+R_{i3})\int_0^{2\pi}(\tau_1+\tau_2+\tau_3)d\vartheta \tag{4.18}$$

4.3 Cylindrical versus Conical Motor Performances

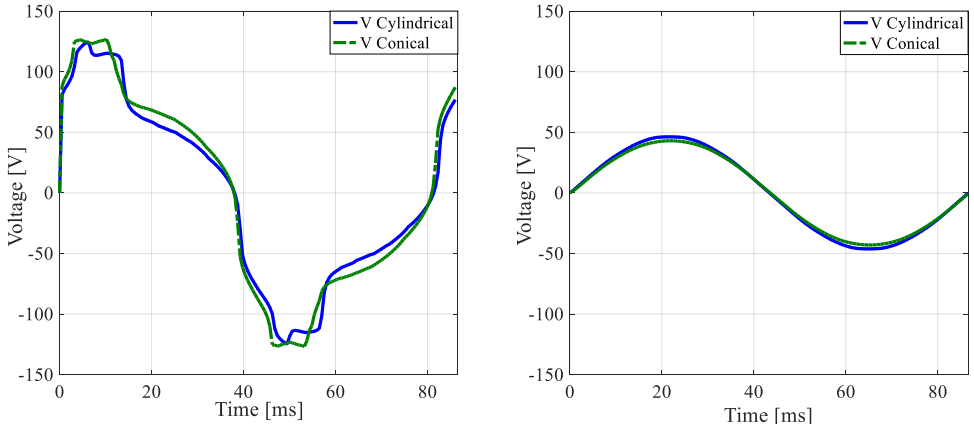
Having developed the full design of both the original cylindrical machine and its conical counterpart, then Figure 4.16-Figure 4.18 offer a direct comparison between torque, voltage and flux of the conical and cylindrical versions. As expected from a PMCM's perspective, the peak load torque is subject to a degradation, due to the smaller volume of the rotor. In this case, the torque of the conical motor reduces by 10.35% with respect to the original motor (Figure 4.16-a)). However, it should be noted that the torque ripple and the peak cogging torque decrease consequently. Torque ripple is 0.3% of the total torque compared to 0.7% of the original cylindrical whereas the peak cogging torque is 32.39% lower than the cylindrical machine (Figure 4.16-b)).

The shape of the terminal voltage and the flux, at load conditions, is maintained, as demonstrated in Figure 4.17-a) and Figure 4.18-a). Back-EMFs are still sinusoidal with only 6.99% reduction on the rms value as shown in Figure 4.17-b). In a similar manner, in Figure 3.18-b), the no-load flux linkage rms value diminishes of 7.9% rate.



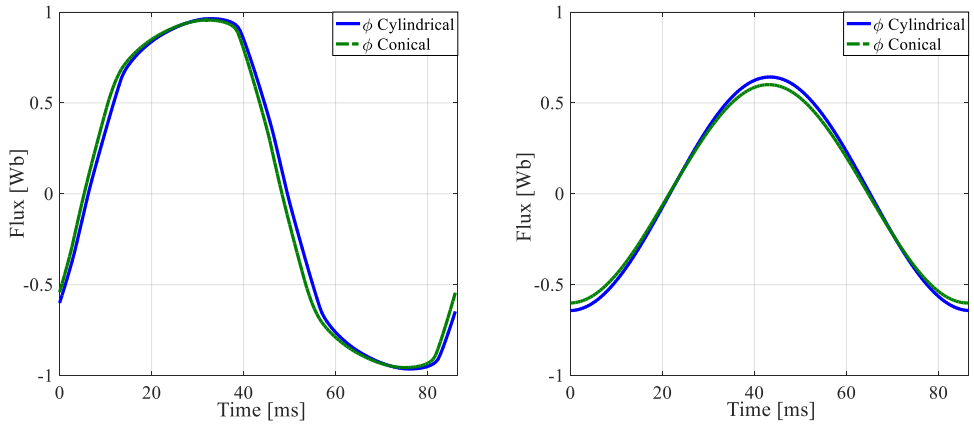
a) Load b) No Load

FIGURE 4.16 – CYLINDRICAL VS CONICAL MOTOR TORQUE



a) Load b) No Load

FIGURE 4.17 – CYLINDRICAL VS CONICAL MOTOR VOLTAGE



a) Load b) No Load

FIGURE 4.18 – CYLINDRICAL VS CONICAL MOTOR FLUX

From the analyses conducted in this section and from the result comparison between the conical and the cylindrical motor performances, some important conclusions can be drawn. As can be observed from Figure 4.16, Figure 4.17 and

Figure 4.18, the quality of the signal generated in the cylindrical motor is preserved when the cylindrical machine is converted into its conical counterpart. The shape of the waveforms is maintained and only a small reduction in the amplitude is experienced, with particular regard to the torque. This represents an important achievement for the conical machine design, as it confirms the validity of the initial idea of performing the design optimization on a cylindrical motor and successively convert the optimized motor into its conical "twin". As expected, considering the smaller dimension of the conical motor, a torque reduction will be experienced during the conversion procedure. However, the torque decrement can be limited to a specific value by choosing the appropriate dimensions of the conical motor, thus, if the most convenient conical angle is chosen, as demonstrated in the next section.

4.4 Torque Design Formula and 2D Model Guidelines

In Chapter 3, an accurate and simple design methodology, combined with a set of design formulae has been proposed for the analytical and numerical evaluation of the conical motor performances. In this section, the validity of the design formulae is further investigated. A closer insight about the torque and force numerical analyses proposed in Section 3.5 is hereafter provided. The numerical approach, based on the equivalent dimensions of the conical motor (length and radius), is compared with FE results obtained using the 2D equivalent FEM from the Section 4.2 and Section 4.3.

Other considerations about the correct methodology to build the 2D equivalent model are also added. The drawbacks of a wrongly conceived 2D equivalent model, in fact, become more evident when the axial force and torque are numerically estimated. After the validation of the previous formulae performed on the high-performing conical machine described before, a design formula that relates the torque and the cone angle is derived.

The validity of designing formulae for the evaluation of the torque that guide to the most convenient choice of the cone angle according to pre-established requirements is assessed. The designing formula for the estimation of the torque in case of conical machines has been already provided in (3.41) of Section 3.5.

In this Section, the analyses conducted on the cylindrical and conical motors are employed to clarify and verify that concept.

4.4.1 Correct 2D Model Approximation

As demonstrated by (4.7) of Section 4.1.2, the torque can be obtained analytically from the tangential force. The same expression of (4.7) can be adopted for the estimation of the analytical torque in case of conical machines. The length and the radius measures that appear in (4.7) must be replaced with the equivalent length of the conical motor $l_{ax,\gamma}$ and the medium rotor bore radius $\bar{r}_i$. The equivalent length $l_{ax,\gamma}$ is calculated implementing the total axial length of the original cylindrical motor l_{ax} in equation (3.2) whereas $\bar{r}_i$ is obtained as in (3.1) using minimum and maximum rotor bore radii of the conical motor, indicated in Figure 3.19 as r_{min} and r_{max}.

The equivalent dimensions of the conical motor depend on the cone angle. In the studies on the conical motor exposed in Section 4.2, a cone angle of 20° has been used to obtain the radii of three sub-motors. The smallest radius R_{i3} has been calculated as in (4.10). If the same cone angle is adopted for the analytical estimation of the torque, the minimum radius at the rotor bore does not correspond to the radius of the third motor R_{i3}, as shown in Figure 4.19-a). In this case, in fact, the minimum radius $r_{min,20}$, calculated as in (4.19) using the total radius reduction $\Delta r_{tot,20}$ of (4.20), corresponds to red one in Figure 4.19-a). This produces a discrepancy between the results obtained from the FE analyses and the analytical evaluation. The analytical calculation of (4.23) returns the torque $T_{\gamma=20°}$ displayed with green colour in Figure 4.20. From the same figure, it is clear that the FE analyses overestimate the performances of the conical motor of Figure 4.19-a); this means that the three motors adopted in the FE analyses do not approximate correctly the volume of a cone with a vertex angle of 20°, and equivalent axial length $l_{ax,\gamma 20}$ and medium radius $\bar{r}_{i,20}$ calculated as in (4.21) and (4.22).

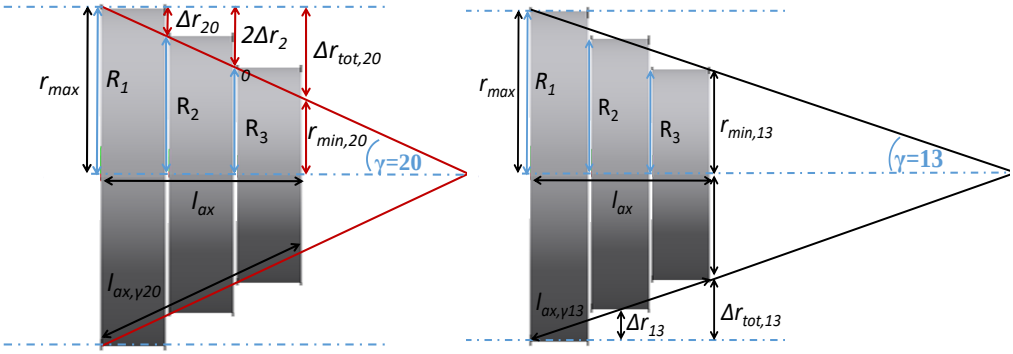
$$r_{\min,20} = r_{\max} - \Delta r_{tot,20} \tag{4.19}$$

$$\Delta r_{tot,20} = l_{ax,\gamma 20} \sin\gamma = l_{ax} \tan\gamma\big|_{\gamma=20^\circ} \tag{4.20}$$

$$l_{ax,\gamma 20} = \left.\frac{l_{ax}}{\cos\gamma}\right|_{\gamma=20^\circ} \tag{4.21}$$

$$\bar{r}_{i,20} = \frac{r_{max} + r_{min,20}}{2} \tag{4.22}$$

$$T_{\gamma=20^\circ} = l_{ax,\gamma} r_{i,20}^2 \int_0^{2\pi} \tau d\vartheta = \frac{l_{ax,\gamma} \bar{r}_{i,20}^{-2}}{\mu_0} \int_0^{2\pi} (B_n B_t) d\vartheta \tag{4.23}$$



a) Cone Angle γ=20° b) Cone Angle γ=13°

FIGURE 4.19 – CORRECT CONE ENCLOSING VOLUME

If the cone volume is drawn in such a way that the radius R_{i3} corresponds to the minimum radius $r_{min,13}$ in Figure 4.19-b) of the conical rotor, a cone angle of 13° is obtained. The minimum radius is calculated as in (4.24) using the total radius reduction $\Delta r_{tot,13}$ of (4.25). In this case, the three sub-motors represent a realistic approximation of the cone volume of Figure 4.19-b) and this has a large influence on the analytical calculations. As in (4.23), the torque $T_{\gamma=13^\circ}$, with 13° cone angle, is calculated as in (4.30) using the medium rotor bore radius $\bar{r}_{i,13}$ of (4.29) and the equivalent axial length $l_{ax,\gamma 13}$ of (4.26).

$$r_{min,13} = R_{i3} = r_{max} - \Delta r_{tot,13} \tag{4.24}$$

$$\Delta r_{tot,13} = l_{ax,\gamma 13} \sin\gamma = l_{ax} \tan\gamma\big|_{\gamma=13^\circ} \tag{4.25}$$

$$l_{ax,\gamma 13} = \left.\frac{l_{ax}}{\cos\gamma}\right|_{\gamma=13^\circ} \tag{4.26}$$

$$R_{i2} = r_{max} - \Delta r_{13} \tag{4.27}$$

$$\Delta r_{13} = \frac{l_{ax}}{3}\tan\gamma\Big|_{\gamma=13^\circ} = \frac{\Delta r_{tot,13}}{3} \tag{4.28}$$

$$\bar{r}_{i,13} = \frac{r_{max} + r_{min,13}}{2} \tag{4.29}$$

$$T_{\gamma=13^\circ} = l_{ax,\gamma} r_{i,13}^2 \int_0^{2\pi} \tau d\vartheta = \frac{l_{ax,\gamma} \bar{r}_{i,13}^2}{\mu_0} \int_0^{2\pi} (B_n B_t) d\vartheta \tag{4.30}$$

As evident from Figure 3.20, the result of the numerical computation of the torque with a cone angle of 13° ($T_{\gamma=13^\circ}$) is closer to FEM conical torque with respect to $T_{\gamma=20^\circ}$. In case of γ=13°, an error of 4.81% is experienced between FE and numerical analyses; in case of γ=20°, the error increases up to 11.01%. In conclusion, the correct 2D FE model should be always built in a way that the motors are included in the cone volume (as showed in case of 13° cone angle). This ensures a better approximation of the conical torque calculated through FE analyses.

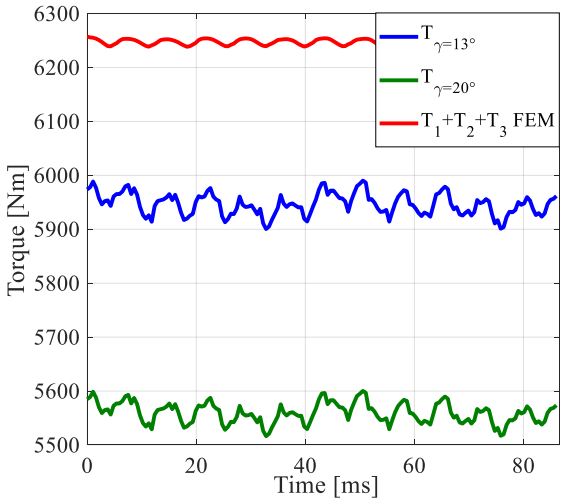


FIGURE 4.20 – ANALYTICAL VS FEM TORQUE OF THE CONICAL MOTOR

The gap between the 2D FE analyses and the analytical evaluation of the torque can be reduced using a higher number of 2D cylindrical sub-motors to discretize the conical volume. The radius of each sub-motor, in fact, depends on the quantity Δr which, in turn, is determined by the number of sub-motors adopted in the 2D equivalent FEM. Generalising the case of the equation (4.28), the value of Δr can be expressed as a function of the number of sub-motors n as in (4.31). If the number of sub-motors is maximised ($n \to \infty$), the quantity Δr tends to zero

meaning that the 2D discretization and the whole volume of the cone perfectly overlap. In this way, the exceeding volume that causes the overestimation of the torque in FEA can be eliminated.

$$\Delta r = \frac{l_{ax}}{n-1}\tan\gamma \tag{4.31}$$

4.4.2 Analytical Torque Rationale

The analytical estimation of the torque as in (4.23) and (4.30) is based on the tangential stress calculated in the cylindrical motor and integrated on the equivalent volume of the conical version obtained through the use of $l_{ax,\gamma}$ and $\bar{r}_i$. With this expedient, the conical volume is actually transformed in a new cylinder in which the length is obtained as the projection of $l_{ax,\gamma}$ and the radius corresponds to the medium radius of the motor, $\bar{r}_i$. This operation is visually explained in Figure 4.21.

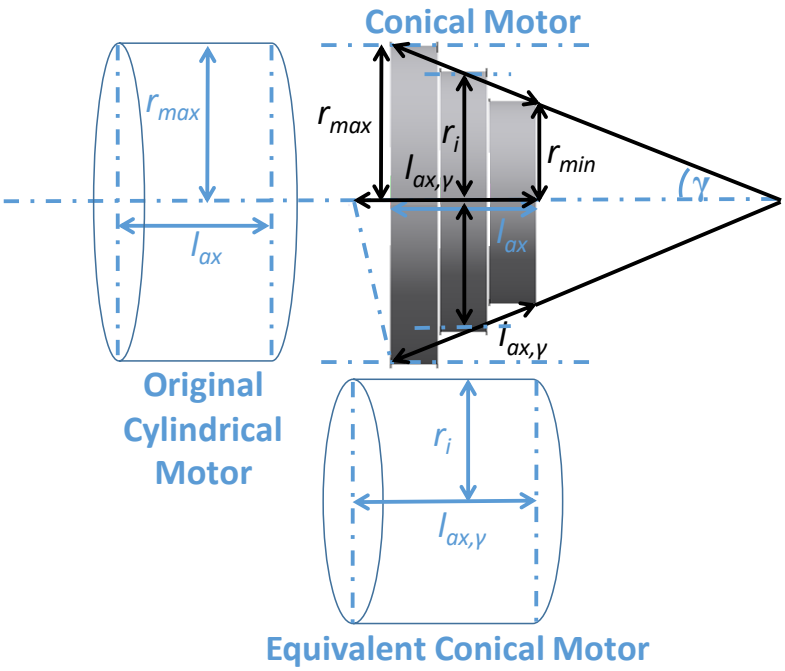


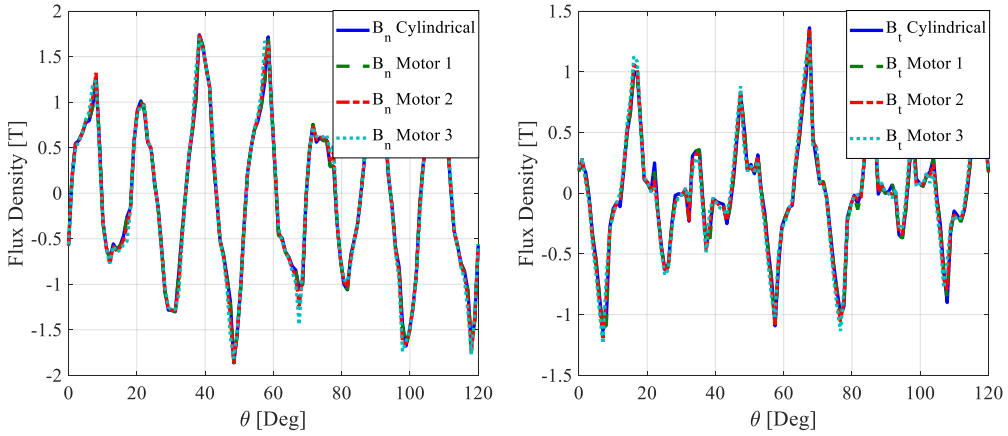
FIGURE 4.21 – EQUIVALENT CYLINDRICAL MODEL OF THE CONICAL MOTOR

Equation (4.18) can be corrected with equation (4.32) where a common value of tangential stress (τ) is adopted and the total length and radius correspond to the dimensions of the "virtual" cylindrical machine ("Equivalent Conical Motor" in Figure 4.21). In this case, the tangential stress (τ) is obtained from the original cylindrical motor since the calculation would lead to similar results if any of the

tangential stresses (τ_1, τ_2, τ_3) is adopted. This derives from a direct evaluation of the flux density in the three motors of the conical equivalent model as well as in the original cylindrical motor. In fact, at peak load and no-load conditions, normal and tangential flux densities remain roughly the same in three motors and in the cylindrical motor, as confirmed in Figure 4.22 and Figure 4.23. Consequently, the stresses in the whole conical machine and original cylindrical remain the same.

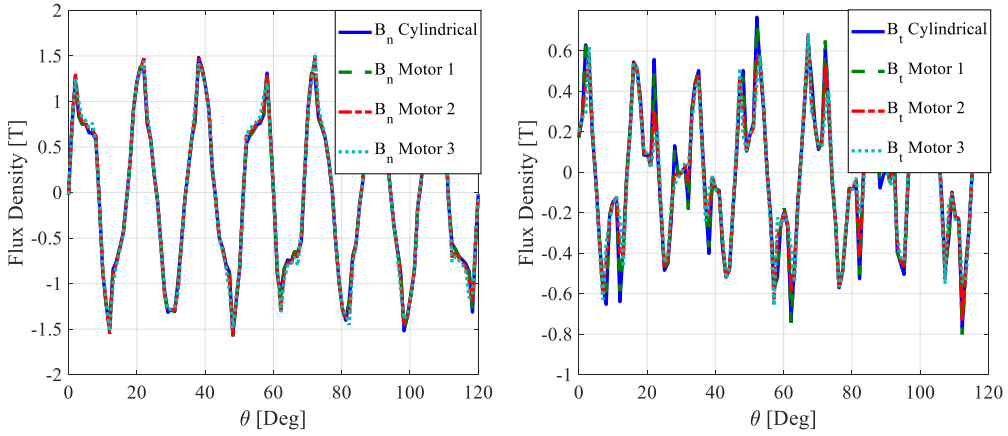
$$\Delta lR_{i1}\int_0^{2\pi}\tau_1 d\vartheta+\Delta lR_{i2}\int_0^{2\pi}\tau_2 d\vartheta+\Delta lR_{i3}\int_0^{2\pi}\tau_3 d\vartheta=l_{ax,\gamma}\overline{r}_i\int_0^{2\pi}\tau d\vartheta \tag{4.32}$$

The considerations that lead to (4.32) represent the basic steps for the analytical torque calculation formula of (4.30).



a) Normal b) Tangential

FIGURE 4.22 – FLUX DENSITY AT PEAK LOAD CONDITIONS CALCULATED AT HALF-WAY AIRGAP



a) Normal b) Tangential

FIGURE 4.23 – FLUX DENSITY AT NO-LOAD CONDITIONS CALCULATED AT HALF-WAY AIRGAP

The analytical formulation of the torque results particularly useful when considering to transform a cylindrical machine into a conical corresponding one. The tangential stress of the cylindrical motor can be adopted for the estimation of the torque reduction and, on this basis, the most suitable cone angle can be chosen to meet individual specifications.

4.4.3 Final Torque Design formula

As emerges from Figure 4.16-a), the total torque obtained using the conical machine results inferior to the torque produced by the original cylindrical motor displayed in Figure 4.3. If the starting torque of $7kNm$ is compared with torque calculated analytically using 13° conical angle, a reduction of 14.66% can be noticed. This might compromise the possibility to meet the initial application requirements. However, as learnt from the argumentations exposed above, the analytical computation of torque is derived from the stress calculated in the original machine multiplied by the equivalent length and radius of the conical machine using the formulation of (4.30). This means that the ratio of the conical torque reduction is primary due to the dimensions of the conical machine $l_{ax,\gamma}$ and $\bar{r}_i$, which in turn depend on the choice of the conical angle.

During the optimisation procedure of the conical machine design, the cone angle should be considered as the major parameter that affects the motor performances. Supposing that the optimal design of the cylindrical machine has been achieved, then the conical angle should be chosen limiting the reduction of the torque due to the rotor tapered shape to a certain value η. Setting the maximum torque reduction η to the preferred value that allows to meet the application requirements, the conical angle can be chosen from (4.34). The expression of the angle as function of the original length and radius of the cylindrical machine has been obtained combining the relations (4.24), (4.25) and (4.29) for the medium radius and the expression of (4.26) for the equivalent axial length, and implementing these relations in (4.33). Equation (4.33) correlates the conical torque and the cylindrical torque using the analytical expressions of the torque (4.30) and (4.7), where the integral part represents the same quantity in both cylindrical and conical motor. If (4.33) is developed further, equation (4.34) is obtained where the cone angle, γ, explicitly appears as a variable determined by the aimed torque reduction, η.

$$l_{ax,\gamma}\bar{r}_i^2 = l_{ax}R_i^2\frac{\eta}{100} \tag{4.33}$$

$$\left(R_i + \frac{l_{ax}}{2}\tan\gamma\right)^2 \frac{l_{ax}}{\cos\gamma} = l_{ax}R_i^2\frac{\eta}{100} \tag{4.34}$$

In the specific case of the conical and cylindrical motors reported in the previous sections, if the experienced torque reduction η =14.66% is implemented in (4.34) a conical angle value of 13° is obtained as expected and vice versa.

4.5 Axial Force Estimation

As formulated in Section 3.5, the estimation of the force can be obtained from the integration of the force over the rotor surface area as in (3.39). However, in order to separate the contribution of the no-load axial force to the axial force due to the current, the force density expression of (3.33) as been simplified as in (4.35). The assumption made passing from the force density expression of (3.33) to (4.35) is that the tangential flux density can be neglected in the normal stress computation; this is, however, valid for low saturated PM machines where the flux lines in the air gap are nearly perpendicular to the stator iron at the stator bore surface [24]. From (4.35), the shorter form of the total axial force appears as in (4.36).

$$\vec{f} = \begin{bmatrix} f_r \\ f_t \\ f_z \end{bmatrix} = \frac{1}{2\mu_0}\begin{bmatrix} B_n^2\cos\gamma \\ 2B_nB_t \\ B_n^2\sin\gamma \end{bmatrix} \tag{4.35}$$

$$F_z = \frac{l_{ax,\gamma}\bar{r}_i}{2\mu_0}B_n^2\sin\gamma \tag{4.36}$$

The force F_z varies according to the magnetic field strength in the air-gap, therefore, the amount of force modifies between no load and load conditions. It is important to quantify separately the amount of axial force due to the remanent flux density of the magnets and the armature reaction effect. If no saturation in the stator iron is experienced, the two effects are considered linear; thus, the total flux density B_n can be calculated as the sum of no load flux density B_{0n} and flux

density due to the flux generated by the current B_{1n}. The formula of (4.36) can be thus developed as in (4.37).

$$F_z = \frac{l_{ax,\gamma}\bar{r}_i}{2\mu_0}\left(B_{0n} + B_{in}\right)^2 \sin\gamma = \\ = \frac{l_{ax,\gamma}\bar{r}_i}{2\mu_0}\left(\hat{B}_{0n}^2 + 2\hat{B}_{0n}\hat{B}_{in}\sin\left(\varphi_0 - \varphi_1\right) + \hat{B}_{in}^2\right)^2 \sin\gamma \tag{4.37}$$

The value $(\varphi_0 - \varphi_1)$ corresponds to the angle of the magnetic field. If it is set to $\pi/2$, the axial force will be maximised and it will depend only on d-axis current. This represents a great benefit since the axial force can be controlled without affecting the torque control (depending on the q-axis current).

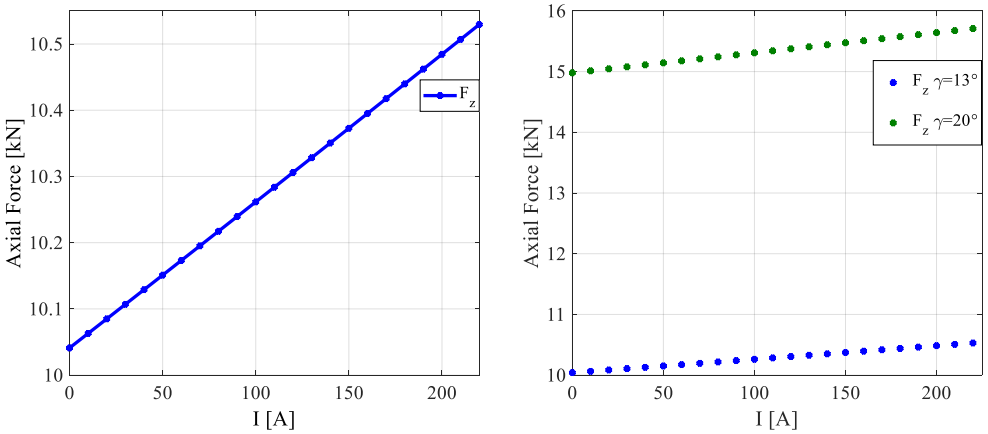
Based on previous considerations, an estimate of the axial force obtained implementing the dimensions of the conical motor ($l_{ax,\gamma}$ and $\bar{r}_i$) and a cone angle of 13° in (4.37) is reported in Figure 4.24-a). The starting point of the curve corresponds to the no-load axial force (10.04kN). When current is applied, the flux density generated by the current contributes to increase or decrease the no-load axial force. The peak value of the flux density due to the armature field has been calculated as in (4.38), where δ is equal to the sum of the air-gap length and magnet length ($g+L_M$), p is the number of pole pairs, m is the number of phases, k_w is the winding factor and N number of turns. Supposing that only the current d-axis is used, the maximum value of the axial force has been calculated for different level of current, as displayed in Figure 4.24-a).

$$\hat{B}_{in} = \sqrt{2}\mu_0 \frac{mk_w NI}{\pi p\delta} \tag{4.38}$$

The direction of the current will determine the direction of the axial force, thus the direction of the axial movement. If positive current is applied, the axial force increases and the rotor moves from Position 2 (unaligned) to Position 1 (aligned), as shown in Figure 3.11. If negative current is applied, the force generated by the current will contrast the no-load axial force of the magnets.

To understand the grade of inaccuracy in the computation of the axial force, F_z, when a wrong cone angle is utilised, in Figure 4.24-b), the axial force in case of 20° cone angle is compared with the one obtained with 13° of taper. In this case, a 5kN difference can be noticed between two curves.

As can be observed in Figure 4.24, the level of axial force becomes particularly high when the conical shape is applied to high-performing machines (due to the strong field of the magnets and high level of current density). This means that a small cone angle is necessary to obtain the necessary axial force. As can be seen later in Chapter 5, for high performing motors, a minor cone angle would be needed. This has a good impact on the torque. If a small cone angle is employed, the reduction of the torque is not significant.



a) 13° Cone Angle b) Comparison

FIGURE 4.24 – CONICAL MOTOR AXIAL FORCE

4.6 Chapter Highlights and Contribution to Research

The main focal and innovative points of this Chapter can be summarised and listed as follow:

1) Proposed a new design methodology for converting an optimized cylindrical machine into a conical machine without experiencing degradation of motor output signals.
2) Defined a structured procedure to build an accurate conical version of the cylindrical machine in order to reduce overestimation errors.
3) Shown how a conical counterpart can achieve very good performance compared to the original cylindrical machine.
4) Achieved a design formula that relates the torque reduction with conical angle.

5) Obtained a simplified formula that relates the level of the current and the axial force produced by the conical machines.

4.7 Conclusion

This Chapter led to various important conclusions regarding the general theory of CMs and the designing features of a high performing conical motor.

The theory and the models formulated in Chapter 3 have been expanded further in this Chapter. An illustrative case of study has been employed to reinforce the validity of the concept of the 2D FE equivalent model rationalized in Chapter 3. Constructive aspects of the 2D equivalent model have been reported. Essential guidelines have been drawn to prevent the reader from conceptual mistakes that lead to different results between the 2D FEM and the numerical calculation where CM equivalent dimensions are used. Other suggestions, such as incrementing the number of sub-motors used to discretize the cone volume, are given in order to reduce the level of approximation of the results obtained from the 2D model. A significant contribution has been provided to the study of [88] where the number of rotor slices has been optimised in relation to the inductance analytical calculation of the ICM of [23]. Based on this study, it has been observed that the optimal number of slices is thirty. However, this is strictly dependent on the motor dimension, thus, the motor volume to be discretised, and on the level of approximation of the considered parameter, i.e. motor inductance, torque, etc.

A detailed analysis of torque and forces has been conducted to prove the concepts exposed in the previous chapters. The performances of a cylindrical machine and its conical equivalent have been compared in terms of torque computed, in both cases, using the formulation of force presented Chapter 3. This proved the general validity of the proposed numerical analyses.

The main outcome of the comparison between the high-performance cylindrical and conical motor is that the quality of the performances obtained transforming the cylindrical machine into its conical counterpart is maintained. This enables the high-performance motor to be optimized using a cylindrical configuration and successively to be converted into a conical machine. The torque reduction

experienced during this conversion can be however limited. In fact, the central milestone of this Chapter is the definition of the torque of the conical motor as function of the conical angle. The formulated relation can be used to define the conical angle during the design of the conical machine setting the level of the desired torque a priori.

An expression of the axial force produced by the conical machine has been derived from the MST method proposed in Chapter 3 and related to the performance characteristics in the motor. This has an extremely important relevance for the CM control techniques and the mechanical system design, as demonstrated in Chapter 5 and Chapter 6.

Chapter 5
Applied Design

This Chapter focuses on the development of a demonstrator prototype of the PMCM, whose main aim is to prove the concept and highlight the feasibility of having a two-degrees of freedom machine that combines the high torque density of PM machines with the linear actuation required in the first Chapter.

At this stage of the project, where the main aim is to prove the overall concept, the design process is simplified by considering the stator of an existing conical machine. Thus from a design perspective, this Chapter focuses mainly on the rotor design. A detailed trade-off study of potential candidates in terms of rotor configurations is done and the best performing candidate is chosen. This is done on the basis of the level and the quality of the delivered torque.

The mechanical system is also designed based on the computed axial force.

5.1 Design Parameters

As mentioned above, the main aim of this Chapter is to develop a PMCM prototype, able to prove the validity of the proposed concept. To do this, a readily available stator of an existing ICM [27] was used. In the following sections, the defined design parameters are presented.

5.1.1 The Machine Stator

The main dimensions of the considered stator are reported in Table 5.1. As presented in Section 3.4.1, the stator has a cylindrical outer surface, thus, its external diameter is invariant with the conical shape. On the contrary, the internal diameters differ if measured on the smaller and larger edges, as indicated in Table 5.1. In accordance with the circumference changes, the back-iron height reaches its maximum thickness where the internal stator diameter is smaller (smaller side) whereas it reduces on the larger side. The dimensions of the slots, specified in Table 5.1, remain constant along the whole axial length; the thickness of the windings, in fact, cannot be adjusted as a function of the conical shape. However, since the diameter decreases in the transition from the larger side to the smaller, the tooth width w_t and $w_{t,tot}$ indicated in Figure 4.2 narrows, whereas the dimensions of the slots h_s, w_{st}, w_b and the slot opening w_{so} of Figure 5.2 do not change along the axial length.

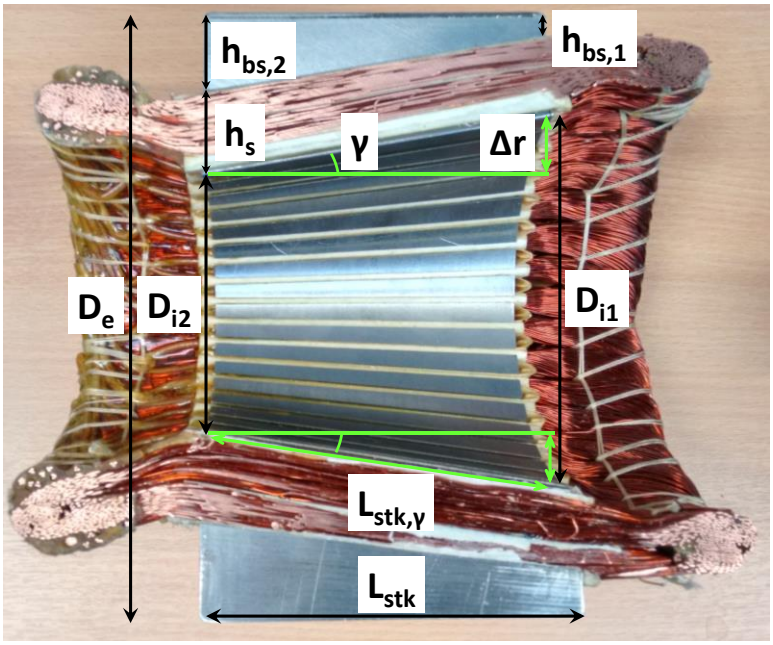


FIGURE 5.1 – PMCM PROTOTYPE STATOR SECTION VIEW

TABLE 5.1 – PMCM PROTOTYPE STATOR DIMENSIONS

Definition	*Symbol*	*SHORTER SIDE (2)*	*LARGER SIDE (1)*
Outer Stator Diameter	D_e	208*mm*	
Total Equivalent Stack Length	$L_{stk,\gamma}$	123*mm*	
Total Effective Stack Length	L_{stk}	121*mm*	
Inner Stator Diameter	D_i	87*mm*	126.96*mm*
Back Iron	h_{sb}	29.55*mm*	9.56*mm*
Slot Height	h_s	30.95*mm*	
Total Height	$h_s + h_{sb}$	60*mm*	40.5*mm*
Slot Opening	w_{so}	2.6*mm*	
Slot Bottom Width	w_{sb}	9.19*mm*	
Slot Top Width	w_{st}	4.33*mm*	
Tooth Width	w_t	3*mm*	6.48*mm*
Tot Tooth Width	$w_{t,tot}$	4.47*mm*	4.99*mm*

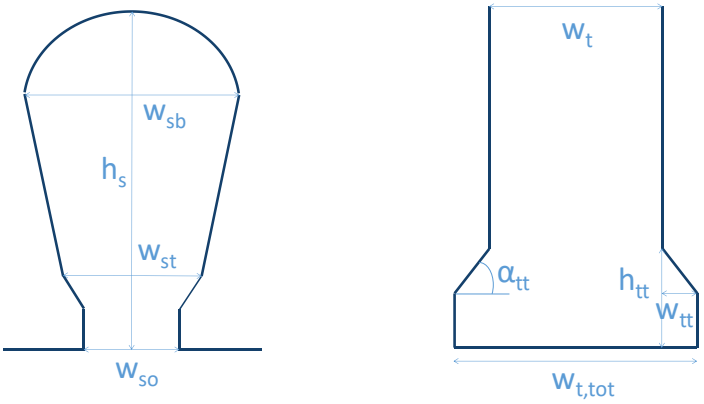


FIGURE 5.2 – SLOT AND TOOTH DIMENSIONS OF THE PMCM PROTOTYPE

From the measurements of the longitudinal and axial length of the lamination stack $L_{stk,\gamma}$ and L_{stk} respectively, a cone angle of 9.35° has been calculated by (5.1), where subscripts $_2$ and $_1$ refer respectively to the side of the machine with minimum internal stator diameter $D_{i,2}$ and the side with maximum internal stator

diameter $D_{i,1}$. An existing difference of 19.98*mm* between the minimum and maximum radius has been confirmed through the equation of (5.2).

$$\gamma = a\tan\left(\frac{\left(D_{i,1} - D_{i,2}\right)/2}{L_{stk}}\right) \tag{5.1}$$

$$\Delta r = L_{stk,\gamma}\sin\gamma \tag{5.2}$$

A. Winding Arrangement

The original machine had been designed with an integral slot/pole combination. The stator coils have a double layer configuration and they have been wounded with a slot pitch of two. In Figure 5.3, the winding arrangement of phase A, phase B and phase C is displayed where phase B and C are shifted of one coil respectively forward and backward from phase A. The second layer of the windings is displayed in Figure 5.4, where phase U corresponds to phase A, phase V to phase B and W to C. The winding properties that appear in Figure 5.3, obtained from the FE software, have been confirmed analytically in the Table A.1 and Table A.2 of Appendix A. In Figure 5.3, only the most relevant winding features are reported.

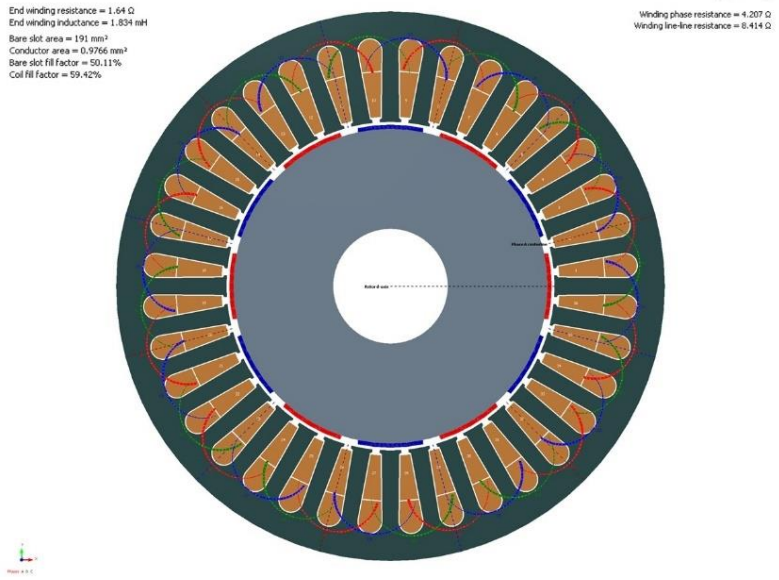


FIGURE 5.3 – WINDING LAYOUT OF THE PMCM PROTOTYPE

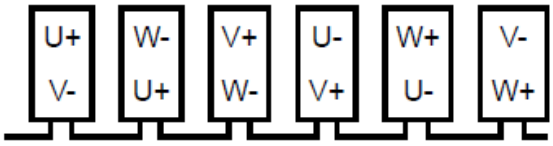


FIGURE 5.4 – WINDING CONFIGURATION OF THE PMCM PROTOTYPE

The lamination material is considered as a common not oriented electrical silicon steel (one grade - 24 Gauge). The copper material is a typical electrical machine conductive material with $5.77e^7 S/m$ of conductivity at 20°C.

TABLE 5.2 – WINDING PROPERTIES OF THE PMCM PROTOTYPE

Definition	*Symbol*	*Value*
Number of Phases	m	3
Number of Slots	N_s	36
Coil Pitch	y_q	2
Number of Coils per Phase	N_c	12
Number of Turns per Coil	N_t	49
Phase Resistance	R_{ph}	4.207Ω
Line-Line Resistance	R_{LL}	8.415Ω
Bare Slot Fill Factor	k_{fill}	50.34%
Bare Wire Diameter		$0.65mm$
Bare Slot Area	A_s	$190.22mm^2$

5.2 Rotor Design Choices

To maintain the same configuration as that of the original machine, a 36/12 slot-pole configuration has been confirmed for the development of the PMCM demonstrator. The design exercise is thus aimed at optimising the remaining degrees of freedom, mainly focused on the choice of the PM array configuration.

5.2.1 Magnets Material Choice

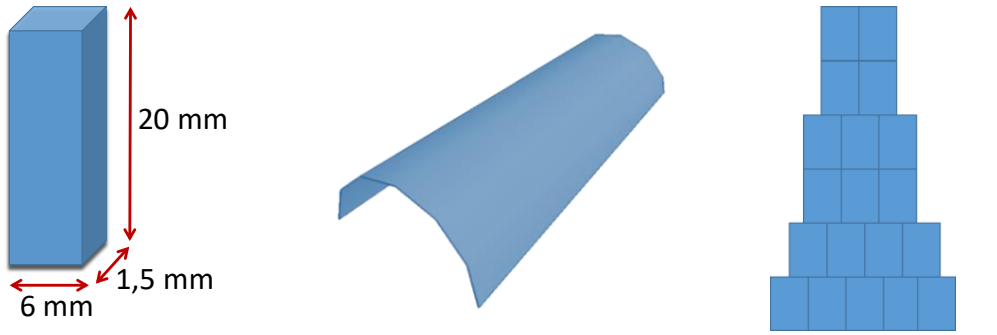
The maximum allowed temperature in the windings of the PMCM is considered as 155°C (relative to a Class H insulation material with a good safety factor). During the selection process of the most appropriate material for the rotor magnets, the maximum operating temperature of the motor and the demagnetization properties of the magnet material constituted the main discriminating parameters.

Rare-earth magnetic materials have been selected for the present application, because of their better performances, especially compared to ferrite magnets

[82]. Between neodymium-iron-boron (NdFeB) and Samarium-Cobalt (SmCo) magnets, the decision was more oriented toward SmCo due to their wider maximum operating temperature range [82]. The demagnetization properties of the SmCo magnets played a decisive role in the choice of the material. Since flux weakening techniques are used to decrease the axial force produced by the magnets, it is essential to have the magnets operating at a safe point on the demagnetization curve for any temperature.

As explained in Chapter 3, the open-circuit working point of the magnet is determined on the demagnetization curve by the Permeance Coefficient (PC) and the magnet material properties as in (3.22). With SmCo magnets, it is possible to work above the knee point of demagnetization curves with a PC in a range between 1 and 5, even when high temperatures are reached. As defined in (3.21), the value of PC equals the ratio between the air-gap and the magnet length. The air-gap length chosen for PMCM is 1*mm*. With a 1*mm* air-gap length, the risk of demagnetization is avoided, even when thin SmCo magnets length is employed. The length of the magnet has been selected using demagnetization curves provided by a preferred magnet supplier. After several considerations about the operating temperature and demagnetization resistance of different SmCo products, with a 1.5 PC, thus, with a magnet length of 1.5*mm* according to (3.21), a Sm_2Co_{17} alloy has been selected for the final design. As demonstrated for the final configuration in Section 5.6, no risk of demagnetization exists using the selected material and magnet length.

Due to the fact that the circumference of the rotor is not consistent along the axial length, the pole span assumes different values accordingly to the circumference variation, as explained in Section 3.2.2. In order to cover each pole arc, a customised magnet with a shape similar to the one shown in Figure 3.2 of Chapter 3 and displayed in Figure 5.5-b) is needed. The main concerns about the realisation of such a shape were the manufacturing amount of time and the brittleness related to thickness choice.



a) Single "off-the-shelf" magnet

b) Customized magnet shape

c) Reconstructed magnet shape

FIGURE 5.5 – MAGNET PMCM PROTOTYPE SHAPE

After a close examination of different possibilities, a convenient solution was the use of rectangular "ready-to-use" magnets found on the market. A commercial product [87] responding to the required characteristics (similar to the magnet features utilised for the preliminary design) was identified. Besides the material composition and magnetic properties, relevant features of the "off-the-shelf" magnets that increased the interest in this specific product were their thickness (matching the thickness selected in the preliminary design procedure), and their length that enabled to combine them in line to equal the total longitudinal length of the motor $L_{stk,\gamma}$. A stack of six magnets in line, in fact, has been used to recreate the longitudinal length of the motor with $3mm$ left; a clearance $0.5mm$ between each magnet has been counted for glueing purposes. The dimensions of the "off-the-shelf" magnets are reported in Figure 5.5-a).

The conical shape of each pole has been reconstructed with six rows of magnets as demonstrated in Figure 5.5-c). The maximum admissible number of magnets present in each row depends on the circumference length of the rotor at the corresponding axial position, thus, it is limited by the full pole pitch β_{PM}. The pole span α_{PM}, obtained as in (3.11), can be varied combining a different number of magnets in a row; this will lead to a different configuration of the rotor that in turn will influence the performances of the motor, as demonstrated in Section 5.4.1.

The magnetic features of the purchased magnets have been reported in Table 5.3. The demagnetization curve of a similar material with the same composition (Sm_2Co_{17}) and correspondent characteristics has been employed and reported in Figure A.1 of Appendix A.

TABLE 5.3 – MAGNET FEATURES OF THE PMCM PROTOTYPE (MAX VALUES)

Definition	*Symbol*	*Value*
Remanence	B_r	$1.58T$
Coercivity	H_{cb}	$783.83kA/m$
Intrinsic Coercivity	H_{ci}	$1914.63kA/m$
Maximum Energy Product	$(BH)_{max}$	$211.83kJ/m^3$

5.3 Two-Dimensional PMCM Model

For reasons stated in the previous section, each magnet of the rotor is constituted of six rows of rectangular magnets. On this account, a convenient approach to build the two-dimensional model of the conical machine, formulated in Section 4.2.1, was to divide the motor into six cylindrical machines, therefore, using a six motor 2D equivalent model.

As explained in Section 4.2.1 and Section 3.3, the analyses of the PM conical motor can be conducted by discretizing the 3D dimensional problem using a 2D stack of motors appropriately dimensioned. For this specific case, six sub-motors have been employed. The six sub-machines have been modelled as suggested in Section 4.2.2. They have the same design as displayed in Figure 5.3. However, the dimensions differ between one sub-motor and the other. The six sub-motors, in fact, have been dimensioned in order to recreate the cone structure, as pictured in Figure 5.6 and Figure 5.7. The cross-section of each sub-motor is reported in Table A. 3 of Appendix A.

In order to reduce any overestimation errors of the torque, the smaller side has been assumed as the starting point within the dimensioning process of the 2D model, as suggested in Section 4.4.1. Starting from the dimensions calculated at the smaller side of the motor (see Table 5.1), the radial dimensions of the subsequent sub-motors have been obtained adding a radius increment Δr to each radial dimension of the preceding machine. As shown in Figure 5.6, the minimum radius of the conical motor equals the radius of the first sub-motor M_1. The following machine dimensions for the sub-motors M_2, M_3, M_4, M_5, M_6 have been obtained using the quantity Δr calculated as in (5.2).

The increment of the radii in each motor Δr_i is obtained as in (5.3) where i the identifies the number of the analysed machine and $l_{stk,\gamma}$ is the equivalent longitudinal length of each single sub-motor as indicated in Figure 5.6. The longitudinal length of each cylinder is equal to the magnet length (20*mm*) plus the admitted clearance between one magnet row and the other equal to 0.5*mm* that has been considered for glueing purposes. Totally, the equivalent axial length of each sub-motor, $l_{stk,\gamma}$, is equal to 20.5*mm* whereas the effective axial length l_{stk} have been calculated using the conical angle as reported in (5.4) in relation to (3.2).

The quantity Δr_i is added to each dimension of the motor apart from the back-iron height where it should be detracted. As already explained in Section 5.1.1, the back-iron thickness decreases as the diameter becomes larger. For this reason, the back-iron thickness has been obtained in the opposite way as for the other radial dimensions, i.e. subtracting the quantity Δr_i progressively to each sub-motor starting from the back-iron length of sub-motor M_1. This emerges more clearly in Table A. 3 of Appendix A where the quantity h_{sb} reduces from Motor 1 to Motor 6 whereas the quantity h_{rb} increases.

$$\Delta r_i = (i-1) l_{stk,\gamma} \sin\gamma \tag{5.3}$$

$$l_{stk} = l_{stk,\gamma} \cos\gamma \tag{5.4}$$

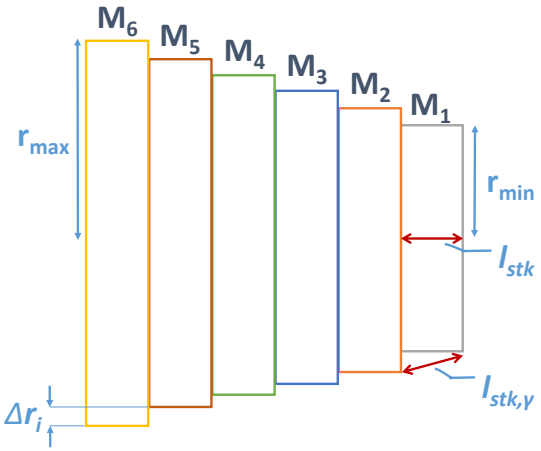


FIGURE 5.6 – EQUIVALENT MODEL OF THE PMCM PROTOTYPE

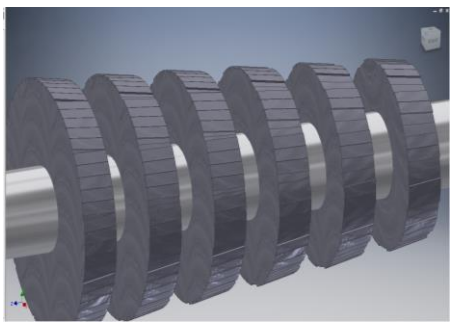


FIGURE 5.7 – GLOBAL VIEW OF THE 2D EQUIVALENT MODEL OF THE PMCM PROTOTYPE

TABLE 5.4 – PMCM PROTOTYPE SUB-MOTORS M_1, M_2, M_3 MAIN FEATURES (IN MM)

Quantity	*Symbol*	**MOTOR 1**	**MOTOR 2**	**MOTOR 3**
Radius Increment	Δr_i	0	3.33	6.66
Slot Opening	w_{so}	2.6	2.6	2.6
Tooth Width	w_t	3	3.58	4.16
Slot Tot Height	h_s	30.95	30.95	30.95
Equivalent Stack Length	$l_{stk,\gamma}$	20.5	20.5	20.5
Stack Length	l_{stk}	20.22	20.22	20.22
Inner Stator Diameter	D_{si}	87	93.66	100.32
Stator Back Iron	h_{sb}	26.21	22.88	19.55
Outer Diameter	D_e	201.33	201.33	201.33
Air-gap Length	g	1	1	1
Magnet Thickness	L_M	1.5	1.5	1.5
Outer Rotor Diameter	D_{re}	85	91.66	98.32
Rotor Back Iron	h_{rb}	20	23.33	26.66
Magnet Diameter	D_m	82	88.66	95.32
Inner Rotor Diameter	D_{ri}	42	42	42

TABLE 5.5 – PMCM PROTOTYPE SUB-MOTOR M_4, M_5, M_6 MAIN FEATURES (IN MM)

Quantity	*Symbol*	**MOTOR 4**	**MOTOR 5**	**MOTOR 6**
Radius Increment	Δr_i	9.99	13.32	16.65
Slot Opening	w_{so}	2.6	2.6	2.6
Tooth Width	w_t	4.74	5.32	5.90
Slot Tot Height	h_s	30.95	30.95	30.95
Equivalent Stack Length	$l_{stk,\gamma}$	20.5	20.5	20.5
Stack Length	l_{stk}	20.22	20.22	20.22
Inner Stator Diameter	D_{si}	106.98	113.64	120.30
Stator Back Iron	h_{sb}	16.22	12.89	9.56
Outer Diameter	D_e	201.33	201.33	201.33
Air-gap Length	g	1	1	1
Magnet Thickness	L_M	1.5	1.5	1.5
Outer Rotor Diameter	D_{re}	104.98	111.64	118.30
Rotor Back Iron	h_{rb}	29.99	33.32	36.65
Magnet Diameter	D_m	101.98	108.64	115.30
Inner Rotor Diameter	D_{ri}	42	42	42

For sake of clarity, the main dimensions of the six sub-motors have been reported in Table 5.4 and Table 5.5 and are indicated in Table A.3. It should be noted that the inner rotor diameter is set to 42*mm* for all the sub-motors. This corresponds to the diameter of the original shaft that has been preserved and employed for the new PM rotor mounting.

The whole machine performances have been evaluated by summing up the performances of each sub-motor (i.e. using a superimposition method), as formulated in Section 3.5 and demonstrated in the Sections 4.2.3, 4.3 and 4.4.

5.4 Magnet Configuration Choice

In this section, different ways to combine the rectangular magnets of Figure 5.5-a) have been analysed. Results obtained with each combination have been compared in order to identify the final configuration for the manufacturing of the PM conical rotor.

5.4.1 Possible Configurations

Considering that a different number of magnets can be employed to cover one pole in each sub-motor, the conical shape of the entire pole Figure 5.5-b) can be recreated using an ample number of combinations, as in Figure 5.5-c). Many configurations have been analysed and compared to each other; however, some of them have been discarded to prevent manufacturing issues. A certain displacement between one pole and the other has been always guaranteed and the use of the entire pitch has been avoided.

The number of magnets per pole on each rotor circumference can vary from a minimum of two up to a maximum set by the full pole pitch β_{PM} calculated for each of the six sub-motors. The minimum number of magnets was fixed to two as this is the minimum quantity for the smallest rotor M_1. One magnet per pole for the sub-motor M_1, in fact, covers only 2/7 of the overall full-pitch of this sub-motor which is less than the half of one pole span; for this reason, having only one magnet per pole has not been considered as a possible option for the sub-motor M_1, as well as for the other sub-machines. In order to recreate the conical shape, a fundamental rule has been employed for the definition of the combinations; the number of magnets per pole, passing from a smaller sub-motor

to a larger one, must always increase (i.e. combinations such as three magnets per pole on the first sub-motor M_1 and two magnets per pole on second sub-motor M_2 have been avoided because they would not reproduce the conical shape of the original conical magnet). The basic criteria adopted for the new rotor design can be summarised as follow: a) minimum two magnets per pole and b) increasing number of magnets per pole for each sub-motor.

Adopting the previous guidelines, only the configurations marked in black in Table 5.6 have been considered feasible and therefore analysed. In Table 5.7, the value *k*, defined as in (3.11), has been calculated for each sub-motor in order to translate the number of magnets in terms of ratio between the pole span α_{PM} with respect to the full pitch of each rotor β_{PM}, reported in the same table. These dimensions give an idea about the number of magnets in a row per pole that can be allocated on each motor circumference; the maximum number of admissible magnets per pole in each machine depends indeed on the pole ratio factor. Ideally, a constant factor *k* would guarantee the same pole span over the axial motor length, as suggested in the magnetic design Section 3.4.2. However, it could have been easier to realise a constant pole span using customised magnets as in Figure 5.5-b) rather than the proposed “made-up” magnet arrangement of Figure 5.5-c).

TABLE 5.6 – ROTOR MAGNET COMBINATIONS

<table>
<tr><td>M_1</td><td colspan="72">**2**</td></tr>
<tr><td>M_2</td><td colspan="24">**2**</td><td colspan="24">**3**</td><td colspan="24">**4**</td></tr>
<tr><td>M_3</td><td colspan="8">**2**</td><td colspan="8">**3**</td><td colspan="8">**4**</td><td colspan="8">2</td><td colspan="8">**3**</td><td colspan="8">**4**</td><td colspan="8">2</td><td colspan="8">3</td><td colspan="8">**4**</td></tr>
<tr><td>M_4</td><td colspan="4">**3**</td><td colspan="4">**4**</td><td colspan="4">**3**</td><td colspan="4">**4**</td><td colspan="4">3</td><td colspan="4">**4**</td><td colspan="4">3</td><td colspan="4">4</td><td colspan="4">**3**</td><td colspan="4">**4**</td><td colspan="4">3</td><td colspan="4">**4**</td><td colspan="4">3</td><td colspan="4">4</td><td colspan="4">3</td><td colspan="4">4</td><td colspan="4">3</td><td colspan="4">**4**</td></tr>
<tr><td>M_5</td><td colspan="2">**3**</td><td colspan="2">**4**</td><td colspan="2">3</td><td colspan="2">**4**</td><td colspan="2">**3**</td><td colspan="2">**4**</td><td colspan="2">3</td><td colspan="2">**4**</td><td colspan="2">3</td><td colspan="2">4</td><td colspan="2">3</td><td colspan="2">**4**</td><td colspan="2">3</td><td colspan="2">4</td><td colspan="2">3</td><td colspan="2">4</td><td colspan="2">**3**</td><td colspan="2">**4**</td><td colspan="2">3</td><td colspan="2">**4**</td><td colspan="2">3</td><td colspan="2">4</td><td colspan="2">3</td><td colspan="2">**4**</td><td colspan="2">3</td><td colspan="2">4</td><td colspan="2">3</td><td colspan="2">4</td><td colspan="2">3</td><td colspan="2">4</td><td colspan="2">3</td><td colspan="2">4</td><td colspan="2">3</td><td colspan="2">4</td><td colspan="2">3</td><td colspan="2">**4**</td></tr>
<tr><td>M_6</td><td>**4**</td><td>**5**</td><td>**4**</td><td>**5**</td><td>4</td><td>5</td><td>**4**</td><td>**5**</td><td>**4**</td><td>**5**</td><td>**4**</td><td>**5**</td><td>4</td><td>5</td><td>**4**</td><td>**5**</td><td>4</td><td>5</td><td>4</td><td>5</td><td>4</td><td>5</td><td>**4**</td><td>**5**</td><td>4</td><td>5</td><td>4</td><td>5</td><td>4</td><td>5</td><td>4</td><td>5</td><td>**4**</td><td>**5**</td><td>**4**</td><td>**5**</td><td>4</td><td>5</td><td>**4**</td><td>**5**</td><td>4</td><td>5</td><td>4</td><td>5</td><td>4</td><td>5</td><td>**4**</td><td>**5**</td><td>4</td><td>5</td><td>4</td><td>5</td><td>4</td><td>5</td><td>4</td><td>5</td><td>4</td><td>5</td><td>4</td><td>5</td><td>4</td><td>5</td><td>4</td><td>5</td><td>4</td><td>5</td><td>4</td><td>5</td><td>4</td><td>5</td><td>**4**</td><td>**5**</td></tr>
<tr><td>M_1</td><td colspan="72">**3**</td></tr>
<tr><td>M_2</td><td colspan="24">2</td><td colspan="24">**3**</td><td colspan="24">**4**</td></tr>
<tr><td>M_3</td><td colspan="8">2</td><td colspan="8">3</td><td colspan="8">4</td><td colspan="8">2</td><td colspan="8">**3**</td><td colspan="8">**4**</td><td colspan="8">2</td><td colspan="8">3</td><td colspan="8">**4**</td></tr>
<tr><td>M_4</td><td colspan="4">3</td><td colspan="4">4</td><td colspan="4">3</td><td colspan="4">4</td><td colspan="4">3</td><td colspan="4">4</td><td colspan="4">3</td><td colspan="4">4</td><td colspan="4">**3**</td><td colspan="4">**4**</td><td colspan="4">3</td><td colspan="4">**4**</td><td colspan="4">3</td><td colspan="4">4</td><td colspan="4">3</td><td colspan="4">4</td><td colspan="4">3</td><td colspan="4">**4**</td></tr>
<tr><td>M_5</td><td colspan="2">3</td><td colspan="2">4</td><td colspan="2">3</td><td colspan="2">4</td><td colspan="2">3</td><td colspan="2">4</td><td colspan="2">3</td><td colspan="2">4</td><td colspan="2">3</td><td colspan="2">4</td><td colspan="2">3</td><td colspan="2">4</td><td colspan="2">3</td><td colspan="2">4</td><td colspan="2">3</td><td colspan="2">4</td><td colspan="2">**3**</td><td colspan="2">**4**</td><td colspan="2">3</td><td colspan="2">**4**</td><td colspan="2">3</td><td colspan="2">4</td><td colspan="2">**3**</td><td colspan="2">**4**</td><td colspan="2">3</td><td colspan="2">4</td><td colspan="2">3</td><td colspan="2">4</td><td colspan="2">3</td><td colspan="2">4</td><td colspan="2">3</td><td colspan="2">4</td><td colspan="2">3</td><td colspan="2">4</td><td colspan="2">3</td><td colspan="2">**4**</td></tr>
<tr><td>M_6</td><td>4</td><td>5</td><td>4</td><td>5</td><td>4</td><td>5</td><td>4</td><td>5</td><td>4</td><td>5</td><td>4</td><td>5</td><td>4</td><td>5</td><td>4</td><td>5</td><td>4</td><td>5</td><td>4</td><td>5</td><td>4</td><td>5</td><td>4</td><td>5</td><td>4</td><td>5</td><td>4</td><td>5</td><td>4</td><td>5</td><td>4</td><td>5</td><td>**4**</td><td>**5**</td><td>**4**</td><td>**5**</td><td>4</td><td>5</td><td>**4**</td><td>**5**</td><td>4</td><td>5</td><td>4</td><td>5</td><td>**4**</td><td>**5**</td><td>**4**</td><td>**5**</td><td>4</td><td>5</td><td>4</td><td>5</td><td>4</td><td>5</td><td>4</td><td>5</td><td>4</td><td>5</td><td>4</td><td>5</td><td>4</td><td>5</td><td>4</td><td>5</td><td>4</td><td>5</td><td>4</td><td>5</td><td>4</td><td>5</td><td>**4**</td><td>**5**</td></tr>
</table>

TABLE 5.7 – MAGNETS PER POLE TO FULL POLE PITCH RATIO

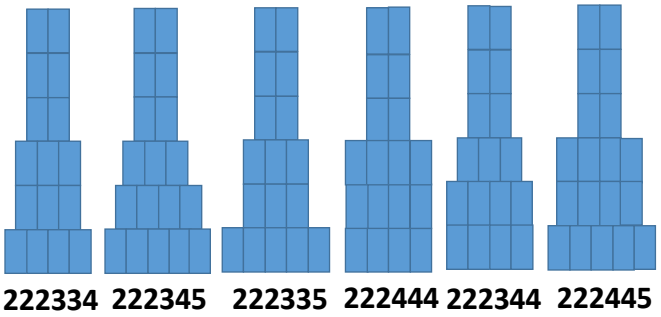
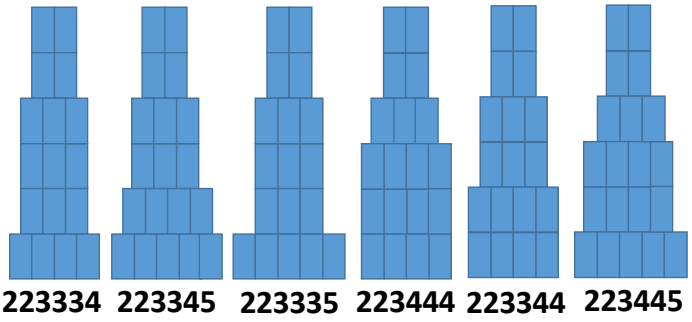
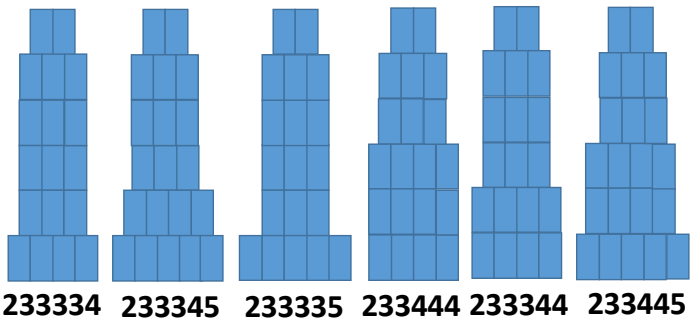
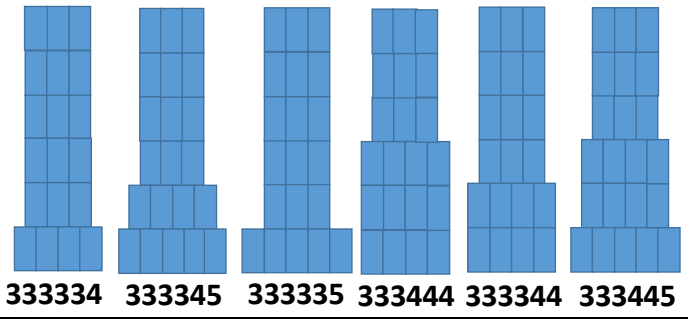
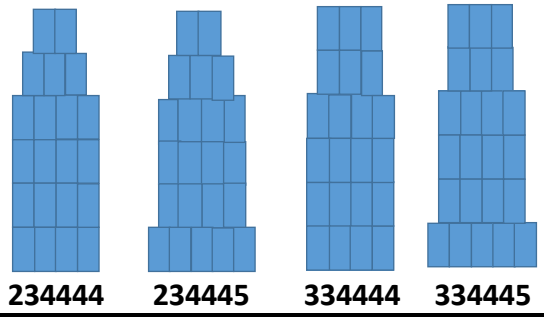
Sub Motor	Full Pole Span β_{PM}	Magnets Per Pole – Pitch Ratio			
		2	3	4	5
M_1	21.4675	0.5589	0.8384	1.1179	1.3974
M_2	23.2114	0.5169	0.7754	1.0339	1.2924
M_3	24.9552	0.4808	0.7213	0.9617	1.2021
M_4	26.6991	0.4494	0.6741	0.8989	1.1236
M_5	28.4429	0.4218	0.6328	0.8438	1.0547
M_6	30.1868	0.3975	0.5963	0.7950	0.9938

Combining Table 5.7 and Table 5.6, it can be observed that, if the pole ratio exceeds the value of one, the configuration becomes impracticable and therefore discarded (e.g. four and five magnets for sub-motor M_1). On the contrary, the case with a pole ratio less than 60% of the full pitch ratio has been excluded for sub-motors M_4, M_5, M_6, in order to exploit a major pole area. This is the case of two magnets on motor M_4 and M_5 and two and three magnets on sub-motor M_6.

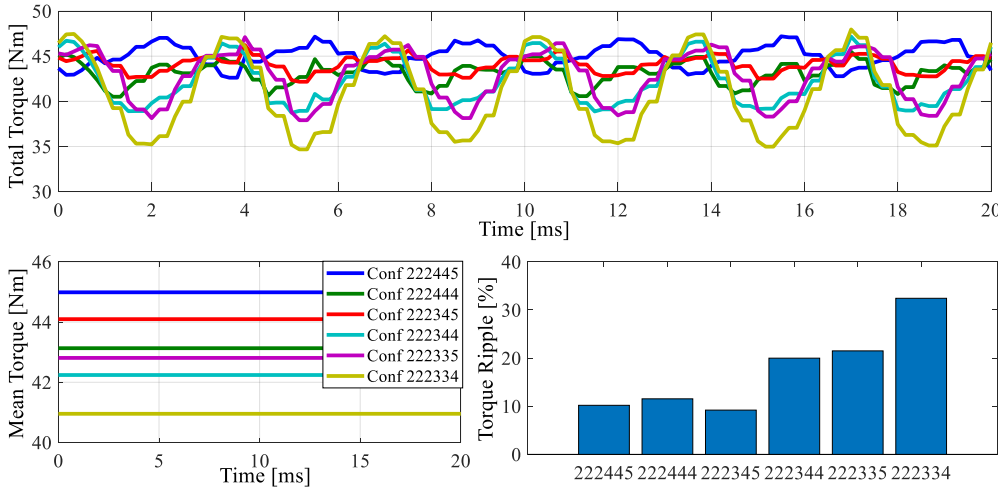
5.4.2 Rotor Configuration

The possible pole combinations (obtained using only the black numbers in Table 5.6) have been classified as in Table 5.8. The organisation of configurations is based on the first three numbers of the combinations. The identifying number utilised to refer to each of the combinations expresses the number of magnets per pole adopted on each rotor. The first number of the combination code is relative to the first sub-motor M_1; consequently, all the other numbers that appear in the combination designation correspond to sub-motors from M_2 to M_6 (e.g. the combination 223345 has two magnets on sub-motors M_1 and M_2, three on sub-motors M_3 and M_4, and respectively four and five magnets on sub-motors M_5 and M_6).

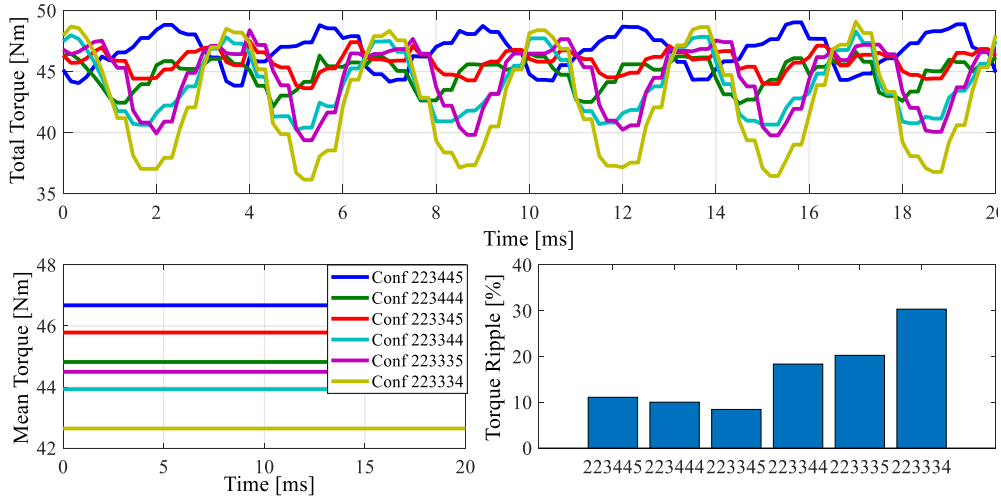
TABLE 5.8 – CONFIGURATION CLASSIFICATION

Configurations 222	
Configurations 223	
Configurations 233	
Configurations 333	
Configurations 234 & 334	

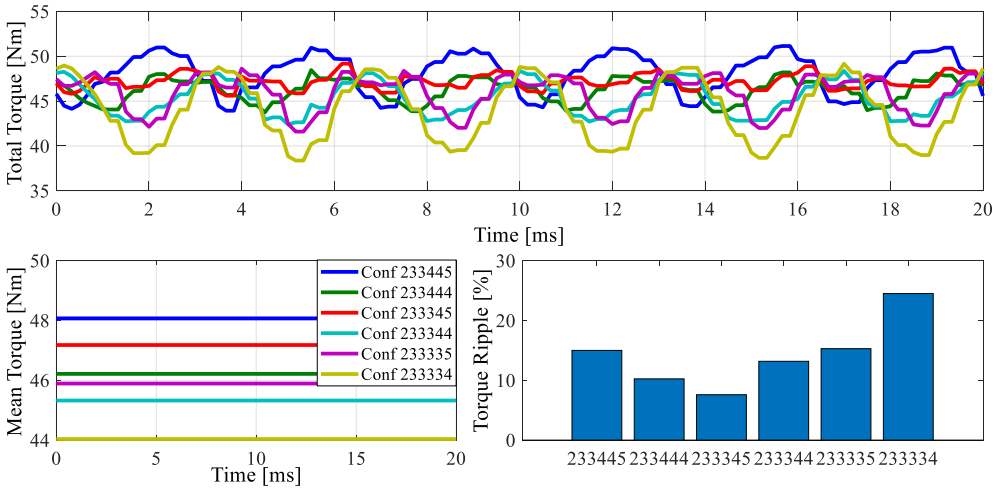
The performances of the sub-motors have been assessed separately, adopting the numbers of magnets per pole indicated by the combination number. Successively, the effects were summed to evaluate the performances of the entire conical motor associated with the corresponding configuration, in the way of the PMCM of Section 4.2.3. The combinations belonging to the same group have been compared to each other. The focal point of comparison is the quality of the torque and the amount of delivered torque. In Figure 5.8, the general trend of the torque, the mean value and the torque ripple for all the admitted configurations are displayed separately, divided into different groups; the groups are organised based on the previous arranging criterion; the organisation of the groups reflects the arrangement of Table 5.8.



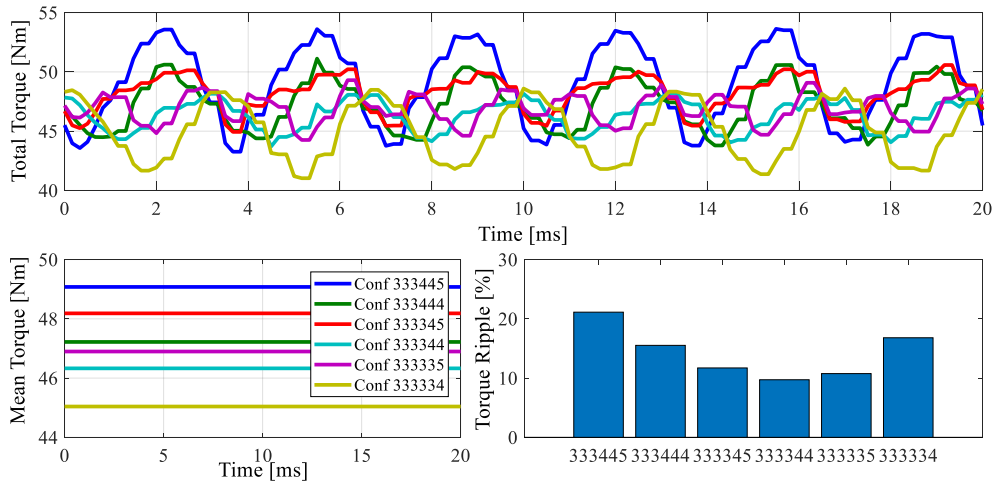
a) Configuration 222



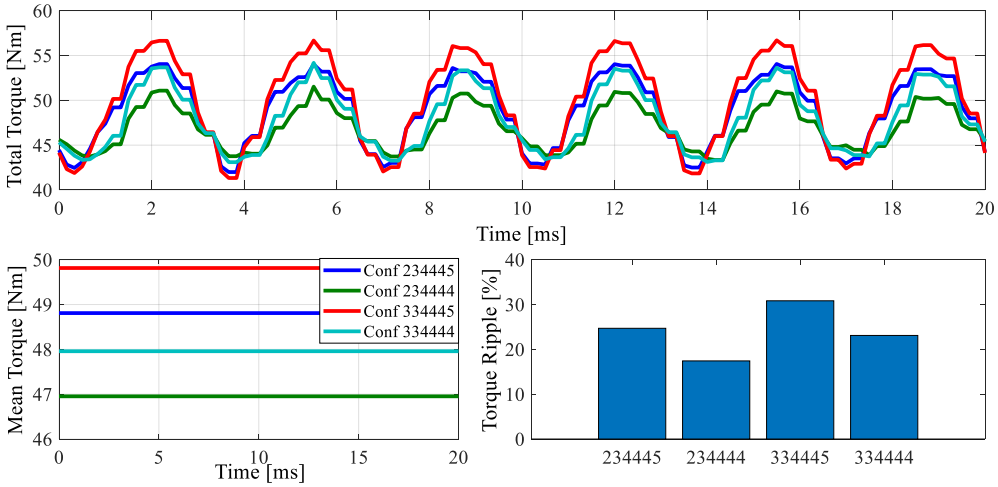
b) Configuration 223



c) Configuration 233



d) Configuration 333



e) Configuration 234 & 334

FIGURE 5.8 – TOTAL CONFIGURATIONS COMPARISON

Only the configurations that presented a torque ripple in the range of 10% have been selected among the configurations belonging to the same group and reported in Table 5.9. After this primary discriminating procedure, the combination with the smallest torque ripple between the one presented in Table 5.9 has been selected as the potential definitive one. Namely, the configuration 233345 has been preferred above all the others as it offers the lowest torque ripple with the highest torque mean value.

According to the considerations presented in Section 3.4.2, the configuration 233345, is the one that resembles a conical shaped magnet more than any other configuration reported in Table 5.8. As already anticipated during the magnetic design guidelines, having a constantly increasing pole span with a constant pole ratio helps to achieve better performances, i.e. reduced torque ripples, thus, higher average torque.

TABLE 5.9 – SELECTED CONFIGURATION COMPARISON

Air-gap 1*mm*			
Type	**Conf Number**	**Mean Torque [*Nm*]**	**Torque Ripple [%]**
Conf 222	445	44.55	10.2
	345	44.1	9.2
Conf 223	445	46.68	11.1
	345	45.78	8.44
Conf 233	444	46.21	10.2
	345	**47.18**	**7.59**
Conf 333	344	46.33	9.72
	335	46.9	10.8
	345	46.18	11.7

5.5 Sensitivity Analyses of the Main Geometric Parameters

Having identified the best performing configurations, further investigations aimed at fine-tuning the design are conducted. The main focus here is the improvement of the back-EMF and torque waveforms of the final motor. The use of different air-gap lengths and magnet arrangements have been analysed. The effects of a possible skewing of the magnets, their offset and the combination of both arrangements have been explored.

5.5.1 Different Air-gap Length

In this section, additional evaluations with different air-gap lengths for all the possible configurations highlighted in Table 5.6 are reported. The procedure exposed in Section 5.4.2 for the choice of the best configuration has been repeated for each case of air-gap length. Due to space limitations, the results obtained for each configuration using different air-gaps are not visually presented. However, in Table 5.10, the best configurations with each air-gap length are displayed. These configurations have been selected using the 10% torque ripple rule employed for Table 5.9. For each air-gap case, this best configuration in terms of torque ripple is highlighted in bold.

TABLE 5.10 – CONFIGURATION COMPARISON WITH DIFFERENT AIR-GAP LENGTH

Air-gap 0.5*mm*			
Type	**Conf Number**	**Mean Torque [*Nm*]**	**Torque Ripple [%]**
Conf 222	445	53.62	9.78
Conf 223	**445**	**55.5**	**7.04**
Conf 233	345	56.02	9.76
Conf 333	345	57.24	13.5
Air-gap 1.5*mm*			
Conf 222	444	35.33	7.93
Conf 223	444	36.79	6.79
Conf 233	344	37.17	7.71
	444	38.02	8.16
Conf 333	**344**	**38.14**	**5.22**
	444	38.99	9.44
Air-gap 2*mm*			
Conf 222	444	29.08	4.43
	344	28.33	5.34
Conf 223	444	30.36	4.38
	344	29.61	5.28
Conf 233	**444**	**31.44**	**4.28**
	344	30.73	4.38
Conf 333	444	31.66	4.54
	344	32.42	5.09

The air-gap length of 0.5*mm* has been discarded due to small tolerances and to avoid risks in case of rotor misalignment. The results selected for 1.5*mm* and 2*mm* air-gap length show an inferior torque ripple whilst a sensitive reduction of the mean torque value with respect to 1*mm* air-gap configuration. Additionally,

with a larger air-gap, a worsening in the back-EMFs shapes has been experienced; in view of this reason, the idea of a different air-gap has been abandoned in favour of the initial choice (1*mm* air-gap).

5.5.2 Combined Skewing and Offset Analysis and Final Selection

On the basis of the analyses conducted with different air-gaps, the use of a 1*mm* air-gap length has been recognised as the best compromise between the delivered torque and the quality of signals. For this reason, the configuration selected in Table 5.10 have been discarded.

Stepping back to Table 5.6, further factors have been taken into account for the choice of the final configuration. Among the configurations presented in Table 5.6, the configurations with five magnets per pole on the last sub-motor M_6 have been abandoned; the pole ratio in this case, in fact, is almost one. With a full pole pitch ratio, the magnets' glueing would have been impracticable. Also the configurations that present two magnets on the second sub-motor M_2 have been excluded, in order to make use of a major pole area. With two magnets per pole, in fact, only the 50% of the pole pitch is covered.

On this account, the remaining combinations appearing in Table 5.11, namely are 233344, 233444, 333344, and 333444, have been employed for a conclusive sensitivity study. This study has been conducted using five degrees of skewing between each row of magnets and applying an offset to the entire pole for the remaining allowed configurations, in order to assess further possible improvements. Positive and negative offsets were adopted, starting from an angle of one degree up to four. The results of this exercise are reported in Table 5.11. No noticeable enhancements were found on the level of delivered torque and torque ripple with respect to the original solutions. In consideration of what emerged from this study, the solution with combined skewing and offset has been neglected since benefits obtained with this approach do not compensate the complications of the manufacturing process.

TABLE 5.11 – COMBINED SKEWING AND OFFSET RESULTS

Conf/Offset		Mean	Ripple	Mean	Ripple	Mean	Ripple	Mean	Ripple	Mean	Ripple
		1Deg		2Deg		3Deg		4Deg		ZeroDeg	
Conf 233344	Pos	44.78	13.9	43.52	13.7	41.95	14.5	40.3	16.3	45.32	9.81
	Neg	45.03	13.9	44.42	14.6	43.39	13.9	41.7	15.7		
Conf 233444	Pos	45.77	10.1	44.36	9.71	42.92	11			46.21	10.2
	Neg	46.01	9.45	45.37	10.4	44.37	10.5				
Conf 333344	Pos	45.96	9.37	44.53	8.94	43.01	8.56	41.39	8.75	46.33	9.72
	Neg	46.1	10.7	45.6	11.9	44.45	12.8	42.87	14		
Conf 333444	Pos	46.94	15.6	45.36	16.1	43.98	17.1			47.22	15.5
	Neg	47.08	14.3	46.55	14.4	45.42	15.1				

During this conclusive part of the designing process, some considerations about the rotor tooling have been taken into account. Moving toward the rotor manufacturing, in fact, some tolerances for the realisation of the recess for the magnet allocations have been observed; a clearance of 0.3*mm* has been considered due to the fillet radius at corners of the magnets seats. This factor led to the exclusion of the configurations with three magnets on the first motor and four magnets on the fourth machine. In this circumstance, the final decision between the aforementioned solutions was in favour of the 233344. The torque mean value registered with this combination is the slightly less than the initial configuration 233345, selected between those presented in Table 5.9; however, with the 233344 configuration, the magnets resulted to be securely allocated ensuring a successful manufacturing. In view of this reason, the 233344 configuration has been employed for the final design.

5.6 Final Design Performances

A cross-section of the definitive design with a 233344 configuration is showed in Table A.3 where the magnet span α_{PM} for each sub-motor is displayed according to number of magnets on each rotor. As it can be noted from Table A.3, the sub-motors with same number of magnets per pole have similar span whereas Motor 2 present the smallest α_{PM}.

In the final design procedure of the rotor, twelve recesses (one for each pole) have been ‘engraved’ onto the conical surfaces. These guides constitute the location where the magnets are glued in stack of six rows. The recesses were

obtained by machining the rotor surface and removing 0.5*mm* of material from the lateral surface of the cone. A hard-stop shoulder of 0.5*mm* has been included on the larger side, in order to facilitate the magnets during the glueing practice. The final rotor design appears as in Figure 5.9.

The material adopted for the rotor is a stainless steel (grade 416) without any laminations. A solid rotor has been preferred due to aforementioned manufacturing complications related to use of laminated materials for conical shapes. This was also a deciding factor in terms of using an already existing stator for the proof of concept motor.

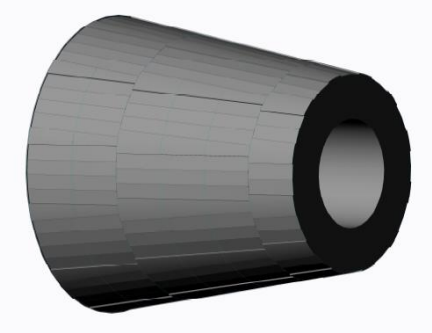
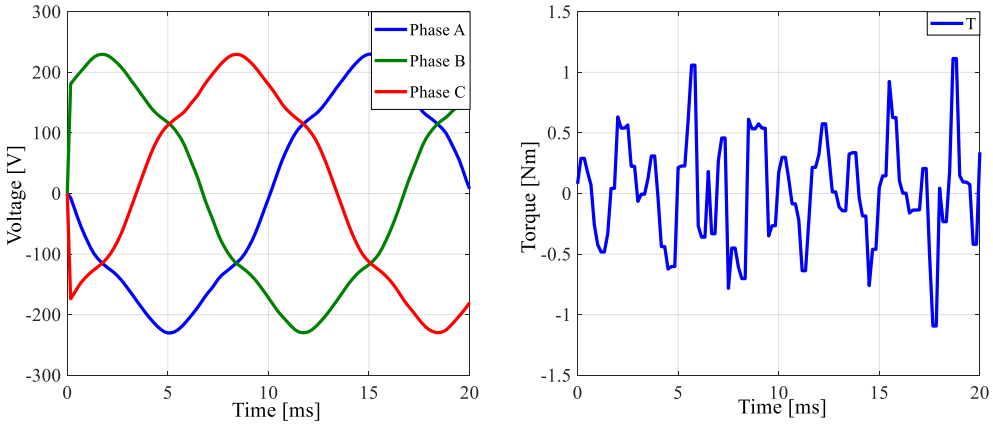


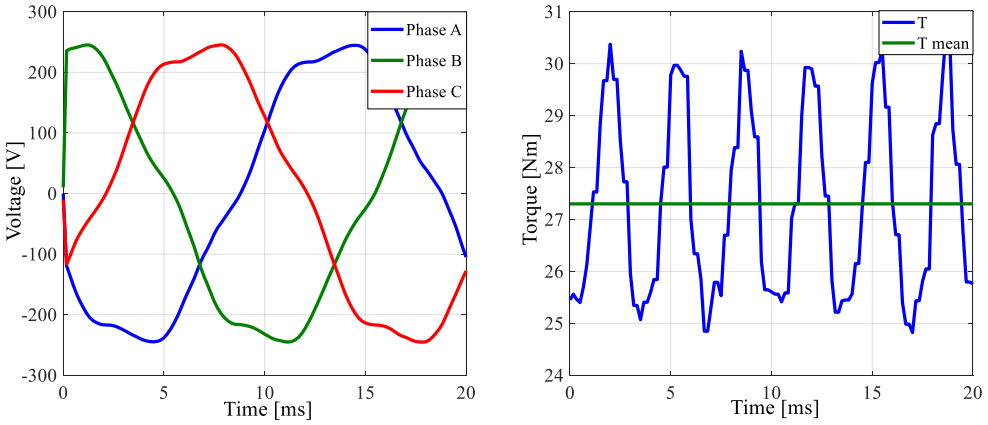
FIGURE 5.9 – FINAL ROTOR DESIGN OF THE PMCM PROTOTYPE

The performances obtained with the definitive configuration are displayed in Figure 5.10 and Figure 5.11. The torque ripple and the cogging torque are within the limits set during the designing procedure. In Figure 5.11, the total voltage and torque are calculated at rated speed (500*rpm*). As already stated, torque and voltage are obtained as the sum of the performances of each sub-motor belonging to the 2D equivalent model.



a) Back-EMFs b) Cogging Torque

FIGURE 5.10 – NO-LOAD PERFORMANCES OF THE PMCM PROTOTYPE



a) Voltage b) Torque

FIGURE 5.11 – LOAD PERFORMANCES OF THE PMCM PROTOTYPE

In order to validate the choice of the magnet length and material selected in Section 5.2.1, demagnetization studies have been conducted to check if there is a potential risk of demagnetization in the magnets, particularly, when the magnets' field is reduced to achieve the rotor disengagement. The studies have been carried out on each sub-motor, using the nominal motor current oriented on d-axis. In Figure 5.12, the results of the study have been reported for the sub-motor M_1, since this represents the "worst case". In fact, M_1 is the sub-motor with the smallest air-gap radius and smallest magnets' dimensions. As can be observed from Figure 5.12, the demagnetization prediction is always zero. This means that the demagnetization proximity, calculated as in [89], is always below zero and no demagnetization risk exists.

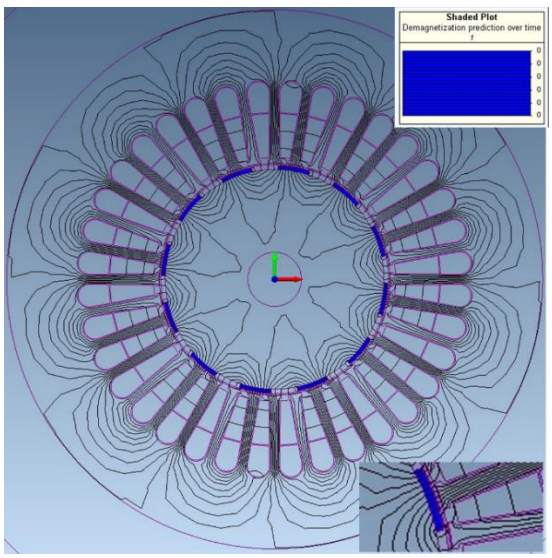


FIGURE 5.12 – DEMAGNETIZATION PREDICTION FOR SUB-MOTOR M_1

5.7 Axial Force Calculation

For this prototype, as for the high-performing PMCM presented in Chapter 4, the axial force has been evaluated at load and no-load conditions.

As presented in (4.37), the axial force can be expressed as function of the current. Implementing the total equivalent axial length $L_{stk,\gamma}$ and medium stator bore radius $\bar{r}_{si}$ of the prototype in (4.37), the axial force trend can be obtained as shown in Figure 5.13. Same results as those of Figure 5.13 can be obtained summing the axial force produced by each sub-motor implementing in (4.37) the sub-motors' equivalent dimensions $l_{stk,\gamma}$, shown in Figure 5.6, and $\bar{r}_{si}$, calculated for each sub-machine, and, successively using the superimposition principle, based on the consideration about the stresses done in Section 4.4.2. In Figure 5.13, both effects of positive and negative current are plotted from -4*A* to 4*A*, considering that the rated current of the motor is 4.8*A*. This gives an idea of the minimum and maximum values of the achievable axial force using this range of d-axis current.

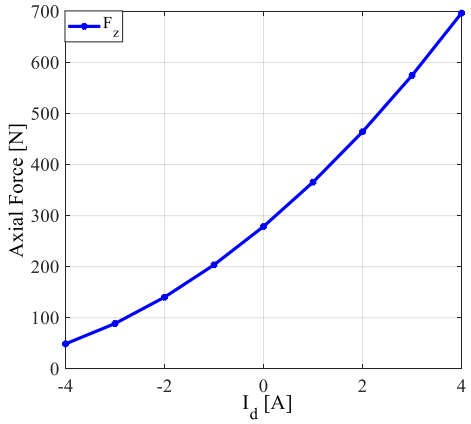


FIGURE 5.13 – AXIAL FORCE OF THE PMCM PROTOTYPE

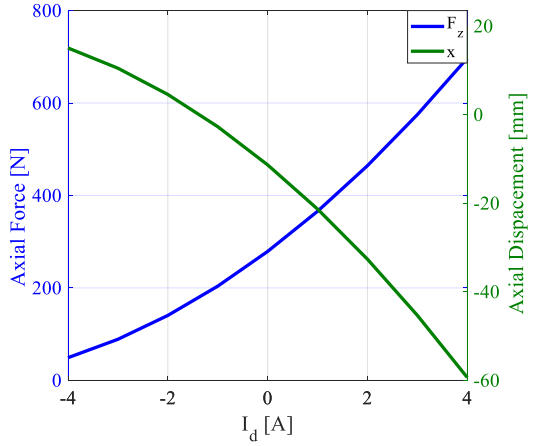


FIGURE 5.14 – AXIAL FORCE AND AXIAL DISPLACEMENT WITH ORIGINAL SPRING

The no-load axial force, calculated as in (4.37) when the current is zero, represents an important parameter for the mechanical system design. As stated in Section 1.3.1, a mechanical system similar to [27] reported in Figure 1.3, has been employed for the PMCM. The motor assembly envisages a spring mounted on the rotor shaft in the front part of the case, on the smaller side of the cone. The spring holds the rotor at the disengaged position and contrasts the magnets' axial force. The original spring, inherited from the induction conical motor assembly, has a constant of $6.67 N/mm^2$, as stated in Chapter 8. With this spring, a negative current of more than $1A$ would have been needed to hold the rotor in its retracted position ($0mm$), as visualised in Figure 5.14. In order to maintain the rotor at its neutral position, when no current is supplied, the axial force produced by the PMs' field should be compensated by the force of the spring. Therefore, the original spring has been replaced with a stronger one. A new spring with a calculated constant of $10.38 N/mm^2$ has been designed to compensate an estimated no-load force of $278.83N$, as observable in Figure 5.14. The spring has been commissioned and realised from an external CNC company.

5.8 Chapter Highlights and Contribution to Research

The following points represent the main highlights and achievements reached in this Chapter:

1) Customised solution for the realisation of conical shaped magnets.
2) A detailed FE study for the electrical design performed through the use of the equivalent model developed in Section 4.2. The conical motor performances have been assessed summing algebrically the performances of each sub-motor of the equivalent model.
3) Demonstration of the numerical computation of the axial force and torque as formulated in Section 4.4.
4) Design of the mechanical system of the PMCM based on the computed axial force.
5) Demonstration of how the no-load axial force represents a focal point for the realisation of a single-ended PMCM.

5.9 Conclusion

In this Chapter, the proposed new conical machine configuration in the form of the proposed PMCM was developed and analysed. The PM rotor configuration has been optimised in order to reach the best quality of the output torque within the limited design options.

The PMCM design represented an exercise realised to prove the concept of a single-ended conical PM machine introduced in Chapter 3 and Chapter 4.

The presence of the no-load axial force has been compensated through the customisation of the "inherited" mechanical system, i.e. choosing an appropriate spring. This proves that a PM conical machine can be built and utilised in association with a mechanical system purposely dimensioned taking into account the effect of the magnets' magnetic field.

From the performances analyses of the of the PMCM final configuration, a higher level of torque, in comparison to the equivalent conical induction machine studied in Chapter 8, has been obtained. This proved the concept exposed in Chapter 1 where a need for a PM conical motor has been claimed. The PM conical machine, in fact, is able to achieve higher performances than an equivalent induction one, particularly in terms of torque per volume ratio. Therefore, the PMCM results more beneficial to traction applications where torque density is often one of the main optimisation objectives.

.

Chapter 6
Manufacturing, Testing and Control

In order to prove and validate the concept of the conical PM motor, a physical demonstrator has been built.

The prototype has been realised integrating the conical PM rotor described in the previous Chapter into the conical stator.

In this Chapter, the manufacturing procedure, mainly focused on the rotor and the assembly aspects, is described. Tests performed to assess the motor capabilities are reported. A section concerning the control of the motor is also included to demonstrate that the current control on the d-axis and q-axis can be used to obtain respectively axial and rotating movements of the machine.

6.1 Conical PM Rotor Manufacturing

The realisation of the PM conical rotor has been completed at the University of Nottingham workshop. The rotor is made of 416-grade stainless steel. The recesses on the rotor surface have been shaped using a five-axis CNC machine on the basis of the final 3D model presented in Figure 5.9.

As a first step, a 3D printed version of the rotor, as shown in Figure 6.1 was done, in order to check all the calculated tolerances. The magnets, shown in Figure 6.2, were glued on the rotor surface. A specific epoxy (i.e. Duralco NM25) was selected based on the motor service temperature, rotor material, roughness of the surface, depth of the magnet castellation. An added benefit of this 3D-printed version is that it allowed for confirming the magnet bonding procedure before starting the definitive glueing on the actual prototype.

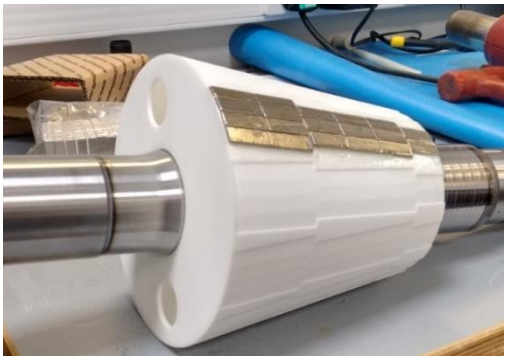


FIGURE 6.1 – 3D PRINTED PM CONICAL ROTOR

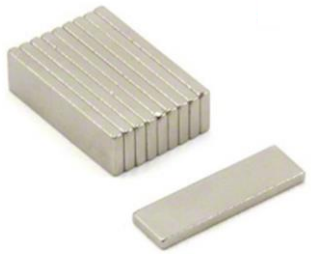


FIGURE 6.2 – "OFF-THE-SHELF" MAGNETS

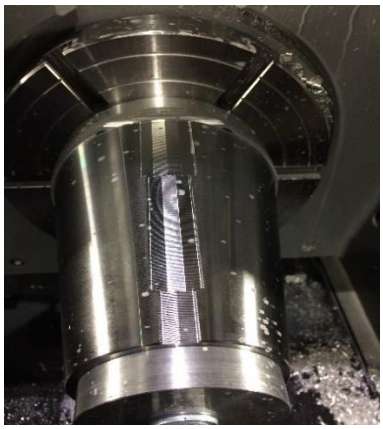


FIGURE 6.3 – ROTOR RECESSES MANUFACTURING

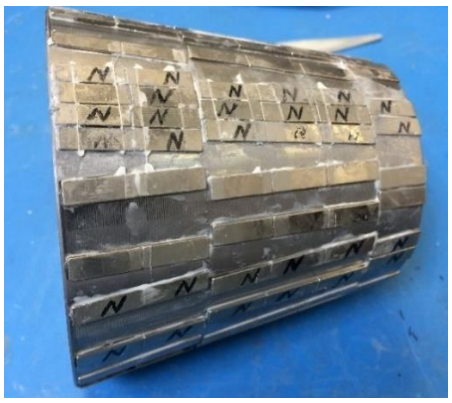


FIGURE 6.4 – PM ROTOR WITH MAGNETS

After the initial processes on the 3D-printed versions were complete, the work on the real rotor was started. Figure 6.3 shows the rotor during the machining done to achieve the castellation required for inserting the magnets. In Figure 6.4, the rotor with one completed pole constituted of six rows of magnets is shown.

The structural properties of the rotor are reported in Table 6.1, showing a good approximation of the cone volume simulated with six sub-motors compared to the real cone volume. The weight of the rotor from FE analyses has been obtained as the sum of the weight of each cylindrical motor compared with the volume of the real truncated cone ring. The total number of magnets is 228 with nineteen magnets per pole. The weight of the rotor core and magnets has been estimated using the density properties of the materials as from the supplier catalogues, namely 7800kg/m^3 for 416-grade stainless steel and 8300kg/m^3 for Sm_2Co_7 magnets.

TABLE 6.1 – FEM VS EXPERIMENTAL STRUCTURAL ANALYSES OF PMCM PROTOTYPE

	FEM	**Experimental**
Rotor Core Mass [kg]	6.07	6.52
Rotor Magnets Mass [kg]	0.3467	0.3406

6.2 Experimental Set-up

The main features of the Motor Under Test (MUT) are reported in Table 6.2.

TABLE 6.2 – MUT MAIN FEATURES

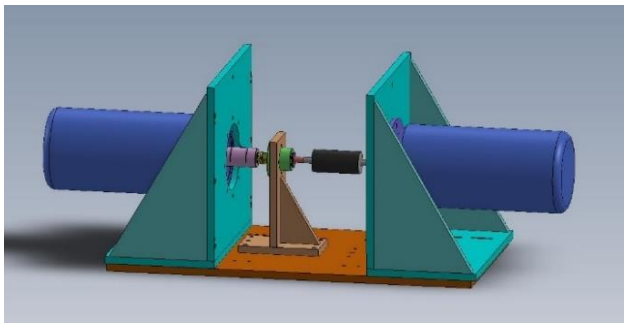
Quantity	*Symbol*	*Value*
Ambient Temperature	T_{amb}	40^oC
Insulation Class	-	H
Rated Current	I	$4.8A$
Number of Poles Pairs	p	6
Rated Frequency	f	$50Hz$
Number of Stator Slots	N_s	36
Mechanical Air-gap	g	$1mm$
Maximum Axial Displacement	x	$4mm$

The experimental tests have been divided into two sections, Section 6.3 and Section 6.4, where tests, respectively, without and with the implementation of the motor control scheme are reported. The test-rig configurations for the two different topologies of tests are described respectively in the following sections A and B.

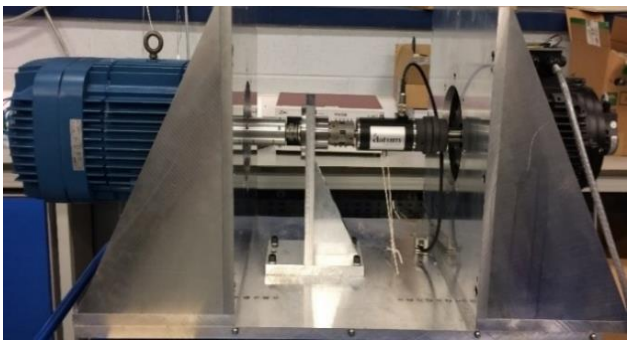
A. Test-rig Set-up without Motor Control

The first part of the tests (Section 6.3) has been conducted driving the MUT through an induction machine, Load Motor (LM), controlled through an industrial driver. The MUT has been connected to the LM through a bearing system and an in-line differential torque sensor T_M interposed between the two motors. The terminal voltages have been recorded using a digital oscilloscope and the torque values, registered by the torque sensor connected to the torque transducer, have been stored in a PC unit.

The test-rig arrangement is displayed in Figure 6.5, where the system design agreed in the preliminary phase (Figure 6.5-a)) is compared with the actual rig configuration (Figure 6.5-b)). The system equipment specifics of the LM and the industrial drive are displayed in Figure B. 3 and Figure B. 5 of Table B. 1, whereas the TM and torque transducer are described in Figure B. 4.



a) Rig Design



b) Experimental Test-Rig

FIGURE 6.5 – TEST RIG CONFIGURATION

This test-rig configuration has been used for the following tests:

- Motor parameter measurements, particularly inductances and resistance measurements (Section 6.3.1).
- Back EMF measurements (Section 6.3.2).
- Load Tests with disengaged rotor (Section 6.3.3). In this case, since no control exists on the MUT, and, therefore no d-axis current is applied, the rotor has been maintained at retracted position.

B. Test-rig Set-up with Motor Control

In Section 6.4, load tests performed with the implementation of the full control of the MUT have been described. The whole test-rig arrangement reflects the scheme reported in Figure 6.6. Apart from the MUT, the LM and the Torque Sensor (T_M) defined above, the test-rig assembly consists of three Current Sensors (CS), one Voltage Sensor (VS), one Position Sensor (PS) and the Control Unit (CU).

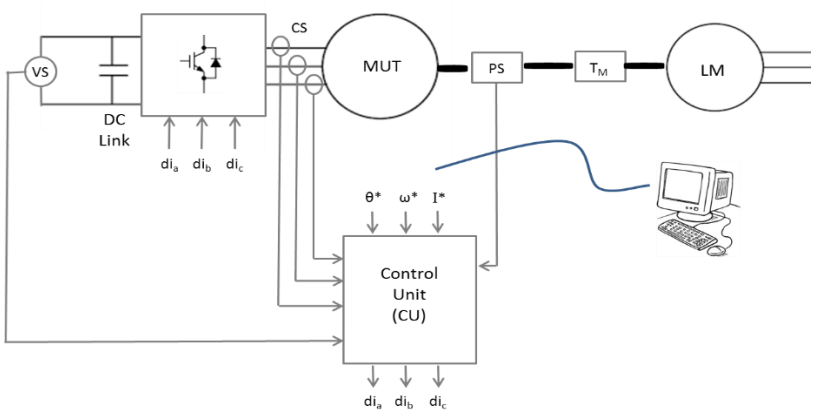


FIGURE 6.6 – TEST-RIG CONNECTION SCHEME

The motor control is loaded onto a dSPACE® Digital Signal Processing (DSP) board, which represents the CU, connected to the PC unit. Main features of the board are listed in Table B. 1. The real-time control has been realised through dSPACE software Graphical User Interface (GUI). The interface can be customised; setting tools have been used for the input variables (i.e. current and frequency) and reading boxes for the feedback signals. The readings have been realised through three A/D converters (CS and VS) connected to the board to measure two current signals and the DC link voltage level. The control output signal duty cycles (di_a, di_b, di_c) are sent to the inverter. A converter of 750W

rated power has been employed to feed the motor, equipped with three phase IGBT inverter. IGBTs features are: 4*Arms* rated current, 400 DC *V* rated voltage and 24*kHz* switching frequency. More details about the converter are provided in Table B. 1.

In order to realise the full motor control, a PS is essential. Due to the axial movement of the motor, a dedicated mechanical system has been engineered for the encoder mounting. The system enables the revolving part of the encoder to rotate with rotor shaft whilst the whole encoder moves axially together with the rotor. In this way, the encoder does not detect any axial movement whereas it is able to read the rotational speed of the rotor. The whole system assembly is shown in Figure 6.7.

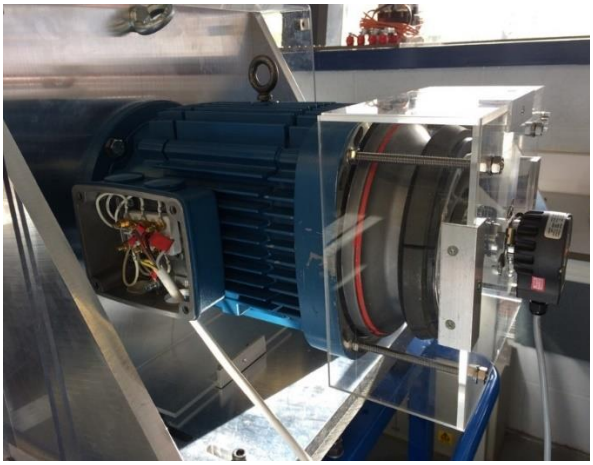


FIGURE 6.7 – PM CONICAL MOTOR WITH ENCODER



FIGURE 6.8 – ENGAGING MECHANISM DETAIL

An additional challenge for the design of the test-rig, due to axial movement, was the realisation of an engaging equipment that avoids the need of synchronisation between the revolving parts of the system (MUT and LM), in order to perform the engagement during rotation. The conical motor and the rest of the system have been coupled through a customised mechanism, shown in Figure 6.8. The two sides of the coupling mechanism have sliding taper teeth. Thus, when the rotor of the PMCM is in the extended position, the motor can still continue to rotate until perfect engagement is reached. The two sides of the coupling are separated by a 4*mm* air-gap. This distance represents the maximum axial movement admitted for the rotor of the PMCM prototype. This limit is related to the inherent feature of the motor envelope, as reported in Table 6.2.

The 4*mm* length, in fact, represents the existing clearance left for the rotor movement within the motor case.

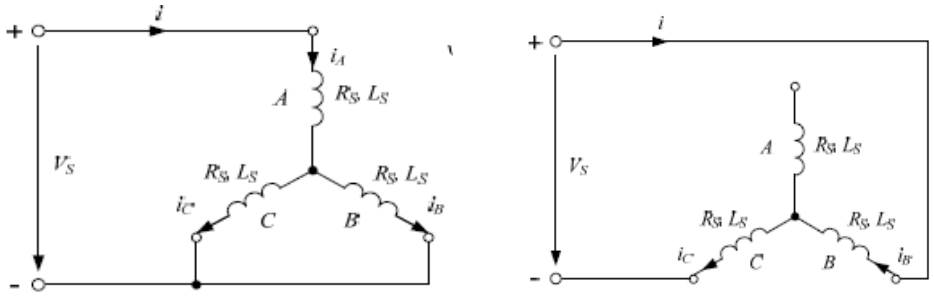
This test rig arrangement has been utilised in order to conduct two topologies of tests, namely 1) load test with rotational movement and engaged rotor (Section 6.4.2) and 2) tests with linear control (Section 6.4.3). In this case, through the use of the d-axis, it is possible to achieve the rotor engagement and the axial movement controlling the axial force of the CM.

6.3 Tests without Motor Control

All the tests performed on the motor have been accomplished following the procedures recommended in the IEEE Standards [90, 91] concerning PM and synchronous machine testing.

6.3.1 Measurements of Motor Parameters

The motor parameters R_s, L_d, L_q, namely the stator resistance and the d-axis and q-axis inductance, have been evaluated supplying a small direct current to the motor windings through a DC supply and using an RLC meter connected to the motor in two different configurations, as suggested in [92, 93]. The current causes the alignment of the machine with the direct and quadrature axes depending on the chosen connection. Specifically, the configuration of Figure 6.9-a) has been implemented to measure the d-axis inductance whereas the configuration of Figure 6.9-b) was employed for the q-axis inductance evaluation. In order to obtain the real parameters, the measurements of configuration Figure 6.9-a) have been divided by a factor of two whereas the measured values of configuration Figure 6.9-b) have been multiplied by a factor of 2/3. These factors have been derived from the equivalent circuits of Figure 6.9 a) and b). The resulting stator resistance R_s is equal to 5.878Ω, corresponding to the resistance calculated in Table A.1 and reported at cold temperature (20 ^{o}C). The measured inductances, L_d and L_q, resulted to be respectively $87.89mH$ and $89.145mH$. The measurements have been accomplished using N4L PSM1735 RLC meter with 10μHz-35MHz resolution.



a) Connection Scheme for d-axis alignment

b) Connection Scheme for q-axis alignment

FIGURE 6.9 – CONNECTION SCHEME FOR MOTOR PARAMETERS EVALUATION

6.3.2 No-Load Tests

Tests at no-load have been performed driving the conical motor with the LM as in the configuration of Figure 6.5. During the tests, no current was supplied to the conical motor, thus no axial movement was generated. The driving motor has been controlled through an industrial drive (see Figure B. 5 and features in Table B. 1) in order to set the rotating speed.

The line-to-line voltages induced in the PM conical motor have been measured using an oscilloscope with a sampling rate of 25*kS/ms*. The experimental voltages registered driving the conical motor at the rated rotational speed of 500*rpm* have been compared with the FE results. The line-to-line no-load FE voltages have been obtained from the phase voltage of Figure 5.10-a) calculated at 500*rpm*.

The experimental and the FE results showed a good matching, as demonstrated in Figure 6.10. The main difference, due to the asymmetry of the experimental waveform, can be attribute to the presence of the 7th harmonic component in the experimental data, as shown in Figure 6.11.

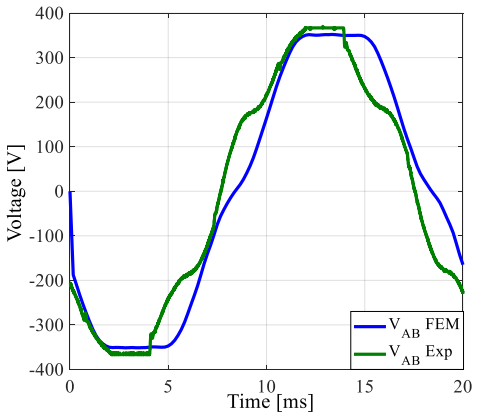


FIGURE 6.10 – FEM VS EXPERIMENTAL NO-LOAD VOLTAGE

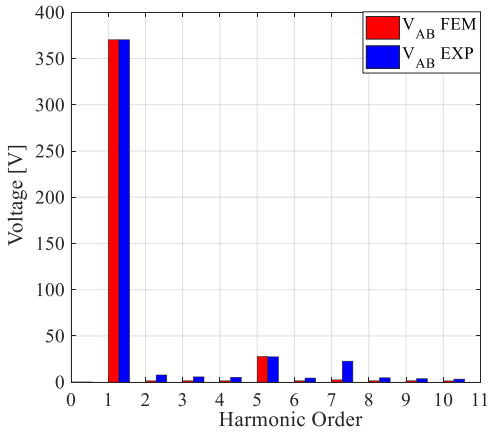


FIGURE 6.11 – FEM VS EXPERIMENTAL NO-LOAD VOLTAGE HARMONICS

6.3.3 Load-Tests with Disengaged Rotor

For this topology of tests, a resistive load has been connected to the conical machine. The rated power of the resistive load is $3kW$, implying the use of 20Ω resistance on each phase of the motor. The rate of the load has been varied using a tri-phase variac connected between the conical machine and the load with the electrical scheme represented in Figure 6.12. The point E represents the floating point that defines the load ratio a. When the quantity a is equal to 100%, the load connected to each phase of the motor is equal to the full resistance (20Ω); with a=0%, a similar condition to open-circuit is obtained.

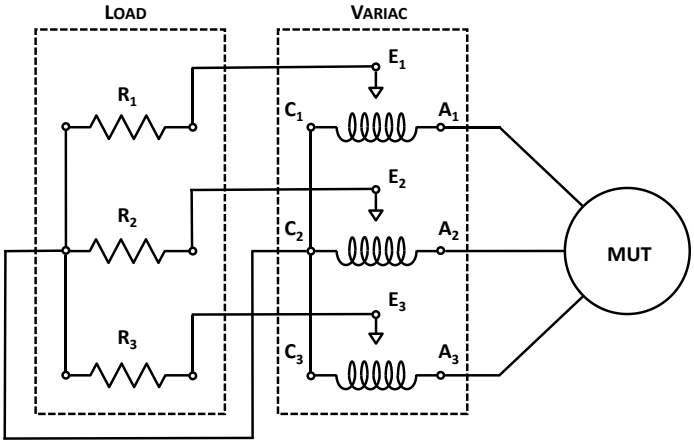


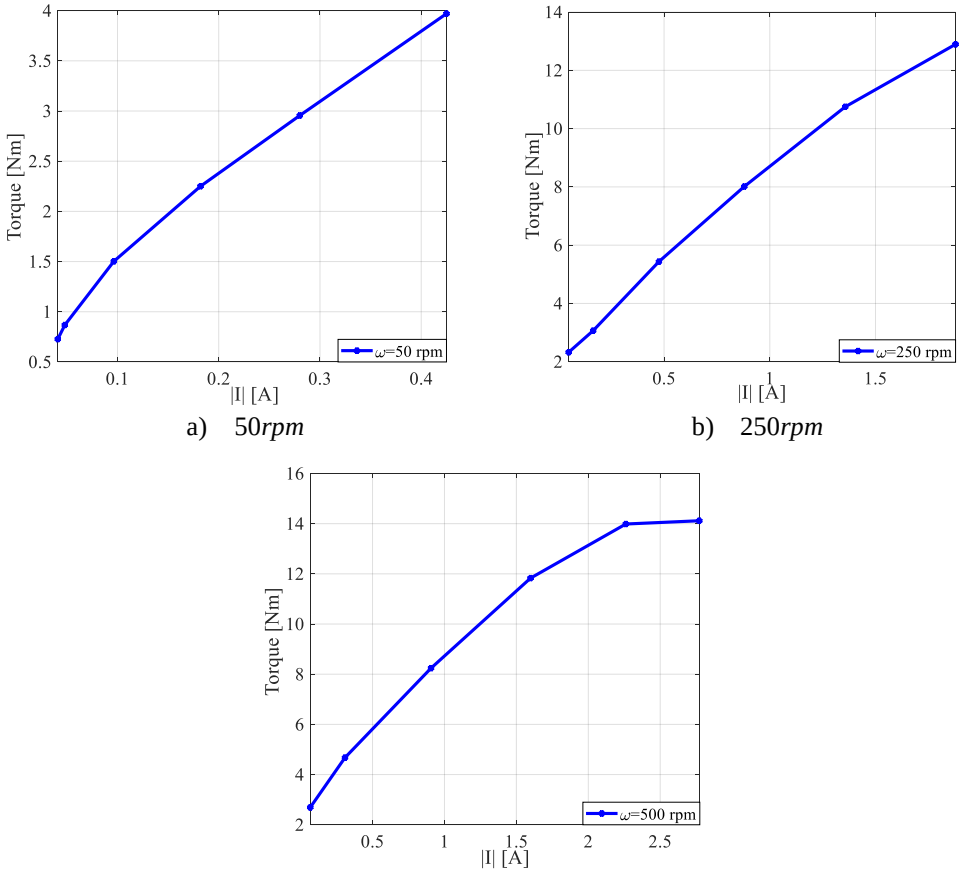
FIGURE 6.12 – LOAD TEST CONFIGURATION

The preferred rotating speed has been selected through the drive system of the LM. The entire system configuration corresponds to the one adopted for no-load tests, displayed in Figure 6.5. The conical motor and the load machine are mechanically coupled as explained above. As in the case of no-load experiments, no control was implemented for the conical motor. Due to the effect of the speed,

the rotor tends to move backwards. Since no current was applied, the spontaneous axial movement of the rotor could not be compensated through the use of the d-axis current for producing the necessary axial force, therefore, tests have been performed with the conical rotor in fully retracted position and the MUT always connected to the LM in order to avoid inconvenient effects due to unwanted rotor axial movement.

As the rotor moves backwards, the air-gap length increases by a quantity Δg calculated in (3.7), where x represents the axial movement of the rotor in mm. When the rotor is completely retracted, the axial displacement is equal to $4mm$ and the increment of the air-gap length is equivalent to $0.67mm$. The FE analyses of the motor at rated speed and rated current, performed in Section 5.4.2 in order to choose the final configuration of the demonstrator, have been realised using the air-gap length corresponding to the engaged configuration and equal to $1mm$. As explained in Section 3.4.1-A, this is the expected working machine configuration corresponding to its nominal performances. However, the load tests with the rotor at retracted position resulted useful in a preliminary testing phase when no encoder was mounted. The load tests with the rotor maintained at the aligned position, in fact, can only be performed having a full control of the motor. Since it is a PM motor, an encoder is essential for the control.

The experiments with the retracted rotor have been conducted at different levels of speed, starting from $50rpm$ up to the rated speed ($500rpm$) with a step of $50rpm$. For each level of speed, different amount of load has been applied, from zero to full load with a step of 20%. However, even in the case of full load at rated speed, the current withdrawn by the motor did not reach the rated current of the motor. In Figure 6.13, the level of torque registered at different speeds in case of full load condition is displayed. As emerges from Figure 6.13-c), the maximum current reached at full load and rated speed condition ($500rpm$) is roughly $2.75A$. The registered current, in fact, is far from the rated current of the machine, equal to $4.8A$.

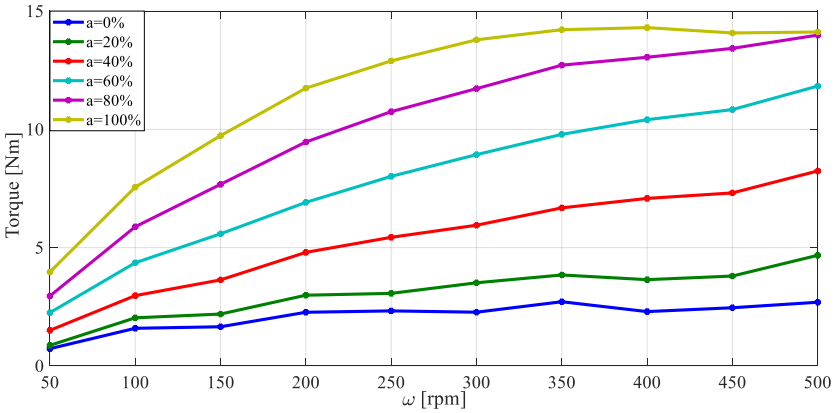


a) 50*rpm* b) 250*rpm*

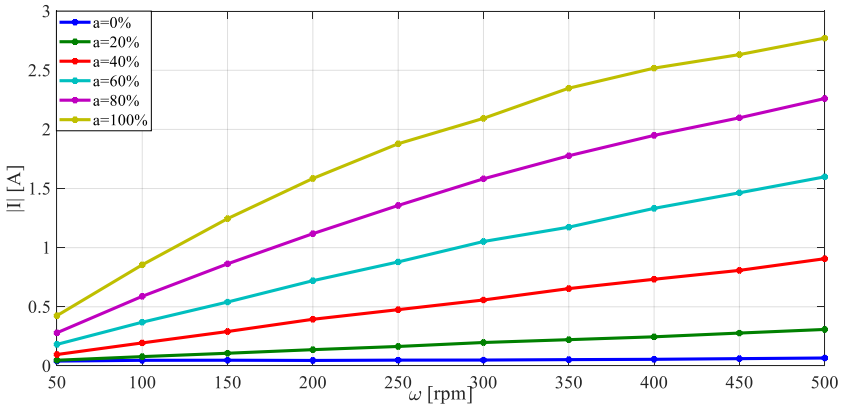
c) 500*rpm*

FIGURE 6.13 – T-I CURVES AT DIFFERENT SPEEDS WITH DISENGAGED ROTOR

In Figure 6.14, torque and current have been reported at each level of speed for different values of load ratio *a*. The torque obtained at 500*rpm* with the maximum load of 20Ω is limited to 14*Nm*. This is due to the fact that only a resistive load is applied and no control exists on the current of the MUT. The current angle is not optimised to obtain the maximum torque.



a) Torque-speed curves



b) Current-speed curves

FIGURE 6.14 – T-ω AND I-ω CURVES AT DIFFERENT LOAD WITH DISENGAGED ROTOR

6.4 Motor Control and Testing

As for conventional PM machines, the control of the conical PM motor has been realized using traditional vector control strategies [94] based on the estimation of a *dq* axis system rotating at the synchronous speed. This alignment operation can be performed only when a shaft encoder is present unless sensorless techniques are adopted. Therefore, in order to achieve the full control of the motor, the presence of the encoder is mandatory.

With the full control of the motor, both movements can be performed at the same time (horizontal and rotational). When the rotor is at the retracted position (0*mm*), the motor is completely disengaged from the rest of the system. If d-axis current is provided, the rotor moves forwards to its fully extended position (4*mm*) and is connected to the load machine. The engagement procedure can happen conjointly to the rotational movement, thus, while the rotor is rotating, or statically so that the rotation starts once the engagement is achieved. In this section, the two topologies of control (axial and rotational) are accomplished respectively in Section 6.4.1 and 6.4.3. For the rotational movement, the current and speed controls have been tuned by using a rotary position encoder, whereas a linear encoder has been employed for tuning the axial position control.

6.4.1 Current Control Loop and Speed Loop

The complete scheme implemented for the control of the PM conical motor has been reported in Figure 6.15. As observable from Figure 6.15, the control of q-axis current is utilised to control the rotational speed and the torque of the motor, whereas d-axis current is controlled in order to move the motor axially. The control has been achieved through the use of proportional-integral controllers experimentally tuned.

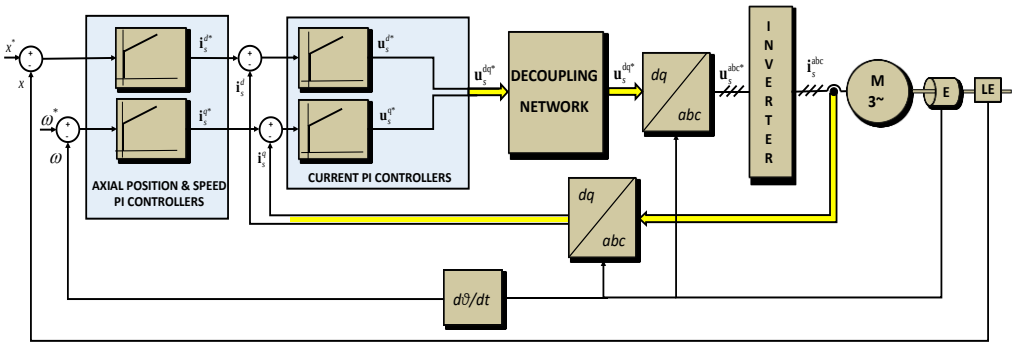


FIGURE 6.15 – COMPLETE CONTROL SCHEME

Figure 6.16 and Figure 6.17 show the step response respectively of the d-axis and q-axis current controllers; the sinewave system of motor currents has been obtained supplying the motor with a set of three balanced voltage signals generated providing to the inverted opportune duty-cycles through dSPACE/ Simulink® interface.

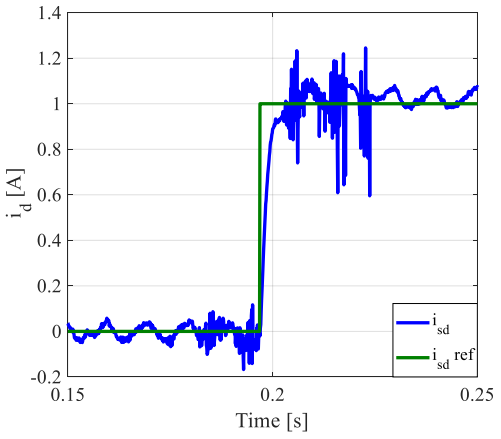


FIGURE 6.16 – D-AXIS CURRENT PI CONTROLLER

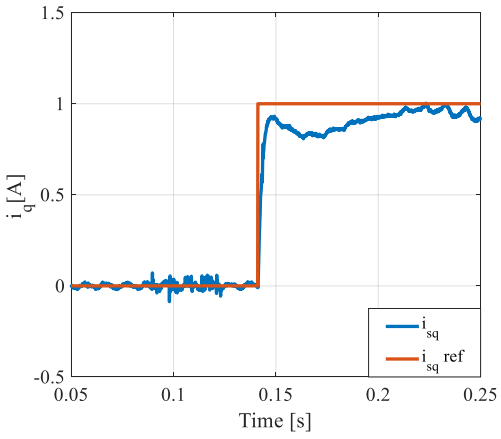


FIGURE 6.17 – Q-AXIS CURRENT PI CONTROLLER

As regards the speed control, a first order filter has been implemented in order to smooth the reference signal. The speed control response to the step signal is displayed in Figure 6.18. A bandwidth of 150 Hz and damping factor of one are employed; this avoids having any overshoot in the step response.

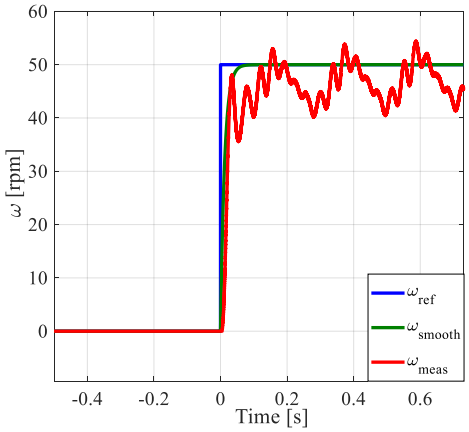


FIGURE 6.18 – SPEED PI CONTROLLER

6.4.2 Load-Tests Engaged Rotor

Load tests with engaged rotor have been performed connecting the PMCM to the same induction LM utilised for the load tests of Section 6.3.3 and displayed in Figure B. 3 of Appendix B. The tests have been conducted controlling the speed of the MUT and the current of the LM. The LM has been controlled through the industrial drive, mentioned in Section 6.3.3 and described in Table B. 1 of Appendix B. Different levels of load have been selected setting the LM current using the industrial drive interface; the current is expressed as the percentage of the rated LM current.

Due to equipment limitations, related to the maximum torque admissible for the LM, the maximum level of torque of the MUT could not be reached. Tests have been performed utilising different level of loads at different speeds. In Figure 6.19, the trend of the torque and q-axis current has been obtained imposing the level of the speed through the control system realised for the MUT and changing the load from zero to 80% (maximum level admitted by the industrial drive) with a step of 10%. This procedure has been reiterated for each speed level; results are displayed in Figure 6.19. Same results have been manipulated in order to

obtained Torque-Speed (T-ω) and Current-Speed ($\mathbf{i_q}$-ω) curves for each level of load, respectively reported in Figure 6.20 and Figure 6.21.

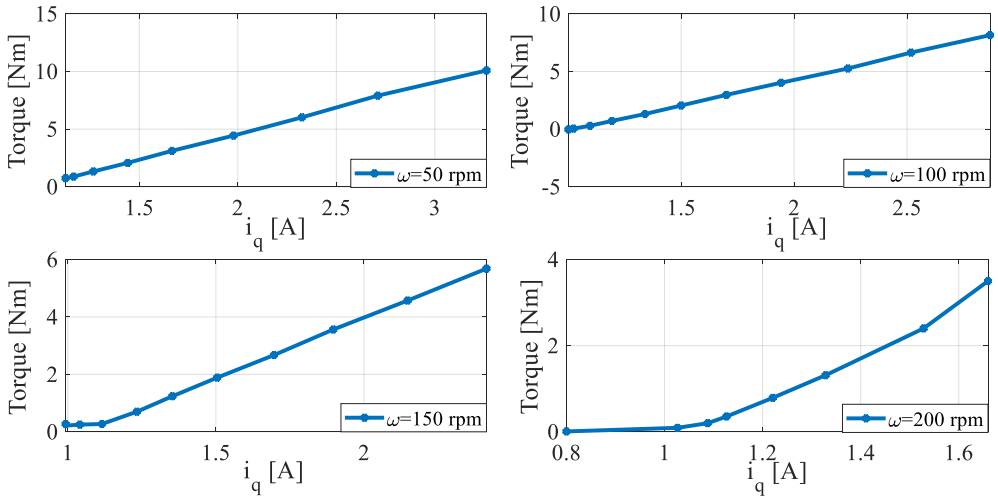


FIGURE 6.19 – T-I_Q CURVES AT DIFFERENT SPEEDS WITH ENGAGED ROTOR

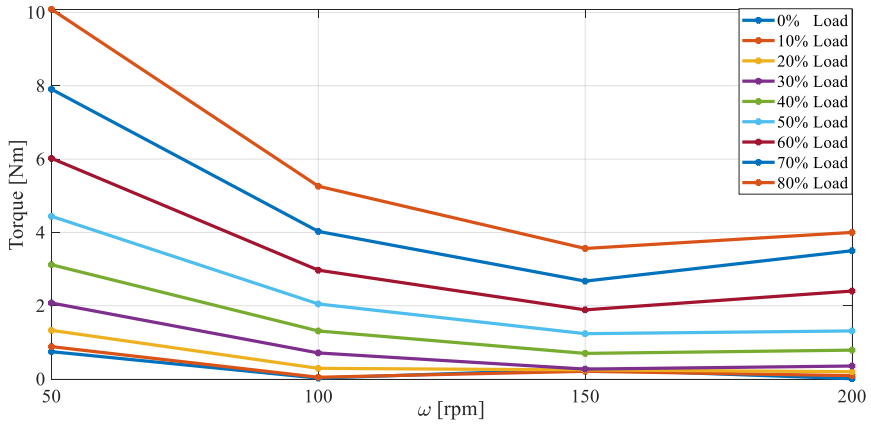


FIGURE 6.20 – T-Ω CURVES AT DIFFERENT LOAD LEVELS WITH ENGAGED ROTOR

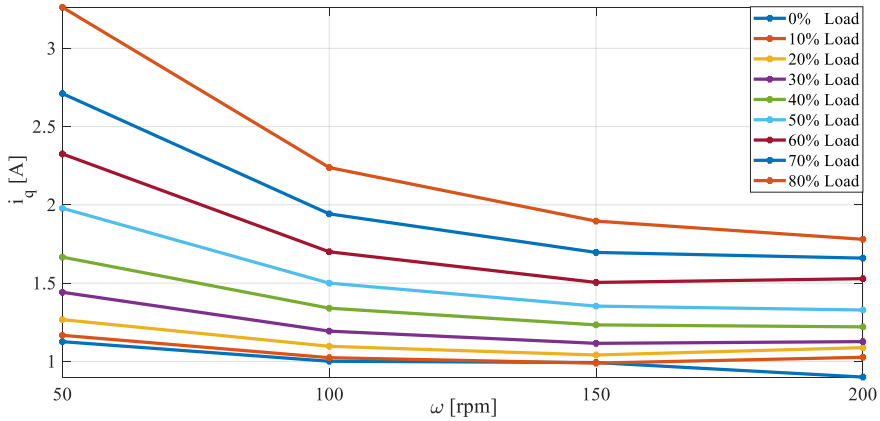


FIGURE 6.21 – $\mathbf{i_q}$-ω CURVES AT DIFFERENT LOAD LEVELS WITH ENGAGED ROTOR

The maximum permissible speed was set to 250*rpm*, mainly because of the absence of the d-axis current control for rotor axial position simultaneously with the speed control. As the speed increases, in fact, the axially oriented force produced by the magnets decreases and the rotor is pushed backwards. This phenomenon must be compensated by increasing the d-axis current to nullify the effect of the speed on the rotor horizontal displacement. A linear encoder operating simultaneously with the conventional rotational encoder is therefore required. The linear actuation control will operate asking the motor to produce the d-axis current required to achieve the desired horizontal movement and forcing the rotor to be at the engaged position. In this work, the control of the axial movement through the d-axis current has been performed separately from the speed control. In order to realise both controls at the same time (for rotation and linear actuation), a linear position sensor that enables the rotation is needed (i.e. laser position sensor). Due to availability reasons, only a traditional linear encoder has been employed to perform the linear control, therefore, the rotor shaft was bounded to a specific angular position during the tests (i.e. alignment position for the *dq* frame), as explained in Section 6.4.3.

6.4.3 Axial Position Control

In order to perform the control of the linear movement and demonstrate that the axial control can be performed utilizing the d-axis current, a linear encoder has been mounted on a support shown in Figure 6.22 (right) and aligned to the magnetic band glued on the motor shaft, as displayed in Figure 6.22 (left). The features of the encoder and the magnetic band are reported in Table B. 1 and Figure B. 7 of Appendix B.



FIGURE 6.22 – LINEAR ENCODER MOUNTING

The axial control has been implemented as outlined in the control scheme of Figure 6.15. At the beginning, the horizontal movement has been monitored without implementing any controller for the axial displacement. The d-axis current, in this case, was decreased until the axial force generated by the magnets diminished and the spring pushed the rotor to the retracted position; in the same way, the current was increased until the aligned position was reached again. As demonstrated in Figure 6.23, after reaching the aligned position (0*mm*), when not sufficient negative d-axis current is applied, the rotor is at resting position; if the amplitude of the d-axis current increases the axial force increases as well. When the current drops over a certain value (specifically 3.6*A*) the axial force produced by the magnets is reduced by the demagnetizing effect of the negative current and the spring pushes the rotor back toward the fully retracted position (4*mm*).

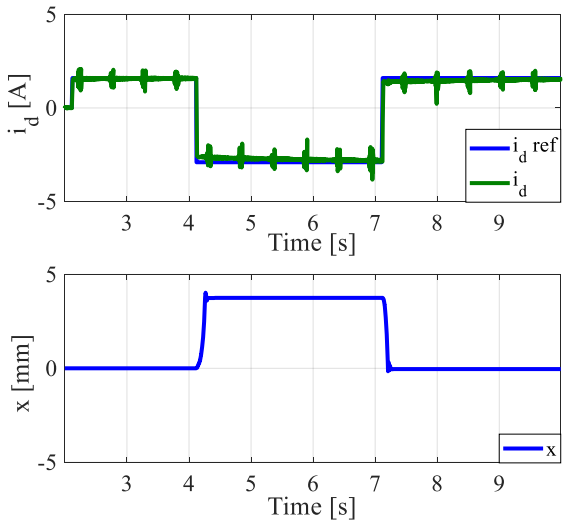
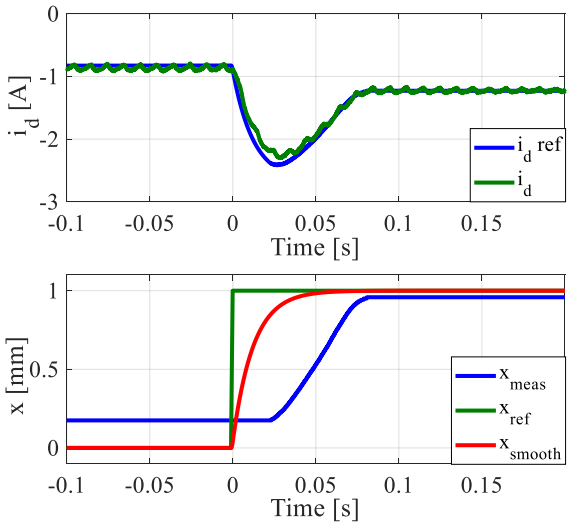
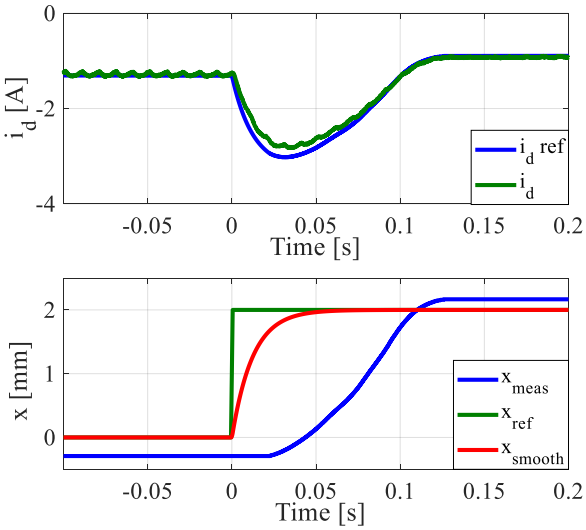


FIGURE 6.23 – AXIAL POSITION MEASUREMENTS

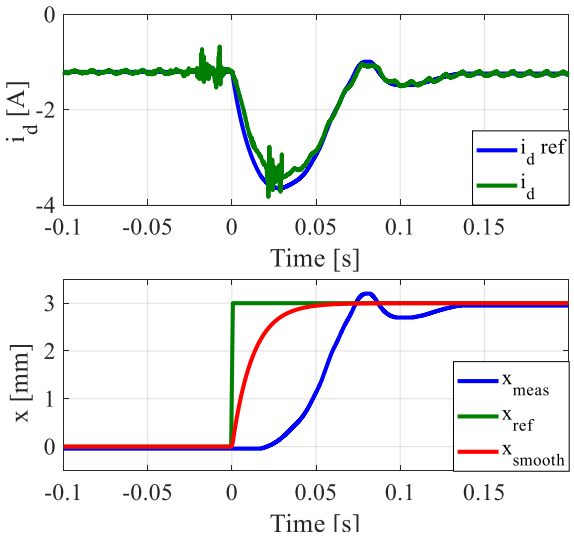
When the linear control is applied, the axial position of the rotor can be decided and set opportunely by varying the level of the d-axis current. Figure 6.24 shows the response of the current controller and the axial position controller to different axial position step input of 1*mm* (Figure 6.24-a)), 2*mm* (Figure 6.24-b)) and 3*mm* (Figure 6.24-c)). In this case, as in the case of the speed control, a first order filter has been included to smooth the reference step signal. A fine tuning of the dynamic response of the system could have been performed using a better equipment; however, this exercise goes beyond the purpose of this thesis.



a) Reference Axial Position 1*mm*



b) Reference Axial Position 2*mm*



c) Reference Axial Position 3*mm*

FIGURE 6.24 – AXIAL POSITION CONTROL

6.5 Axial Force Measurements

The total axial force produced by the motor has been measured utilising an end stop plate displayed in Figure 6.26 that is able to hold the rotor at a specific axial position; in this way the linear force, obtained applying increasing the level of the d-axis current, has been measured at different axial positions. The force has been quantified using a load cell, glued on the end-stop plate bar, as shown in Figure 6.26.

The measured force has been plotted in Figure 6.25 as function of the d-axis current. The axial force measured for the PM conical machine shows very good similarity with the axial force measured for the conical IM motor and displayed in Figure 8.20 of Chapter 8. This is due to the compensating effect of the spring opportunely calibrated to nullify the effects of the magnets; the current, in fact, is utilised to produce the axial movement which results to be similar in both motors.

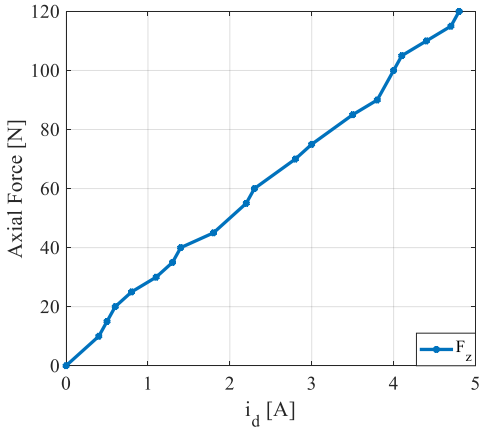


FIGURE 6.25 – AXIAL FORCE MEASUREMENTS

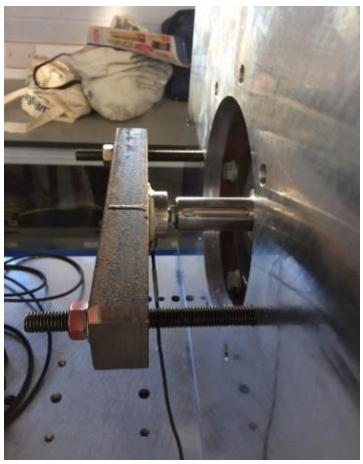


FIGURE 6.26 – END-STOP PLATE AND LOAD CELL

6.6 Chapter Highlights and Contribution to Research

A conclusive list of the main objectives achieved in this Chapter can be summarised as in the following points:

1) Implementation of an innovative control scheme for the linear movement of a PMCM, within the traditional control scheme of PM machines.
2) A new methodology for the decoupling of linear and rotational control using respectively d-axis and q-axis.
3) The proposal of how to perform axial force measurement using the d-axis current.

6.7 Conclusion

In this Chapter, the PMCM functioning principle has been demonstrated with a PM conical machine built and assembled in the University of Nottingham laboratories. The complete implementation, as envisaged during the preliminary designing phase, has been accomplished with successful results.

The main features of the conical machine have been assessed. An efficient control scheme has been implemented to achieve the control of the motor in terms of axial and rotary movements. Having a linear sensor and a rotational sensor working contemporary might have helped in controlling the d-axis and q-axis current simultaneously in order to compensate the pushing-back effects of the speed.

The axial force calculation obtained using the end-stop plate technology showed very good similarities with axial force obtained with the ICM, reported in Chapter 8. This means that the effect of the axial force due to the magnets are totally compensated through the new spring selection completed in Section 5.7. The variation of the axial force is, therefore, due to the d-axis current in case of PM conical machine and magnetising current in case of conical, as demonstrated in Chapter 8.

With the achievements of this Chapter, it can thus be concluded that one of the main aims of this project, i.e. a proof of concept with a PMCM prototype, is achieved.

Chapter 7
Implementation of the PMCM for a Particular Aerospace Traction Application

This Chapter is dedicated to the implementation of conical machines in a real-world application.

A mock-up system for a particular aerospace traction application described in Chapter 2 where the implementation of a PMCM can have significant advantages is developed.

A detailed investigative study is done comparing the integration of the CM with an induction motor and permanent magnet technology for the electric-taxiing system.

The conical version of the ETS is introduced together with a new taxiing procedure customised for the conical ETS.

.

7.1 Conical E-Taxiing System

In the previous chapters, the performances of the conical actuator have been assessed separately from the rest of the system. The torque and the axial force developed by the motor have been calculated looking at the electrical configuration of the machine and their formulation has been confirmed through the comparison between the present taxiing actuator (cylindrical) and its conical version, as reported in Chapter 4. It is worth to understand how the axial force will be exploited within the ETS and in which way the conical actuator will benefit to the electric-taxiing procedure.

As displayed in Figure 7.1, the taxi procedure starts when the aircraft is standing at the gate. Before taxiing begins, thus before the aircraft starts to move, the conical actuator needs to be engaged to the wheel. As demonstrated in Chapter 6, for the control of the CM, the d-axis current is utilized to develop the axial force necessary to achieve the complete attachment of the motor to the wheel; thus, the current is increased until attachment is reached, as shown in Figure 7.2.

Once the engagement is securely ensured, electric traction begins. During traction, the electric motor is asked to produce convenient torque and speed. The q-axis current control and the speed control loop determine the aircraft movements on the ground (as demonstrated in Section 6.4.1 through the control scheme of Figure 6.15). Once the taxiing procedure terminates, the axial force is reduced by decreasing the d-axis current; the motor is completely disengaged from the wheel. If the disengagement is completed successfully, the main engine is switched on (see Figure 7.1) and the aircraft is ready to take off.

A similar procedure is followed when the aircraft is on the runway after landing. During landing, the actuator is detached from the wheel preventing the motor from high speeds. When the landing procedure is complete and the main engine is cooled down (see Figure 7.1), the motor is attached to the wheel and taxiing system starts driving the aircraft to the gate. In Figure 7.2, the schematic summarizes the taxiing scheme for take-off, however, the same control is employed during landing.

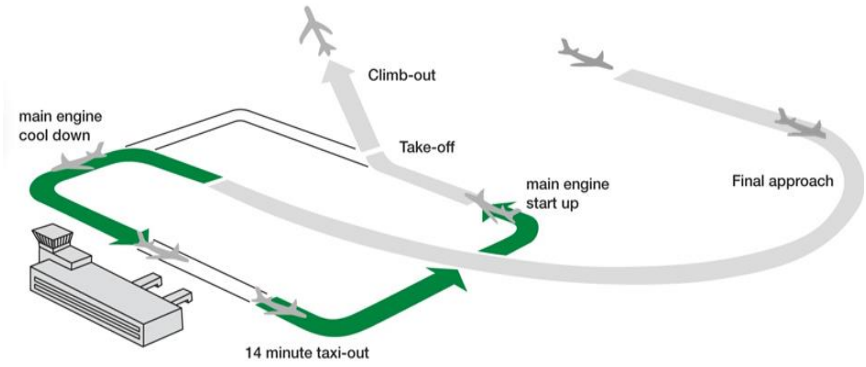


FIGURE 7.1 – TAXI ROUTE [95]



FIGURE 7.2 – TAXIING PROCEDURE BEFORE TAKE-OFF

In order to access the motor axial position and determine if the actuator is safely engaged and disengaged from the wheel, the whole system can be accessorised with an axial monitoring system. This implies the use of linear position sensor; however, a "sensor-less" axial position monitoring algorithm that is able to assess if the motor reached the extended position and is properly engaged to the wheel has been realized in Avio Aero s.p.a. laboratories and it is described in Chapter 8. The monitoring system envisages the use of high frequency voltage injection techniques to determine the axial position of the rotor inside the stator. No sensor is required, making the whole system more reliable.

7.2 Small-size Demonstrator

The idea of a representative demonstrator originates from the willingness of having a physical proof of the concept of the conical electric-taxiing system. The plan for a full-scale demonstrator was discarded on the basis of time and cost requirements (a full-scale prototype was estimated to have cost in the region of £200k). Due to all this, it was felt that a small-scale version can still be extremely beneficial and prove the concept proposed here.

Different solutions were contemplated to realise the mock-up model without exceeding the accessible budget and reducing the amount of time required for the manufacturing. After several investigations, the adoption of a system arrangement similar to the one of Figure 7.3 has been found the most convenient solution. A meticulous design of the entire system has been accomplished; the final configuration is displayed in Figure 7.3 where the conical small-size actuator has been connected to a trailer wheel. The wheel and the motor are coupled through the customised mechanism displayed in Figure 6.8. As explained in Section 6.4, the two sides of the mechanical artifact have sliding tapered teeth and they are separated by a 4*mm* air-gap, corresponding to the maximum extension of the rotor reported in Table 6.2. The distance represents the maximum axial movement admitted for the rotor within the rotor case, as described in Chapter 5.

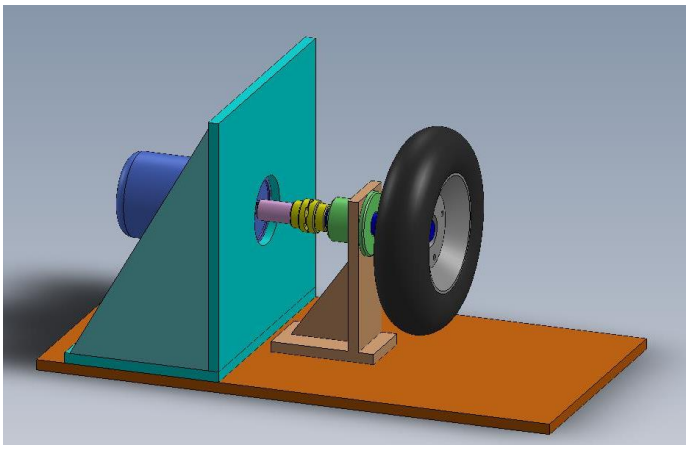


FIGURE 7.3 – E-TAXIING SYSTEM DESIGN

The axial movement is generated as illustrated in the conceptual scheme of Figure 7.2. When the force of the spring wins on the no-load axial force, the rotor is in the retracted position and it is free to rotate. When the rotor is in the extended position, the motor rotates until the perfect engagement with the wheel is reached. This engaging equipment avoids any synchronisation between the rotor and the wheel.

As described in Figure 6.4, the control strategies, employed for the system functioning, have been implemented in a general Simulink® structure that envisages the presence of a state flow machine. The state flow machine enables different topologies of control to be chosen within the same control scheme; the role of the state flow machine, is also to set safe operational limits such as voltage, current and speed. The ET control scheme has been proven using an "off-the-shelf" conical induction machine, described in Chapter 8, and with the PMCM prototype designed Chapter 5 and tested in Chapter 6. The same experimental equipment described in Section 6.2-B and detailed in Table B. 1 has been adopted in both cases. The two system prototypes are reported in the below, respectively in Section 7.2.1 and Section 7.2.2.

7.2.1 System Implementation with ICM (as proof of concept)

The working principle of the conical actuator within the ET system has been demonstrated firstly with the "off-the-shelf" conical induction motor, proving very smooth transition from disengaged to engaged position. No particular

torque requirements were set for the miniature E-Taxiing scheme and therefore the use of the ICM was suitable for the demonstration objective here.

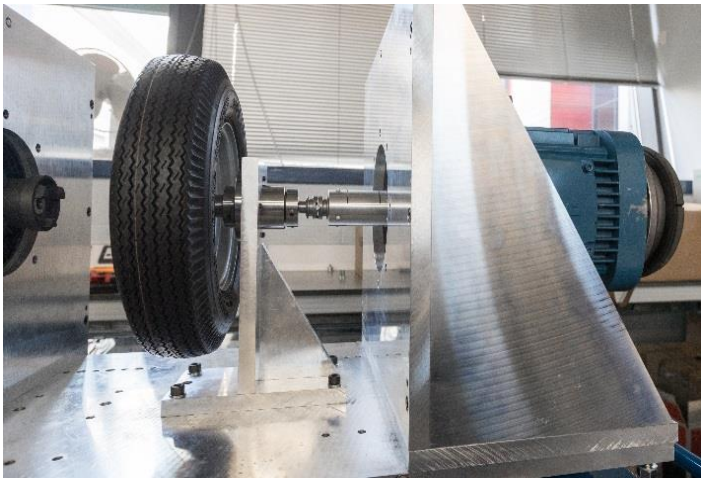


FIGURE 7.4 – CONICAL E-TAXIING DEMONSTRATOR

The small-scale version of the conical ETS presented in Figure 7.4 reproduces accurately the preliminary design of Figure 7.3. The same mechanism of Figure 6.8 can be recognised between the motor and the wheel of Figure 7.4. At that point, the mechanical system for the encoder mounting had not been designed yet. Therefore, the control of the system with the IM has been realised without any sensor.

The rotational movement of the actuator, when connected to the wheel, has been obtained with an open loop control. The open loop control strategy is similar to V/Hz technique; however, the controlled values are the amplitude of the current I^* and the reference frequency f^*. This control methodology is called *I-f* and is particularly useful to realise a smooth motor starting [96-99]. With this topology of control, it is possible to ask the motor to produce a current either on d-axis or q-axis with I^* amplitude. The reference frequency f^* is increased smoothly, particularly if there is a heavy load condition. The motor velocity increases gradually until the synchronous speed is reached; an abrupt transition in the frequency reference signal, in fact, might cause the loss of synchronism between the generated signal and the motor speed.

The control system is represented in Figure 7.6. In this specific case, a quadratic variation law as in (7.1) has been applied for the generation of reference frequency signal. From the generated frequency, the reference angle ϑ_{ctrl}

implemented for the *dq* reference frame transformation is obtained as reported in the equation (7.2). The obtained reference angle signal is similar to the one showed in Figure 7.5.

$$f^* = kt^2 \tag{7.1}$$

$$\vartheta_{ctrl} = \int 2\pi f^* dt \tag{7.2}$$

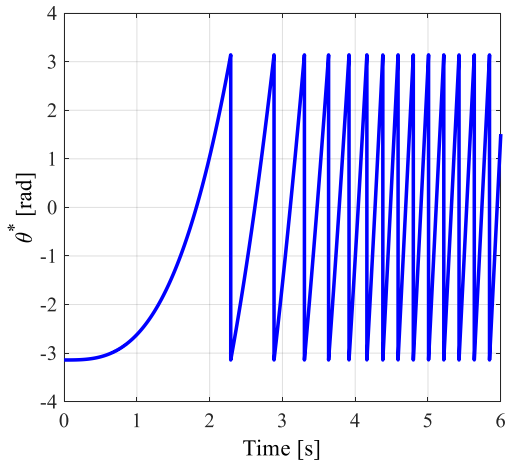


FIGURE 7.5 – REFERENCE ANGLE FOR I-F CONTROL SYSTEM

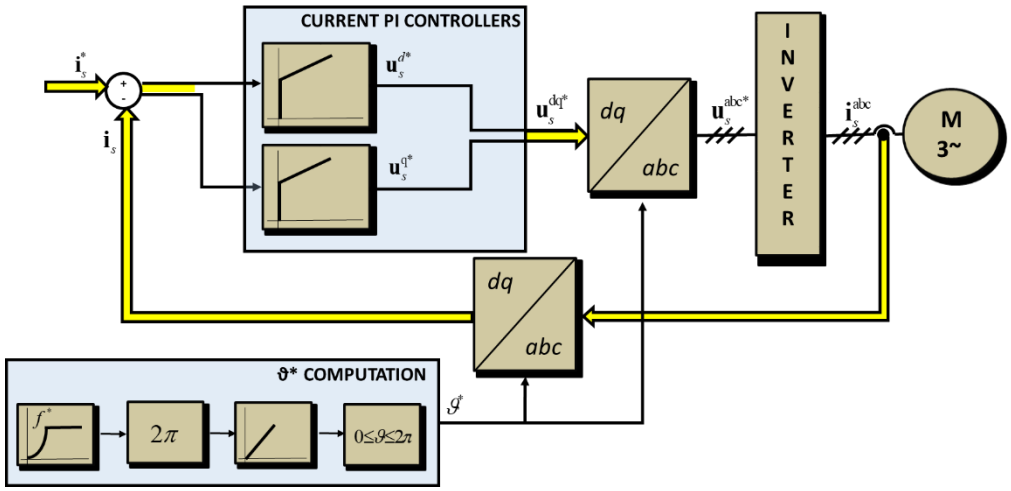


FIGURE 7.6 – CONTROL SCHEME OF THE INDUCTION CONICAL E-TAXIING MOTOR

The *I-f* control was preferred to the V/Hz open-loop control because it is possible to effectively adjust the current amplitude; the desired response to the current demand is obtained with a proper setting of the current PI controllers. When the motor reaches the synchronism, the frequency of the variables (i.e. the currents) corresponds to the frequency imposed by the *I-f* control, as emerges from Figure 7.7 where a current reference signal of 2.3*A* amplitude and a reference frequency

signal of 125*rad/s* (corresponding to 20*Hz*) has been generated. The use of this topology of control is particularly relevant in case of synchronous machines since the imposed frequency set the actual rotating speed of the motor. As demonstrated in Chapter 8 where the same control scheme is implemented for axial position estimation of the rotor, the reference frequency and the rotational velocity do not match because of the presence of the slip.

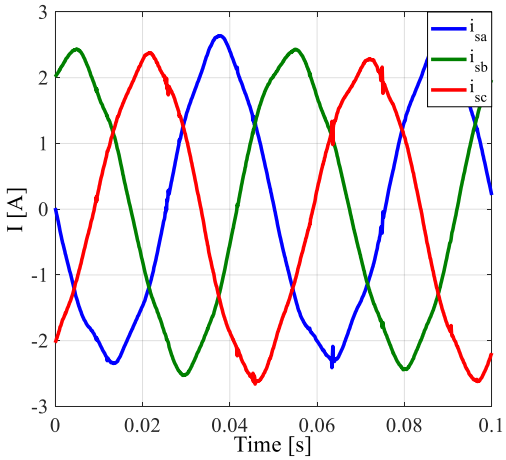


FIGURE 7.7 – MEASURED PHASE CURRENTS FOR I-F CONTROL

7.2.2 System Implementation with PMCM

The next step was to implement the system functioning with the PMCM developed in Chapter 5. The main challenge here is that while the induction conical machine has zero no-load axial force, the PMCM version envisages a constant presence of the axial force, due to the field generated by the magnets. This main dissimilarity between the two motor configurations led to a different motor control strategy for the mock-up system.

The main hardware of the test-rig for the PMCM remained exactly the same as that of the ICM. The control strategy for the PM conical machine also remained the same as in Figure 6.15. No modification of the taxiing strategy is applied when the PM conical motor is implemented. The substantial difference is in the management of the d-axis current in order to determine the axial movement. The axial movement of the induction conical rotor is obtained utilising the magnetising current of the motor. As demonstrated in Chapter 8, for the ICM, when the magnetising current reaches the rated value, engagement happens whereas when the magnetizing current is zero the motor stays disconnected. On

the contrary, for the PM conical machine, the movement is determined by the orientation and amplitude of the d-axis current. The disengagement and the engagement can be performed only decreasing and increasing respectively the d-axis current. This is the main reason that makes the use of rotary position sensor compulsory for PM conical machine. It is important to estimate the exact position of the synchronous reference frame in order to proceed to the motor axial control.

7.3 Chapter Highlights and Contribution to Research

The major achievements reached in this chapter are listed below:

1) Provided a real-world application for the conical machines that shows tangible benefits of the axial force and linear motion obtained in CMs.
2) Proposed a new electric taxiing system that avoids the use of the clutch and makes use of CMs.
3) Proposed a new system-level management of the E-Taxiing procedures when a CM E-Taxiing system is implemented.
4) Demonstrated the easy implementation of CMs for traction applications.
5) Demonstrated the use of conical machines for traction applications with two different technologies: induction and PMs.
6) Implemented a sensorless control scheme for the ICM that does not require any rotational position sensor.

7.4 Conclusion

In this Chapter, the conical E-Taxiing principle has been demonstrated on a small mock-up assembly. The complete implementation, as envisaged during the preliminary designing phase, has been accomplished with successful results. The motor has been connected to a small trailer wheel to prove the concept of the engagement and disengagement through the use of the d-axis current.

The concept has been proven on IM and PM conical motors, where for the ICM a sensorless control strategy for the motor control has been adopted.

Furthermore, for the induction conical machine, an external algorithm that can be implemented for the monitoring of the axial movement of the rotor has been developed. The algorithm is fully described in Chapter 8; it has been built and experimented on the induction conical machine as a parallel activity before the completion of the conical PM rotor. As demonstrated in the first part of Chapter 8, the monitoring scheme helps to increase the level of redundancy of the system. It is important, in fact, to guarantee that the ET motor is actually attached to the wheel before starting the taxi procedure whilst it is imperative ensuring that the motor is effectively detached from the LG every time take-off and landing occur.

Chapter 8
Sensorless Monitoring of Rotor Axial Position

In this Chapter an additional feature is added to the ETS mock-up realised with ICM in Chapter 7.

A customised algorithm is realised to monitor the rotor axial movement of the rotor inside the stator. The monitoring system makes use of a voltage injection technique, without including any sensor. This represents a great advantage for an aerospace application since the presence of a sensor can reduce the reliability of the entire system.

The position of the rotor is associated to the motor inductance variation. A complete mapping of the inductance is achieved locking the rotor at different axial positions through a purposely designed mechanical system.

The same mechanical arrangement is utilised to measure the axial force produced by the motor at different levels of current.

8.1 The Available ICM

The ICM utilized in Section 7.2.1 for the initial conical ET demonstrator, has been employed for further additional studies. In fact, the ICM corresponding to the configuration of [27] has been used for the development of a special sensorless control technique for determining the axial position of the rotor inside the stator. This study has been presented in [1, 2]. The sensorless monitoring algorithm has been implemented in the demonstrative prototype described in Section 7.2.1. This exercise has been completed in Avio Aero s.p.a. laboratories, where the sensorless *I-f* control for the ICM presented in Section 7.2.1 has been also realised and implemented. The system uses the same test-rig configuration presented in Section 6.2-B and shown in Figure 6.6.

Details about the induction conical motor are reported in Table 8.1.

TABLE 8.1 – ICM FEATURES

Quantity	*Symbol*	*Value*
Rated Current	I	$4.8A$
Rated Torque	T	$14.3Nm$
Rated Speed	n	$500rpm$
Rated Voltage – Wye Connection	V	$400V$
Number of Pole Pairs	p	6
Rated Frequency	f	$50Hz$
Number of Turns per Phase	N	588
Number of Stator Slots	N_s	36
Number of Phases	m	3
Stator Resistance	R_s	4.87Ω
Stator Transient Inductance	σL_s	$107.34mH$
Mechanical Air-gap	g	$1mm$
Max Stator Bore Radius	$r_{si,max}$	$62.75mm$
Min Stator Bore Radius	$r_{si,min}$	$42.5mm$
Active Length	l_{Fe}	$123mm$
Cone Angle	γ	$9.35°$
Maximum Axial Displacement	x	$4mm$

The winding configuration corresponds to the one of Figure 5.3 and Figure 5.4. Stator and rotor are displayed in Figure 8.1. The induction motor has an aluminium squirrel cage rotor. The rotor has a tapered shape with seven degrees of skewing of the bar.

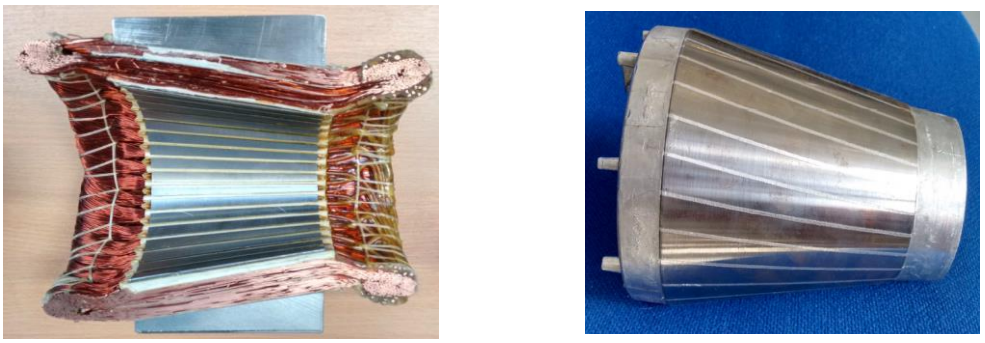


FIGURE 8.1 – ICM STATOR AND ROTOR

8.2 Axial Position Monitoring Procedure

An external algorithm has been implemented for the monitoring of the axial movement of the rotor of the induction conical machine. The algorithm has been built and experimented on the induction conical machine as a parallel activity before the completion of the conical PM rotor. In agreement with the plan established for secondment period in Bari, this study has been developed and tested in Avio Aero labs. The axial position observer has been realised without the use of any sensor; thus, its implementation within the conical ET system does not imply any allocation issues. The axial monitoring system is an additional measure of safety that should be implemented within the whole system in order to prove that the motor is correctly engaged to the wheel.

This task concerned with the control and monitoring aspects of the axial movement of the conical IM. Traditionally, linear positioning has always been achieved by the use of sensors such as for example linear encoders. However, for the ET application, this is not ideal as it would be increasing the component count. Apart from space limitations, the inherent fragility and low robustness of sensors can be a significant limiting factor, also due to the high level of vibration and temperature inside the LG [100]. A solution to this particular problem is to adopt a reliable and accurate sensor-less technique for axial position monitoring of the

conical motor, i.e. a transducer-less position monitoring methodology for the axial position of the conical IM.

Over the last decade, sensor-less techniques for electric machine control have become a common and robust [101] way to achieve high levels of reliability, especially where costs need to be reduced and the space allocated to the drive represents a compelling factor [102]; thus, for the application at hand, a proven sensor-less technique has been proposed and investigated for monitoring the rotor's axial position.

8.2.1 Monitoring System Rational

The axial position of the rotor can be estimated by using the motor itself as a sensor (self-sensing technique). In the proposed method, in fact, a traditional sensor-less technique, based on the exploitation of saliency due to the saturation of the main path [103-106] has been adopted. The axial position of the rotor inside the stator is evaluated by detecting changes in motor features with the axial rotor position. The proposed strategy takes advantage of the variation in the main magnetic circuit of the motor when the rotor is moving axially in and out of the stator. As the conical motor moves between full extension and full retraction, the air-gap length changes by the quantity calculated in (3.7). This means that the machine flux and its paths will also change according to the instantaneous axial position of the rotor. It is clear that the saturation levels in the machine will be in constant transients. The tendency of the motor to be saturated can be expressed by the inductance parameters. The magnetic saliency, defined as the variation in the stator inductance measured at motor terminals, quantifies the rate of change in the motor parameters due to saturation. The saturation effects have been tracked and made to relate to an appropriate parameter that represents the axial position of the rotor. This allowed for a sensor-less, position monitoring scheme to be implemented.

The High Frequency (HF) Injection Technique represents an efficient method to analyse the effect of saturation in the machine and track the magnetic saliency, especially in applications at zero or low speed [100, 104]. This methodology takes advantage of the interaction between the carrier signal excitation and the stator transient inductance to estimate machine parameters [103]. In fact,

saturation effects induced in the machine are capable to spatially modulate the quantity $\sigma\mathbf{L}_{S,}$ representing the stator transient inductance. The response of the motor to the carrier signal contains information about saliency. Namely, when a high-frequency voltage signal is injected (carrier voltage signal) the current response is demodulated and examined in order to gain this information. The carrier current response contains one positive and one negative sequence [107]. In this specific case, the negative sequence current has been monitored in order to assess the axial position of the motor.

As already anticipated in Chapter 7, for the ICM, the axial movement is realised by acting on the magnetising current, $\boldsymbol{i}_s^d$. The magnetizing current, in fact, produces the necessary magnetic force, responsible for the attraction between the rotor and the stator. The amplitude of the negative sequence current is strictly dependent on the magnetizing current. These two parameters are influential in determining the axial rotor position; thus, observing the negative counterpart of the high frequency current, for each level of the magnetizing current, and relating this quantity to the axial position of the rotor is the core aspect of the monitoring system.

8.2.2 The Basic Theory

In the proposed scheme, the ICM has been modelled in a similar manner as for rotational IMs, i.e. using space vectors. The voltage equations are expressed either in the time-dependent stationary reference frame $\alpha\beta$ as given in (8.1) and/or in the time-independent synchronous reference frame dq as described by (8.2), where subscripts S and R refer to stator and rotor quantities respectively, L_m is the magnetizing inductance, $\sigma\mathbf{L}_S$ is the stator transient inductance, ω_φ is the angular speed of rotor flux space vector λ_R and σ is the leakage factor as described by (8.3).

$$\mathbf{u}_s^{\alpha\beta} = R_s\mathbf{i}_s^{\alpha\beta} + \sigma\mathbf{L}_s\frac{d\mathbf{i}_s^{\alpha\beta}}{dt} + \frac{L_m}{L_R}\frac{d\boldsymbol{\lambda}_R}{dt} \tag{8.1}$$

$$\mathbf{u}_s^{dq} = R_s\mathbf{i}_s^{dq} + \sigma\mathbf{L}_s\frac{d\mathbf{i}_s^{dq}}{dt} + \frac{L_m}{L_R}\frac{d\boldsymbol{\lambda}_R}{dt} + j\omega_\varphi\sigma\mathbf{L}_s^{dq} + j\omega_R\frac{L_m}{L_R}\boldsymbol{\lambda}_R \tag{8.2}$$

$$\sigma = \frac{1 - L_m{}^2}{L_R L_s} \tag{8.3}$$

When the high-frequency carrier signal is superimposed on the fundamental excitation, the behaviour of the motor at high frequencies can be modelled as in (8.4). If the injection frequency ω_{Inj} is sufficiently higher than the fundamental frequency, then the voltage drop on the resistance can be neglected and the model can be approximated by using the stator transient inductance, as the carrier signal excitation is faster than the stator transient constant time [108-112].

$$\mathbf{u}_{shf}^{\alpha\beta} \cong j\omega_{Inj}\sigma\mathbf{L}_s^{\alpha\beta}\mathbf{i}_{shf}^{\alpha\beta} \tag{8.4}$$

The rotating high-frequency voltage $\boldsymbol{u}_{shf}^{\alpha\beta}$ is generated by injecting, in the stationary frame $\alpha\beta$, two continuous signals with same amplitude U_{Inj} and frequency ω_{Inj}. The injected signal, describing a circumference in the stationary reference frame, with radius equal to U_{Inj} and centre in the origin of the reference frame, is implemented in the following form:

$$\mathbf{u}_{shf}^{\alpha\beta} = \begin{bmatrix} u_{shf}^{\alpha} \\ u_{shf}^{\beta} \end{bmatrix} = U_{Inj}\begin{bmatrix} \cos\omega_{Inj}t \\ \sin\omega_{Inj}t \end{bmatrix} = U_{Inj}e^{j\omega_{Inj}t} \ . \tag{8.5}$$

The stator transient inductance, containing saturation-induced saliency, in the saliency synchronous reference frame can be represented as follow:

$$\sigma\mathbf{L}_s^{dq} = \begin{bmatrix} \sigma L_s^d & 0 \\ 0 & \sigma L_s^q \end{bmatrix} . \tag{8.6}$$

When transformed to the stationary (stator) reference frame, the stator transient inductance can be expressed as the sum of two quantities, as shown in (8.7), where ϑ_e is the angle of rotating saliency and where the average stator inductance $\sum\sigma\mathbf{L}_s$ and the differential stator transient inductance $\Delta\sigma\mathbf{L}_s$ are given in (8.8) and (8.9), respectively.

$$\sigma\mathbf{L}_S^{\alpha\beta} = \begin{bmatrix} \sum\sigma L_S + \Delta\sigma L_S\cos(2\vartheta_e) & -\Delta\sigma L_S\sin(2\vartheta_e) \\ -\Delta\sigma L_S\sin(2\vartheta_e) & \sum\sigma L_S - \Delta\sigma L_S\sin(2\vartheta_e) \end{bmatrix} \tag{8.7}$$

$$\sum\sigma L_s = \frac{\sigma L_s^q + \sigma L_s^d}{2} \tag{8.8}$$

$$\Delta\sigma L_s = \frac{\sigma L_s^q - \sigma L_s^d}{2} \tag{8.9}$$

Due to the interaction between the magnetic saliency and the voltage carrier signal, a carrier current signal $\boldsymbol{i}_{shf}^{\alpha\beta}$, with same the frequency of the injected voltage (ω_{Inj}), is induced in the stator. The high frequency currents signal consists of positive and negative sequence components and they can be summarized as in (8.10).

$$\mathbf{i}_{shf} = i_{sp} e^{j\omega_{inj}t} + \sum_m \sum_k i_{sn_{mk}} e^{-j(\omega_{inj}t + h_{mk}\vartheta_m)} \tag{8.10}$$

The negative sequence current arises from different topologies of saliency [113-115]. When the specific case of saturation saliency in correspondence of m_1=1 and $\vartheta_1=\omega_e t$ is considered [106], the total high-frequency current can be expressed in the stationary reference frame $\alpha\beta$ as shown in (8.11) and where I_p and I_n are the amplitudes of the positive and negative sequence, respectively, of the carrier current signal, as described in (8.12).

$$\begin{aligned} \mathbf{i}_{shf}^{\alpha\beta} &= \begin{bmatrix} i_{shf}^{\alpha} \\ i_{shf}^{\beta} \end{bmatrix} = \begin{bmatrix} I_p \cos\omega_{Inj}t + I_n \cos(2\vartheta_e - \omega_{Inj}t) \\ I_p \sin\omega_{Inj}t + I_n \sin(2\vartheta_e - \omega_{Inj}t) \end{bmatrix} = \\ &= I_p e^{j\omega_{Inj}t} + I_n e^{j(2\vartheta_e - \omega_{Inj}t)} = \mathbf{i}_p^{\alpha\beta} + \mathbf{i}_n^{\alpha\beta} \end{aligned} \tag{8.11}$$

$$\begin{aligned} I_p &= \frac{U_{Inj}}{\omega_{Inj}} \frac{\sum \sigma L_s}{\sum \sigma L_s^2 - \Delta\sigma L_s^2}; \\ I_n &= \frac{U_{Inj}}{\omega_{Inj}} \frac{\Delta\sigma L_s}{\sum \sigma L_s^2 - \Delta\sigma L_s^2} \end{aligned} \tag{8.12}$$

The positive sequence is proportional to the average stator transient inductance $\sum\sigma\mathbf{L_s}$ whereas the negative sequence of the carrier signal current is proportional to the differential stator inductance $\Delta\sigma\mathbf{L}_s$. When the motor moves from a completely disengaged position to fully engaged position, the magnetic saliency becomes more significant. The saturation effects due to the high-frequency injection are at a maximum when the stator and rotor are fully aligned. When moving from one position to another, both the average $\sum\sigma\mathbf{L_s}$ and the differential $\Delta\sigma\mathbf{L}_s$ stator inductances increase. However, $\Delta\sigma\mathbf{L}$ presents a considerably larger increment than the $\sum\sigma\mathbf{L_s}$. Due to its direct proportionality to $\Delta\sigma\mathbf{L}_s$ quantity, the

amplitude of the negative sequence signal I_n will represent the signal of interest for the axial position tracking.

It is important to note that the amplitude of both sequences is strictly dependent on the choice of the injection frequency. If the chosen injected frequency is too high, the amplitude of the high-frequency currents reduces; and thus, difficulties can be faced during the tracking procedure. On the other hand, if the injection frequency is very close to the speed and current control loop bandwidths, the performances of the control scheme will be affected. Practical understanding of these effects is given in the experimental Section 8.3.

8.2.3 Monitoring System Implementation

A. Filtering

From all the above it is clear that whilst the high-frequency negative-sequence component of the current will be used for the axial position computation, the fundamental frequency counterpart will operate as the feedback signal for the current control loop. Thus, before entering into the current control loop, the two components of the current need to be separated. The whole current signal is processed and demodulated, in order to isolate two different frequency levels of the current. This operation is implemented using two different topologies of filters.

The feedback current of the current control loop component is obtained excluding the injection frequency component of the current with a Notch Filter. The demodulation of the negative sequence carrier current can be achieved by shifting the negative-sequence to dc through the use of a new reference frame and attenuating the fundamental-frequency current component by means of a Low Pass Filter (LPF). Current carrier signal in the negative sequence synchronous frame is calculated as in (8.13). The entire filtering action has been implemented in a Simulink model that reproduces the block of Figure 8.2 designated as “Filtering and Demodulation” block.

$$\mathbf{i}_s^n = \mathbf{i}_{shf}^{\alpha\beta} e^{j(\omega_{Inj}t - 2\vartheta_e)} \tag{8.13}$$

In order to associate the axial position x to a certain amplitude of negative sequence signal I_n, a Look-Up Table (LUT) is has been created. However, since

the amplitude of I_n is strictly related to level of magnetising current ($\boldsymbol{i}_s^d$), a specific axial position will be determined by the level of $\boldsymbol{i}_s^d$ and I_n current in a 3D map.

$$x = f(\mathbf{i}_s^d, I_n) \tag{8.14}$$

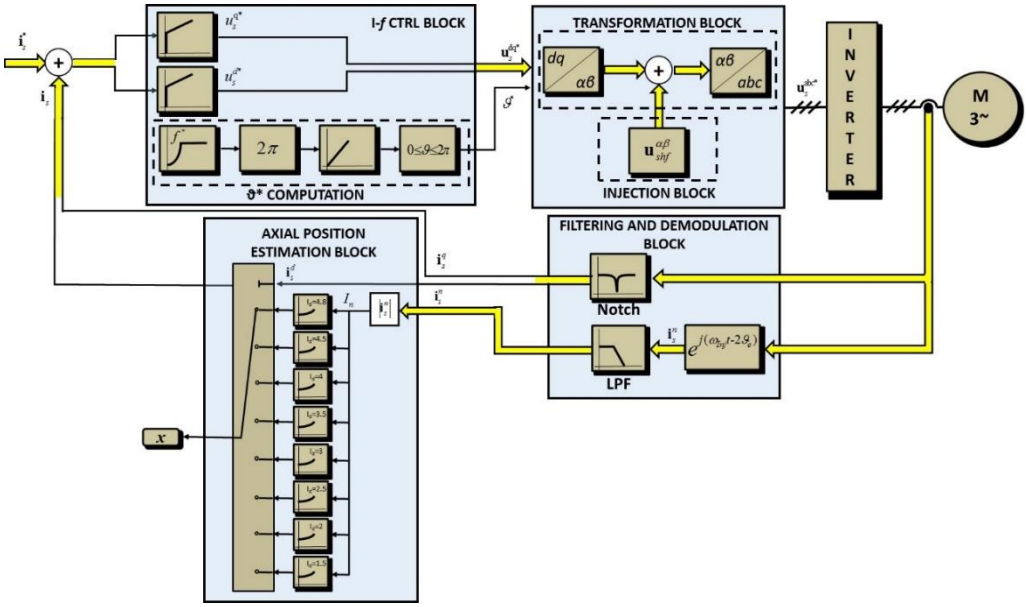


FIGURE 8.2 – AXIAL ESTIMATION AND CONTROL SCHEME

The LUT has three dimensions. Values of the negative sequence current amplitude have been estimated and recorded by using the mean value of the high-frequency current in the negative sequence reference frame, as computed in (8.15).

$$I_n = mean(|\mathbf{i}_s^n|) \tag{8.15}$$

This reiterative procedure has been executed for each position at each level of magnetising current in order to obtain a 3D LUT similar to the one reported in Figure 8.10 of the experimental section.

B. Implementation

The 3D LUT built through the mapping procedure can be also obtained from the interpolation between parallel planes (x, I_n) in which the magnetising current $\boldsymbol{i}_s^d$ represents a constant value and the axial position is obtained as function of the negative sequence signal amplitude I_n, as in (8.16).

$$x = f(\mathbf{i}_s^d, I_n) \rightarrow x = f(I_n)|_{\mathbf{i}_s^d} \tag{8.16}$$

Each (x, I_n) plane can be reported in a 2D LUT. The level of magnetising current, in this case, will be used for choosing between different 2D LUTs. Each 2D LUT will contain curves that relate the axial position to the amplitude of the negative sequence of the current. This strategy has been preferred in order to make the entire axial estimation procedure smoother and to have more accurate results. The scheme has been implemented in the "Axial Position Estimation Block" of Figure 8.2.

The 2D LUTs receives as input the output of the LPF of the filtering block of Figure 8.2. The system will choose the most appropriate 2D LUT standing on the measured values of the feedback magnetizing current signal (output of the Notch filter) and return the value of the axial position associated with the negative sequence signal reported in that specific 2D LUT.

8.3 Experimental Results

As already anticipated in Section 1.3, the ICM is equipped with a braking system, composed of a disk and a spring. In this configuration, the rotor is always disengaged from the stator (similar to a normally off condition) due to the presence of the spring. In correspondence of the rated current, the motor will develop an axial force able to overcome the spring thrust. The spring will be compressed and the rotor will align to the stator. The spring constant is equal to $6.67 N/mm^2$ and clearance from completely disengaged to completely engaged position is $4 mm$.

The real-time control of the motor has been realised with the same equipment mentioned in Section 6.2-B and described in Appendix B.

In order to build the axial estimation procedure, different topologies of tests have been carried out. Each of the experiment has the aim of separately developing the steps mentioned in Section 8.2.3 for the implementation of the final system.

8.3.1 Preliminary Experiments

A. High-Frequency Signal Selection

As mentioned in Section 8.2.2, frequency injection techniques depend heavily on the right choice of the signal to be injected. In order to select the most appropriate injection signal, several tests were performed on the machine with injected voltage on a range of frequencies from 500 to 1000*Hz* and different amplitudes. The tests consist in an exercise to estimate the rate of change of the negative-sequence of the carrier current signal when a magnetising current sequence of steps is applied. The magnetising current sequence increases until the engagement is reached. Starting from this point, a symmetrical decreasing sequence is performed for returning to the disengaged position (Figure 8.3). The rotor stays at the initial 0*mm* position until the rated current is reached, at which point the rotor moves to the 4*mm* extended position. The fully engaged position is maintained until the force of the spring prevails again: this happens when the magnetising current reaches values lower than 2*A*.

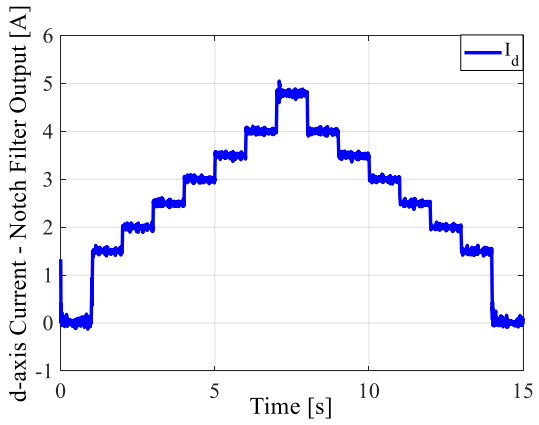


FIGURE 8.3 – MAGNETIZING CURRENT SEQUENCE

Using the same sequence, with different injection signals, levels of negative sequence current have been recorded by using (8.15) and processed by comparing the level of negative-sequence signals obtained with different injection frequencies. From these procedures, it was found that the better-performing operation points were for signals in the region of 500*Hz* voltage injection. An example has been reported in Figure 8.4, where the trends of I_n amplitude with a 500*Hz* and 1000*Hz* injected signals are displayed. The magnitude of I_n has been reported for each level of $\boldsymbol{i}_s^d$. The left-hand side graph

of Figure 8.4 represents the level of negative-sequence current before the engagement happens and the axial position is equal to 0*mm*; the values correspond to the first part of the magnetizing current sequence of Figure 8.3. On the right-hand side of Figure 8.4, experimental results are reported for the descending part of the magnetizing current sequence of Figure 8.3, when the rotor is in the extended position (4*mm*). The negative-sequence current amplitude with 500*Hz* injected voltage is two times greater than the one produced by using 1000*Hz* injected signal; this is particularly noticeable when the rotor is engaged. In the same way, the magnitude of the saturation- reflected signal increases for a signal injection at lower frequencies. This effect makes the tracking procedure of the negative sequence signal amplitude quite simpler. However, if the frequency is close to the current control loop frequency, some issues can be experienced in the regulation of the current.

Since the amplitude of the negative current results easier to monitor when a 500*Hz* signal is adopted, all the experiments have been conducted by injecting a 500*Hz*-120*V* voltage. The amplitude of the carrier signal has been selected in accordance with the converter ratings.

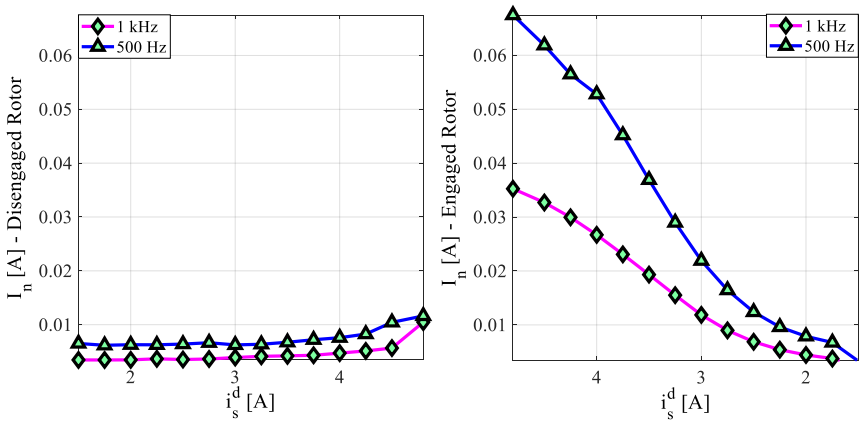


FIGURE 8.4 – I_N TRENDS WITH 500HZ AND 1000HZ INJECTED SIGNAL (ORIGINAL SPRING)

For sake of clarity, during the experiments, both sequences of positive and negative current have been recorded. From the results obtained using the selected voltage injection frequency, the high-frequency impedance of the machine has been calculated in case of positive and negative frequency of the injected signal (i.e. 500*Hz*) for different levels of magnetising current. The values of the impedance have been calculated and compared in case of both engaged and

disengaged rotor cases. Results are shown in the Figure 8.5 and Figure 8.6. As it can be observed from Figure 8.5 and Figure 8.6, in the case of the positive sequence, the values of the impedance for the disengaged and engaged rotor perfectly overlap. For the negative sequence, the trends of the impedance calculated with the rotor in disengaged position and engaged position are different. The impedance variation in the case of the negative frequency is more appreciable as the level of magnetising current increases and the effects of saturation become more significant. The different behaviours of the positive and negative impedance with respect to the axial position are associated with the values of the positive and negative sequence signals of the current. In Table 8.2, values of the negative current sequence are reported; the variation of the I_n current is a consequent effect of the impedance variation displayed in Figure 8.6.

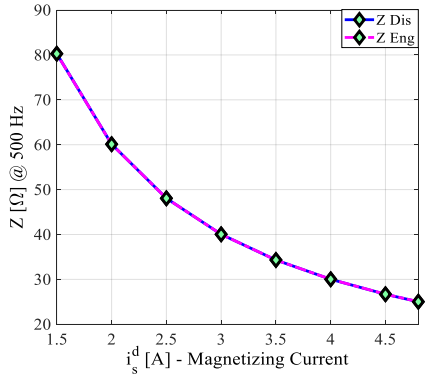


FIGURE 8.5 – IMPEDANCE CALCULATION AT POSITIVE FREQUENCY OF THE INJECTED SIGNAL

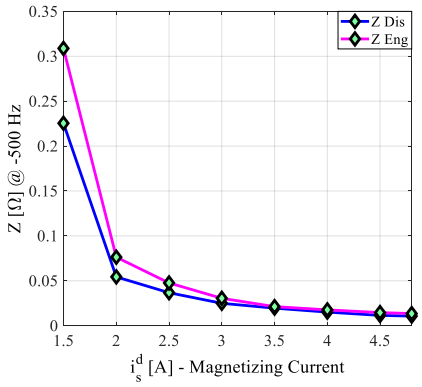


FIGURE 8.6 – IMPEDANCE CALCULATION AT NEGATIVE FREQUENCY OF THE INJECTED SIGNAL

TABLE 8.2 – MEASURED NEGATIVE-SEQUENCE OF CARRIER CURRENT SIGNAL AT DIFFERENT LEVEL OF MAGNETIZING CURRENT AND AXIAL ROTOR POSITION WITH 30% WEAKER SPRING

i_s^d	Rotor Axial Position - *x*								
	0*mm*	**0.5*mm***	**1*mm***	**1.5*mm***	**2*mm***	**2.5*mm***	**3*mm***	**3.5*mm***	**4*mm***
4.8A	0.0134	0.0138	0.0153	0.0163	0.0183	0.0193	0.0230	0.0266	0.0323
4.5A	0.0118	0.0121	0.0134	0.0141	0.0153	0.0156	0.0184	0.0215	0.0257
4.0A	0.0103	0.0103	0.0110	0.0116	0.0122	0.0128	0.0135	0.0154	0.0176
3.5A	0.0095	0.0096	0.0100	0.0100	0.0100	0.0101	0.0108	0.0119	0.0130
3.0A	0.0091	0.0093	0.0094	0.0096	0.0097	0.0099	0.0101	0.0102	0.0104
2.5A	0.0086	0.0086	0.0086	0.0086	0.0086	0.0087	0.0087	0.0087	0.0087
2.0A	0.0081	0.0081	0.0082	0.0082	0.0083	0.0084	0.0084	0.0085	0.0085
1.5A	0.0076	0.0077	0.0078	0.0079	0.0080	0.0081	0.0082	0.0083	0.0084

B. Filtering

The demodulation operation of (8.13) occurs within the "Filtering and Demodulation" block of the scheme reported in Figure 8.2. The output signal of the block represents the current in a reference frame synchronous with negative sequence signal. This signal has been filtered using a LPF with 70*dB* attenuation in correspondence of 500*Hz* (see magnitude response reported in Figure 8.7). Different filters have been designed with traditional methods (i.e. Butterworth) [116] and compared in order to reach the lowest level of noise in the output signal with the smallest delay time.

The Notch Filter, utilised for obtaining the current feedback deprived of the high-frequency signal, has been centred in correspondence of 500*Hz* as this represents the chosen injection frequency (Figure 8.8). The output of this filter is the input of the feedback signal of the current control loop.

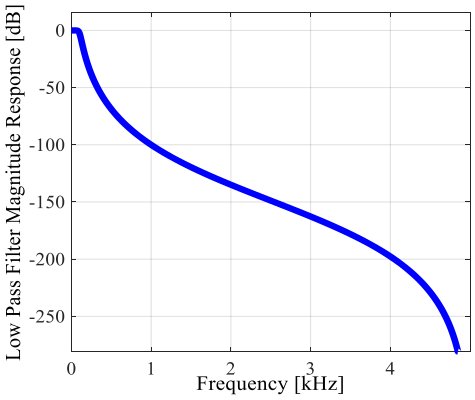


FIGURE 8.7 – LPF MAGNITUDE RESPONSE

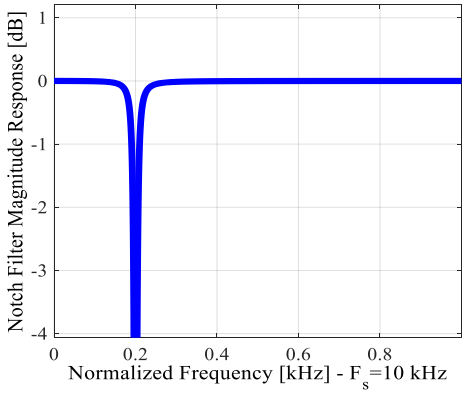


FIGURE 8.8 – NOTCH FILTER MAGNITUDE RESPONSE

C. Mapping and Implementation

The mapping procedure required a specific set of experiments. With the objective of evaluating the amplitude of the negative sequence for each level of magnetising current and each axial position, the rotor has been locked at different horizontal points using an end-stop plate in the test-rig configuration represented in Figure 8.9 and experimentally reproduced as displayed in Figure 8.19. The axial position has been set through a calibrated set of spacers. The spacers have a 0.5*mm* difference in length between each other. For each axial position, the level of negative sequence current has been monitored and registered using a

descending sequence of magnetising current, from the rated current down to zero. The values have been reported in a table similar to Table 8.2 and then transformed in the 3D LUT of Figure 8.10. Individually, the rows of Table 8.2 define the curves of Figure 8.11. They have been implemented separately in each of the 2D LUTs of the "Axial Position Estimation" block of the scheme reported in Figure 8.2. The curves define the axial position in relation to the level of the negative sequence of the carrier signal of the current.

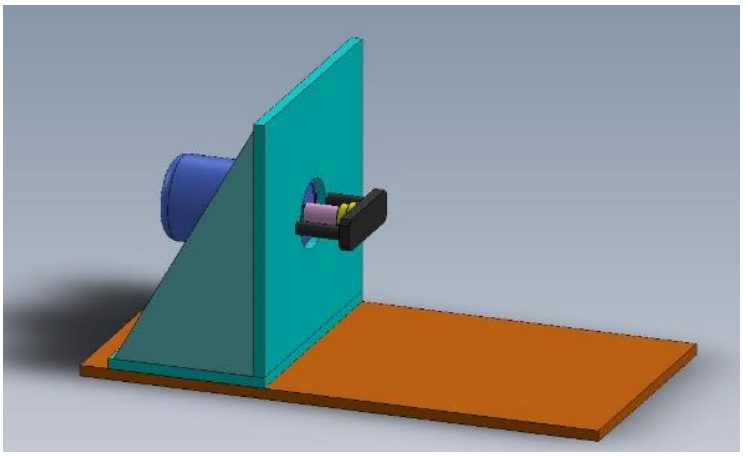


FIGURE 8.9 – END-STOP PLATE TEST-RIG CONFIGURATION

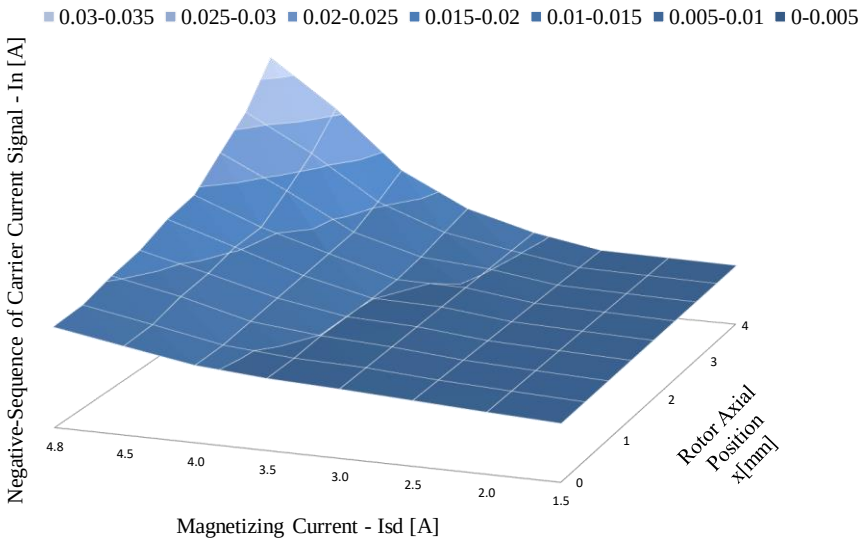


FIGURE 8.10 – 3D LUT WITH 30% WEAKER SPRING

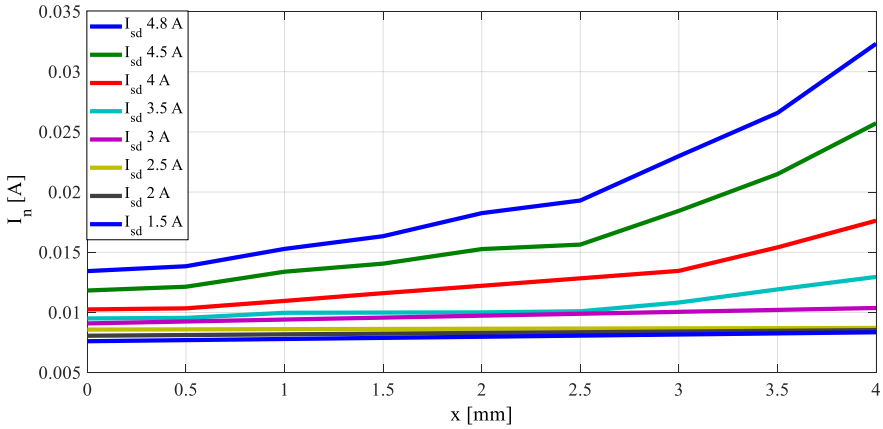


FIGURE 8.11 – I_N VS AXIAL POSITION CURVES FOR 2D LUT EXTRACTED FROM FIGURE 8.10

8.3.2 Monitoring Results

In order to verify the axial position estimation algorithm, tests at standstill and with the rotational movement have been conducted.

1) Test At standstill

At standstill, the frequency of monitored signal will correspond to the injected frequency (500*Hz*). In Figure 8.12, the spectrum of the current is reported and compared between two different cases: a) magnetising current of 2*A* and disengaged rotor, b) magnetising current of 4.8*A* (rated current) and rotor in engaged position.

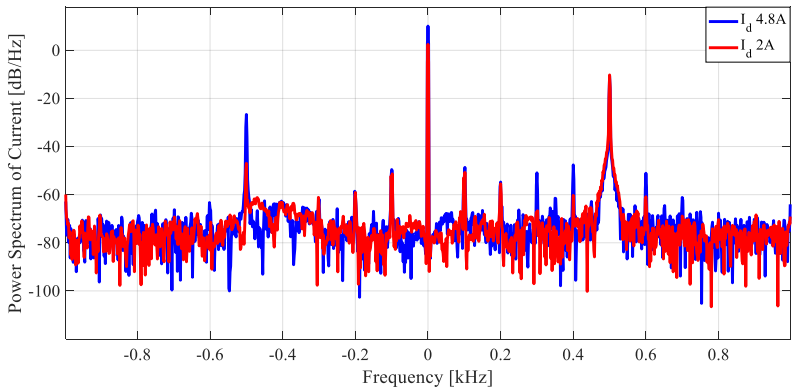


FIGURE 8.12 – SPECTRUM COMPARISON BETWEEN DISENGAGED AND ENGAGED POSITION

As proof that the negative counterpart of the carrier current signal is the best signal to be associated with axial position variation, amplitudes of the most evident harmonics have been recorded and compared during the engaging and disengaging phases. In correspondence of the frequency of negative-sequence, the maximum rate of variation has been recorded. Particularly, a difference of

up to 20*dB* in magnitude has been registered when current is lowered from 4.8*A* to 2*A* and rotor changes from engaged to disengaged position.

The I_n values, logged at standstill, were implemented in the axial position algorithm in order to check its consistency. When a sequence of magnetising current, similar to Figure 8.3, is introduced, negative-sequence current variations happen consistently. It was observed that, as expected, the magnitude of the negative sequence signal is related to the magnitude of the magnetising current. However, when the rated current is reached (last highest step of Figure 8.3), even though the magnetising current remains constant, an incremental step occurs in the negative-sequence signal. When the magnetising current value is equal to 4.8*A*, an axial force, comparable to the spring force, is then generated and thus axial displacement or movement of the rotor is achieved. For the operating conditions mentioned above (rated current and the spring), once engagement starts, a mechanical transient is observed in the magnetising current feedback signal of Figure 8.13. The machine reaches steady state in approximately 0.1*s*, as can be noticed in Figure 8.13. During the mechanical transient, the step in the negative-sequence current amplitude occurs (Figure 8.14). The output of the axial position estimation algorithm, in Figure 8.15, is able to track changes in the negative-sequence of the carrier current signal during this transitional phase. As it can be observed in Figure 8.14 and Figure 8.15, the negative-sequence current (output of the LPF) and the axial position show similar behaviours, as the axial position computational system has been optimised to be synchronised with changes in LPF current output.

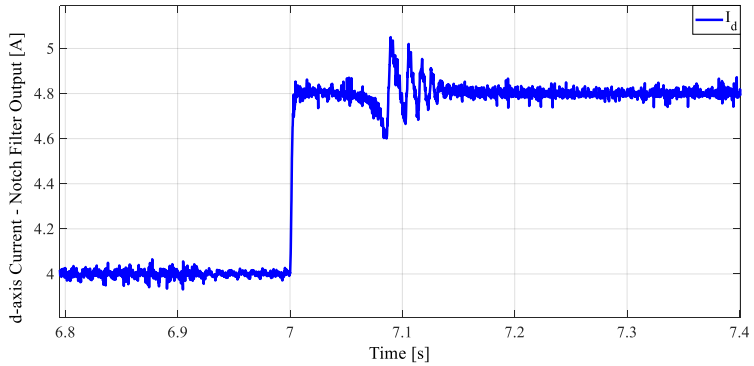


FIGURE 8.13 – TRANSIENT IN D-AXIS CURRENT

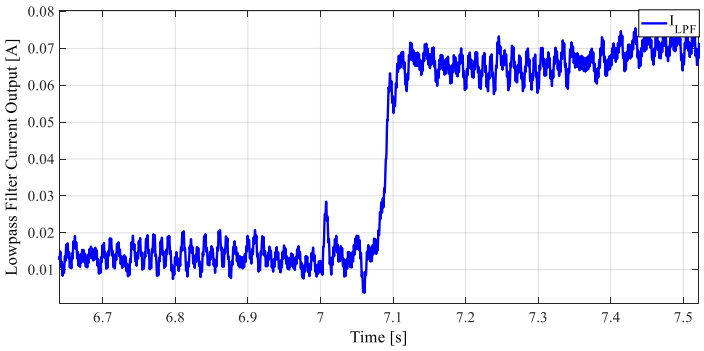


FIGURE 8.14 – LPF OUTPUT CURRENT (ORIGINAL SPRING)

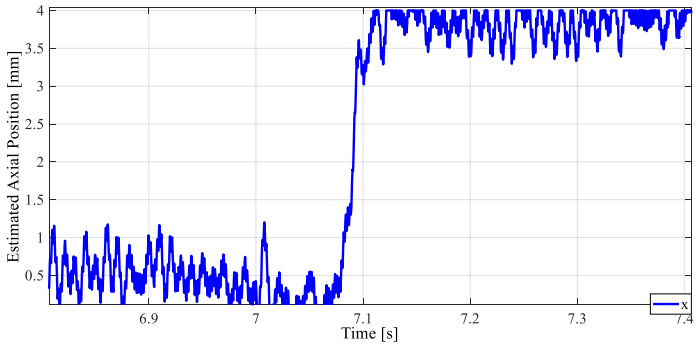


FIGURE 8.15 – AXIAL POSITION ESTIMATION

2) Test with Rotational Movement and weaker spring

Tests were performed having a rotational movement and axial movement simultaneously. The rotation has been generated without using any position transducer. Due to the translational operation, the normal functioning of an encoder or resolver would have been affected. The reference speed has been generated using the *I-f* control algorithm explained in Section 7.2.1 and implemented in the complete control scheme of Figure 8.2.

Figure 8.16 reports spectral analyses of the current in case of rotation. Low speed is applied (≈30*rad/s*). The current frequency is 5*Hz*. The negative sequence signal is monitored in correspondence of 490*Hz*. As already anticipated in Section 7.2.1, contrarily to the PM conical machine, when the *I-f* control is applied to the ICM, the reference frequency signal and the actual current frequency do not correspond. This is due to the presence of the slip.

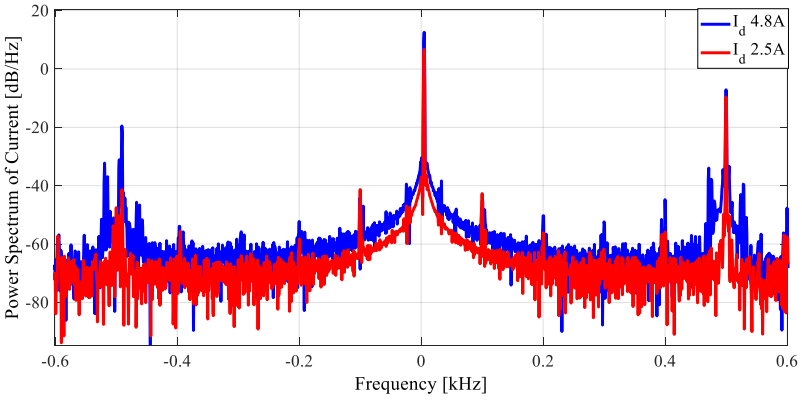


FIGURE 8.16 – SPECTRUM COMPARISON WITH I-F CTRL

During these tests, a different spring was used. The original spring has been replaced with a new one with 30% weaker linear coefficient spring rate (N/mm^2). The aim was to increase the time of the mechanical transient. From Figure 8.17, it can be noted that less magnetising current is needed to overcome the spring load and reach the fully engaged position. However, it is also true that with this new spring, the amplitude of the negative sequence current decreases and becomes difficult to track. Specifically, the LUT represented in Figure 8.10 and Table 8.2 have been built with the weaker spring. If compared with Figure 8.4 and Figure 8.18 (where the original spring was used), it can be noted that the registered values of I_n, in correspondence of 4.8A and 4mm, double.

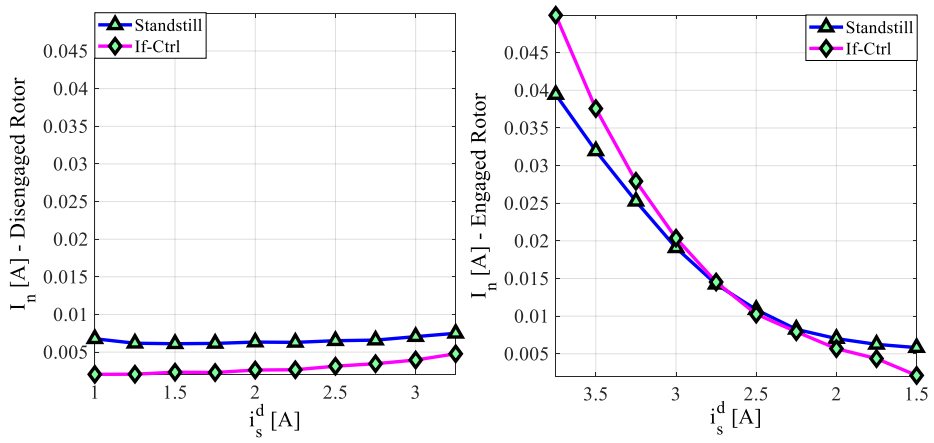


FIGURE 8.17 – I_N COMPARISON AT STANDSTILL AND ROTATION (30% WEAKER SPRING)

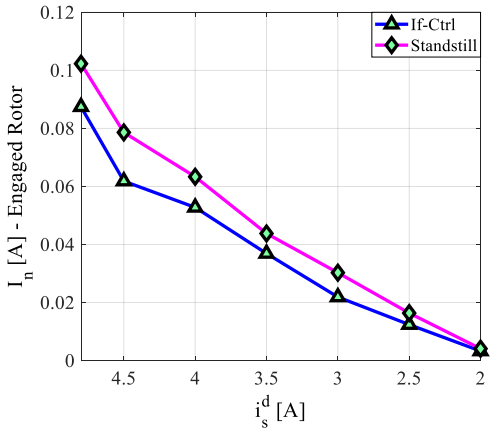


FIGURE 8.18 – I_N COMPARISON AT STANDSTILL AND ROTATION (ORIGINAL SPRING)

In both circumstances, when the trends of I_n, in case of rotation, are compared with the case at standstill minor differences are found. As a consequence, the LUT adopted during operations at standstill will be still valid in case of rotation. Figure 8.17 and Figure 8.18 show the measured values of I_n in case of rotational movement and standstill, respectively with weaker and original spring, where in both cases, the performances of the axial position algorithm are similar to those reported in Figure 8.15.

8.4 Axial Force Measurements

In order to prove the existing proportionality between the magnetising current and the axial force, in case of ICM, experiments were conducted using the configuration system illustrated in Figure 8.9. The axial force has been measured by locking the motor on each fixed axial position through the architected system explained in Section 8.3.1 - C. A load-cell has been glued on the end-stop plate as shown in Figure 8.19. The required magnetising current has been obtained through the current control loop PI regulator. At each level of magnetising current, the axial force exerted by the motor on the load-cell has been registered. Experimental data have been compared with results calculated analytically. The analytical results have been obtained following the method suggested in Section 4.5. However, it should be noted that in correspondence of zero current there is no axial force; this is due to the absence of magnets that determines the no-load contribution to the axial force calculation of equation (4.37). As observable from Figure 8.20, very good matching has been found between analytical and

experimental results, as a proof that the estimation procedure, using (4.37), returns reliable values.

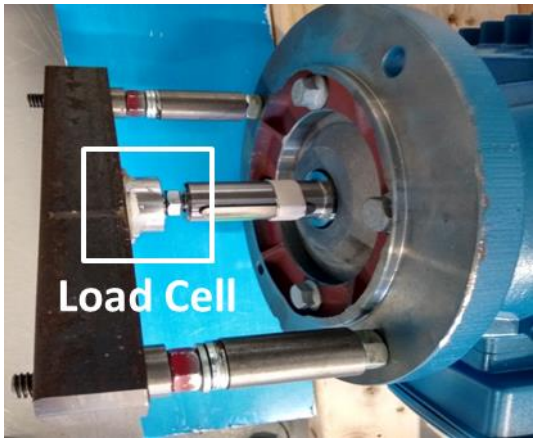


FIGURE 8.19 – END STOP PLATE WITH LOAD CELL

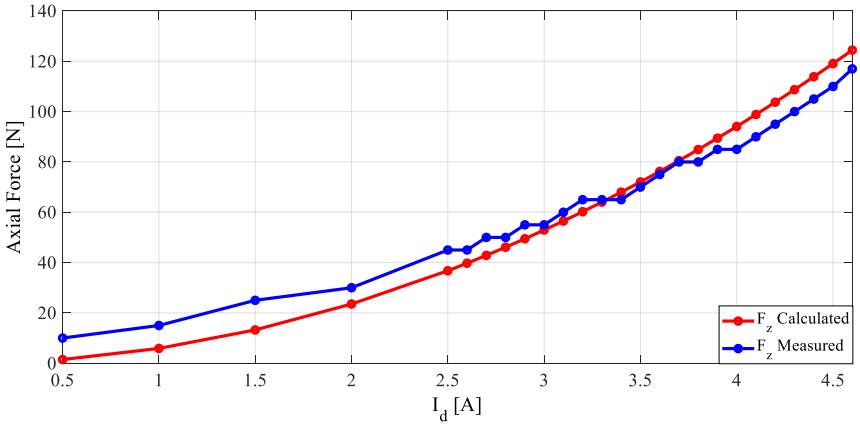


FIGURE 8.20 – ANALYTICAL VS EXPERIMENTAL AXIAL FORCE

8.5 Chapter Highlights and Contribution to Research

Main achievements of this Chapter can be reassumed as follow:

1) Realised a sensorless technique for monitoring the ICM rotor axial position, detailed in [96] [1].
2) Accomplished a complete mapping of the motor inductance variation with axial position.
3) Used common voltage injection techniques for a completely new application.
4) Developed a real-time monitoring system through the use of filtering actions.
5) Transformed the 3D inductance mapping of into a 2D problem that allows an easy system implementation.
6) Designed a mechanical arrangement for the axial force measurements.
7) Experimentally proven the calculation of axial force based on the motor d-axis current.

8.6 Conclusion

In this Chapter a novel way to use common and consolidated voltage injection techniques has been presented.

The motor inductance variation associated to the air-gap modification due to rotor axial movement has been rationalized and successively proven through an experimental set-up.

The axial force has been measured at different levels of d-axis current. Results have been compared against the analytical axial force predicted using the theory exposed in Section 4.5. Experimental and analytical measurements showed a very good matching proving the validity of the calculation of the axial force with current when proposed simplification assumptions are used.

The entire algorithm could be developed further for the development of a closed-loop sensorless control of the axial position achieved acting on the magnetizing current of the ICM.

Chapter 9
Conclusion

In this Chapter, the main outcomes of the work described in this thesis are outlined. The main conclusions for each critical point of the work are drawn, with particular reference to a) the 2D modelling of the CM, b) the performances of the ICM and PMCM, c) the comparison between the cylindrical and conical motors and d) the proposed application for the PMCM.

The Chapter concludes with a summary of the main contributions to research and some suggestions about further investigations that can be accomplished as the prosecution of the study undertaken in this research work.

9.1 Overview of the Work

9.1.1 2D Approach for Analyses and Design of CMs

While the shape of the conical machines and the presence of an extra component of the force and of an additional degree of freedom makes the PMCM significantly different from conventional machines, however, the emphasis in this work of the thesis has been placed on their similarities. The whole design procedure discussed in Chapter 3 hinges on the formulation of an equivalent model that allows the use of a pseudo-conventional approach for the design and the analyses of conical machines.

The classical torque per volume equation can be employed for the preliminary sizing procedure, if the concepts of an equivalent axial length and mean radius are implemented in the calculations. The magnetic circuit has been built based on these two concepts. In parallel to the numerical equivalent model, a simplified equivalent FE model has been suggested. This proposes the use of a stack of cylindrical machines appropriately sized in order to recreate the cone shape. The formulated FE approach has been rationalized and validated in Section 3.3 through a 3D FE study conducted on a simplified conical motor. The combination of the equivalent analytical model and the equivalent 2D FEM led to the numerical formulation of the forces generated by the conical machine with the main objective of quantifying the axial force produced by the motor, where the determination of the horizontal force is essential for accessing the axial displacement and dimensioning the mechanical system of the conical motor. As explained in Section 3.5, forces can be derived from the MST calculated at the stator bore. The 3D MST can be recreated from the 2D FE equivalent model using the flux density of one of the motors included in the equivalent model.

The presented approach has been validated in Chapter 4. In Section 4.2, in fact, the analytical computation of the force and torque first developed in Chapter 3 has been adopted for the conical version of the benchmark conventional machine and the results have been compared with the values obtained from the equivalent FEM. The 2D FEM of the conical motor has been created using three cylindrical sub-motors, whose dimensions have been computed as in Section 4.2.2. A considerable level of consistency between the analytical and the FE results

exists, if the motors are constructed following the suggestions presented in Section 4.4.1. As reported in Figure 9.1, only 4.23% difference exists between the torque calculate using the 2D FEM and the numerical method. However, as explained in 4.4.1, a more accurate approximation can be obtained by increasing the number of sub-motors as described by (4.31) and studied in [88].

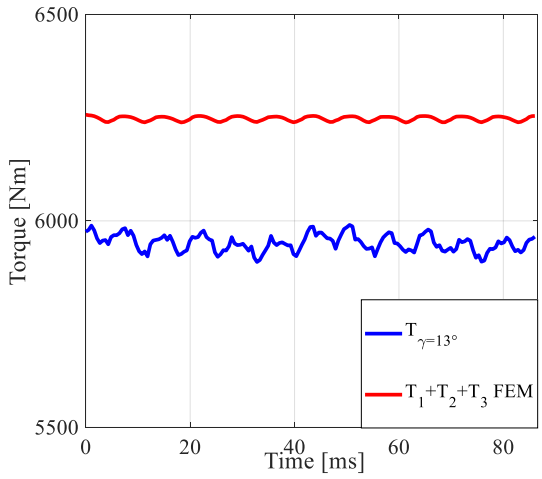


FIGURE 9.1 – ANALYTICAL VS FEM TORQUE COMPUTATION

9.1.2 Single-Sided PMCM Advantages

The theoretical journey outlined above converged into a physical demonstration. A small-scale prototype of a PMCM has been realized. The rotor configuration of this prototype has been chosen relative to a combination of "off-the-shelf" magnets and the need to attain the best quality of torque. The equivalent model of the PM conical demonstrator has been built in Chapter 5 using six cylindrical motors. An excellent compatibility between the numerical and the experimental results was reported in Chapter 6. The determination of the no-load axial force represented an important step for the PM conical machine design (the no-load axial force is the distinguishing element between IM and PM conical motor). The mechanical system, in fact, must be able to contrast the no-load axial force produced by the magnets when no current is applied. This has been achieved in Section 5.7 where a strong spring has been purposely calibrated to handle the no-load horizontal force component.

In Chapter 6, the control of the motor for both movements (rotational and linear) has been experimentally implemented, showing the possibility to regulate the axial actuation through the d-axis current and, separately, use the q-axis to spin

the machine and obtain the demanded level of torque. Comparing the performances obtained with the PM conical demonstrator and the specifics provided for the available induction conical motor, described in Chapter 8, it is clear that, with the same configuration, a higher level of torque can be achieved using the PM technology. However, since the forces produced by the PM conical machine are higher, the axial force produced by the PM conical motor, synonymous with the better magnetic circuit utilisation, increases as well. Thus, a smaller cone angle can be selected to achieve the required linear actuation, which is, of course, one of the more important benefits of having a higher performing system in terms of torque production. A small cone angle implies less reduction of the rotor volume (with the respect to a cylindrical machine), thus even better performances in terms of torque.

Based on the experiments conducted on the custom-built PMCM, in Chapter 6, and the commercial ICM, in Chapter 8, some important considerations emerge when comparing the proposed new technology of single-sided CM (PM) with the existing one (IM). As summarised in Table 9.1, besides the higher performances in terms of torque offered by the PMCM, the other main advantage is the possibility to move the motor in both directions using field-weakening techniques. This implies more flexibility in the use of PMCM. The motor, in fact, could be used for specific applications where the rotor works in a continuously engaged condition and then it can be temporarily retracted using a specific control technique. This is not possible in ICMs, where the rotor is always retracted if the system is not powered. The proposed different employment of the PMSM requires extra-effort in control techniques that need to be specifically developed for the considered application. This is particularly true for high-speed applications where the demagnetization effect of the speed needs to be compensated through the d-axis current, as demonstrated in Section 6.4.2.

Despite the initial concerns about to the presence of the no-load axial force due to the magnets, this work has shown that no extra-effort is required for the mechanical system design for a PMCM with respect to an ICM. As shown in Section 5.7, for a PMCM the mechanical system is calibrated based on the axial forces developed by the magnets in the same way as for an ICM where this is

realised by considering the axial force developed by the rated magnetizing current.

TABLE 9.1 – ICM VS PMCM QUALITATIVE COMPARISON

	ICM	PMCM
Linear Control in Both Directions	-	✓
No-Load Axial Force	-	✓
Mechanical Design	+	+
Motor Control	++	+
Performances	+	+++

9.1.3 Cylindrical versus Conical Machines

The basic idea behind this research work is that, potentially, any PM synchronous motor can be turned into a conical machine to produce an axial force that, in turns, causes the horizontal movement of the rotor. This concept emerges in Chapter 4, where an existing high performing machine was selected and a conical equivalent achieved. The main challenge here was to evaluate the level of reduction of the motor performances when this operation is accomplished. The configuration of the cylindrical actuator, formerly optimized to fulfil customers' specifications reported in Table 4.1, has been maintained for this specific study. The 2D FEM of the cylindrical actuator that has been built to reproduce the original cylindrical design is presented in Section 4.1.1. In Section 4.1.2, further analyses have been conducted to investigate the forces acting on the machine. From the force calculation based on the MST proposed in Section 3.5, the analytical computation of the torque has been accomplished. These studies led the way for the evaluation of the conical actuator performances conducted in Section 4.2. The forces calculated on the cylindrical actuator, in fact, were estimated considering a null cone angle in the formulae suggested in Chapter 3. This proved the validity of the analytical method for the force estimation also in the case of cylindrical machines.

From the comparison between the high-performance cylindrical machine and its conical counterpart reported in Section 4.3, only a 10.35% of torque reduction has been recorded while the other motor properties maintained the achieved wave-form shape with a small reduction in the amplitude of the signals, as summarized in Table 9.2.

TABLE 9.2 – CYLINDRICAL VS CONICAL MOTOR PERFORMANCES

Quantity	PM Cylindrical Motor	PM Conical Motor
No-Load Voltage	$46.23V_{rms}$	$42.97V_{rms}$
No-Load Flux	$0.64Wb_{rms}$	$0.60Wb_{rms}$
Cogging Torque	$8.7Nm_{pk}$	$5.7Nm_{pk}$
Torque	$7kNm_{pk}$	$6.3kNm_{pk}$
Torque Ripple	0.7%	0.3%

As can be observed in all the above, the main ambition for the introduction of conical actuator concept is the effort to maintain the performances achieved with the optimized cylindrical configuration whilst producing a sufficient axial force to move the rotor horizontally. Inevitably, the smaller dimensions of the rotor cause a reduction of the delivered torque. The diminution of the torque is related to the cone angle. In Chapter 4, a relatively wide cone angle has been employed to show appreciable effects on the torque and the axial force. However, due to the presence of the strong magnets, as demonstrated through the studies conducted in Chapter 6 on the PMCM demonstrator, a considerable level of axial force can be obtained with a smaller cone angle. As demonstrated in Section 4.4.3, the torque reduction can be limited to the desired value during the optimization procedure of the conical machine using (4.34). The cone angle selected through this procedure can be successively used to verify if the amount of axial force obtained with the chosen taper is sufficient for the required axial motion.

9.1.4 Applicability of PMCM

To prove that the conical machine is not simply an abstract concept and to demonstrate its valuable impact on the traction systems, in Chapter 7, a real application has been specifically identified for this motor. The application in hand is the electric-taxiing application (largely commented in Chapter 2). Among the different electric-taxiing system arrangements analysed in Section 2.1, the direct-drive solution designed at the UoN represents the best achievement in terms of torque density. However, as underlined in Section 2.1, the amount of delivered torque does not represent the only requirement to observe for the electric-taxiing implementation, in fact, reliability is an equivalently restrictive parameter. The current direct-drive electric-taxiing scheme incurs the risk of high voltages induced in the motor during landing and take-off. Three different solutions to this problem have been presented and compared in Section 2.2.

In this part of the thesis, an innovative idea for the development of the "second generation" of the e-taxiing actuator realized at UoN has been presented. The employment of the conical motor as the actuator in the electric-taxiing system resulted to be a very appealing solution to the technical difficulties addressed in direct-drive configuration, exposed in Section 2.1.1. The main advantage offered by the introduction of such a motor is the accomplishment of the engagement and disengagement of the rotor from the wheel during the critical stages mentioned above without using any extra added component. The conical motor, in fact, exploits the generation of the axial force on the rotor conical surface to attach and detach the motor from the wheel when needed. In this way, the level of compactness obtained through the direct-drive solution can be combined with advantages of having a disengaging system without the involvement of any other mechanical device.

The main figure of merit of the E-Taxiing conical configuration can be summarised as follow:

- Enhancement of the reliability of the system; no risk of high-voltage exists.

- The risk of jamming in the mechanical parts is avoided since no gear system is involved.
- Lighter and compact solution, compared to the geared version of the ETS.

The conical actuator has been implemented in a system mock-up where the motor is attached and detached from a small trailer wheel. The system has been tested with both induction and PM conical motors. A new control strategy has been proposed and employed for both machines. When the motor is inactive, the rotor is held in the retracted position by a spring positioned on the rotor shaft. The axial spring force is contrasted using the d-axis current in order to attach and detached the motor. For the ICM a sensorless control scheme has been implemented, as illustrated in Section 7.2.1. An additional sensorless axial position estimation tool has been realised for the IM conical motor as explained in Chapter 8. The rotational movement is guaranteed through the implementation of the open-loop control that acts on the current amplitude and frequency of the machine, as illustrated in Figure 7.6. For the PM version of the conical e-taxiing, the current, speed and axial control strategies, exposed in Section 6.4, have been implemented. An easy and smooth transition from engaged to disengaged position even when the rotor is contemporary spinning has been experienced in both cases.

9.2 Main Contributions to Research

The work presented in this thesis and actualized through the realization of a small prototype contributed to enhance the state-of-the-art of conical motors. As stated in Section 1.1 and proven in the literature review exercise presented in Section 1.3, no previous technology that envisages the presence of single-sided PM conical motor has been found. The studies and experiments conducted for the analyses of the PM conical machines and the evaluation of the forces acting in electrical motors are summarised in the list below; the following points represent the major contributions to the research for the design and implementation of conical PM motors.

a) *Formulation of 3D MST for the conical machine with the analytical computation of the third dimension from a 2D equivalent model.*

A simple 3D FE conical model has been realized to demonstrate that the flux density does not vary along the axial length; the axial flux density can be analytically calculated from the radial flux density, knowing the cone angle.

b) *Formulation of the 2D FEM for the analyses of conical motors to be preferred to three-dimensional studies.*

The model utilizes several cylindrical machines to recreate the cone volume. The assumptions validated at point a) legitimate the adoption of the superimposition principle for the calculation of the total torque and axial force; these quantities have been obtained as the sum of effects of the concentric cylindrical motors.

c) *Analytical computation of the torque and force exploiting one symmetry of a magnetically balanced motor*.

This concept has been illustrated within the analytical computation of the torque and axial force on a cylindrical configuration in which the sum of the radial stress on the rotor surface approaches to zero.

d) *Formulation of the forces in conical motors using equivalent motor dimensions and the stress produced by a corresponding cylindrical machine.*

This process has been demonstrated proving that the flux density in the conical and the cylindrical motors do not differ.

e) *Implementation and control of the conical motor without the use of any sensor.*

An open-loop technique has been applied for the control the conical motor. The motor is controlled independently on d and q axes, proving that the decoupling theory is still valid for this topology of machines.

f) Implementation of a rotational and linear actuation control for a single-ended PM conical machine.

The control strategy is able to compensate the effect of the axial force produced by the magnets.

g) Realization of a sensorless axial monitoring algorithm that envisages the injection of high-frequency signals for the estimation of the horizontal position of the rotor.

9.3 Future Work

Due to the novelty of the topic, a number of technical areas related to the conical machines remained unexplored. Hereafter some open-questions related to further developments of a single-ended conical machine have been highlighted.

The main studies proposed as the scientific prosecution of the present work are listed as follows.

a) Find an optimization strategy for the conical machines, using the formula suggested in (4.34), that includes the cone angle in the list of variables employed for the common design of the cylindrical motors. Quantify the axial force with regard to the entire system configuration and relate the magnet field, thus the magnet thickness, and the cone angle to the amount of delivered force.
b) Define a method to identify the right number of cylindrical motors that approximate properly the conical machine behaviour with the 2D equivalent model.
c) Define a model of the motor that includes the variation of the inductance with the axial position of the rotor; the aim is to realize a closed loop control of the axial position as a continuation of axial monitoring algorithm development.
d) Evaluate the effect that the q-axis current has with the speed on the axial force and optimize the control strategy in order to compensate this effect using the d-axis current and the axial position control.

REFERENCES

[1] S. Roggia, F. Cupertino, C. Gerada, and M. Galea, "A two degrees of freedom system for wheel traction applications," *IEEE Transactions on Industrial Electronics*, vol. 65, pp. 4483-4491, 2017.

[2] S. Roggia, F. Cupertino, M. Galea, and C. Gerada, "Axial position estimation of conical shaped motor for electric taxiing application," presented at the IEEE Energy Conversion Congress and Expo (ECCE), Milwaukee, WI, 2016.

[3] S. Roggia, F. Cupertino, C. Gerada, and M. Galea, "Axial position estimation of conical shaped motors for aerospace traction applications," *IEEE Transactions on Industry Applications,* vol. 53, pp. 5405 - 5414, 2017.

[4] K. Asano, Y. Inaguma, H. Ohtani, E. Sato, M. Okamura, and S. Sasaki, "High performance motor drive technologies for hybrid vehicles," in *2007 Power Conversion Conference - Nagoya*, 2007, pp. 1584-1589.

[5] P. Lazari, J. Wang, and L. Chen, "A computationally efficient design technique for electric-vehicle traction machines," *IEEE Transactions on Industry Applications*, vol. 50, pp. 3203-3213, 2014.

[6] T. Raminosoa, T. Hamiti, M. Galea, and C. Gerada, "Feasibility and electromagnetic design of direct drive wheel actuator for green taxiing," in *2011 IEEE Energy Conversion Congress and Exposition*, 2011, pp. 2798-2804.

[7] A. Boglietti, A. Cavagnino, A. Tenconi, S. Vaschetto, and P. d. Torino, "The safety critical electric machines and drives in the more electric aircraft: A survey," in *2009 35th Annual Conference of IEEE Industrial Electronics*, 2009, pp. 2587-2594.

[8] M. Galea, "High performance, direct drive machines for aerospace applications," Doctor of Philosophy, Electrical and Electronic Engineering, The University of Nottingham, 2013.

[9] B. Deok-je, H. Polinder, G. Shrestha, and J. A. Ferreira, "Comparative design of radial and transverse flux PM generators for direct-drive wind turbines," in *Electrical Machines, 2008. ICEM 2008. 18th International Conference on*, 2008, pp. 1-6.

[10] B. Deok-je and H. Polinder, "Design of transverse flux permanent magnet machines for large direct-drive wind turbines," Master, Electrical Engineering, Pukyong National University, 2010.

[11] Z. Rahman, "Evaluating radial, axial and transverse flux topologies for 'in-wheel' motor," in *Power Electronics in Transportation (IEEE Cat. No.04TH8756)*, 2004, pp. 75-81.

[12] J. F. Gieras, "Performance characteristics of a transverse flux generator," in *IEEE International Conference on Electric Machines and Drives, 2005.*, 2005, pp. 1293-1299.

[13] J. F. Gieras, "Transverse flux machine," ed: Google Patents, 2010.

[14] J. F. Gieras, *Permanent Magnet Motor Technology: Design and Applications, Third Edition*: CRC Press, 2011.

[15] M. J. Melfi, S. Evon, and R. McElveen, "Permanent magnet motors for power density and energy savings in industrial applications," in

Conference Record of 2008 54th Annual Pulp and Paper Industry Technical Conference, 2008, pp. 218-225.

[16] A. Vagati, G. Pellegrino, and P. Guglielmi, "Comparison between SPM and IPM motor drives for EV application," in *Electrical Machines (ICEM), 2010 XIX International Conference on*, 2010, pp. 1-6.

[17] G. Pellegrino, A. Vagati, P. Guglielmi, and B. Boazzo, "Performance comparison between surface-mounted and interior PM motor drives for electric vehicle application," *IEEE Transactions on Industrial Electronics*, vol. 59, pp. 803-811, 2012.

[18] T. Raminosoa, C. Gerada, N. Othman, and L. D. Lillo, "Rotor losses in fault-tolerant permanent magnet synchronous machines," *IET Electric Power Applications*, vol. 5, pp. 75-88, 2011.

[19] D. Gerada, A. Mebarki, R. P. Mokhadkar, N. L. Brown, and C. Gerada, "Design issues of high-speed permanent magnet machines for high-temperature applications," in *Electric Machines and Drives Conference, 2009. IEMDC '09. IEEE International*, 2009, pp. 1036-1042.

[20] H. Bitsch and H. Mall, "Sliding rotor motor," ed: Google Patents, 1992.

[21] B. C. Guo, Y. K. Huang, Y. G. Guo, and J. G. Zhu, "Thermal analysis of the conical rotor motor using LPTN combined with fluid simulation," in *2015 IEEE International Conference on Applied Superconductivity and Electromagnetic Devices (ASEMD)*, 2015, pp. 128-129.

[22] B. Guo, Y. Huang, J. Dong, and T. Zhou, "Transient thermal analysis of the conical rotor motor using LPTN and Finite Volume Method," in *2015 IEEE Magnetics Conference (INTERMAG)*, 2015, pp. 1-1.

[23] P. Kascak, R. Jansen, T. Dever, A. Nagorny, and K. Loparo, "Motoring performance of a conical pole-pair separated bearingless electric machine," in *Energytech, 2011 IEEE*, 2011, pp. 1-6.

[24] G. Munteanu, A. Binder, and S. Dewenter, "Five-axis magnetic suspension with two conical air gap bearingless PM synchronous half-motors," in *Power Electronics, Electrical Drives, Automation and Motion (SPEEDAM), 2012 International Symposium on*, 2012, pp. 1246-1251.

[25] W. Ding, L. Liu, and J. Lou, "Design and control of a high-speed switched reluctance machine with conical magnetic bearings for aircraft application," *IET Electric Power Applications*, vol. 7, pp. 179-190, 2013.

[26] A. M. Mohamed and F. P. Emad, "Conical magnetic bearings with radial and thrust control," in *Decision and Control, 1989., Proceedings of the 28th IEEE Conference on*, 1989, pp. 554-561 vol.1.

[27] Demag. (2016). *Demag Conical-rotor brake motors*. Available: http://www.demagcranes.co.uk/Drives/Motors/Conical-rotor-brake-motors

[28] M. B. Priebe. (2016) Exciting MEA Plane Designs via Thermal Management, Electric Components, and More - New MEA Plane Designs & Interview with Safran Engineering. *MEA - SPECIAL*.

[29] J. C. Shaw, S. D. A. Fletcher, P. J. Norman, and S. J. Galloway, "More electric power system concepts for an environmentally responsible aircraft," in *2012 47th International Universities Power Engineering Conference (UPEC)*, 2012, pp. 1-6.

[30] ACARE. (2016). *ACARE Flightpath 2050 - Europe's Vision for Aviation*. Available: http://www.acare4europe.com/documents/latest-acare-documents/acare-flightpath-2050

[31] J. A. Rosero, J. A. Ortega, E. Aldabas, and L. Romeral, "Moving towards a more electric aircraft," *IEEE Aerospace and Electronic Systems Magazine*, vol. 22, pp. 3-9, 2007.

[32] J. A. Weimer, "The role of electric machines and drives in the more electric aircraft," in *Electric Machines and Drives Conference, 2003. IEMDC'03. IEEE International*, 2003, pp. 11-15 vol.1.

[33] W. Cao, B. C. Mecrow, G. J. Atkinson, J. W. Bennett, and D. J. Atkinson, "Overview of electric motor technologies used for More Electric Aircraft (MEA)," *IEEE Transactions on Industrial Electronics*, vol. 59, pp. 3523-3531, 2012.

[34] B. Sarlioglu and C. T. Morris, "More electric aircraft: Review, challenges, and opportunities for commercial transport aircraft," *IEEE Transactions on Transportation Electrification*, vol. 1, pp. 54-64, 2015.

[35] A. Radun, "Generating with the switched reluctance motor," in *Applied Power Electronics Conference and Exposition, 1994. APEC '94. Conference Proceedings 1994., Ninth Annual*, 1994, pp. 41-47 vol.1.

[36] G. M. Raimondi, T. Sawata, M. Holme, A. Barton, G. White, J. Coles, *et al.*, "Aircraft embedded generation systems," in *2002 International Conference on Power Electronics, Machines and Drives (Conf. Publ. No. 487)*, 2002, pp. 217-222.

[37] P. H. Mellor, S. G. Burrow, T. Sawata, and M. Holme, "A wide-speed-range hybrid variable-reluctance/permanent-magnet generator for future embedded aircraft generation systems," *IEEE Transactions on Industry Applications*, vol. 41, pp. 551-556, 2005.

[38] M. J. Provost, "The More Electric Aero-engine: a general overview from an engine manufacturer," in *Power Electronics, Machines and Drives, 2002. International Conference on (Conf. Publ. No. 487)*, 2002, pp. 246-251.

[39] C. Anghel, "A novel start system for an aircraft auxiliary power unit," in *Collection of Technical Papers. 35th Intersociety Energy Conversion Engineering Conference and Exhibit (IECEC) (Cat. No.00CH37022)*, 2000, pp. 7-11 vol.1.

[40] P. J. Masson, D. S. Soban, E. Upton, J. E. Pienkos, and C. A. Luongo, "HTS motors in aircraft propulsion: design considerations," *IEEE Transactions on Applied Superconductivity*, vol. 15, pp. 2218-2221, 2005.

[41] R. E. Colyer, "Progress in electrically-propelled aircraft," in *2007 International Aegean Conference on Electrical Machines and Power Electronics*, 2007, pp. 357-362.

[42] J. E. McNamara, "Electrically driven environmental control system," *IEEE Transactions on Aerospace and Electronic Systems*, vol. AES-20, pp. 257-260, 1984.

[43] J. W. Mildice, I. G. Hansen, K. E. Schreiner, and M. E. Roth, "Variable-speed induction motor drives for aircraft environmental control compressors," in *IECEC 96. Proceedings of the 31st Intersociety Energy Conversion Engineering Conference*, 1996, pp. 209-214 vol.1.

[44] C. Gerada, K. Bradley, C. Whitley, and G. Towers, "Integrated machine design for electro mechanical actuation," in *2007 IEEE International Symposium on Industrial Electronics*, 2007, pp. 1305-1310.

[45] M. Christmann, S. Seemann, and D. P. Jänker, "Innovative approaches to electromechanical flight control actuators and systems," presented at the Recent Advances in Aerospace Actuation Systems and Components,May 5-7 2010, Toulouse, France, 2010.

[46] J. W. Bennett, B. C. Mecrow, D. J. Atkinson, and G. J. Atkinson, "Safety-critical design of electromechanical actuation systems in commercial aircraft," *IET Electric Power Applications*, vol. 5, pp. 37-47, 2011.

[47] C. Gerada and K. J. Bradley, "Integrated PM machine design for an aircraft EMA," *IEEE Transactions on Industrial Electronics*, vol. 55, pp. 3300-3306, 2008.

[48] Safran. (2015). *More-electric aircraft: to power the future*. Available: http://www.safran-electrical-power.com/media/20150408_more-electric-aircraft-power-future

[49] M. Sinnett, "787 No-bleed systems: Saving fuel and enhancing operational efficiencies," *Boeing Commercial Aeromagazine*, 2016.

[50] M. Galea, C. Gerada, T. Raminosoa, and P. Wheeler, "Design of a high force density tubular permanent magnet motor," in *The XIX International Conference on Electrical Machines - ICEM 2010*, 2010, pp. 1-6.

[51] A. G. Jack, B. C. Mecrow, and J. A. Haylock, "A comparative study of permanent magnet and switched reluctance motors for high-performance fault-tolerant applications," *IEEE Transactions on Industry Applications*, vol. 32, pp. 889-895, 1996.

[52] M. T. Abolhassani, "A novel multiphase fault tolerant high torque density permanent magnet motor drive for traction application," in *IEEE International Conference on Electric Machines and Drives, 2005.*, 2005, pp. 728-734.

[53] S. Messier-Bugatti-Dowty. (2008). *Messier-Bugatti's "Green Taxiing" solutions for smarter ground operations.* Available: http://www.safranmbd.com/actualites/actu-et-communiques-de-presse/article/messier-bugatti-s-green-taxiing?lang=en

[54] F. Re, "Assessing environmental benefits of electric aircraft taxiing through object-oriented simulation," *SAE Int. J. Aerosp.*, vol. 5, pp. 503-512, 2012.

[55] F. Re. An object-oriented model for development and assessment of green taxiing systems [Online]. Available: http://elib.dlr.de/89055/

[56] F. Re, "Viability and state of the art of environmentally friendly aircraft taxiing systems," in *2012 Electrical Systems for Aircraft, Railway and Ship Propulsion*, 2012, pp. 1-6.

[57] T. F. Johnson. Electric Green Taxiing System (EGTS) for aircraft [Online]. Available: http://tec.ieee.org/newsletter/march-april-2014/electric-green-taxiing-system-egts-for-aircraft

[58] Enviro.aero. (2016). *Electric taxiing takes aircraft efficiency to a new level; Aviation: benefits beyond borders.* Available: http://aviationbenefits.org/case-studies/electric-taxiing-takes-aircraft-efficiency-to-a-new-level/

[59] J. Careless. (2015). *Aversan aiding "WheelTug" taxiing system (November 12, 2015 ed.).* Available:

http://www.ainonline.com/aviation-news/business-aviation/2015-11-12/aversan-aiding-wheeltug-taxiing-system

[60] WheelTug. (2014). *New WheelTug E-Taxi system will save up to 20 minutes per flight (June 14, 2015 ed.)*. Available: http://www.marketwired.com/press-release/new-wheeltug-e-taxi-system-will-save-up-to-20-minutes-per-flight-2029391.htm

[61] WheelTug. (2016). *Aircraft efficiency: new WheelTug system saves about 7 minutes every flight departure (April 04, 2016 ed.)*. Available: http://www.marketwired.com/press-release/aircraft-efficiency-new-wheeltug-system-saves-about-7-minutes-every-flight-departure-2111601.htm

[62] (2016). *Airlines For America | Per-minute cost of delays to U.S. airlines*. Available: http://airlines.org/data/per-minute-cost-of-delays-to-u-s-airlines/

[63] (2016). *A flight ops challenge and the case for E-Taxi documented (2016-03-31 ed.)*. Available: http://airinsight.com/2016/03/31/case-e-taxi-documented/

[64] P. Thompson. (2014). *Electric taxiing motors could save airlines millions of dollars (13-4-2014 ed.)*. Available: http://flightclub.jalopnik.com/electric-taxiing-motors-could-save-airlines-millions-of-1562593360

[65] Safran. (2011). *Electric green taxiing: a promising new aircraft system.* Available: http://www.lebourget2011.com/news/electric-green-taxiing-a-promising-new-aircraft-system

[66] TaxiBot. (2016). *TaxiBot-International*. Available: http://www.taxibot-international.com

[67] T. Dubois. (2014). *WheelTug, Safran-Honeywell and IAI offer three rival solutions for airline engine-off taxiing (11 February 2014 ed.)*. Available: http://www.ainonline.com/aviation-news/air-transport/2014-02-11/wheeltug-safran-honeywell-and-iai-offer-three-rival-solutions-airline-engine-taxiing

[68] M. Monaghan. (2014). *Airbus exploring electric taxiing solution for A320 Family* Available: http://articles.sae.org/12708/

[69] C. Kjelgaard. (2014). *AIAA runway taxiing goes green (February 20144 ed.)*. Available: http://www.wheeltug.com/news/AIAA_Runway_Taxiing_Goes_Green.pdf

[70] Boeing. (2005). *Boeing demonstrates new technology for moving airplanes on the ground (Aug 1, 2005 ed.)*. Available: http://boeing.mediaroom.com/2005-08-01-Boeing-Demonstrates-New-Technology-for-Moving-Airplanes-on-the-Ground

[71] C. Motors. (2010). *Chorus Motors - Aerospace*. Available: http://www.chorusmotors.gi/aerospace.php

[72] (2013). *E-Taxi systems – The hidden technical challenges* Available: http://airinsight.com/2013/06/24/e-taxi-systems-the-hidden-technical-challenges/

[73] R. W. Jenny, "Aircraft wheel drive apparatus and method," ed: Google Patents, 1976.

[74] I. W. Cox, H. J. Walitzki, and J. S. Edelson, "Motor for driving aircraft, located adjacent to undercarriage wheel," ed: Google Patents, 2012.

[75] D. J. Christensen, T. Langston, D. L. Charles, and R. Velasquez, "Aircraft electric taxi system with friction actuated, bi-directional clutch," ed: Google Patents, 2013.
[76] N. Gilleran, R. Sweet, and S. Perkins, "Split circumference aircraft wheel assembly with integrated drive motor assembly," ed: Google Patents, 2013.
[77] M. Galea, S. Roggia, L. Papini, Z. Xu, C. Tighe, M. Hamiti, *et al.*, "Design aspects of a high torque density machine for an aerospace traction application," in *Electrical Machines and Systems (ICEMS), 2014 17th International Conference on*, 2014, pp. 2773-2778.
[78] Z. Xu, M. Galea, C. Tighe, T. Hamiti, C. Gerada, and S. J. Pickering, "Mechanical and thermal management design of a motor for an aircraft wheel actuator," in *2014 17th International Conference on Electrical Machines and Systems (ICEMS)*, 2014, pp. 3268-3273.
[79] J. Deur, Z. Herold, and M. Kostelac, "Modeling of electromagnetic circuit of a magnetorheological fluid clutch," in *2009 IEEE Control Applications, (CCA) & Intelligent Control, (ISIC)*, 2009, pp. 113-118.
[80] N. Mikhaeil-Boules, "Design analysis of electromagnetic particle clutch," in *Proceedings of 1994 IEEE Industry Applications Society Annual Meeting*, 1994, pp. 357-360 vol.1.
[81] W. Xiaogang, W. Xudong, Y. Tengwei, and X. Xianping, "Control of electromagnetic clutch during vehicles start," in *2008 IEEE Vehicle Power and Propulsion Conference*, 2008, pp. 1-5.
[82] J. R. Hendershot and T. J. E. Miller, *Design of brushless permanent-magnet machines*: Motor Design Books, 2010.
[83] J. Pyrhonen, *Design of rotating electrical machines / Juha Pyrhonen, Tapani Jokinen, Valeria Hrabovcova translated by Hanna Niemel*. Chichester: Chichester : John Wiley & Sons, 2008.
[84] T. Miller. (2002-2014). *SPEED's Electric Machines (with problems and solutions)*.
[85] Z. Q. Zhu, M. L. M. Jamil, and L. J. Wu, "Influence of Slot and Pole Number Combinations on Unbalanced Magnetic Force in PM Machines With Diametrically Asymmetric Windings," *IEEE Transactions on Industry Applications*, vol. 49, pp. 19-30, 2013.
[86] N. Bianchi, M. D. Prè, and L. Alberti, *Theory and Design of Fractional-slot PM Machines*: CLEUP, 2007.
[87] First4Magnets. (2016). *Samarium Cobalt Magnet - 0.86kg Pull*. Available: http://www.first4magnets.com/rectangular-magnets-c35/20-x-6-x-1-5mm-thick-samarium-cobalt-magnet-0-86kg-pull-p6427#ps_1-6591
[88] A. Daiu, "Controllo sensorless di un motore conico per applicazioni aeronautiche," Master, Dipartimento di ingegneria e architettura, Universitá di Parma, 2017.
[89] I. Corporation. (2017). *Demagnetization*. Available: https://www.infolytica.com/secured/customer/elite/livedocs/MagNet/#05-Materials/PER-PermanentMagnets/Demagnetization.htm?Highlight=proximity
[90] "IEEE Trial-use guide for testing permanent magnet machines," *IEEE Std 1812-2014*, pp. 1-56, 2015.

[91] "IEEE Guide for test procedures for synchronous machines, Part I - Acceptance and performance testing, Part II - Test procedures and parameter determination for dynamic analysis," *IEEE Std 115-2009 (Revision of IEEE Std 115-1995)*, pp. 1-219, 2010.

[92] M. Musak and M. Stulrajter. (2013) Novel method for parameters investigation of PM synchronous motor. *ACTA TECHINCA CORVINIENSIS - Bulletin of Engineering*

[93] V. Bobek, "PMSM electrical parameters measurement ", 02/2013 ed, 2013.

[94] D. W. Novotny and T. A. Lipo, *Vector Control and Dynamics of AC Drives*: Clarendon Press, 1996.

[95] S. Jaber, presented at the IAT Annual Showcase, Nottingham, 2016.

[96] M. Fatu, R. Teodorescu, I. Boldea, G. D. Andreescu, and F. Blaabjerg, "I-F starting method with smooth transition to EMF based motion-sensorless vector control of PM synchronous motor/generator," in *2008 IEEE Power Electronics Specialists Conference*, 2008, pp. 1481-1487.

[97] I. Boldea, A. Moldovan, and L. Tutelea, "Scalar V/f and I-f control of AC motor drives: An overview," in *2015 Intl Aegean Conference on Electrical Machines & Power Electronics (ACEMP), 2015 Intl Conference on Optimization of Electrical & Electronic Equipment (OPTIM) & 2015 Intl Symposium on Advanced Electromechanical Motion Systems (ELECTROMOTION)*, 2015, pp. 8-17.

[98] S. C. Agarli, x, x, F. M, x, tu, *et al.*, "I-f starting and active flux based sensorless vector control of reluctance synchronous motors, with experiments," in *Optimization of Electrical and Electronic Equipment (OPTIM), 2010 12th International Conference on*, 2010, pp. 337-342.

[99] L. I. Iepure, I. Boldea, and F. Blaabjerg, "Hybrid I-f starting and observer-based sensorless control of single-phase BLDC-PM motor drives," *IEEE Transactions on Industrial Electronics*, vol. 59, pp. 3436-3444, 2012.

[100] J. Holtz, "Sensorless control of induction machines; with or without signal injection?," *IEEE Transactions on Industrial Electronics*, vol. 53, pp. 7-30, 2005.

[101] M. Pacas, "Sensorless drives in industrial applications," *IEEE Industrial Electronics Magazine*, vol. 5, pp. 16-23, 2011.

[102] F. Gabriel, F. D. Belie, X. Neyt, and P. Lataire, "High-Frequency issues using rotating voltage injections intended for position self-sensing," *IEEE Transactions on Industrial Electronics*, vol. 60, pp. 5447-5457, 2013.

[103] F. Briz, M. W. Degner, A. Diez, and R. D. Lorenz, "Measuring, modeling, and decoupling of saturation-induced saliencies in carrier-signal injection-based sensorless AC drives," *IEEE Transactions on Industry Applications*, vol. 37, pp. 1356-1364, 2001.

[104] F. Briz, M. W. Degner, P. Garcia, and R. D. Lorenz, "Comparison of saliency-based sensorless control techniques for AC machines," *IEEE Transactions on Industry Applications*, vol. 40, pp. 1107-1115, 2004.

[105] F. Briz, M. W. Degner, A. Diez, and R. D. Lorenz, "Measuring, modeling and decoupling of saturation-induced saliencies in carrier signal injection-based sensorless AC drives," in *Industry Applications*

Conference, 2000. Conference Record of the 2000 IEEE, 2000, pp. 1842-1849 vol.3.

[106] P. L. Jansen and R. D. Lorenz, "Transducerless field orientation concepts employing saturation-induced saliencies in induction machines," *IEEE Transactions on Industry Applications*, vol. 32, pp. 1380-1393, 1996.

[107] J. Holtz, "Sensorless control of induction motor drives," *Proceedings of the IEEE*, vol. 90, pp. 1359-1394, 2002.

[108] S. Damkhi, M. S. N. Said, and N. N. Said, "Slotting effects and high frequency signal injection for induction machine rotor speed estimation," in *Electrical and Power Engineering (EPE), 2012 International Conference and Exposition on*, 2012, pp. 401-408.

[109] M. W. Degner and R. D. Lorenz, "Position estimation in induction machines utilizing rotor bar slot harmonics and carrier frequency signal injection," in *Power Conversion Conference - Nagaoka 1997., Proceedings of the*, 1997, pp. 69-72 vol.1.

[110] M. W. Degner and R. D. Lorenz, "Using multiple saliencies for the estimation of flux, position, and velocity in AC machines," *IEEE Transactions on Industry Applications*, vol. 34, pp. 1097-1104, 1998.

[111] H. Zatocil, "Sensorless control of AC machines using high-frequency excitation," in *Power Electronics and Motion Control Conference, 2008. EPE-PEMC 2008. 13th*, 2008, pp. 1024-1032.

[112] P. L. Jansen and R. D. Lorenz, "Transducerless position and velocity estimation in induction and salient AC machines," in *Proceedings of 1994 IEEE Industry Applications Society Annual Meeting*, 1994, pp. 488-495 vol.1.

[113] N. Teske, G. M. Asher, M. Sumner, and K. J. Bradley, "Analysis and suppression of high-frequency inverter modulation in sensorless position-controlled induction machine drives," *IEEE Transactions on Industry Applications*, vol. 39, pp. 10-18, 2003.

[114] N. Teske, G. M. Asher, M. Sumner, and K. J. Bradley, "Suppression of saturation saliency effects for the sensorless position control of induction motor drives under loaded conditions," *IEEE Transactions on Industrial Electronics*, vol. 47, pp. 1142-1150, 2000.

[115] H. Zatocil, "Physical understanding of multiple saliencies in induction motors and their impact on sensorless control," in *Power Electronics, Electrical Drives, Automation and Motion, 2008. SPEEDAM 2008. International Symposium on*, 2008, pp. 1503-1508.

[116] V. K. Ingle and J. G. Proakis, *Digital Signal Processing Using MATLAB*: Cengage Learning, 2011.

Appendixes

Appendix A

PM Conical Rotor Design Parameters: Additional Tables

TABLE A.1 – SLOT AND WINDING PROPERTIES CALCULATION

Bare Wire Diameter[i]	D_w	0.644mm
Conductor Area	$A_w = \frac{{D_w}^2}{2} \times \pi \times strands\ in\ hand$	0.9772mm^2
Coil Resistance	$R_c = \frac{2 \times N_t \times L_{stk}}{g \times A_w}$	0.21378Ω
Phase Resistance	$R_{ph} = \frac{2 \times N_t \times N_c \times L_{stk}}{g \times A_w}$	2.56539Ω
End Winding Gap Height	h_g	10mm
End Winding Outer Diameter	D_{ew}	148mm
End Winding Height	h_{ew}	30mm
Mean Length of Turn	$MLT = 2 \times L_{stk} + 2 \times (h_g + h_{ew}) + \frac{D_w \times \pi}{Q} \times y_q \times 2$	403.4926mm
Tot Phase Resistance	$R_{ph,tot} = \frac{MLT \times N_t \times N_c}{g * A_w}$	4.20779Ω
Line-Line Resistance	$R_{LL} = R_{ph_tot} \times 2$	8.41558Ω
Stator Inductance	L_s	94.7mH
Bare Slot Area	$A_s = \left(\frac{(w_{st} + w_{sb}) \times (h_s + r_{sb})}{2} + {r_{sb}}^2 \times \frac{\pi}{2}\right) \times k$[ii]	190.2257mm^2
Bare Slot Fill Factor	$k_{fill} = \frac{A_w \times N_t \times 2}{A_s} \times 100$	50.34306 %

[i] *Commercial diameter AWG #22*

[ii] *k=reduction factor due to insulation*

TABLE A.2 – STAR OF SLOTS AND K_W CALCULATION

Periodicity	t =GCD{Q,p}	6
Phasors	Q	36
Spokes	Q/t	6
Phasor per Spoke	t	6
Angle between Adjacent Slots	$\alpha_s = 2 \times \frac{\pi}{Q}$	10°
Angle between Adjacent Slots - Electrical	$\alpha_s^e = \alpha \times pp$	60°
Angle between Adjacent Spoke - Electrical	$\alpha_{ph} = \alpha_e \times \frac{t}{p}$	60°
Spokes per Phase	$q_{ph} = \frac{Q}{m \times t}$	2
Distribution Factor	$k_d = \frac{sin(\frac{\pi}{2 \times m})}{\frac{q_{ph}}{2} \times sin(\frac{\alpha_{ph}}{2})}$	1
Pole Pitch Factor	$\sigma_\omega = 2 \times \pi \times p \times \frac{y_q}{Q}$	2/3π
Pitch Factor	$k_p = sin\frac{\sigma_\omega}{2}$	0.8660
Winding Factor	$K_w = k_p \times k_d$	0.8660

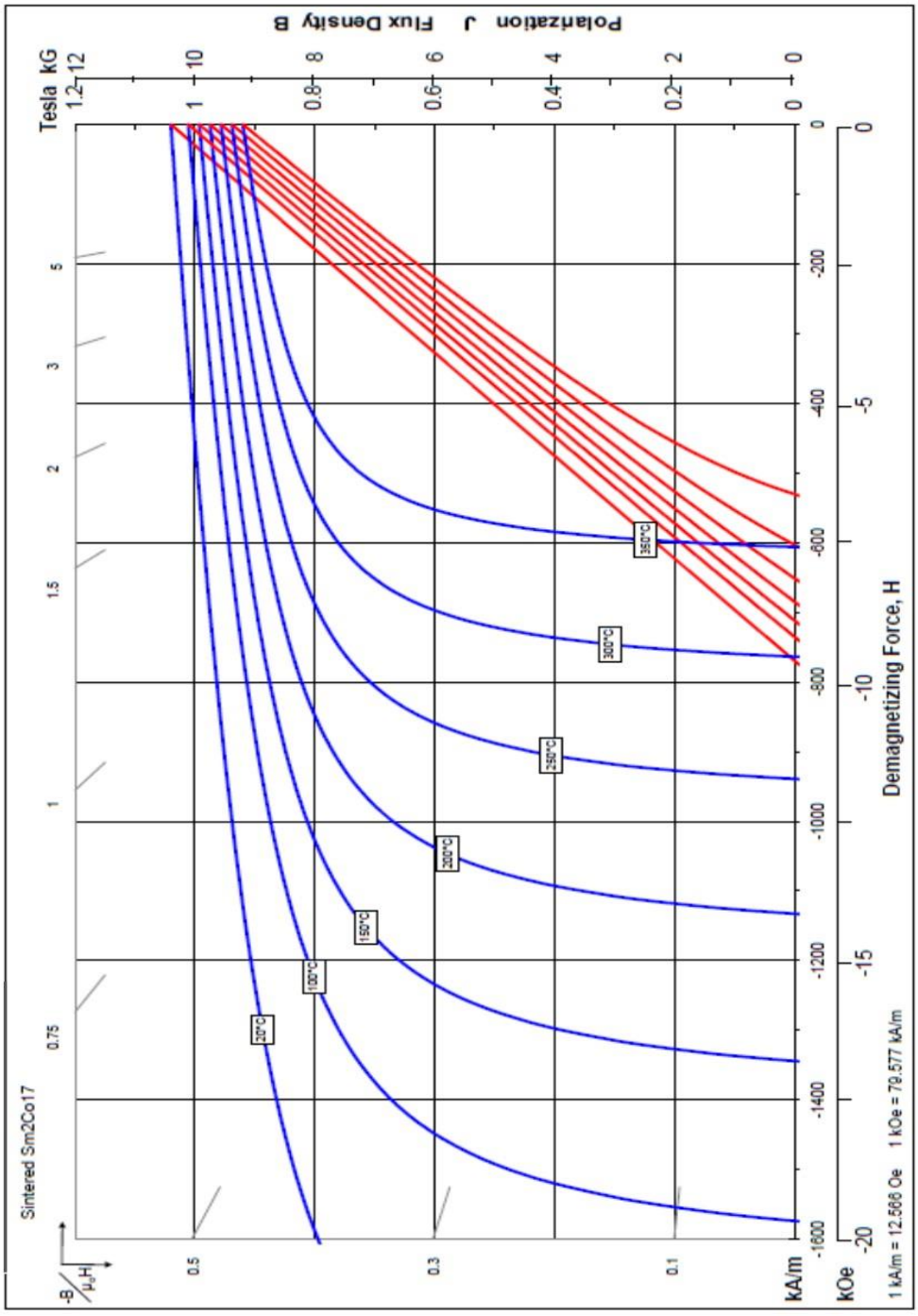
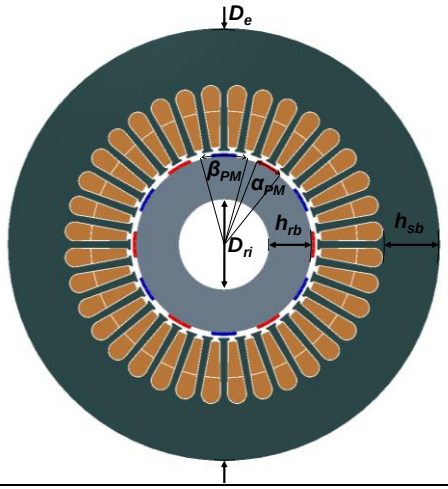
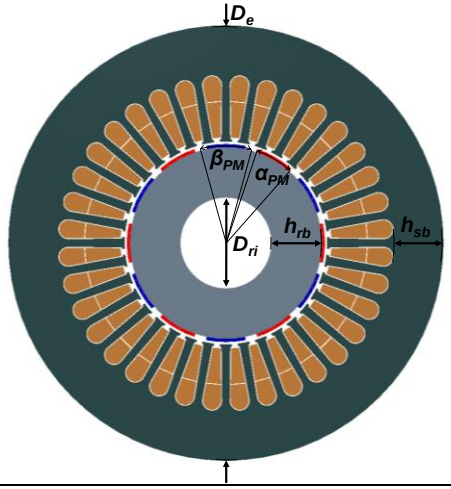
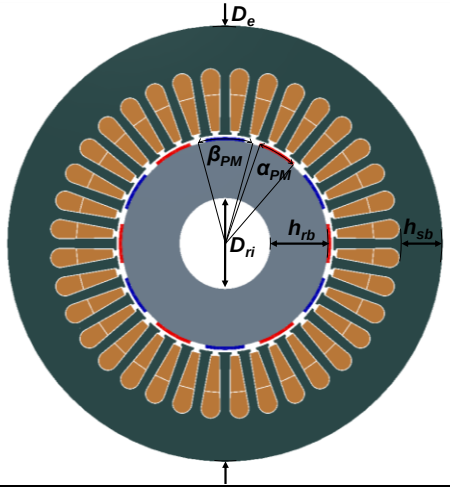
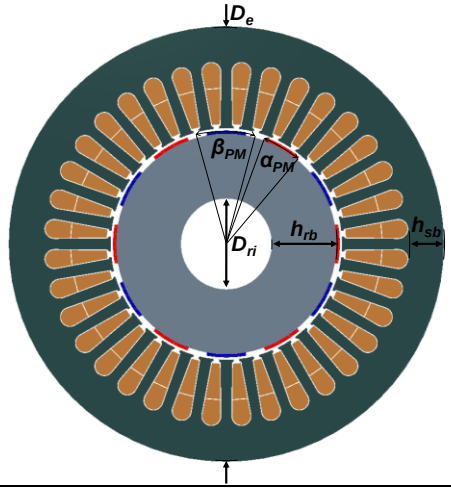
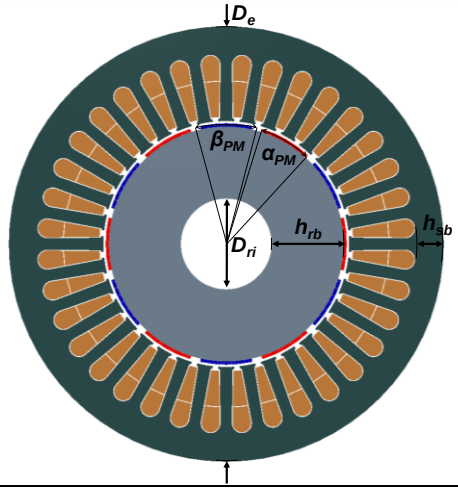
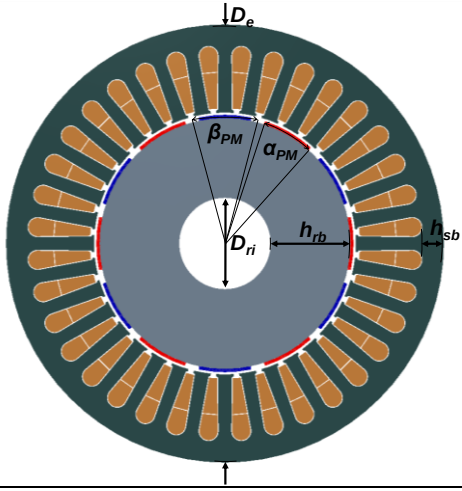


FIGURE A.1 – Sm_2Co_{17} MAGNET DEMAGNETIZATION CURVE

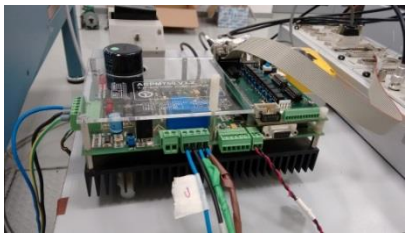
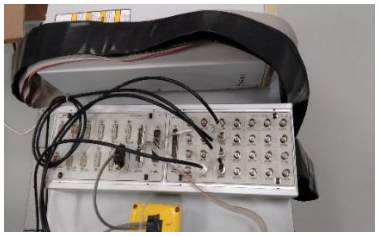
TABLE A. 3 – SUB-MOTOR CROSS-SECTIONS

		
MOTOR 1	**MOTOR 2**	**MOTOR 3**
		
MOTOR 4	**MOTOR 5**	**MOTOR 6**

Appendix B

Test-Rig Equipment Specifics

TABLE B. 1 – TEST-RIG COMPONENTS

ACPM TECHNOSOFT INVERTER
 **FIGURE B. 1 – TECHNOSOFT INVERTER** • Single phase voltage 220*Vrms* • V Dc-Link 400*V* • Output voltage 230*Vrms* • Nominal motor power 750*W* • Nominal motor current 3,5*Arms* • Switching frequency 0-24*kHz*
DS1103 PPC CONTROLLER BOARD + CONTROL PANEL CP1103
 **FIGURE B. 2 – DSPACE CONTROLLER BOARD** • 20 A/D Channels: Resolution 16-bit; Input voltage range ±10*V* • 8 D/A Channels: Resolution 16-bit; Output range ±10*V* • 32 Parallel Digital I/O Channels: Voltage TTL input/output levels: $I_{out,max}$ ±10*mA* • Digital incremental encoder interface: 6 independent channels; Single-ended (TTL) or differential (RS422); Encoder supply voltage 5*V*/1.5*A*
INDUCTION LOAD MACHINE
 **FIGURE B. 3 – INDUCTION LOAD MACHINE** • Output power 4*kW* • Efficiency 87.38% • 4 poles • Full load current 8.30*A* at 400*V*, 50*Hz*, delta connection

DATUM TORQUE SENSOR M420-S1-100NM



FIGURE B. 4 – TORQUE SENSOR

- Torque range 0-100*Nm*
- Max speed 12000*rpm*
- Signal output RS232 data
- Output data serial data 100 sample per sec
- Resolution 1:2000 (inc. *rpm*) based on 24-bit strain/torque

EMERSON UNIDRIVE SP



FIGURE B. 5 – INDUSTRIAL DRIVE

- Normal duty maximum continuous output current 11*A*
- Normal duty nominal power at 400*V* 5.5*kW*
- Normal duty peak current 12.1*A*
- Heavy duty maximum continuous output current 9.5*A*
- Heavy duty nominal power at 400*V* 4*kW*
- Heavy duty open loop peak current 14.2*A*
- Heavy duty closed loop peak current 16.2*A*

BRITISH ENCODER 25T THRU-BORE



FIGURE B. 6 – INCREMENTAL ENCODER

- 28*mm* through bore shaft
- FE flex mount
- 2500 pulses per revolution
- A, B, & Z channels with complement signals
- Line Driver output circuit

LINEAR ENCODER MAGNETIC SENSOR MSK320 AND MAGNETIC BAND



FIGURE B. 7 – LINEAR ENCODER AND MAGNETIC BAND

Linear Encoder

- Operating voltage 5*V* DC
- Output signals A, /A, B, /B,
- Reading distance up to 2*mm*

Magnetic Band

- Pole length 3.2*mm*
- Band width 5*mm*
- Thickness 1.4*mm*
- Accuracy class 100μm